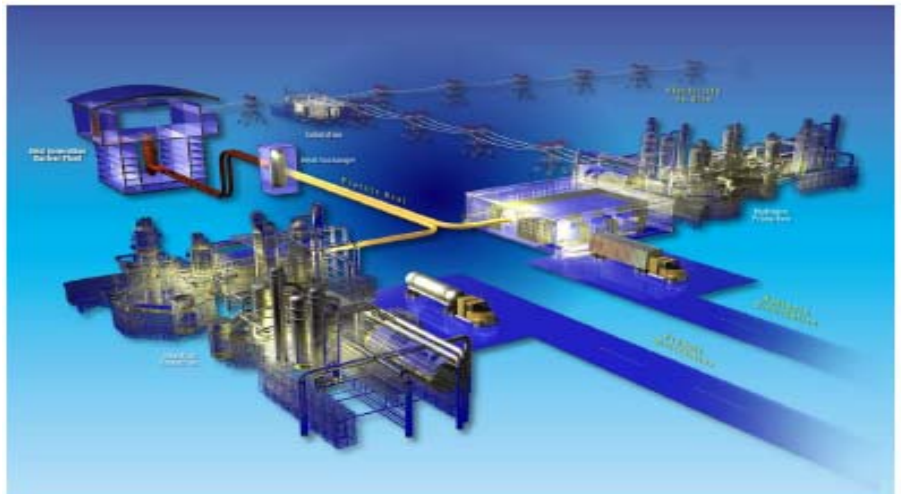


Experimental Validation of Stratified Flow Phenomena, Graphite Oxidation, and Mitigation Strategies of Air Ingress Accidents

Chang H. Oh
Eung S. Kim
Hee C. NO
Nam Z. Cho

December 2008



The INL is a U.S. Department of Energy National Laboratory operated by Battelle Energy Alliance



Experimental Validation of Stratified Flow Phenomena, Graphite Oxidation, and Mitigation Strategies of Air Ingress Accidents

Chang H. Oh
Eung S. Kim
Hee C. NO¹
Nam Z. Cho¹

¹KAIST

December 2008

**Idaho National Laboratory
Next Generation Nuclear Plant Project
Idaho Falls, Idaho 83415**

<http://www.inl.gov>

Prepared for the
U.S. Department of Energy
Office of Nuclear Energy
Under DOE Idaho Operation Office
Contract DE-AC07-05ID14517

INTERNATIONAL NUCLEAR ENERGY RESEARCH INITIATIVE
**Experimental Validation of Stratified Flow Phenomena, Graphite
Oxidation, and Mitigation Strategies of Air Ingress Accidents**

PI (U.S.): Chang H. Oh, Idaho National Laboratory (INL)

PI (Korea): Hee C. NO, Korea Advanced Institute of Science and Technology (KAIST)

Collaborators: Nam Z. Cho, Korea Advanced Institute of Science and Technology (KAIST)

Project Number: 2007-001-K

Project Start Date: October 1, 2007

Project End Date: September 31, 2010

EXECUTIVE SUMMARY

The U.S. Department of Energy is performing research that focuses on key phenomena important during challenging scenarios that may occur in the Next Generation Nuclear Plant (NGNP)/Gen-IV very high temperature reactor (VHTR). Phenomena Identification and Ranking Studies (PIRT) to date have identified the air-ingress event, following on the heels of a VHTR depressurization, as very important. Consequently, the development of advanced air ingress-related models and verification and validation (V&V) are very high priority for the NGNP Program.

A VHTR air-ingress event occurs following a loss of coolant and system depressurization, when air enters the core through the break, leading to oxidation of the in-core graphite structure and fuel. The oxidation will accelerate heat-up of the bottom reflector and reactor core, eventually causing the release of fission products. The potential collapse of the core bottom structures and the release of CO lead to serious safety problems. Estimating the proper safety margin requires experimental data and tools, including accurate multidimensional thermal-hydraulic and reactor physics models, a burn-off model, and a fracture model. It will also require effective strategies to mitigate the effects of oxidation. The results from this research will provide crucial inputs to the Idaho National Laboratory (INL) NGNP/VHTR Methods Research and Development project.

This research project is focused on (a) the analytical and experimental study of air ingress caused by density-driven, stratified, countercurrent flow, (b) advanced graphite oxidation experiments, (c) the experimental study of burn-off in the core bottom structures, (d) structural tests of the oxidized core bottom structures, (e) implementation of advanced models developed during the previous tasks into the GAMMA code, (f) full air ingress and oxidation mitigation analyses, (g) development of core neutronic models, (h) coupling of the core neutronic and thermal hydraulic models, and (i) verification and validation of the coupled models.

E-1. RESEARCH OBJECTIVES

The major goal of this project is to perform air-ingress-related analyses and experiments to reliably predict the consequences of air-ingress in the NGNP. The associated research objectives are as follows:

- Conduct experiments to supply information needed to validate GAMMA and CFD codes to model important phenomena during air-ingress accidents. These experiments will measure:
 - The effects of density-driven, stratified flow on air ingress into the reactor core
 - The internal pore area density of nuclear grade graphite, which is an important parameter for determining the oxidation rate
 - The oxidation and density variation in terms of burn-off in the core bottom structures
 - The effects of the burn-off on the structural integrity of the core bottom structures.
- Perform analyses to simulate air-ingress accidents. The major objective of these analyses is to evaluate various methods for mitigating the effects of air ingress.
- Develop coupled neutronics and thermal-hydraulic capability in the GAMMA code, which involves:
 - Development of core neutronics models
 - Coupling neutronic-thermal hydraulic tools
 - Coupled core model verification and validation (V&V).

This will allow the simulation of recriticality in conduction cool-down accidents without scram and accurate initial and transient power distribution, which are both essential for the accurate estimation of the safety margin.

E-2. REPORT CONTENT AND ORGANIZATION

This report highlights the key project accomplishments summarized in this Executive Summary. The executive summary also lists the students who supported the project. Section 1 introduces the organization on which the project is focused. Sections 2–10 discuss the task objectives and accomplishments completed during the project. Section 11 highlights results and conclusions drawn from task results.

E-3. PROJECT APPROACH AND ORGANIZATION

The proposed plan was to carry research work out over a 3-year period (FY-08 through FY-10). The plan consists of the following nine major tasks, lead by the organization in parentheses:

1. Density-difference induced stratified flow analysis (INL)
2. Experimental study on the stratified flow (INL)
3. Advanced graphite oxidation study (INL)
4. Air ingress mitigation study (INL)
5. Experiment of burn-off in the core bottom structures (KAIST)
6. Structural tests of oxidized core bottom structures (KAIST)
7. Coupling neutronic-thermal hydraulic tools (KAIST)
8. Core neutronic model (KAIST)
9. Coupled core model V&V (KAIST).

Figure E-1 shows a detailed schematic of tasks involved in this project.

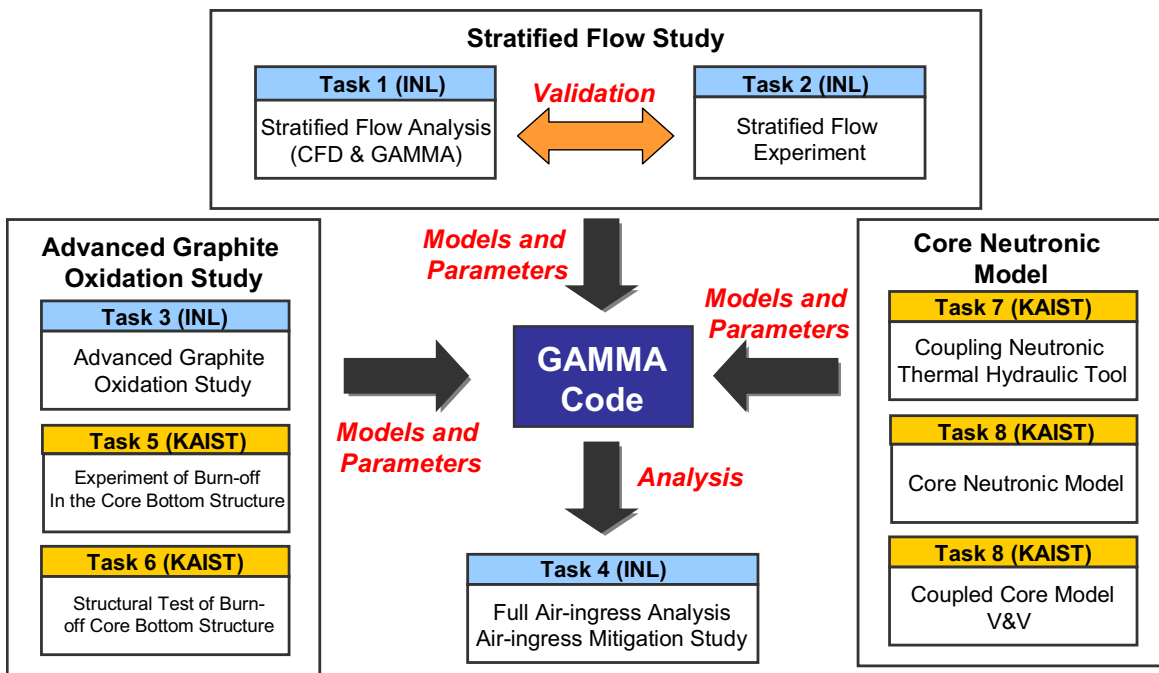


Figure E-1. Schematic diagram of all tasks involved.

E-4. KEY PROGRAM ACCOMPLISHMENTS

Highlights of key accomplishments during this fiscal year (FY-08) for the nine tasks listed above are summarized in this section. These accomplishments include items required to meet task objectives outlined in the original proposal for this project and items that meet overall I-NERI objectives. As indicated below, this project not only advanced the state-of-art in research pertaining to the VHTR, but also helped prepare graduate students to join the nuclear engineering workforce.

E-4.1 Task 1—Density-difference Induced Stratified Flow Analysis (INL)

In Task 1, a preliminary computational fluid dynamics (CFD) analysis was performed to understand density-driven stratified flow in the VHTR air-ingress accident. Various parameters were taken into consideration: turbulence model, core temperature, initial air mole-fraction, flow resistance in the core, etc. The gas turbine modular helium reactor (GT-MHR) 600 MWt was selected as the reference reactor and was simplified in modeling as a 2-D geometry. The core and the lower plenum were assumed to be porous bodies. Following the preliminary CFD results, the analysis of the air-ingress accident has been performed by two different codes; GAMMA code (system analysis code) and FLUENT code (CFD code). Eventually, the analysis results showed that the actual onset time of natural convection (~160 sec) would be significantly earlier than the previous predictions (~150 hours) calculated based on the molecular diffusion air-ingress mechanism. This leads to the conclusion that the consequences of this accident will be much more serious than expected so far.

E-4.2 Task 2—Experimental Study on the Stratified Flow (INL)

An experimental plan for the density-driven stratified flow has been established in order to validate the computer codes for air-ingress analysis. The important phenomena to be validated were identified by a design matrix, and the basic concepts of the experiments were established. The experiments are divided into two parts: isothermal and nonisothermal tests. In the isothermal test, which focuses on the separate effect of the stratified flow, the facility dimensions and sizes are determined by a simple scaling analysis in order to generate the flow similar to the reference VHTR. In the nonisothermal test, which focuses on the coupling effects with the stratified flow, including heat transfer, porous media, and chemical reactions, the onset of natural convection was selected to be the main measuring parameter. Preliminary CFD analysis showed that the onset natural circulation can be measured by the detection of mass flow and temperature changes. All the experiments were designed to be transparent for instrumentation and detection by optical devices.

E-4.3 Task 3—Advanced Graphite Oxidation Study (INL)

Various characteristics of graphite oxidation have been studied for detailed analysis of air-ingress accident. The characteristics being considered include the effect of oxidation degree on the graphite strength, effect of oxidized graphite density on the oxidation rate, and surface area density in the graphite internal pores. During this task, an experimental methodology was newly developed to validate the previous correlations related to the oxidized graphite strength, which is essential for analysis of graphite structure collapse. Following the graphite experiment, the collapse of the graphite structure was estimated for the reference VHTR by two computer codes; GAMMA code (system analysis code) and ABAQUS code (stress analysis code). The graphite oxidation and corrosion were predicted by the GAMMA code, and the information was implemented into the ABAQUS code to estimate the core collapse. Finally, the collapse time of the core bottom structures was predicted to be about 5 days after natural convection starts.

E-4.4 Task 4—Air Ingress Mitigation Study (INL)

Task 4 was not within the FY-08 scope.

E-4.5 Task 5—Experiment of Burn-off in the Core Bottom Structures (KAIST)

Korea Advanced Institute of Science and Technology (KAIST) experimentally investigated the burn-off in the core bottom graphite structure of VHTR. There are several candidate graphite materials for the core bottom structures. KAIST selected IG-110 and IG-430 for the test. Kinetics, mass diffusion, and the combined effect of kinetics and mass diffusion were investigated. Burn-off effect, moisture effect, and Boudouard reaction will be investigated next year. As a result, the order of reaction (n), activation energy (E_a) and heat/mass transfer rate coefficient were estimated. The reaction rates and CO/CO₂ were also measured in a temperature range of 700 to 1500°C and an oxygen/helium condition. IG-110 data was compared from the previous investigations. IG-430 data will be obtained and compared in FY-09. The other graphite will also be investigated in FY-09.

E-4.6 Task 6—Structural Tests of Oxidized Core Bottom Structure (KAIST)

Mechanical testing of core bottom structure graphite was carried out. Compressive strength degradation because of burn-off of graphite was investigated, as were the buckling limit and strength degradation of the oxidized graphite support column in temperatures ranging from 600 to 1050°C. As a result, the compressive strength of IG-110 was obtained as 79.46 MPa. Correlation between slenderness and buckling ratio and its applicable range were estimated. GAMMA code calculation was performed to predict the trend and condition of oxidation in the core bottom structure. Correlation of strength and various oxidized graphite samples were also obtained. Graphite columns of the same slenderness ratio have the same strength, but the graphite columns have different diameters. The slenderness ratio can thus be the scaling parameter for a simple cylindrical graphite column in strength. The critical strength of graphite, which is uniformly oxidized, can be expressed by the Knudsen relation. It turns out that the strength degradation trend of oxidized graphite structure is independent of geometry, while the strength degradation of a uniformly oxidized graphite structure is dependent on the initial strength of the structure and the bulk density change. The volume measurement technique was studied for analysis of graphite oxidized in the in-pore diffusion regime. This method will be used in analysis of graphite that is not uniformly oxidized.

Fracture model of oxidized graphite structure will be proposed for FY-09.

E-4.7 Task 7—Coupling Neutronic-Thermal Hydraulic Tools (KAIST)

KAIST proposed coupled neutronics-thermal hydraulic tools to analyze VHTR. KAIST developed a multidimensional gas multicomponent mixture analysis code (GAMMA) and multigroup 3-D (three-dimensional) hexagonal geometry neutronics code (COREDAX). These codes were coupled into a system code GAMMA/COREDAX so that the VHTR core could be analyzed. The codes were coupled by determining coupling factors, mapping nodes between the GAMMA and COREDAX, and organizing calculation logic.

E-4.8 Task 8—Core Neutronic Model (KAIST)

KAIST developed the COREDAX code based on the analytic function expansion nodal (AFEN) method in 3-D hexagonal geometry. The AFEN method includes the use of node-interface flux moments

as nodal unknowns. These nodal unknowns increase the accuracy of 3-D calculation results. In this project, multigroup extension based on matrix function theory and coarse group rebalance (CGR) acceleration were applied into the COREDAX code. The COREDAX code implementing the AFEN method was verified by testing the VVER-440 benchmark problem, a simplified VVER-1000 benchmark problem, and the SNR-300 benchmark problem.

In preparation for verification and validation of the COREDAX code for VHTR, the neutronics of a simple GT-MHR core was calculated. This core is geometrically based on the GT-MHR benchmark problem, but the cross-sections are informally obtained.

E-4.9 Task 9—Coupled Core Model V&V (KAIST)

This task involves the verification of GAMMA code coupled with COREDAX code and the validation of prediction results of thermal power distribution in the hexagonal reactor core. This task will be performed in FY-09.

E-5. STUDENT PARTICIPATION

List of Students (U.S.)

University of Wisconsin

Jong Bin Lim

List of Students (ROK)

KAIST

Ji-Hwan Kim

Ho Joon Yoon

Hyeonil Kim

Jong Woon Kim

Hyung Gon Jin

Jae-Jun Lee

Sung-Hwan Yoon

Young Soo Kim

Byung Ha Park

Han Jong Ryu

Jae Hoon Song

CONTENTS

EXECUTIVE SUMMARY	v
ACRONYMS.....	xxi
1. INTRODUCTION.....	1-1
1.1 Objectives.....	1-1
1.2 Background.....	1-1
1.3 Research and Development Plan.....	1-2
1.3.1 Task 1: Density-Difference Induced Stratified Flow Analysis (INL)—FY-08 and FY-09 Task.....	1-2
1.3.2 Task 2: Experimental Study on the Stratified Flow (INL)—FY-09 Task.....	1-3
1.3.3 Task 3: Advanced Graphite Oxidation Study (INL)—FY-08 and FY-09 Task.....	1-3
1.3.4 Task 4: Air Ingress Mitigation Study (INL)—FY-10 Task	1-3
1.3.5 Task 5: Experiment of Burn-off in the Core Bottom Structures (KAIST).....	1-3
1.3.6 Task 6: Structural Tests of Oxidized Core Bottom Structures (KAIST)—FY-09 and FY-10 Task	1-4
1.3.7 Task 7: Coupling Neutronic-Thermal Hydraulic Tools (KAIST)—FY-09 Task.....	1-4
1.3.8 Task 8: Core Neutronic Model (KAIST)—FY-08 and FY-09 Task.....	1-4
1.3.9 Task 9: Coupled Core Model V&V (KAIST)—FY-09 Task.....	1-4
1.4 Research and Development Collaboration.....	1-5
2. TASK 1: DENSITY-DIFFERENCE INDUCED STRATIFIED FLOW ANALYSIS (INL).....	2-1
2.1 Introduction.....	2-1
2.2 Preliminary CFD Analysis for Density-Difference Induced Stratified Flow	2-3
2.2.1 Problem Description	2-3
2.2.2 Solver and Model Set-up.....	2-5
2.2.3 Operating, Boundary, and Initial Conditions	2-6
2.2.4 Turbulence Models	2-8
2.2.5 Determination of Porous Body Parameters.....	2-11
2.2.6 Determination of Core Temperature	2-19
2.2.7 Determination of Air Mole Fraction	2-20
2.2.8 Preliminary CFD Analysis of Density Driven Stratified Flow	2-21
2.3 Air-ingress Analysis Including Stratified Flow in the VHTR.....	2-40
2.3.1 Simulation of Stratified Flow by CFD.....	2-40
2.3.2 Air-Ingress Analysis by GAMMA Code	2-43
2.3.3 Summary of the Air-ingress Analysis, including Stratified Flow Effect	2-52
3. TASK 2: EXPERIMENTAL STUDY ON THE STRATIFIED FLOW (INL).....	3-1
3.1 Introduction.....	3-1
3.2 Required Validation Data for Stratified Flow Driven Air-ingress Analysis.....	3-1
3.3 Planned Experiment	3-5
3.3.1 Isothermal Experiment in the Horizontal Circular Pipe (TEST 1).....	3-5
3.3.2 Stratified Flow and Natural Convection Test (TEST2) under Nonisothermal Conditions	3-10

3.3.3	Stratified Flow and Natural Convection Tests with Pebbles (or Structure) (TEST3) Under Nonisothermal conditions	3-15
3.3.4	Stratified Flow and Natural Convection Test with Graphite Pebbles (or Structure) (TEST4) Under Nonisothermal Conditions.....	3-16
3.3.5	Isothermal Stratified Flow Test (TEST5)	3-17
4.	TASK 3: ADVANCED GRAPHITE OXIDATION STUDY (INL).....	4-1
4.1	Introduction.....	4-1
4.2	Experiment on Validation for the Fracture of Oxidized Graphite.....	4-1
4.2.1	Introduction.....	4-1
4.2.2	Main Idea	4-2
4.2.3	Experimental Facility and Setup	4-3
4.2.4	Results and Discussions	4-6
4.3	Graphite Surface Area Density	4-14
4.4	Effect of Graphite Burn-off on the Oxidation Rate.....	4-15
4.5	Modeling of Graphite Oxidation and Fracture in Air-ingress.....	4-19
4.5.1	Stress Analysis Strategy.....	4-19
4.5.2	Structural Dimensions.....	4-22
4.5.3	Change of Temperature, Burn-off and Corrosion Thickness	4-24
4.5.4	Material Database	4-25
4.5.5	Treatment of Material Properties during Analysis.....	4-28
4.5.6	Initial Unoxidized State Results.....	4-29
4.5.7	Oxidized State Results	4-32
5.	TASK 4: AIR INGRESS MITIGATION STUDY (INL).....	5-1
6.	TASK 5: EXPERIMENT OF BURN-OFF IN THE CORE BOTTOM STRUCTURES (KAIST).....	6-1
6.1	Graphite Selection.....	6-1
6.2	Graphite Oxidation Model	6-2
6.2.1	Kinetics Effect.....	6-2
6.2.2	Mass Diffusion Effect	6-3
6.2.3	Combined Effect of Kinetics and Mass Diffusion	6-4
6.2.4	Hybrid Oxidation Model.....	6-5
6.2.5	Burn-off Effect.....	6-5
6.2.6	Effect of Moisture and Boudouard Reaction	6-5
6.3	Nomenclatures for Task 5	6-7
7.	TASK 6: STRUCTURAL TESTS OF OXIDIZED CORE BOTTOM STRUCTURES (KAIST).....	7-1
7.1	Failure Mechanism of Graphite Column.....	7-2
7.2	Compressive Strength and Buckling without Oxidation.....	7-3
7.3	Estimation of Burn-off of Graphite Support Columns by GAMMA	7-7
7.3.1	GAMMA Air Ingress 1-D and 2-D Pipe Comparison	7-7
7.3.2	GAMMA Air ingress 1-D Pipe with Pulse Signal	7-9
7.4	Compressive Strength and Bucking Strength with Graphite Oxidation.....	7-10
7.5	Measurement Technique	7-15
7.6	Summary	7-17

7.7	Nomenclature for Task 6.....	7-17
8.	TASK 7: COUPLING NEUTRONIC-THERMAL HYDRAULIC TOOLS (KAIST).....	8-1
8.1	Coupling Procedure.....	8-1
8.1.1	Coupling Variables	8-1
8.1.2	Calculation Node Mapping Method.....	8-1
8.1.3	Calculation Procedure in a Coupling System.....	8-2
9.	TASK 8: CORE NEUTRONIC MODEL (KAIST)	9-1
9.1	Basic Theory and Method	9-1
9.1.1	Nodal Unknowns and Nodal Equations	9-1
9.1.2	Multigroup Extension	9-4
9.1.3	Coarse Group Rebalance Acceleration	9-4
9.2	Verification of the COREDAX Code	9-6
9.2.1	VVER-440 Benchmark Problem	9-6
9.2.2	A Simplified VVER-1000 Benchmark Problem.....	9-7
9.2.3	SNR-400 Benchmark Problem.....	9-9
9.3	Test on GT-MHR Core Model.....	9-10
9.3.1	Description	9-10
9.3.2	Test Results	9-12
10.	TASK 9: COUPLED CORE MODEL V&V (KAIST).....	10-1
11.	SUMMARY AND CONCLUSIONS	11-1
12.	REFERENCES	12-1

FIGURES

Figure E-1.	Schematic diagram of all tasks involved.	vi
Figure 2-1.	Density-driven induced stratified flow.....	2-1
Figure 2-2.	Geometry and size of GT-MHR 600 MWt reactor.	2-4
Figure 2-3.	Simplified 2-D geometry of GT-MHR 600 MWt for preliminary stratified flow simulation.	2-4
Figure 2-4.	Geometry and mesh for stratified flow analysis.....	2-5
Figure 2-5.	Time advancement schemes in the FLUENT (FLUENT user's guide, 2007).	2-6
Figure 2-6.	Heat capacities for air and helium gases (P = 1.0 atm).	2-7
Figure 2-7.	Thermal conductivities for air and helium gases (P = 1.0 atm).....	2-7
Figure 2-8.	Viscosities for air and helium gases (P = 1.0 atm).	2-8
Figure 2-9.	Core pattern (d = 1.58 cm, p = 3.27 cm). (Internal Design Review Presentation Material, General Atomics, San Diego, 1997).....	2-12
Figure 2-10.	Typical geometry of lower plenum (d _{LP} = 0.212 m, P _{LP} = 0.36 m). The red circle represents rod (McEligot and McCreery 2004).	2-12
Figure 2-11.	Detail view of lower plenum in GT-MHR 600 MWt.....	2-13

Figure 2-12. Friction factor correlation.....	2-14
Figure 2-13. Equally spaced triangular tube array (Vassallo and Symolon 2007).	2-16
Figure 2-14. Cross-flow friction factor data for staggered tube arrays (Vassallo and Symolon 2007).....	2-16
Figure 2-15. GT-MHR 600 MWt GAMMA nodalization.	2-19
Figure 2-16. Time variations of the temperatures in the reactor core during an air-ingress accident.	2-20
Figure 2-17. Grid sensitivity (Normal: 31,232 meshes, Fine: 53,601 meshes).....	2-21
Figure 2-18. Variations of air distributions in the reactor during stratified flow.....	2-22
Figure 2-19. Air distributions before and after stratified flow.....	2-23
Figure 2-20. Variations of averaged air mole fractions.	2-23
Figure 2-21. Comparisons between original and stratified flow assumption.....	2-24
Figure 2-22. Velocity vectors and air mole fraction contour at the broken pipe.	2-24
Figure 2-23. Variations of air mole fractions in the reactor cavity for different reactor temperatures during stratified flow process (k-ε realizable model).....	2-26
Figure 2-24. Effect of core temperature on the air distribution in the reactor (after 90 sec).	2-27
Figure 2-25. Air profile at the center of the reactor core after stratified flow process (k-ε realizable model).	2-27
Figure 2-26. Average air mole fractions in the lower plenum for different turbulence models.	2-28
Figure 2-27. Average air mole fractions in the reactor cavity for different turbulence models.....	2-29
Figure 2-28. Quasi-equilibrium states for different turbulent models. Nonisothermal (core temperature = 300K [27°C]).....	2-29
Figure 2-29. Average air mole fractions in the lower plenum for different turbulence model ($T_{core}=1300K$ [1027°C]).....	2-30
Figure 2-30. Average air mole fractions in the reactor cavity for different turbulence model ($T_{core}=1300K$ [1027°C]).....	2-30
Figure 2-31. Quasi-equilibrium states for different turbulent models ($T_{core}=1300K$ [1027°C]).....	2-31
Figure 2-32. Comparisons of air mole fractions at the center of the reactor core between laminar model and k-ε realizable turbulence model ($T_{core}=1300K$ [1027°C]).....	2-31
Figure 2-33. Normalized air mole fractions in Zone 5. (MF: initial mass fraction, mf: initial mole fraction)	2-32
Figure 2-34. Normalized air mole fractions in Zone 5. (MF: initial mass fraction, mf: initial mole fraction)	2-33
Figure 2-35. Air mole fractions vs. semi-onset time for equilibration.....	2-33
Figure 2-36. Distribution of air-mole fractions for different initial air concentration in the reactor cavity (MF: initial mass fraction)—isothermal.	2-34
Figure 2-37. Distribution of air-mole fractions for different initial air concentration in the reactor cavity (MF: initial mass fraction)—nonisothermal.	2-34

Figure 2-38. Effects of initial cavity concentration in the heated condition. (k-ε realizable model, 1300 K [1027°C])	2-35
Figure 2-39. Air mole fractions in the reactor cavity.....	2-36
Figure 2-40. Air mole fraction distributions for internal resistance (90 seconds).	2-36
Figure 2-41. Air mole fractions in the reactor cavity.....	2-37
Figure 2-42. Air mole fraction distributions for different permeability (90 sec) ($T_{\text{core}}=1300\text{K}$ [1027°C]).....	2-37
Figure 2-43. Original air-ingress accident scenarios with diffusion assumption.....	2-38
Figure 2-44. Air-ingress accident scenarios, including stratified flow phenomenon.....	2-39
Figure 2-45. Reference reactor (GT-MHR 600 MWt) and Mesh of FLUENT 6.3.....	2-41
Figure 2-46. Initial condition of temperature and air mole fraction for CFD analysis (nonconservative).	2-42
Figure 2-47. CFD analysis results (air mole fraction) of stratified flow in VHTR (nonconservative).	2-42
Figure 2-48. GT-MHR 600 MWt code nodalization (GAMMA).	2-43
Figure 2-49. Temperature variations at the reactor core (hot spot).....	2-46
Figure 2-50. Temperature variations at the bottom reflector.	2-46
Figure 2-51. Temperature variations at the lower plenum.	2-47
Figure 2-52. Temperature variations at the top reflector.	2-47
Figure 2-53. Oxygen mole fraction in the reactor core (SFDA-2) during natural convection stage (estimated by the GAMMA code).	2-48
Figure 2-54. Localized degree of graphite oxidation in the lower plenum.	2-49
Figure 2-55. Localized degree of graphite oxidation in the bottom reflector.	2-49
Figure 2-56. Localized degree of graphite oxidation in the reactor core.	2-50
Figure 2-57. Void fraction of graphite structure at the lower plenum.	2-51
Figure 2-58. Void fraction of graphite structure at the bottom reflector.....	2-51
Figure 2-59. Void fraction of graphite structure at the reactor core.	2-52
Figure 3-1. Isothermal experiment in the horizontal pipe (schematic).	3-6
Figure 3-2. State view of laser induced fluorescence.	3-7
Figure 3-3. Schematics of the countercurrent stratified flow behavior in the VHTR hot duct.	3-8
Figure 3-4. Stratified flow and natural convection test (schematics).....	3-10
Figure 3-5. FLUENT simulation for flow driven air-ingress experiment (air mole fraction).....	3-13
Figure 3-6. Time vs. mass flow at the cold side outlet.	3-14
Figure 3-7. Time vs. temperature at the cold side outlet.....	3-14
Figure 3-8. Comparisons of different experimental cases.	3-14
Figure 3-9. Stratified flow and natural convection test with pebbles (schematics).	3-15

Figure 3-10. Stratified flow and natural convection test with structures (schematics).....	3-16
Figure 3-11. Stratified flow and natural convection test with graphite pebbles (schematic).....	3-16
Figure 3-12. Stratified flow and natural convection test with graphite structure (schematic).....	3-17
Figure 3-13. Isothermal Stratified Flow Test (Schematic).....	3-17
Figure 4-1. Experimental data of compressive strength with burn-off (Eto and Growcock 1983).....	4-2
Figure 4-2. Basic idea on the prediction of graphite compressive strength.	4-3
Figure 4-3. Schematic of the graphite oxidation test station setup.	4-4
Figure 4-4. LabVIEW program user interface.	4-4
Figure 4-5. Data file example.	4-5
Figure 4-6. Schematic of the sample holder and loader setup.	4-6
Figure 4-7. Variations of sample mass with time (IG-110 Case 1, 650°C).	4-7
Figure 4-8. Variations of sample mass with time (IG-110 Case 2, 650°C).	4-8
Figure 4-9. Variations of sample mass with time (IG-110 Case 3, 650°C).	4-9
Figure 4-10. Variations of sample mass with time (H451 Case 1, 650°C).....	4-10
Figure 4-11. Variations of sample mass with time (H451 Case 2, 650°C).....	4-11
Figure 4-12. Variations of sample mass with time (H451 Case 3, 650°C).....	4-12
Figure 4-13. Normal compressive strength vs. burnoff (IG-110).	4-13
Figure 4-14. Normal compressive strength vs. burnoff (H451).....	4-14
Figure 4-15. Measurement of BET surface area by Contescu (2008).....	4-15
Figure 4-16. Burn-off vs. F_b (IG-110 and H451).....	4-17
Figure 4-17. Comparisons of surface area density and oxidation rate between IG-110 and H451.....	4-17
Figure 4-18. Burn-off vs. F_b (NBG-10).	4-18
Figure 4-19. Burn-off vs. F_b (NBG-18).	4-18
Figure 4-20. Burn-off vs. F_b (V484T).....	4-19
Figure 4-21. GT-MHR core side view(Shenoy 2007).	4-20
Figure 4-22. Top cutaway view of the core (Cocheme 2004).....	4-20
Figure 4-23. ABAQUS generated whole and cut view of the support block and plenum.	4-21
Figure 4-24. The dimensions of a General Atomics GT-MHR fuel block.	4-22
Figure 4-25. Plenum: (a) side views (with dimensions) and (b) wireframe top view.....	4-23
Figure 4-26. Corrosion depths and section assignments.....	4-24
Figure 4-27. GAMMA results of temperature over time.	4-24
Figure 4-28. GAMMA results of burn-off over time.....	4-25
Figure 4-29. (a) Tensile strength as function of the burn-off; (b) compressive strength as function of the burn-off (Ishihara et al. 2004).	4-26
Figure 4-30. Tensile strength as function of temperature (Eto et al. 1986).	4-26

Figure 4-31. (a) The change in Young’s modulus because of oxidation as a function of temperature (best fit of experiment data); (b) the correlations for Young’s modulus as a function of temperature and burn off (Eto et al. 1986).....	4-27
Figure 4-32. Young’s modulus (a) and mechanical strength (b) as function of dpa caused by irradiation (Burchell et al. 1996).	4-28
Figure 4-33. (a) Compressive stress-strain curve for UNS31803 Steel (Rasmussen 2001) (b) Compressive stress-strain curve for IG-110 (Fujii et al. 1997).	4-29
Figure 4-34. Compressive stress distribution on unoxidized support block and plenum.....	4-30
Figure 4-35. The principal stress components (Beer et al. 2006).	4-31
Figure 4-36. (a) Upper part of support block with triangular prism; (b) mesh and temperature distribution; (c) compressive stress; (d) tensile stress.	4-32
Figure 4-37. Modification of plenum head’s height.	4-32
Figure 4-38. 1/6 cyclic symmetry unit of the modified plenum head for each day.	4-33
Figure 4-39. Maximum compressive stress (a) and tensile stress (b) over time.	4-35
Figure 4-40. Compressive stress distribution on plenum head, 12.25 days after LOCA.....	4-35
Figure 4-41. Tensile stress distribution on plenum head, 12.25 days after LOCA.....	4-36
Figure 4-42. Thermal and load stress distributions for bottom half of the pillar, 11.25 days after LOCA.	4-37
Figure 6-1. Schematic of experimental facility.....	6-2
Figure 6-2. Experimental facility.....	6-3
Figure 6-3. Oxidation rate of IG-110 (Oh et al. 2006).....	6-4
Figure 6-4. CO/CO ₂ Ratio for IG-110.	6-4
Figure 6-5. Schematic on the moisture supply device (Kim 2005).....	6-6
Figure 7-1. Schematics of GT-MHR 600MWt and graphite support column in the lower plenum.	7-1
Figure 7-2. Schematics of oxidation in graphite column.	7-2
Figure 7-3. Compression test facility, INSTRON Model 4204.	7-3
Figure 7-4. Buckling strength.	7-6
Figure 7-5. Buckling strength of Φ 15 mm columns.	7-7
Figure 7-6. GT-MHR 600MWt 1-D pipe nodalization.....	7-8
Figure 7-7. GT-MHR 600MWt 2-D pipe nodalization.....	7-8
Figure 7-8. Corroded graphite density of bottom reflector after air-ingress occurred.....	7-9
Figure 7-9. Pulse signal applied junction (JB265).....	7-10
Figure 7-10. Pulse induced mass flow rate at hot leg inlet (JB265).....	7-10
Figure 7-11. Test facility with an electrical furnace.	7-11
Figure 7-12. Inside of the electrical furnace.	7-11
Figure 7-13. Changes in compressive strength as a function of bulk density.....	7-12

Figure 7-14. Normalized buckling strength of oxidized graphite columns.....	7-13
Figure 7-15. Normalized strength of oxidized graphite column.	7-13
Figure 7-16. Fracture load changes of oxidized samples.	7-14
Figure 7-17. Strength changes of wet samples.	7-16
Figure 8-1. Example of calculation node mapping.	8-2
Figure 8-2. Calculation procedure in neutronics code.	8-3
Figure 9-1. Coordinates in a hexagon.	9-2
Figure 9-2. Interface flux moments on six radial interfaces.	9-3
Figure 9-3. Rebalance factors.	9-6
Figure 9-4. Core configuration of 3-D VVER-440.	9-7
Figure 9-5. Radial core geometry of simplified 3-D VVER-100.	9-8
Figure 9-6. Axial core geometry of 3-D VVER-1000.	9-8
Figure 9-7. Radial core geometry of 3-D SNR-300.	9-9
Figure 9-8. Axial core geometry of 3-D SNR-300.	9-10
Figure 9-9. Active core and its component arrangement.	9-11
Figure 9-10. Fuel block cell (type 1FA).	9-11
Figure 9-11. Fuel block with cavity for control rod or reserve shutdown system (type 2FA).	9-12
Figure 9-12. Radial core configuration of simplified 3-D GT-MHR.	9-12

TABLES

Table 1-1. Organization responsibilities by task.....	1-5
Table 2-1. Polynomial coefficient for gas properties (Air) (in Equation 2-1).	2-8
Table 2-2. Polynomial coefficient for gas properties (helium) (in Equation 2-1).	2-8
Table 2-3. Correlation for the friction factor and their mean absolute errors. (Kosar et al., 2005)	2-17
Table 2-4. Assumed size of the GT-MWR 600 MWt system components.....	2-40
Table 2-5. Predicted onset of natural convection time.....	2-44
Table 3-1. Experiments and validation data for the air-ingress analysis.	3-2
Table 3-2. Design matrix for diffusion driven air-ingress validation experiments.	3-4
Table 3-3. Design matrix for stratified flow driven air-ingress analysis.	3-5
Table 3-4. Summary of scaling results (ratio = prototype/fullscale).	3-9
Table 4-1. Parameters in Equation (4-1) for various graphite materials (Eto and Growcock 1983).	4-2
Table 4-2. Summary of the experimental data.	4-12
Table 4-3. Summary of surface area density for graphite.	4-15
Table 4-4. Basic thermo-mechanical properties of IG-110 at standard conditions. (Ishihara et al. 2004, Burchell 1991).	4-25

Table 4-5. Comparison of the analytical solution to the ABAQUS result.....	4-31
Table 4-6. Material properties at each day.....	4-34
Table 6-1. Graphite selection matrix.....	6-1
Table 6-2. Properties of IG-110 and IG-430 manufactured by Toyo Tanso in Japan.....	6-2
Table 6-3 Activation energy and order of reaction	6-3
Table 7-1. Test matrix.....	7-4
Table 7-2. Compressive strength of IG-110.....	7-4
Table 7-3. Specimens for the buckling test.....	7-5
Table 7-4. Specimens for additional buckling test.....	7-6
Table 7-5. Geometry and number of graphite columns.	7-12
Table 7-6. Graphite samples of complicated-shapes.....	7-14
Table 7-7. Comparison of bulk density.....	7-16
Table 8-1. Coupling variables.....	8-1
Table 9-1. Results of VVER-440 benchmark problem ^a	9-6
Table 9-2. Results on CGR acceleration of VVER-440 benchmark problem ^a	9-7
Table 9-3. Results on k_{eff} of simplified VVER-1000 benchmark problem.	9-9
Table 9-4. Results of SNR-300 benchmark problem.....	9-10
Table 9-5. Results on k_{eff} of simplified GT-MHR benchmark problem.....	9-13

ACRONYMS

AFEN	analytic function expansion nodal
ASTM	American Society for Testing and Materials
BET	Brunaur-Emmett-Teller
CFD	computational fluid dynamics
DDA	diffusion dominated air-ingress
DOE	Department of Energy
DP	design parameters
FA	fuel assembly
FR	function requirements
GA	General Atomic
GT-MHR	gas turbine modular helium reactor
HTGR	high temperature gas reactor
HTTR	High Temperature Engineering Test Reactor
ICCD	intensified charge-couple device
INL	Idaho National Laboratory
KAIST	Korea Advanced Institute of Science and Technology
LIF	laser-induced fluorescence
LOCA	loss-of-coolant accident
LWR	light water reactor
NGNP	Next Generation Nuclear Plant
ONC	onset of natural convection
ORNL	Oak Ridge National Laboratory
PIRT	Phenomena Identification Ranking Table
PIV	particle image velocimetry
PLIF	planar laser-induced fluorescence
PBMR	pebble bed modular reactor
R&D	research and development
RCCS	reactor cavity cooling system
RSM	Reynold's Stress Model
SFDA	stratified flow dominated air-ingress
V&V	verification and validation
VHTR	very high temperature gas-cooled reactor

Experimental Validation of Stratified Flow Phenomena, Graphite Oxidation, and Mitigation Strategies of Air Ingress Accidents

1. INTRODUCTION

A loss-of-coolant accident (LOCA) is considered a critical event for a very high temperature gas-cooled reactor (VHTR). Following helium depressurization, it is anticipated that, unless countermeasures are taken, air will enter the core through the break leading to oxidation of the in-core graphite structure. Thus, without mitigation features, a LOCA will lead to an air ingress event, which in turn will lead to exothermic chemical reactions of graphite with oxygen, core collapse, and toxic gas release, potentially resulting in significant safety problems.

The U.S. Department of Energy is performing research and development (R&D) that focuses on key phenomena important during challenging scenarios that may occur in the Next Generation Nuclear Plant (NGNP)/GEN-IV VHTR. Phenomena Identification and Ranking Table (PIRT) studies to date have identified the air ingress event, following on the heels of a VHTR depressurization, as very important (Schultz et al. 2006). Consequently, the development of advanced air ingress-related models and verification and validation (V&V) requirements are high priorities for the NGNP Program.

1.1 Objectives

The major goal of this 3-year study is to perform air-ingress-related experiments and validate the computer codes, such as computational fluid dynamics (CFD) and GAMMA, so they can be reliably used to predict the consequences of air-ingress in the NGNP. The associated research objectives are as follows:

- Conduct experiments to supply information needed to validate GAMMA and CFD codes to model important phenomena during air-ingress accidents. These experiments will measure:
 - The effects of density-driven, stratified flow on air ingress into the reactor core
 - The internal pore area density of nuclear grade graphite, which is an important parameter for determining the oxidation rate
 - The oxidation and density variation in terms of burn-off in the core bottom structures
 - The effects of the burn-off on the structural integrity of the core bottom structures.
- Perform analyses to simulate air-ingress accidents. The major objective of these analyses is to evaluate various methods for mitigating the effects of air ingress.
- Develop coupled neutronics and thermal-hydraulic capability in the GAMMA code, which involves:
 - Development of core neutronics models
 - Coupling neutronic-thermal hydraulic tools
 - Coupled core model verification and validation (V&V).

This will allow the simulation of recriticality in conduction cool-down accidents without scram and accurate initial and transient power distribution, which are both essential for the accurate estimation of the safety margin.

1.2 Background

The VHTR is a graphite-moderated, uranium-fueled, helium-cooled reactor using a direct or indirect gas cycle to convert the heat generated by nuclear fission into electrical energy by means of a helium

turbo-generator. High temperature gas reactor (HTGR) technology has been researched and developed since the 1950s. The VHTR produces a higher outlet temperature than the HTGR. VHTRs work on the principle of passing a cooling gas through the core, then running the heated gas directly to a steam generator or a gas turbine. VHTRs have been built in Japan and China for their nuclear research. VHTRs have several advantages over light water reactors (LWRs), including fuel integrity, proliferation resistance, a relatively simple fuel cycle, easy refueling, and modularity to supply electricity to remote areas and energy-starved underdeveloped countries with a smaller power generation infrastructure. The characteristics of the VHTR are helium coolant, higher than 900°C outlet temperature, and a modularity of 600 MWt. Benefits of the VHTR concept are high thermal efficiency compared to other concepts, hydrogen production using VHTR process heat, and a high degree of passive safety. However, the VHTR faces some technical and economical challenges, particularly reactor safety and costs. The plant design should be streamlined to be technically sound, robust, proliferation-resistant, and economical. Even though gas reactors have been developed in the past with limited success, the innovations of modularity and integrated state-of-the-art safety systems make the VHTR design attractive from a technical and economic perspective.

Although the VHTR has many advantages over LWRs, it faces some technical and economical challenges, particularly reactor safety and cost. Concerns about the VHTR are the safety-related technical issues. The very high temperatures of this reactor concept can be detrimental to safety if a LOCA occurs that results in the loss of coolant through the break and coolant depressurization, allowing air to enter the core through the break by molecular diffusion and ultimately by natural convection. This LOCA will lead to the oxidation of the in-core graphite structure and fuel, which will accelerate heat-up of the reactor core and the release of toxic gasses (CO and CO₂) and fission products. Without effective countermeasures, a pipe break may lead to significant fuel damage and fission product release.

To resolve these concerns, a well-validated safety and design analysis tool is needed. As the first step, the GAMMA code was successfully developed, which has a capability to analyze the air-ingress accident under a VHTR LOCA as part of the International Nuclear Energy Research Initiative program (Oh et al. 2006). To complete the mission of solving the technical challenges, the GAMMA code will be further improved so it can deal with all the possible transient situations expected in air ingress.

Two important new issues are associated with air-ingress in a VHTR. One concerns the potential core collapse accident caused by fracture of the graphite support structure following oxidation. The other is associated with stratified flow caused by density differences that will accelerate the air ingress into the lower plenum of the reactor. It is obvious that both phenomena have the potential to cause some serious physical consequences to VHTR safety. However, little attention has been paid to either one until recently. It is therefore necessary to significantly investigate these phenomena to better estimate VHTR safety.

1.3 Research and Development Plan

1.3.1 Task 1: Density-Difference Induced Stratified Flow Analysis (INL)—FY-08 and FY-09 Task

This task involves computational analyses to validate the density-difference induced air ingress phenomena expected in the VHTR following air ingress. After the break in the hot duct hypothesized in a depressurized conduction cool-down, air present in the reactor cavity will enter the reactor vessel via a density-driven stratified flow. Because of the significantly higher molecular weight and lower initial temperature of the reactor cavity air, the air-helium mixture in the cavity is heavier than the helium discharging through the break. In the later stages of the helium blow-down, the momentum of the helium flow decreases sufficiently that the heavier cavity air can flow into the reactor vessel lower plenum through the lower portion of the broken hot duct while helium flows in the opposite direction in the upper portion of the hot duct. Once it enters the reactor, the heavier gas will pool at the bottom of the lower

plenum where it will diffuse upwards into the core. This condition (based on the countercurrent stratified flow assumption) is considerably different from the standard assumption used in calculations to date where the air is assumed to diffuse into the lower plenum through the hot duct. Preliminary calculations performed as part of this FY-08 task show that countercurrent stratified flow occurs and significantly accelerates air ingress. In this task, the characteristics and behaviors of these phenomena are analyzed and estimated by computational and theoretical methods. The following activities will be carried out in this task:

- CFD analysis of the stratified flow (part of FY-08 task)
- Development of stratified flow model for GAMMA
- Air-ingress analyses including stratified flow phenomena
- Validation of GAMMA using experimental data from Task-2.

1.3.2 Task 2: Experimental Study on the Stratified Flow (INL)—FY-09 Task

This task involves experimental data collection to provide a baseline for validation of CFD and GAMMA codes based on experimental results. In this task, a test flow loop will be set up mimicking the density-difference induced air ingress phenomena. The following parameters will be investigated:

- Test flow loop setup
- Flow visualization
- Parametric study.

1.3.3 Task 3: Advanced Graphite Oxidation Study (INL)—FY-08 and FY-09 Task

This task measures the transient graphite oxidation with burn-off and the internal pore surface area density of nuclear-grade graphite, which was found to be a very important parameter in the early stage of graphite oxidation. The results of these measurements will be implemented into the upgraded GAMMA code. The following activities will be carried out in this task:

- Measurement of surface area density of nuclear graphite using Brunaur-Emmett-Teller (BET) method
- Measurement of transient graphite oxidation with burn-off
- Implementation of the advanced graphite material parameters into GAMMA code.

1.3.4 Task 4: Air Ingress Mitigation Study (INL)—FY-10 Task

This task develops potential methods of air-ingress mitigation and evaluates the effects of those methods by computational means. Full air-ingress analyses will be performed by the upgraded GAMMA code. These analyses will consider all the possible physical phenomena expected in an air-ingress accident, including: gas diffusion, natural convection, stratified flow, radiation, conduction and convection, and porous media. The following activities will be carried out in this task:

- Set up the advanced air-ingress analysis
- Develop air-ingress mitigation methods (Conceptual study)
- Analyze full air-ingress and evaluate mitigation methods.

1.3.5 Task 5: Experiment of Burn-off in the Core Bottom Structures (KAIST)

This task measures the oxidation rate and the density of the nuclear graphite and will develop oxidation models of the core bottom structures, which would be exposed to air in a LOCA. The main

parameters that affect the rate of oxidation and the density of the graphite of the core bottom are kinetics, mass diffusion, combined effect of kinetics and mass diffusion, moisture, shape and size, and degree of burn-off. The following activities will be carried out in this task:

- Measurement of oxidation rate of nuclear graphite
- Measurement of density of nuclear graphite with burn-off.

1.3.6 Task 6: Structural Tests of Oxidized Core Bottom Structures (KAIST)—FY-09 and FY-10 Task

This task involves the fracture model regarding the oxidation of the nuclear graphite. Because of the density changes in the nuclear graphite, structural characteristics will be investigated and the fracture model of the core bottom structures will be developed by fracture test, including the internal pressure test, uniaxial compression test, diametrical compression test, and fracture toughness test. The following activities will be carried out in this task:

- Fracture test of nuclear graphite with burn-off
- Development of fracture model of burnt-off bottom reflector.

1.3.7 Task 7: Coupling Neutronic-Thermal Hydraulic Tools (KAIST)—FY-09 Task

This task involves the enhancement of thermal-hydraulic capability of GAMMA code. Thermal power distribution in the reactor core is needed to improve the reliability of thermal-hydraulic analysis. The knowledge of accurate thermal distribution is also needed to generate exact cross-section of nuclei. Neutronics/thermal-hydraulics feedback effects will be therefore investigated and the feedback parameters will be implemented into an upgraded GAMMA code. The following activities will be carried out in this task:

- Set up parameters for neutronics/thermal-hydraulics code coupling
- Code coupling of COREDAX with GAMMA.

1.3.8 Task 8: Core Neutronic Model (KAIST)—FY-08 and FY-09 Task

This task involves an advanced neutronics code for both steady and transient analysis of a VHTR core. Korea Advanced Institute of Science and Technology (KAIST) developed COREDAX code to analyze the hexagonal-z 3-D (three-dimensional) geometry. The COREDAX code is based on analytic function expansion nodal (AFEN) method, which does not use the transverse-integration procedure, but uses analytic basis functions to represent solution with utmost accuracy. The COREDAX and GAMMA coupled code will provide accurate analysis of initial condition power distribution of VHTR by feedback calculation with each other. In this task, the COREDAX code will be developed to deal with the hexagonal-z 3-D geometry. COREDAX code will be used to investigate the feedback between neutronics and thermal-hydraulics. The following activities will be carried out in this task:

- Development of a VHTR core neutronics analysis code in hexagonal 3-D geometry
- Investigation of neutronics/thermal-hydraulics feedback effects.

1.3.9 Task 9: Coupled Core Model V&V (KAIST)—FY-09 Task

This task involves the verification of GAMMA code coupled with COREDAX code and the validation of prediction results of thermal power distribution in the hexagonal reactor core. The following activities will be carried out in this task:

- Verification of GAMMA and COREDAX coupling
- Validation of coupled code with reference data.

1.4 Research and Development Collaboration

The proposed research was carried out as collaboration between Idaho National Laboratory (INL) in the United States and KAIST in Korea. Both INL and KAIST provided project management and integration in addition to performing work on technical tasks. This collaboration exploited unique capabilities and resources available at these organizations.

The individual task responsibilities of INL and KAIST are listed in Table 1-1. Activities for the tasks where INL and KAIST shared the leadership and technical performance responsibilities were planned and executed with a high degree of coordination between the organizations.

Table 1-1. Organization responsibilities by task.

Task No.	Lead	INL Responsibilities	KAIST Responsibilities
0.0	Shared	Project management at INL	Project management at KAIST
0.1	Shared	Prepare annual reports	Prepare annual reports
1.0	INL	Analysis of stratified flow	Review and comments
2.0	INL	Experiment on stratified flow	Review and comments
3.0	INL	Experiment and analysis on graphite oxidation	Review and comments
4.0	INL	Full air ingress analysis for reference reactor Method development for air-ingress mitigation	Modeling and method validation Review and comments
5.0	KAIST	Review and comments	Experiment on burn-off of bottom reflector graphite
6.0	KAIST	Review and comments Generating backup data	Fracture test and analysis
7.0	KAIST	Review and comments	Coupling neutronic-thermal hydraulic tool
8.0	KAIST	Review and comments	Development of core neutronic model
9.0	KAIST	Review and comments	Validation of coupled code

2. TASK 1: DENSITY-DIFFERENCE INDUCED STRATIFIED FLOW ANALYSIS (INL)

2.1 Introduction

The potential for air ingress into the VHTR vessel stems from consideration of postulated LOCAs. The VHTR is located in a reactor cavity that is filled with air under normal operational conditions. If a LOCA occurs, air may be given the opportunity to move into the reactor vessel. It is presently thought that the worst-case scenario will occur if a double-ended guillotine break is postulated in the hot duct. The hot duct is a large pipe (exact dimensions presently not defined, but the outer diameter is over a meter) that connects the reactor vessel with the vessel housing the power conversion equipment.

For a double-ended guillotine rupture, the transient will commence with a depressurization from operating pressure (assumed to be approximately 7 to 9 MPa) as helium is discharged into the reactor cavity. During the depressurization phase hot helium from the vessel will mix with the air in the reactor cavity. Hence, a helium-laced air mixture will be available to move into the reactor vessel once the break is unchoked and the flow behavior at the break changes from momentum-driven flow from the reactor vessel into the reactor cavity to density-gradient driven stratified countercurrent flow with helium moving into the reactor cavity and helium-laced air moving into the reactor vessel from the reactor cavity.

The potential for density-gradient governed stratified air ingress into the VHTR following a large-break LOCA was first described in the NGNP Methods Technical Program (Schultz et al. 2006) based on stratified flow studies performed with liquid (Liou et al. 1997, 2005). Studies on density-gradient-driven stratified flow in advanced reactor systems has been the subject of active research for well over a decade because density-gradient dominated stratified flow is an inherent characteristic of passive systems used in advanced reactors.

The work done on Generation 3+ systems, although for LWRs, is conceptually identical and directly applicable to the phenomenological behavior that occurs in the NGNP. Even though the earlier studies were based on Generation 3+ systems using water as the working fluid, the governing equations are identical. The boundary conditions change to reflect the differences in the working fluid and the reactor vessel geometry. Recently a simple computational fluid dynamic calculation was made to mimic the LOCA between two tanks filled with helium and oxygen, respectively. The scenario is depicted in Figure 2-1.

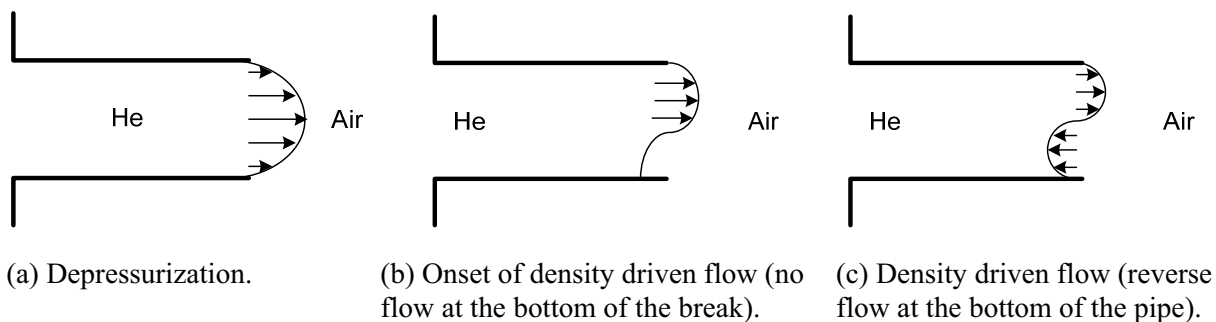


Figure 2-1. Density-driven induced stratified flow.

Earlier studies of the mechanisms leading to air ingress into the reactor vessel were focused on diffusion as described by Fick's Law (Takeda 1997, Takeda and Hishida 1996, Oh et al. 2006, Kim et al. 2007, NO et al. 2007) and ignored the effects of density gradients on the interactions between helium (low density) and air or helium-laced air (high density) flow.

Air ingress into the reactor vessel stemming from density-gradient-driven stratified flow occurs in a much quicker time scale than diffusion, resulting in a depressurized conduction cooling scenario with a different set of boundary conditions than previously assumed. Hence experiments are needed to study these phenomena as noted in the NNGP Methods Thermal-Fluids Experiment Plan (Schultz et al. 2006). Subsequent to the break in the hot duct hypothesized in depressurized conduction cool-down, air present in the reactor cavity will enter the reactor vessel, and because of the significantly higher molecular weight and lower initial temperature of the reactor cavity air, the air-helium mixture in the cavity is always heavier than the helium discharging from the reactor vessel through the break into the reactor cavity. Once the air-helium mixture enters the reactor vessel, it will pool at the bottom of the lower plenum. It will move from the lower plenum into the core via diffusion and density-gradients induced by heating. When density-gradient-driven stratified flow is considered as a contributing phenomena for air ingress into the reactor vessel, the following factors contribute to a much earlier natural circulation-phase in the reactor vessel: (a) density-gradient-driven stratified flow is a much more rapid mechanism (at least one order of magnitude) for moving air into the reactor vessel lower plenum than diffusion, and consequently, (b) the diffusion dominated phase begins with a much larger flow area and a much shorter distance for air to move into the core than earlier scenarios that attribute all air ingress from the reactor cavity into the core to diffusion only.

In essence, the stratified flow assumption is based on the formation of a wedge of air at the lower portion of the hot duct break which will advance into the reactor vessel as a function of the density-gradients when the blowdown has become unchoked. Such flows are well characterized by the densimetric Froude number F , which correlates the densities of helium and the air mixture to a constant value representative of the flow condition at different times in the scenario.

$$F = \frac{u}{\sqrt{g'd}} \quad (2-1)$$

where u = discharge velocity of air, d = hydraulic depth of air, and g' = reduced gravity defined by

$$g' = \frac{g(\rho_2 - \rho_1)}{\rho_2 + \rho_1} \quad (2-2)$$

The buoyancy induced by the density difference of the two fluids necessitates the usage of reduced gravity g' instead of the standard gravity g . The magnitude of F indicates the magnitude of inertia force relative to the buoyancy created by stratification, and is a controlling parameter in stratified flows. This idea and experimental confirmation can be found in Liou et al. (1997) and Yih (1980).

A stratified flow experiment is required to better understand this phenomenon and provide data for code validation because the codes will be used in conjunction with systems analysis codes to model this inherently multidimensional phenomenon. It is expected the densimetric Froude number will be found to be a function of

$$F = f\left(\alpha, L/D, \frac{V_{vessel}}{V_{vault}}, Pr, R\right) \quad (2-3)$$

where α = orientation of the break with respect to the vertical, L = length of the separated hot duct on the reactor vessel side, D = diameter of the hot duct, V = volume, Pr = Pressure coefficient, and R = Reynolds number.

Thus, as shown above in Figure 2-1(a), outward flow of helium into the reactor cavity from the reactor vessel continues until the reactor pressure is sufficiently reduced to unchoke the blowdown flow. Thereafter, air starts to intrude into the pipe through the lower portion of the break as depicted in Figure 2-1(b) and Figure 2-1(c). In a rectangular flow cross section, it can be shown theoretically that the volumetric flow rate of the two fluids through the break is the same (Liou 1997). Therefore it is assumed that the helium volumetric flow and air volumetric flow are equal. The heavy air will enter the vessel and collected (allowing dome turbulent mixing) at the bottom of the VHTR and air will penetrate the VHTR lower plenum and the core through the diffusion. The diffusion will trigger a natural circulation in the reactor, resulting in graphite oxidation, which will be detrimental to VHTR safety. If the stratified air flow induces the natural circulation flow to begin earlier than previously thought, the time frame for graphite oxidation will occur earlier and at a more rapid rate. Earlier predictions from the GAMMA code (NO et al. 2007) predict oxidation between 150 and 200 hours following pipe rupture, depending on the initial air volume in the containment. Calculations using MELCOR predict that oxidation begins at 220 hours (Yih 1980) following pipe rupture. However, recent CFD calculations (Oh et al., 2008), using the stratified flow approach, predict that natural circulation commences much earlier than 150 hours. Hence, the need to clarify the understanding of this phenomena and its effect on the progression of the scenario are quite important.

2.2 Preliminary CFD Analysis for Density-Difference Induced Stratified Flow

2.2.1 Problem Description

Preliminary calculations were performed using commercial CFD code FLUENT 6.3 (2007) in order to estimate the air ingress that stems from density-gradient driven stratified flow. A short description of the underlying assumptions is given below. The FLUENT code has been used to model the hot duct and reactor vessel of the gas turbine modular helium reactor (GT-MHR) 600 MWt (GA, 1997)—a General Atomic, Inc. (GA) design with a prismatic core. Figure 2-2 shows the reactor configuration; overall size and dimensions are specified here.

For the first simulation, the reactor core was highly simplified because the detailed geometry of the reactor is too complicated to be rigorously modeled. For simplification, the core, reflector and lower plenum were considered as porous bodies. The simplified geometry is illustrated in Figure 2-3. The flow path between the cavity and the core (the break) includes only the core and a portion of the reactor cavity. The volume of the containment was not taken into consideration for these preliminary calculations. The effect of containment volume will be discussed in the Section 2.3. The fluid region was divided into five parts: Zone 1 represents the core, Zone 2 represents the lower plenum, Zone 3 represents the hot duct, Zone 4 represents the vessel inside, and Zone 5 represents the reactor cavity.

Figure 2-4 shows the geometry and mesh of this reactor core developed by GAMBIT mesh generation software (FLUENT 2007). The total number of meshes for the reactor and the cavity is 31,232, and they are all hexagonally meshed.

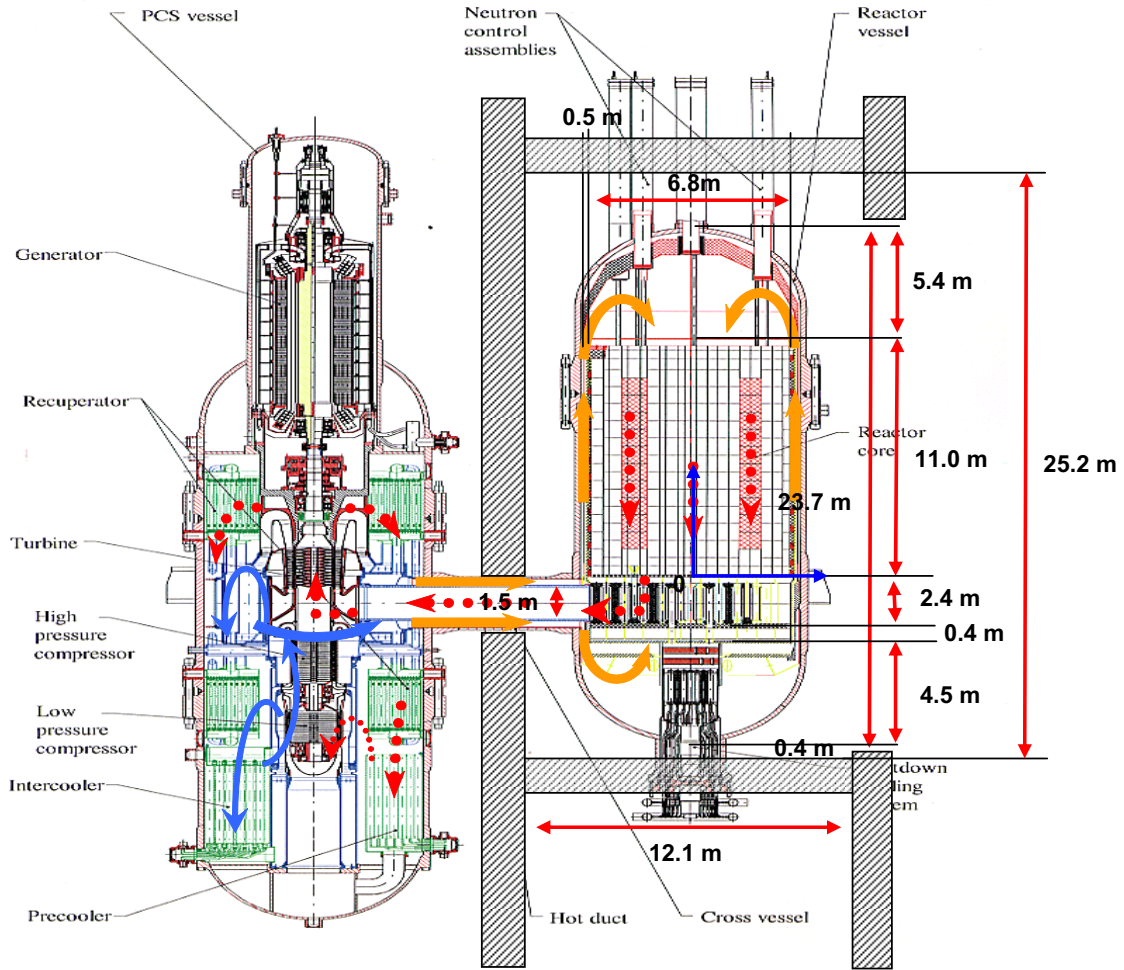


Figure 2-2. Geometry and size of GT-MHR 600 MWt reactor.

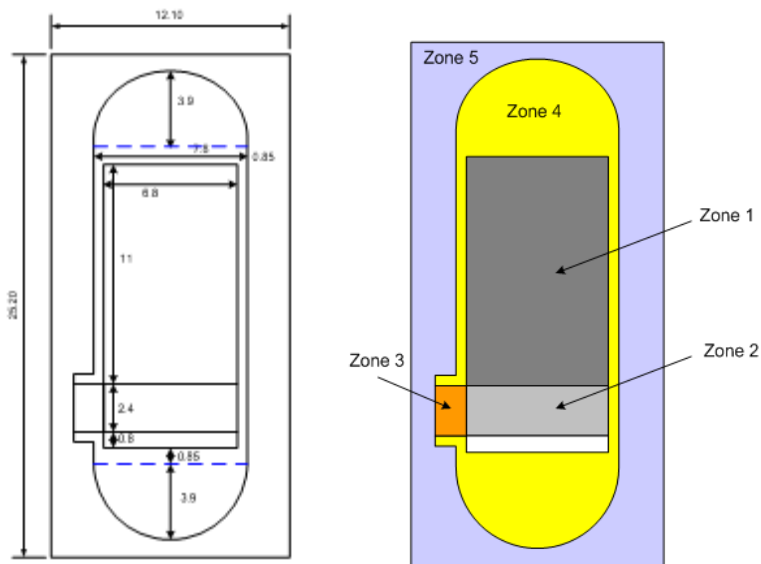


Figure 2-3. Simplified 2-D geometry of GT-MHR 600 MWt for preliminary stratified flow simulation.

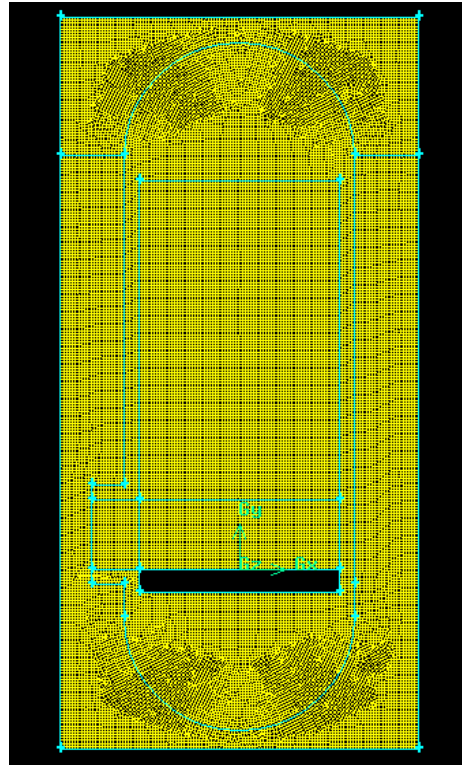


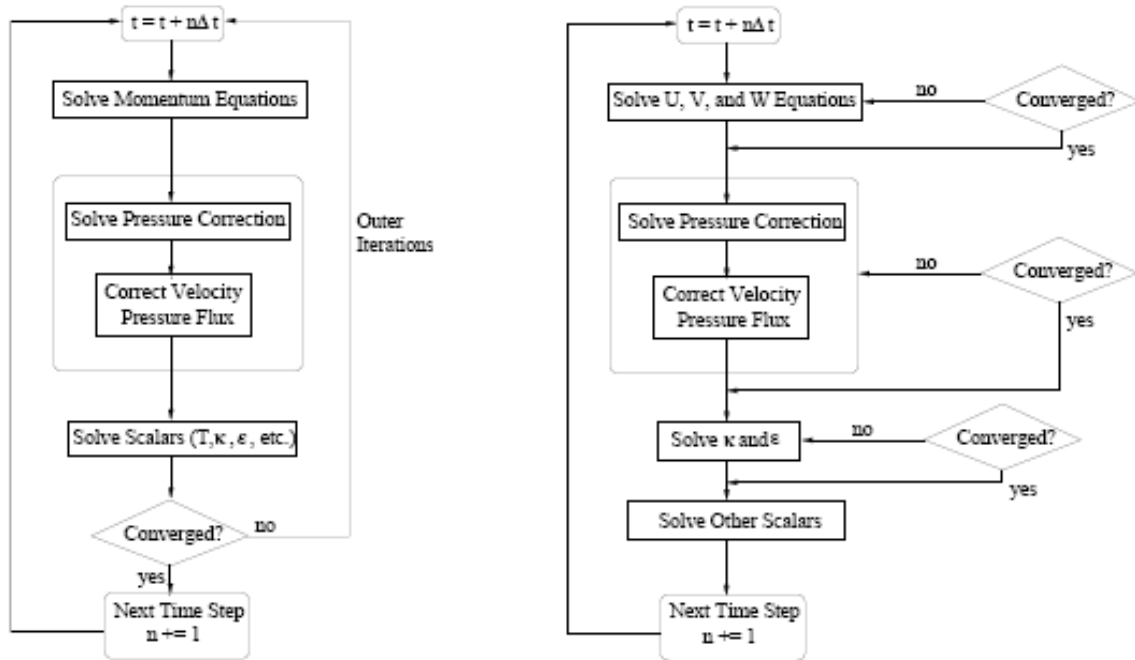
Figure 2-4. Geometry and mesh for stratified flow analysis.

2.2.2 Solver and Model Set-up

The solver and model set-up of this first calculation are as follows:

- Solver
 - 2-D (hexagonal mesh (31,232 cells))
 - Segregated solver
 - First order implicit
 - Unsteady
 - Noniterative time advancement
 - Absolute velocity formulation
 - Cell-based gradient
 - Superficial velocity in porous formulation
- Energy Equation
- Viscous Model
 - Laminar/Turbulence (k-e or Reynolds stress model [RSM])
 - Standard k-e
 - Standard wall function
- Species Model
 - Species transport equation
 - 2 gas species: Air/Helium.

This simulation adapts a noniterative time-advancement scheme. The traditional iterative time-advancement scheme requires a considerable amount of computational effort because of a large number of outer iterations performed for each time-step. The idea underlying the noniterative time-advancement (NITA) scheme is that, in order to preserve overall time accuracy, there is no need to reduce the splitting error to zero, only make it the same order as the truncation error. Thus, the NITA scheme shown in Figure 2-5 does not need the outer iterations because it performs only a single outer iteration per time-step, which significantly speeds up transient simulations (FLUENT 2007).



(a) Iterative time-advancement scheme

(b) Noniterative time-advancement scheme

Figure 2-5. Time advancement schemes in the FLUENT (FLUENT user's guide, 2007).

2.2.3 Operating, Boundary, and Initial Conditions

For the first calculation, the operating pressure was set equal to be 1.0 atm (101,325 Pa) in all the fluid zones. Gravity force (acceleration of gravity = 9.8 m/s^2) was defined in the negative y-direction in order to consider the density driven force.

Air and helium were the two gas species considered. The detail mixture model is summarized as follows:

- Mixture species: air/helium
- Density calculation: incompressible ideal gas law
- Heat capacity calculation: mass weighted mixing law
- Thermal conductivity calculation: mass weighted mixing law
- Viscosity calculation: ideal gas mixing law
- Mass diffusion calculation: constant dilute approximation.

The property model of each species was set using National Institute of Science and Technology's (NIST's) chemistry Web book (2008) as a form of a polynomial function. Figure 2-6 through Figure 2-8 show the gas properties as a function of absolute temperature for air and helium gases. Tables 2-1 and 2-2 summarize the polynomial coefficients for property equations. The property equations have the form

$$\phi(T) = A1 + A2 \cdot T + A3 \cdot T^2 + A4 \cdot T^3 + A5 \cdot T^4. \quad (2-4)$$

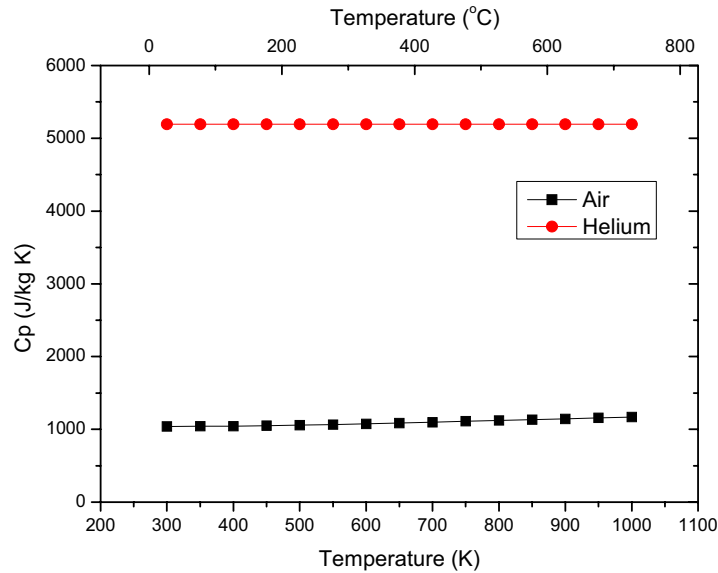


Figure 2-6. Heat capacities for air and helium gases (P = 1.0 atm).

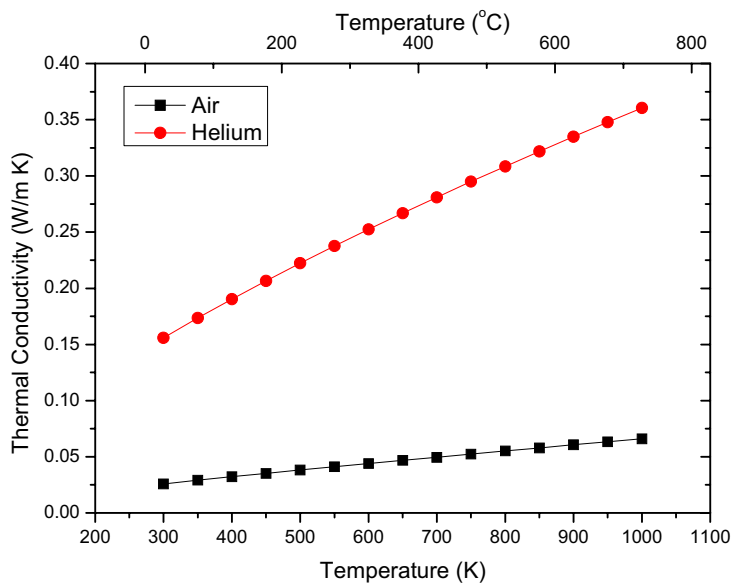


Figure 2-7. Thermal conductivities for air and helium gases (P = 1.0 atm).

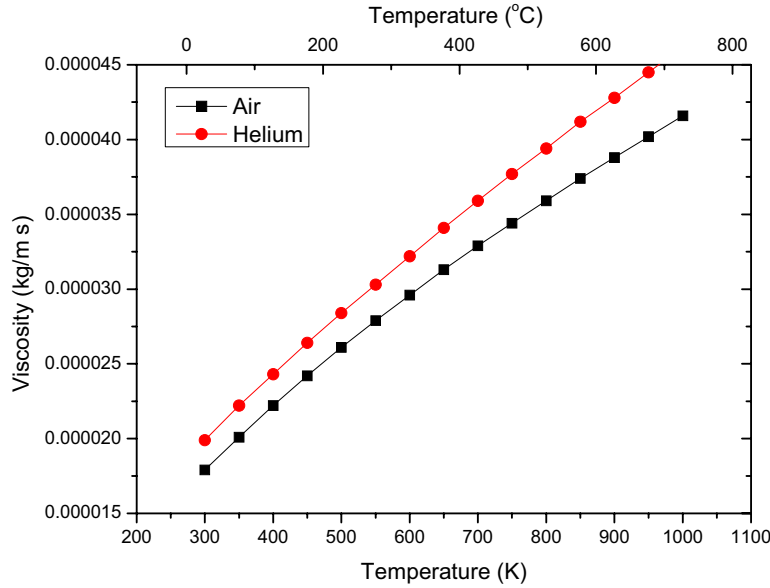


Figure 2-8. Viscosities for air and helium gases (P = 1.0 atm).

Table 2-1. Polynomial coefficient for gas properties (Air) (in Equation 2-1).

	Cp (J/kg K)	k (W/m K)	Viscosity (kg/m s)
A1	1108.53	0.00939	4.26E-06
A2	-4.61E-01	5.71E-05	4.97E-08
A3	9.09E-04	0	-1.25E-11
A4	-3.90E-07	0	0
A5	0	0	0

Table 2-2. Polynomial coefficient for gas properties (helium) (in Equation 2-1).

	Cp (J/kg K)	k (W/m K)	Viscosity (kg/m s)
A1	5193	0.07497	6.35E-06
A2	0	2.90E-04	4.81E-08
A3	0	0	-8.39E-12
A4	0	0	0
A5	0	0	0

2.2.4 Turbulence Models

Currently, no single turbulence model is universally accepted as being superior for all classes of problems. The choice of turbulence model will depend on considerations such as the physics encompassed in the flow, the established practice for a specific class of problem, the level of accuracy required, the available computational resources, and the amount of time available for the simulation.

In the stratified flow, the driving force is the density difference between air and helium, so the flow velocity is not very fast. For this reason, it is expected that the flow has a low Re number. However, because of the large pipe diameter and the low viscosity, it is not clear if the flow is within a laminar regime or a low Reynolds number turbulent regime.

This study considered the following turbulence models (the below summary refers to the FLUENT user's guide (2007)).

- Laminar model
- Standard k- ϵ model
- RNG k- ϵ model
- Realizable k- ϵ model
- k- ω model
- Reynolds stress model

2.2.4.1 Standard k- ϵ Model

The standard k- ϵ turbulence model is the simplest complete model of turbulence. It consists of two equations and determines the turbulence and length scale independently by solving two separate transport equations. The standard k- ϵ model was first proposed by Launder and Spalding (1974). It is the most popular turbulence model at this time in the industry thanks to its robustness, economy, and reasonable accuracy for a wide range of turbulent flows. It is a semi-empirical model, and the derivation of the model equations relies on phenomenological consideration and empiricism. The strength and weakness of this model are very well known. Many variants were developed to improve its performance. The advantages and disadvantages of this model is as follows (Fluent User's Guide (2007)):

- Advantages
 - Relatively simple to implement
 - Leads to stable calculations that converge relatively easily
 - Reasonable predictions for many flows
- Disadvantages
 - Poor prediction for:
 - Swirling and rotating flows
 - Flows with strong separation
 - Axi-symmetric Jets
 - Certain unconfined flows
 - Fully developed flows in noncircular ducts
 - Valid only for fully turbulent flows
 - Simplistic ϵ equation.

2.2.4.2 RNG k- ϵ model

The RNG k- ϵ model was derived using a rigorous statistical technique (renormalization group theory) (Fluent User's Guide). It is similar in form to the standard k- ϵ model but includes:

- Additional term in ϵ equation for interaction between turbulence dissipation and mean shear
- The effect of swirl on turbulence
- Analytical formula for turbulent Prandtl number
- Differential formula for effective viscosity.

This modification improved the predictions for high stream line curvature and strain rate, transitional flow and wall heat and mass transfer. But it does not correctly predict the spreading of a round jet.

2.2.4.3 Realizable k - ϵ Model

The realizable k - ϵ model is a relatively recent development and differs from the standard k - ϵ model in two important ways [Fluent User's Guide (2007)]:

- The realizable k - ϵ model contains a new formulation for the turbulent viscosity.
- A new transport equation for the dissipation rate, ϵ , has been derived from an exact equation for the transport of the mean-square vorticity fluctuation.

These modifications improved the predictions for planar and round jets, boundary layers under strong adverse pressure gradients, separation, rotation, recirculation, and strong streamline curvature. This model has shown substantial improvement over the standard k - ϵ model. However, since the model is still relatively new, it is not clear in exactly which instances the realizable k - ϵ model consistently outperforms the RNG model. Initial studies show that the realizable model provides the best performance of all the k - ϵ model versions for several validations of separated flows and flows with complex secondary flow features. One limitation of this model is that it produces nonphysical turbulent viscosities in situations when the computational domain contains both rotating and stationary zones.

2.2.4.4 k - w Model

The k - w model is another two-equation model in which w is an inverse time scale associated with the turbulence. This model solves two additional partial differential equations:

- A modified version of the k equation used in the k - ϵ model
- A transport equation for w .

Its numerical behavior is similar to that of k - ϵ models. This model predicts free shear flow spreading rates that are in close agreement with measurements for far wakes, mixing layers, and plane, round, and radial jets, and is thus applicable to wall-bounded flows and free shear flows (Fluent User's Guide).

2.2.4.5 Reynolds Stress Model

The RSM is the most elaborate turbulence model in the FLUENT code. This model closes the Reynolds-Averaged Navier-Stokes equations by solving additional transport equations for the six independent Reynolds stresses in 3-D and four in 2-D. These transport equations are derived by Reynolds averaging of the product of the momentum equation with a fluctuating property. For closure, it also requires one equation for turbulence dissipation. This model avoids the isotropic eddy viscosity assumption that was considered in the two-equation model.

The RSM has greater potential to give accurate predictions for complex flows because it accounts for the effect of streamline curvature, swirl, rotation, and rapid changes in strain rate in a more rigorous manner than the one-equation and two-equation models. It is therefore good for accurately predicting the following complex flows:

- Cyclone flows (swirling combustor flows)
- Rotating flow passages (secondary flows)
- Flows involving separation.

2.2.5 Determination of Porous Body Parameters

As mentioned, the core and the lower plenum of the reactor were simplified to be porous bodies. In the FLUENT code, porous media are modeled by the addition of a momentum source term to the standard fluid equation below. The source term is composed of two parts: a viscous loss term (Darcy, the first term), and an inertial loss term.

$$S_i = -\left(\sum_{j=1}^3 D_{ij} \mu v_j + \sum_{j=1}^3 C_{ij} \frac{1}{2} \rho v_{mag} v_j \right) \quad (2-5)$$

where S_i is the source term for the i th (x,y, or z) momentum equation, and D and C are prescribed matrices. This momentum sink contributes to the pressure gradient in the porous cell, creating a pressure drop that is proportional to the fluid velocity (or velocity squared) in the cell.

A homogeneous porous media equation is expressed in the following formula:

$$S_i = -\left(\frac{\mu}{\alpha} v_i + C_2 \frac{1}{2} \rho v_{mag} v_i \right) \quad (2-6)$$

where α is the permeability and C_2 is the inertial resistance factor, simply specifying D and C as diagonal matrices with $1/\alpha$ and C_2 , respectively, on the diagonals (and zero for the other elements).

The FLUENT code also allows the source term to be modeled as a power law of the velocity magnitude:

$$S_i = -C_0 |v|^{C_1} \quad (2-7)$$

where C_0 and C_1 are user-defined empirical coefficients.

The two important parameters for defining porous media are porosity and permeability. The detail processes to determine these parameters for the reactor core and the lower plenum are as follows.

2.2.5.1 Determination of Porosities

The porosity is the volume fraction equal to the fluid volume over the total volume (where the total volume equals the fluid volume plus the structural volume) of the region in question. The porosity is used in the calculation of heat transfer in the medium and in the time-derivative term in the scalar transport equations for unsteady flow. It also influences the calculation of the reaction source terms and body forces in the medium. These sources will be proportional to the fluid volume in the medium.

This study defined the porosities in the two regions: the reactor core and the lower plenum. Figure 2-9 shows the single pattern element for the VHTR reactor core block. The porosity of the core zone in the FLUENT input can be determined by the following equations.

$$\gamma_{core} = \frac{V_{fluid}}{V_{total}} = \frac{A_{fluid}}{A_{total}} = \frac{\frac{1}{8} \pi d^2}{\frac{\sqrt{3}}{4} p^2} \quad (2-8)$$

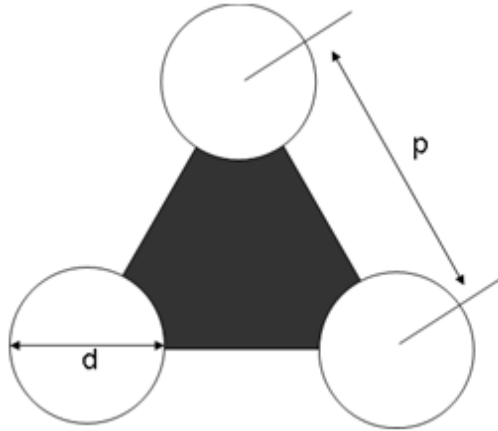


Figure 2-9. Core pattern ($d = 1.58$ cm, $p = 3.27$ cm). (Internal Design Review Presentation Material, General Atomics, San Diego, 1997)

The porosity of the lower plenum can be determined from the geometry of Figure 2-10 and Figure 2-11. The porosity of the lower plenum in the FLUENT input can be determined by the following equations.

$$\gamma_{lowerplenum} = \frac{V_{fluid}}{V_{total}} = \frac{A_{fluid}}{A_{total}} = \frac{\frac{\sqrt{3}}{4} P_{LP}^2 - \frac{1}{8} \pi d_{LP}^2}{\frac{\sqrt{3}}{4} P_{LP}^2} \quad (2-9)$$

where P_{LP} is the pitch of the lower plenum, and d_{LP} is the diameter of the lower plenum.

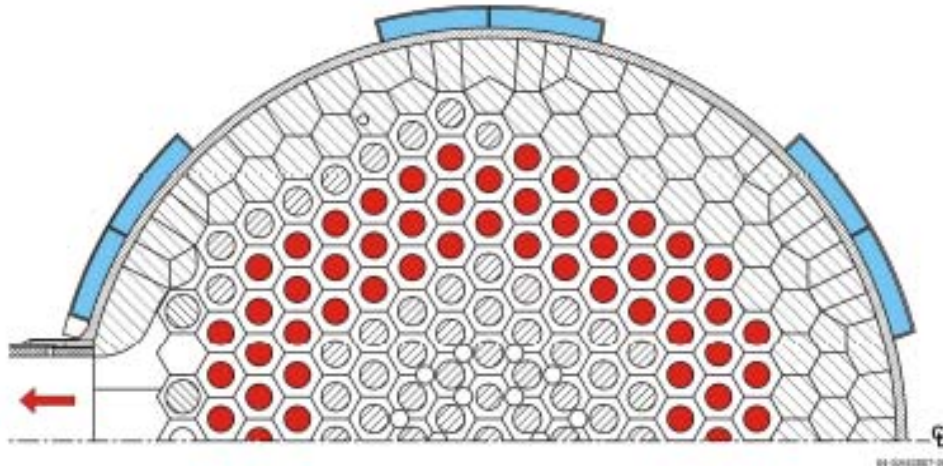


Figure 2-10. Typical geometry of lower plenum ($d_{LP} = 0.212$ m, $P_{LP} = 0.36$ m). The red circle represents rod (McEligot and McCreery 2004).

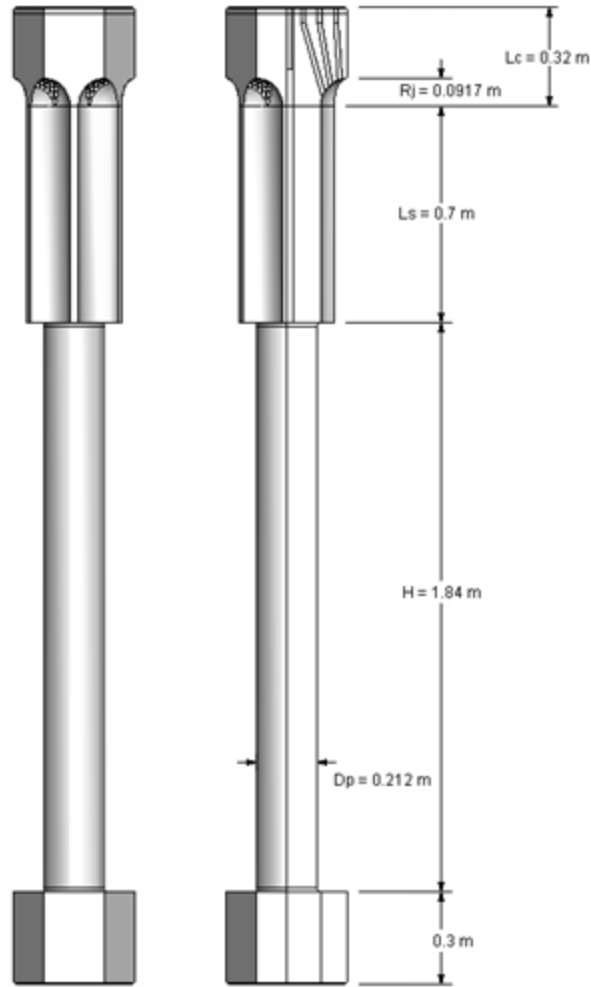


Figure 2-11. Detail view of lower plenum in GT-MHR 600 MWt.

From the above equations, the porosities of the reactor core and the lower plenum were calculated as follows:

- Core
 - $\gamma_{core} = 0.21$
- Lower Plenum
 - $\gamma_{core} = 0.68$

2.2.5.2 Permeability (Viscous and Inertial Resistance Coefficients)

The porous media model incorporates an empirical determined flow resistance in a region of the model defined as porous. In essence, the porous media model is nothing more than an added momentum sink in the governing momentum equations.

In the reactor core, two permeabilities for different directions require definition: x-direction (horizontal) and y-direction (vertical). Because there is no flow in the horizontal direction of the core, the permeability of the x-direction in the core region is zero. The permeability of vertical direction was determined using the friction loss correlation. In this simulation, the flow rate of the core is governed by

density-gradients and is very low. Hence, the flow field in the core for y-direction is assumed to be laminar flow (Lindburg 1997).

In the laminar flow, the friction loss of the circular channel is expressed by Equations (2-10) through (2-14):

$$\frac{\Delta P}{L} = f \frac{1}{2} \rho v^2 \frac{1}{D} \quad (2-10)$$

$$f = \frac{64}{\text{Re}} \quad (2-11)$$

$$\frac{\Delta P}{L} = \left(\frac{64}{\frac{\rho v D}{\mu}} \right) \frac{1}{2} \rho v^2 \frac{1}{D} = \frac{32 \mu v}{D^2} \quad (2-12)$$

Therefore,

$$\frac{\Delta P}{L} = \frac{\mu}{\alpha} v = \frac{32 \mu v}{D^2} \quad (2-13)$$

$$\alpha = \frac{D^2}{32} \quad (2-14)$$

The diameter of the channel in the core is 0.0158 m, so the permeability of the y-direction is $7.8\text{e-}6 \text{ m}^2$.

In the turbulent flow, the friction loss of the circular channel can be determined by the Moody diagram (see Figure 2-12). Figure 2-12 shows the friction loss data from laminar to turbulent region.

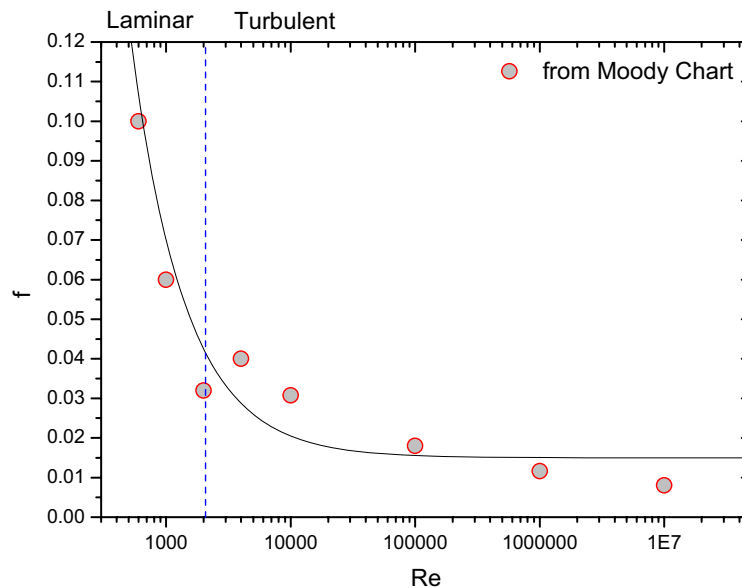


Figure 2-12. Friction factor correlation.

Based on the above graph, the friction factor equation can be correlated as

$$f = 0.015 + \frac{55}{\text{Re}}; \quad (2-15)$$

and the pressure drop equation as

$$\Delta P = f \left(\frac{1}{2} \rho u^2 \right) \left(\frac{L}{D} \right) \quad (2-16)$$

Inserting Equation (2-15) into Equation (2-16) derives

$$\Delta P = \left(0.015 + \frac{55}{\text{Re}} \right) \left(\frac{1}{2} \rho u^2 \right) \left(\frac{L}{D} \right). \quad (2-17)$$

$$\Delta P = \left(0.015 + \frac{55}{(\rho u D / \mu)} \right) \left(\frac{1}{2} \rho u^2 \right) \left(\frac{L}{D} \right). \quad (2-18)$$

$$\frac{\Delta P}{L} = \frac{55}{2D^2} \mu u + \frac{0.015}{D} \left(\frac{1}{2} \rho u^2 \right). \quad (2-19)$$

Therefore, permeability and C_2 is

$$\alpha = \frac{2}{55} D^2 \quad \text{and} \quad (2-20)$$

$$C_2 = \frac{0.015}{D} \quad (2-21)$$

Because the diameter of the channel in the core is 0.0158 m, the permeability and C_2 can be determined as

$$\alpha = 9.07782 \times 10^{-6} \text{ m}^2 \quad \text{and} \quad (2-22)$$

$$C_2 = 0.949 \text{ m}^{-1} \quad (2-23)$$

Simulations involving highly anisotropic porous media like this may, over time, pose convergence trouble. This issue can be addressed by limiting the anisotropy of the porous media coefficients to 2 or 3 orders-of-magnitude. Even if the medium's resistance in one direction is infinite, it is not necessary to set the resistance in that direction to be greater than 1,000 times the resistance in the primary flow direction (FLUENT user's guide (2007)). The permeability of the x-direction was therefore defined to be $7.8\text{e-}9 \text{ m}^2$, even though it has zero permeability.

The permeability of the lower plenum y-direction was determined in the same manner to the core, but in the lower plenum, the flow is not the circular channel flow. The hydraulic diameter was therefore used to determine the permeability. The hydraulic diameter of the lower plenum can be calculated as

$$D_h = \frac{4 \text{ Area}}{\text{Perimeter}} = 0.46 \text{ m (for lower plenum)} \quad (2-24)$$

Then, the permeability of the lower plenum y-direction can be calculated. The estimated permeability and C_2 are calculated by Equation (2-20) and (2-21) as

$$\alpha = 0.00769 \text{ m}^2 \tag{2-25}$$

$$C_2 = 0.0326 \text{ m}^{-1} \tag{2-26}$$

The permeability of the lower plenum in x-direction is different. In this region, the cross flow through the tube array is dominant. Figure 2-13 shows the flow and tube configuration. Figure 2-14 shows some experimental data and correlations considering this type of flow.

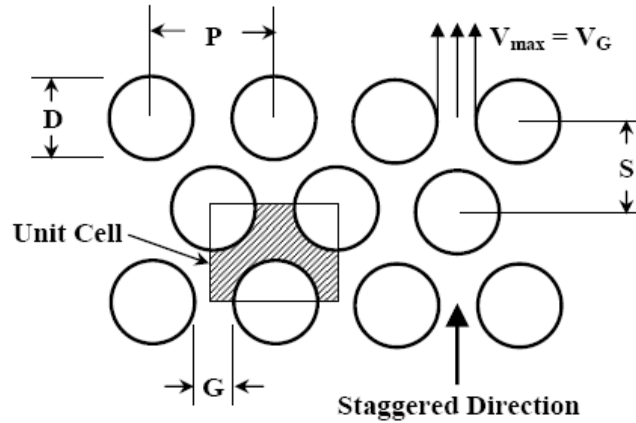


Figure 2-13. Equally spaced triangular tube array (Vassallo and Symolon 2007).

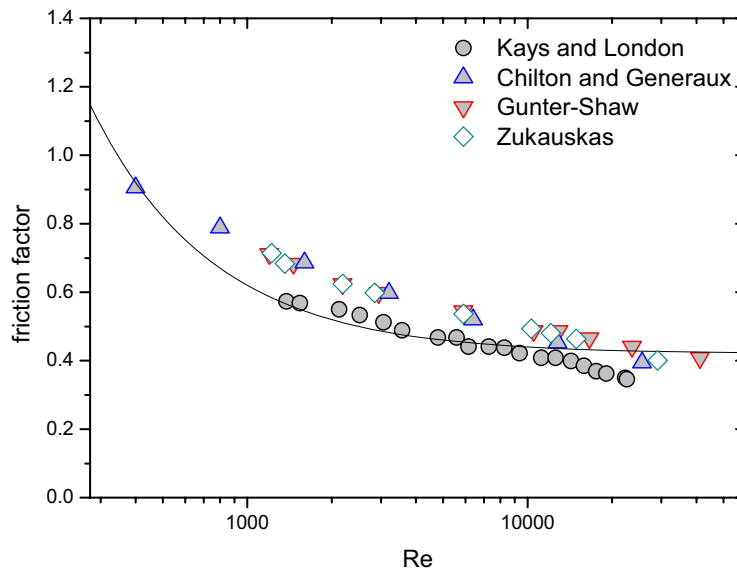


Figure 2-14. Cross-flow friction factor data for staggered tube arrays (Vassallo and Symolon 2007).

Table 2-3 shows the friction factor correlations for the cross flow through the tube array summarized by Kosar (2005).

Table 2-3. Correlation for the friction factor and their mean absolute errors. (Kosar et al., 2005)

Correlation	Reference	Fluid	Reynolds Number	H/D	Configuration	Friction Factor
1	Chilton and Generaux (1933)	Air	Laminar Region	Long Tubes	Circular Staggered	$f = \frac{106}{Re}$
2	Chilton and Generaux (1933)	Air	Turbulent Region	Long Tubes	Circular Staggered Inline	$f = \frac{C}{Re^{0.2}}$ C = 3 for in-line tube configuration C = 1.32 for staggered tube configuration
3	Jacob (1983)	Air	Turbulent Region	Long Tubes	Circular Staggered Inline	For inline configuration $f = \frac{1}{Re^{0.35}} \left(0.176 + \frac{0.32(S_L/D)}{(S_T/D-1)^{0.43+(1.13D/S_T)}} \right)$ For staggered configuration $f = \frac{1}{Re^{0.16}} \left(1 + \frac{0.47}{(S_T/D-1)^{1.08}} \right)$
4	Gunter and Shaw (1945)	Air	Laminar Region	Long Tubes	Circular In-line Staggered	$f = \frac{180}{Re} \left(\frac{4S_T S_L}{\pi D^2} - 1 \right)^{0.4} \left(\frac{D b_G}{S_T} \right)^{0.6}$ $b_G = \frac{S_L}{D}$ (for inline tube configuration) $b_G = \frac{S_d}{D}$ (for staggered tube configuration)
5	Gunter and Shaw (1945)	Air	Turbulent Region	Long Tubes	Circular In-line Staggered	$f = \frac{1.92}{Re^{0.145}} \left(\frac{4S_T S_L}{\pi D^2} - 1 \right)^{0.4} \left(\frac{D b_G}{S_T} \right)^{0.6}$ b_G is defined in the previous row
6	Bergelin et al. (1950)	Mobile Oil	Laminar Region	Long Tubes	Circular In-line Staggered	$f = \frac{280}{Re} \left(\frac{1}{a_B} \right)^{1.6}$ where $a_B = \frac{S_T}{D}$ $\frac{S_L}{D} \geq \sqrt{2 \frac{S_T}{D} + 1}$ (Inline configuration) or $a_B = \frac{S_T}{D}$ $\frac{S_L}{D} < \sqrt{2 \frac{S_T}{D} + 1}$ (Staggered configuration)
7	Damerow (1972)	Air	Turbulent Region	Short Tubes 2<H/D<4	Airfoils	$f = [8.24(S_T/D)^{-1.1}] Re_D^{-0.16}$
8	Kast (1974)	Air	Laminar and Turbulent	Long Tubes	Circular In-line Staggered	$f = \frac{128}{Re} + \frac{4}{Re^{0.16}}$
9	Metzger et al. (1982)	Air	1,000–100,000	Short tubes H/D=1	Rectangular Staggered Short Tubes H/D=1, P _T =2.5 P _L =1-5	For 1,000 < Re < 10,000 $f = 1.268 Re^{-0.132}$ For 10,000 < Re < 100,000 $f = 7.04 Re^{-0.318}$
10	Taborek (1983)	All Fluids	All Re	Long Tubes	Circular Both inline and staggered	$f = 4b_1 \left(\frac{1.33}{S_T/D} \right)^b (Re)^{b_2}$ $b = \frac{b_3}{1 + 0.14(Re)^{b_4}}$

11	Gaddis and Gnielski (1985)	All Fluids	Laminar Regime	Long Tubes	Circular Both inline and staggered	$f = \frac{280\pi \left(\left(\frac{S_L}{D} \right)^{0.5} - 0.6 \right)^2 + 0.75}{\text{Re} \left(4 \frac{S_L S_T}{D^2} - \pi \right) c^{1.6}}$ <p>where $c = S_T / D$ $\left(\frac{S_L}{D} \geq \frac{1}{2} \sqrt{2 \frac{S_T}{D} + 1} \right)$ or $c = S_D / D$ $\left(\frac{S_L}{D} < \frac{1}{2} \sqrt{2 \frac{S_T}{D} + 1} \right)$</p>															
12	Sparrow and Grannis (1985)	Air	20 – 2200	Long Tubes	Diamond 45° deg vertex 90° deg vertex P _T =1.15-2 P _L =1-2 Staggered	<p>For $P_L = 0.886 P_T$</p> $f = \frac{127}{\text{Re}} + 0.90, \quad P_T < 1.35$ <p>For $P_L = P_T$</p> $f = \frac{155}{\text{Re}} + 0.82, \quad P_T < 1.35$ $f = \frac{98}{\text{Re}} + 0.72, \quad P_T < 1.35$															
13	Moore and Joshi (2003)	Water	200 – 10000	Short Tubes 0.5 < H/D < 1	Circular Staggered P _T =1.3-1.36 P _L =1.13-1.18	$f = 4a_0 \left(\frac{H}{D} \right)^{a_1} \left(\frac{cl + H}{H} \right)^{a_2} \text{Re}^{a_3}$ <table border="1"> <thead> <tr> <th></th> <th>10² < Re < 10³</th> <th>10³ < Re < 10⁴</th> </tr> </thead> <tbody> <tr> <td>a₀</td> <td>4.76</td> <td>3.2</td> </tr> <tr> <td>a₁</td> <td>-0.742</td> <td>-0.138</td> </tr> <tr> <td>a₂</td> <td>0.505</td> <td>-0.183</td> </tr> <tr> <td>a₃</td> <td>-0.502</td> <td>-0.42</td> </tr> </tbody> </table>		10 ² < Re < 10 ³	10 ³ < Re < 10 ⁴	a ₀	4.76	3.2	a ₁	-0.742	-0.138	a ₂	0.505	-0.183	a ₃	-0.502	-0.42
	10 ² < Re < 10 ³	10 ³ < Re < 10 ⁴																			
a ₀	4.76	3.2																			
a ₁	-0.742	-0.138																			
a ₂	0.505	-0.183																			
a ₃	-0.502	-0.42																			
14	Short et al. (2004)	Air	175 - 4500	Short Tubes 1.9 < H/D < 7.5	Circular Staggered P _T =1.3-1.36 P _L =2.0-6.4	<p>For Re < 1000</p> $f = 140.4 \left(\frac{S_L}{D} \right)^{-1.3} \left(\frac{S_T}{D} \right)^{-0.78} \left(\frac{H}{D} \right)^{-0.55} \text{Re}^{-0.65}$ <p>For Re > 1000</p> $f = 0.884 \left(\frac{S_L}{D} \right)^{-1.4} \left(\frac{S_T}{D} \right)^{-0.54} \left(\frac{H}{D} \right)^{-0.056} \text{Re}^{-0.08}$															

Permeability and inertia resistance for staggered tube arrays was determined by correlating the friction factor in Figure 2-14 as

$$f = 0.42 + \frac{200}{\text{Re}} \quad (2-27)$$

Finally, the following correlation can be derived as

$$\frac{\Delta P}{L} = \frac{100}{D_h^2} \mu u + \frac{0.42}{D_h} \left(\frac{1}{2} \rho u^2 \right). \quad (2-28)$$

Permeability and C_2 can therefore be determined by Equation (2-28) and hydraulic diameter ($D_h = 0.46$ m) as

$$\alpha = 0.002116 \text{ m}^2 \quad (2-29)$$

$$C_2 = 0.913 \text{ m}^{-1} \quad (2-30)$$

2.2.6 Determination of Core Temperature

Right after the pipe break accident, the maximum temperature of the reactor is higher than 1000°C (1273 K). This high temperature would significantly affect the behaviors of the flow when the air is ingressed into the reactor core. These behaviors would include sudden changes of density, viscosity, heat capacity, and thermal conductivity of the fluid. The modeling in this section considers the effect of heating in the reactor core and compares the results to the simple isothermal results (where the heating effect has not been considered).

The initial temperature distribution in the lower plenum, bottom reflector, and the core were calculated by modeling the depressurization process using the GAMMA systems analysis code (Oh et al. 2006). Figure 2-15 shows the GAMMA nodalization for GT-MHR 600 MWt. This simulation considered pipe break, depressurization, and the diffusion process. For simplicity, the density driven flow was not considered, because this calculation focuses on the only depressurization process in which the stratified flow does not yet occur.

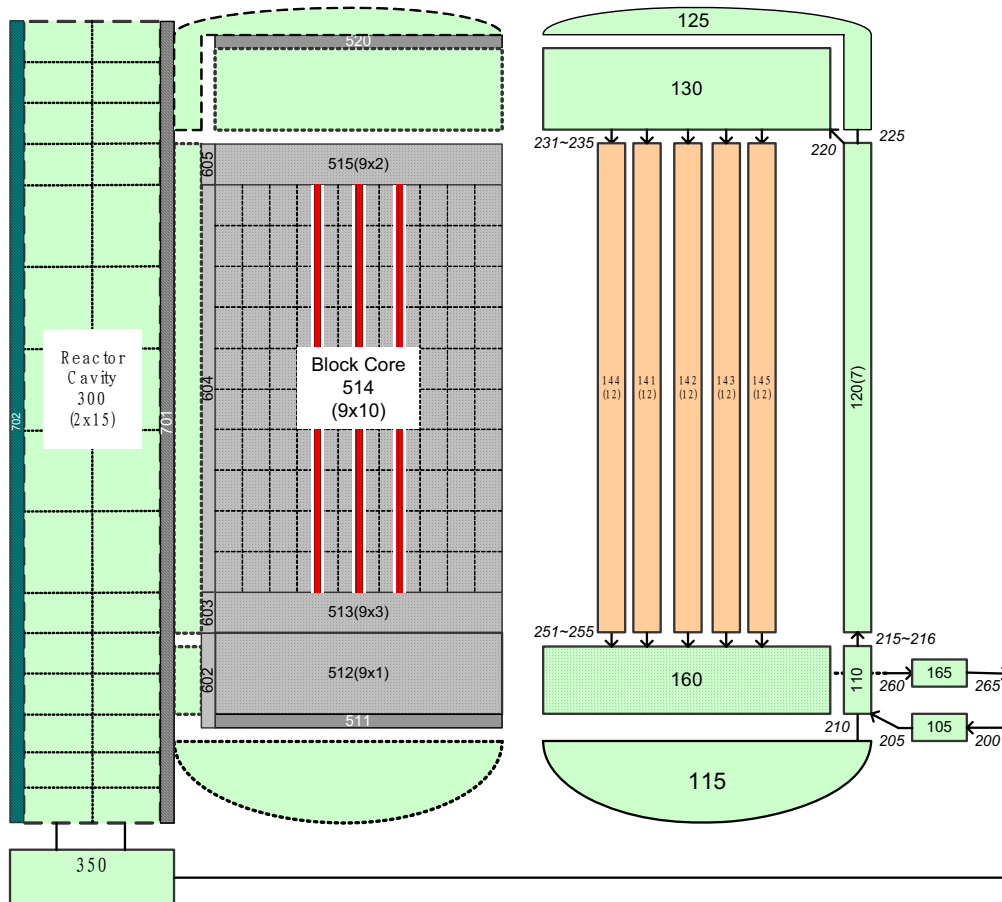


Figure 2-15. GT-MHR 600 MWt GAMMA nodalization.

Figure 2-16 shows the temperature distributions during the initial 500 seconds following a postulated pipe break. The depressurization phase was completed by 200 seconds when the pressure and the flow between the inside and the outside reactors are equalized. In this calculation, the accident scenario transits to the molecular diffusion process in which the air diffuses into the reactor core slowly by 1-D pipe assumption. However, in the actual accident, the density driven flow will be generated. According to the estimation performed by CFD analyses described in the Section 2.2.8, the stratified flow is maintained within ~60–90 seconds (until ~260–290 seconds into the scenario (See Figure 2-16)) when an air-helium mixture was filled in the bottom of the lower plenum. Movement of the air-helium mixture into the reactor core was subsequently driven by a combination of diffusion and heating of the gases in the lower plenum.

Based on the calculated results displayed in Figure 2-16, the material temperature boundary conditions for the reactor core and other structures were prescribed for the CFD calculation. To examine the effect of the reactor temperature, uniform temperature distribution was assumed in the current preliminary analysis, and a parametric study was performed instead. The selected temperatures were 300, 700, 1000, 1300 and 1600K (27, 427, 727, 1027, and 1327°C). The temperatures in the real core and the lower plenum are distributed between 800 and 1000°C (See Figure 2-16). Therefore, the results of 1000 and 1300K cases can be considered to be similar to the real situation. The sensitivity study on the core temperature was performed in the Section 2.2.8. The stratified flow simulation results considering detailed temperature profile in the core are described in the Section 2.3.

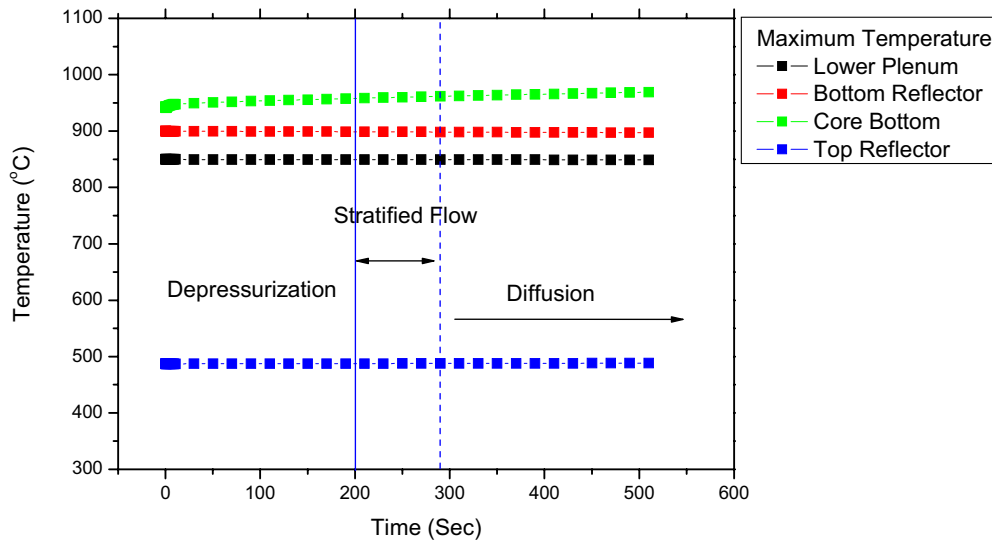


Figure 2-16. Time variations of the temperatures in the reactor core during an air-ingress accident.

2.2.7 Determination of Air Mole Fraction

The density difference between the reactor cavity and the internal vessel is the main driving force in the stratified flow induction. It can therefore be easily understood that the stratified flow calculation will be highly affected by the air mole fractions. For being the most conservative approach, the value 1.0 (mole fraction = 1.0) was selected to be the starting point of the initial air mole fraction in the cavity. However, a parametric study has been performed in this research in order to see the effect of air-mole fractions.

2.2.8 Preliminary CFD Analysis of Density Driven Stratified Flow

This section summarizes the results of the preliminary CFD analyses and parametric studies performed in order to understand the density driven stratified flow in the VHTR air-ingress accident and to find the effective parameters of this phenomenon. The experience and information from this analysis were finally used for the more detailed modeling presented in the Section 2.3.

2.2.8.1 Basic Options for the Reference Case

The following CFD options and initial conditions for the reference case were used.

- Turbulence model: k-e model realizable
- Initial core temperature (uniform temperature assumption): 1300K (Zone 1, 2, 3, 4)
- Initial cavity temperature: 300K (Zone 5)
- Gas species: air and helium
- Initial air mole fraction in the reactor cavity (Zone 5): 1.0
- Calculation time (Transient): 90.0 seconds
- Initial operating pressure: 1.0 atm at the bottom of the broken pipe.

2.2.8.2 Grid Sensitivity

The grid sensitivity was simply checked (see Figure 2-17). Figure 2-18 shows the average air mole fractions at each zone for two different meshes: the normal mesh (reference mesh) is composed of 31,232 numbers of grid points, and the fine mesh is composed of 53,601 numbers of grids. The lines represent the normal mesh scheme, and the points represent the fine mesh scheme. As a result, the differences between the two mesh sizes were very slight to be negligible within the maximum error of 3%.

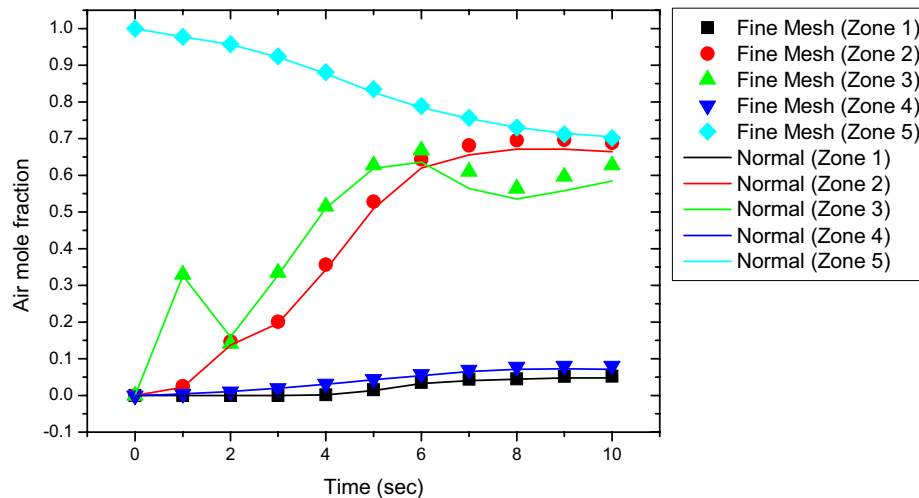


Figure 2-17. Grid sensitivity (Normal: 31,232 meshes, Fine: 53,601 meshes).

2.2.8.3 Reference Results

The stratified flow was first calculated for the reference case. The calculated results are expected to be conservative because the initial air-mole fraction in the reactor cavity was assumed to be 1.0, which maximizes the initial density gradient. In the real accident, the mole fraction is usually much less than 1.0 by mixing of the discharged helium coolant and the air in the containment. The actual air-mole fraction in the reactor cavity depends on the reactor design, containment (or confinement) geometry, and size.

Figure 2-18 shows the calculated air distributions in the reactor core and the cavity for different times. It also shows rapid air intrusion into the reactor core along the hot duct and lower plenum. In this calculation, flow transition was very fast, and all the bottom part of the reactor core was filled up with air within 10 sec. After the ingress of air, some heated air was stretched into the reactor core by thermal expansion (8 Sec), and some air rebounded back to the reactor cavity (16 sec). After the density gradients are attenuated, the flow is finally stabilized (90 sec), at which time only the diffusion mechanism dominates air penetration into the reactor core. This can be designated as a state of quasi-equilibrium. This CFD calculation showed that about half of the reactor core was covered by air after the state of equilibrium.

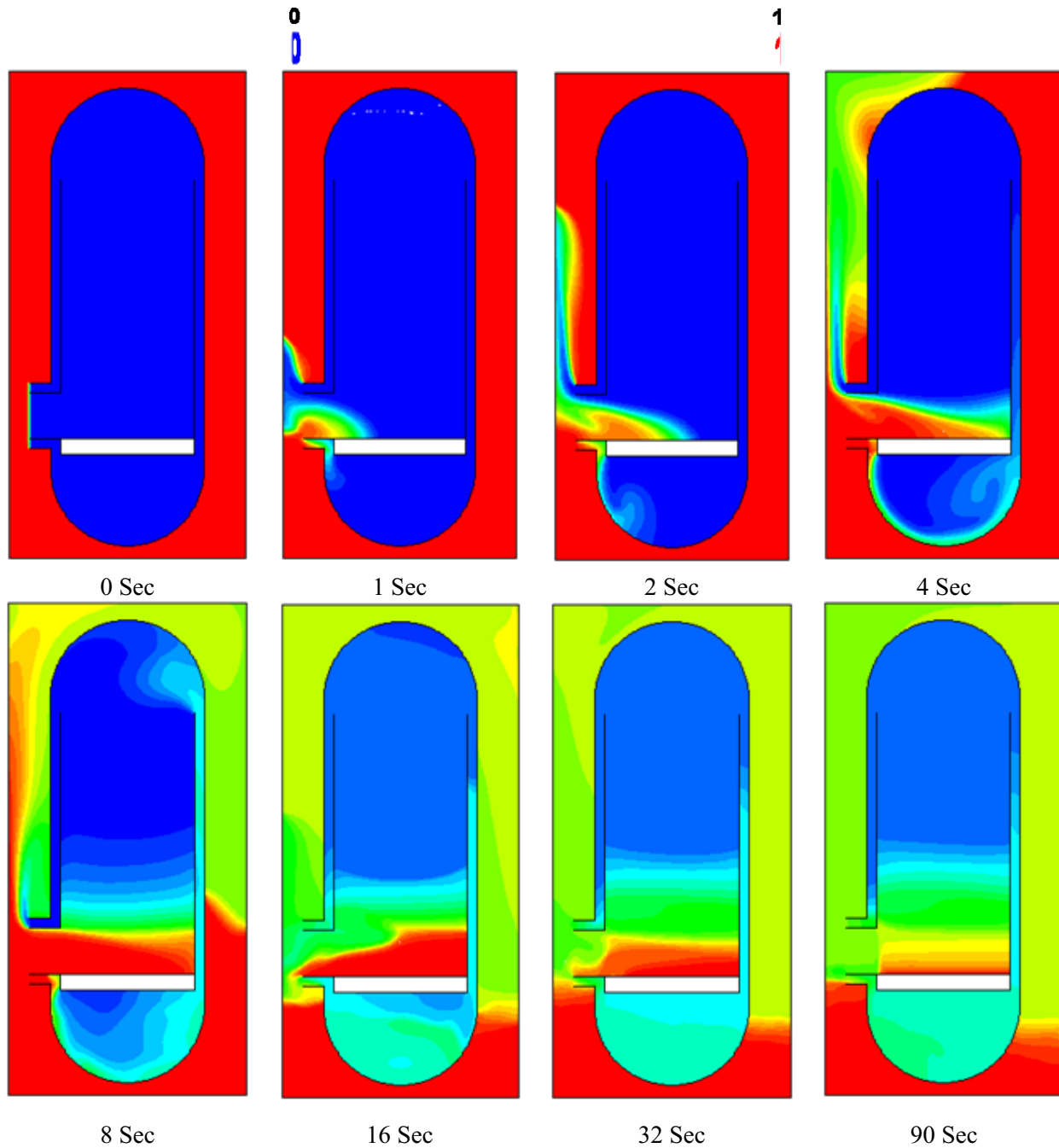
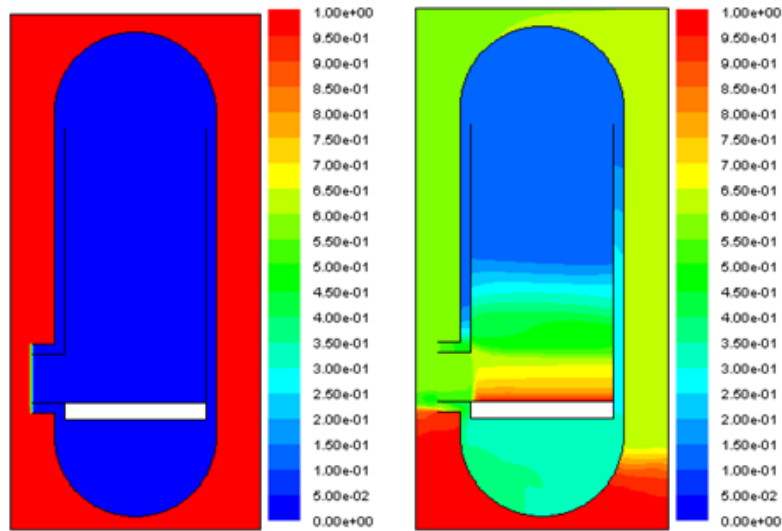


Figure 2-18. Variations of air distributions in the reactor during stratified flow.

Figure 2-19 compares the air distributions in the reactor core between the initial (0 seconds) and the final state of equilibrium (90 seconds). According to calculations, it only takes about 60 seconds for the whole process to reach the state of equilibrium (See Figure 2-20). This time frame is negligibly small compared to that of the molecular diffusion (>100 hours), which was the dominant air-ingress mechanism in the original air-ingress scenario. Figure 2-21 compares the molecular diffusion and the stratified flow mechanism in the air-ingress accident. Figure 2-21(a) was calculated based on only molecular diffusion consideration, and the Figure 2-21(b) was calculated based on the both density driven flow and molecular diffusion. As shown in this comparison, the air distribution considering stratified flow is significantly different from the original scenario. In the diffusion-only scenario, the lower plenum in the reactor vessel is still filled with almost helium coolant even after 40,000 seconds. However, in the new assumption, the whole lower plenum is filled with air within 60 seconds. It means that the previous analyses, based on the molecular diffusion mechanism, significantly under-predict and mislead the consequences of an air-ingress accident. It is obvious that the density driven flow needs to be considered to correctly estimate an accident. Figure 2-22 shows the variations of velocity vectors at the broken pipe and the lower plenum in the initial stage of the calculations.



(a) Air mole fractions at 0.0 sec (b) Air mole fraction at 90.0 sec
 Figure 2-19. Air distributions before and after stratified flow.

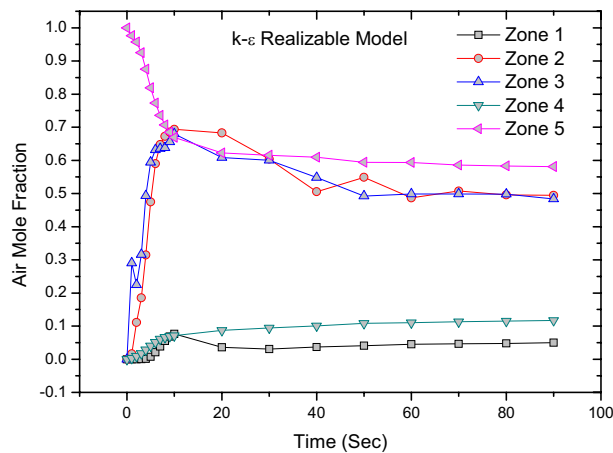
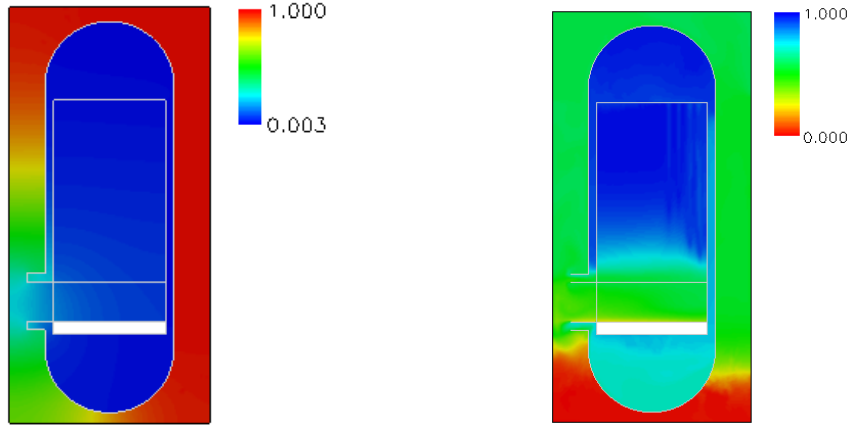


Figure 2-20. Variations of averaged air mole fractions.



(a) Original diffusion assumption (40000 sec) (b) Stratified flow assumption (60 sec)

Figure 2-21. Comparisons between original and stratified flow assumption.

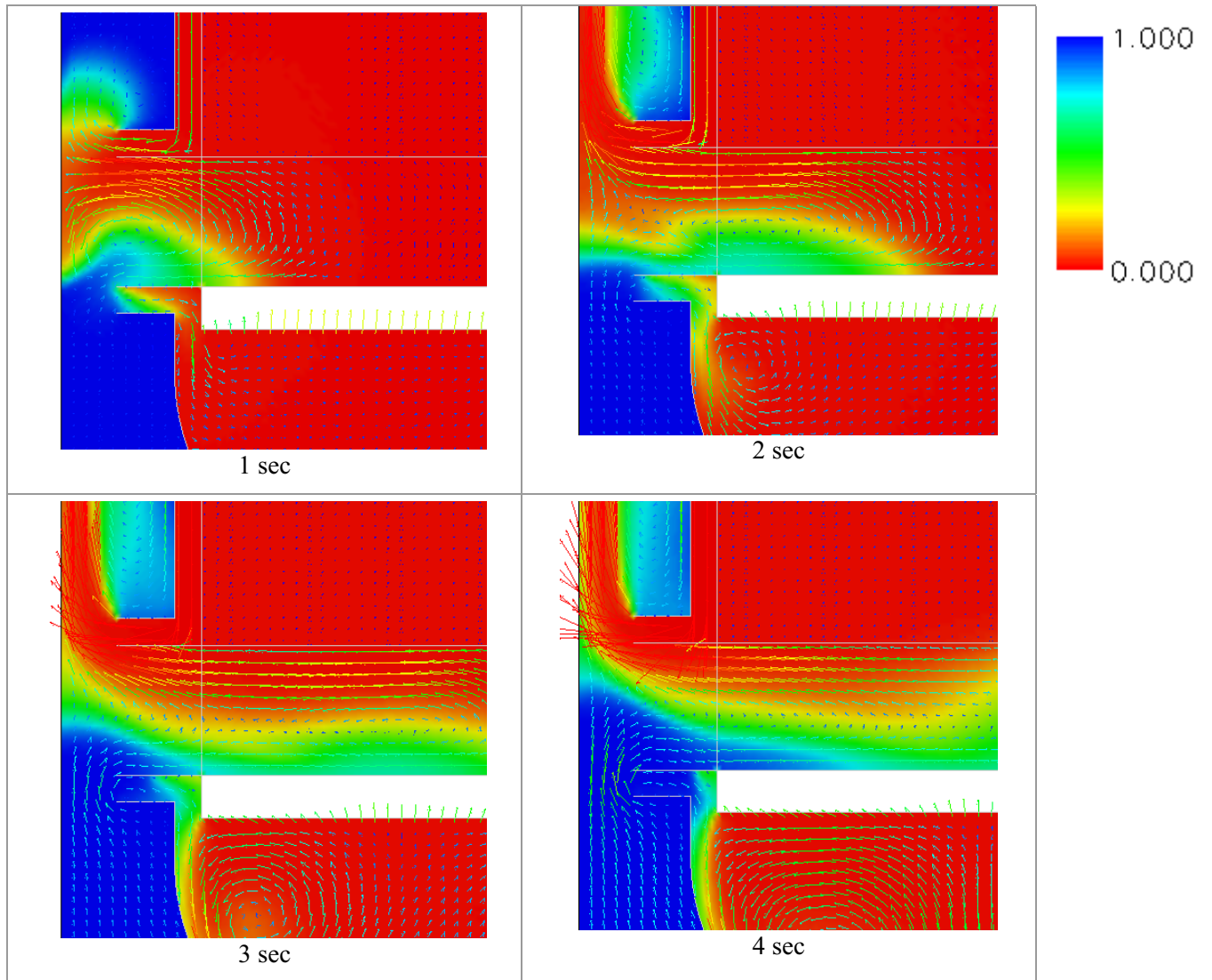


Figure 2-22. Velocity vectors and air mole fraction contour at the broken pipe.

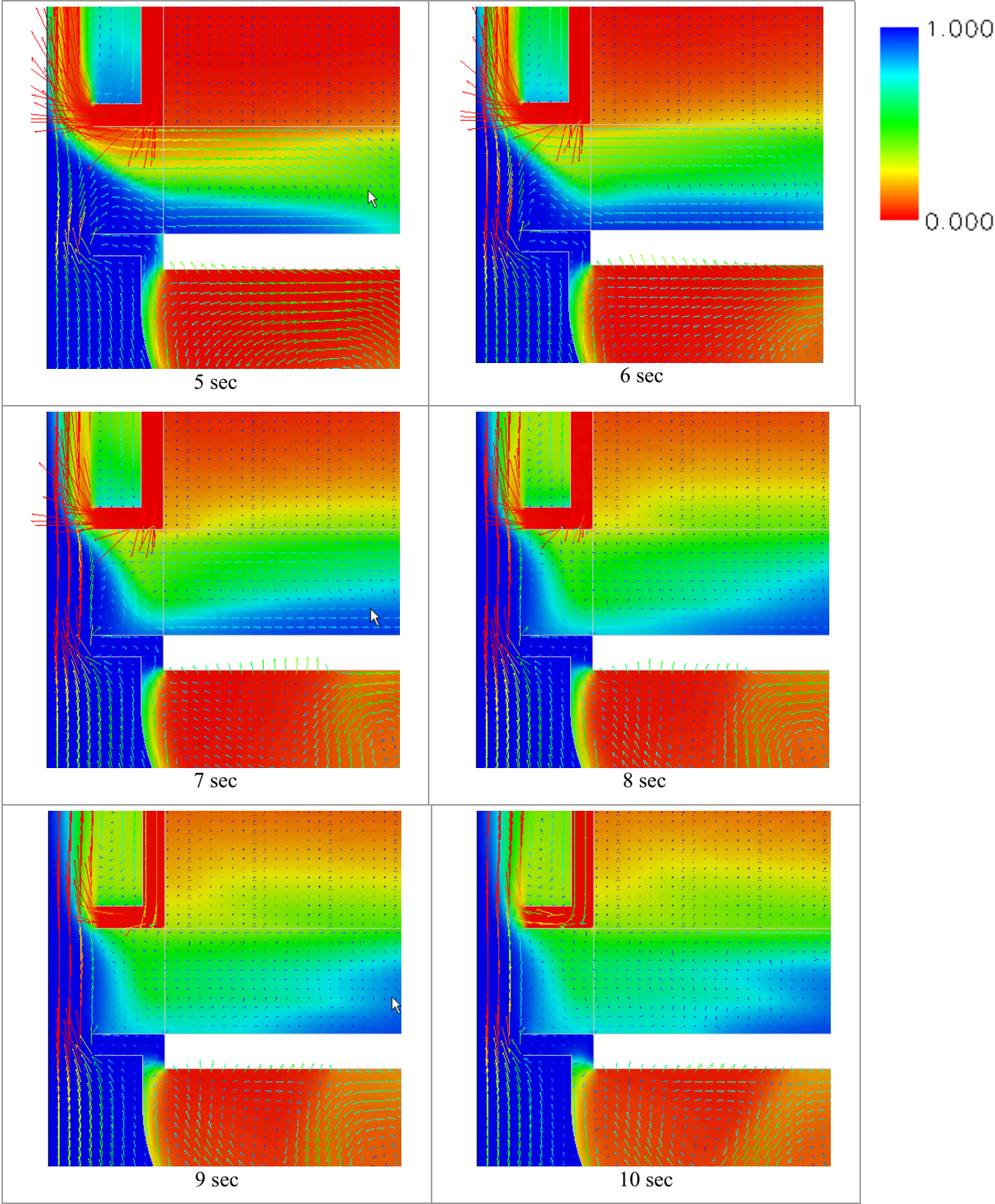


Figure 2-22. (continued).

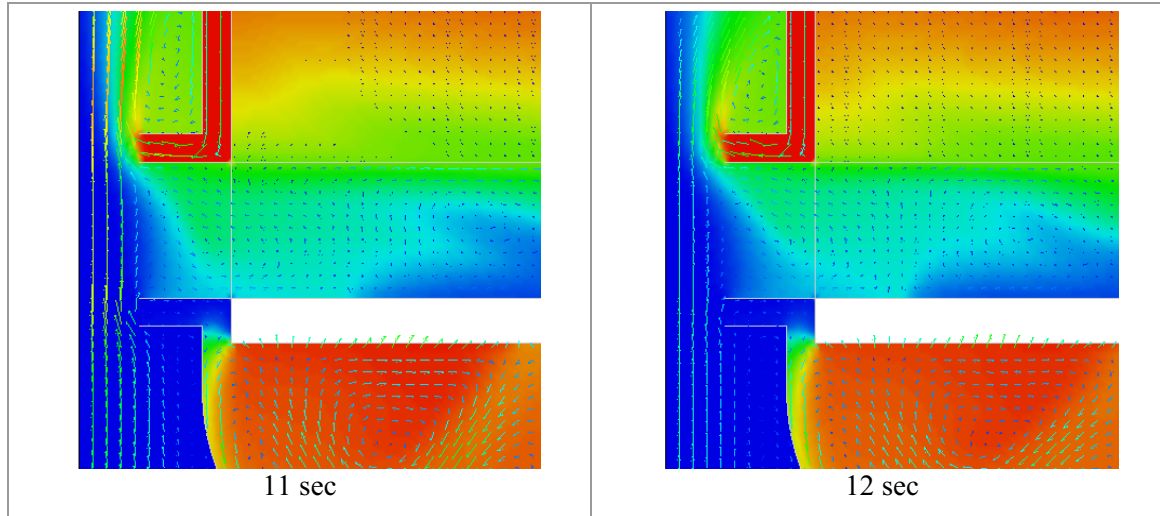


Figure 2-22. (continued).

Effect of Core Temperature

The temperature of the reactor core is an important parameter for the analysis of the density-driven stratified flow because the temperature affects the gas density distributions, eventually changing the driving force. This section summarizes the results of the CFD analysis for the core temperature effect on the stratified flow. For simplicity, uniform temperature distribution was assumed, and four initial temperatures (300K (isothermal), 700, 1000, 1300 and 1600K) were taken into consideration.

Figure 2-23 shows the transient air mole fractions in the reactor cavity for the starting from the different core temperatures. In this graph, the x-axis represents time and the y-axis represents air mole fraction. As shown, the transient patterns and stabilization times are not affected by the temperature, but as the temperature increases, the final air mole fraction in the reactor cavity becomes lower because the higher core temperature has the lower initial helium inventory. However, in all cases, the flow reached a quasi-equilibrium state within 60 seconds. It is still a negligibly small time-scale compared to that of the molecular diffusion (usually more than 150 hours). During the calculation, the temperature was maintained consistently because of the large heat capacity of the core graphite.

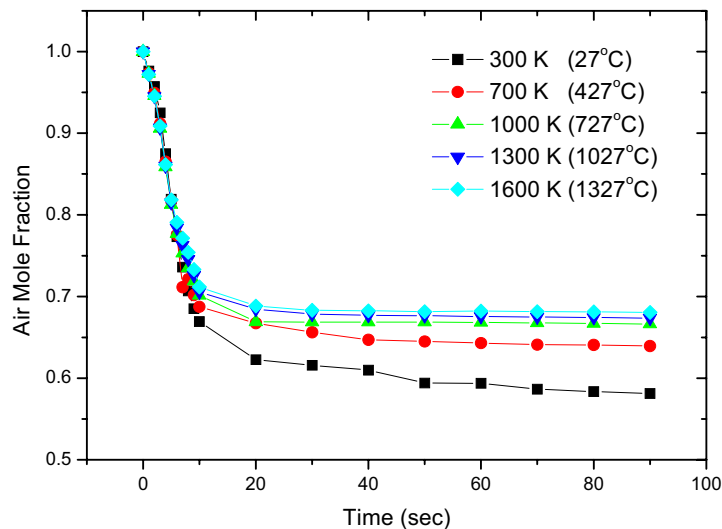


Figure 2-23. Variations of air mole fractions in the reactor cavity for different reactor temperatures during stratified flow process (k-ε realizable model).

Figure 2-24 shows the air distributions in the reactor 90 seconds after the stratified flow starts. It shows that increasing the core temperature increases the air level in the reactor core. For example, the air intrusion level at 1300K (1027°C) is rather higher than at 300K (27°C) because of the air expansion effect of heating. If the cold air enters into the reactor, the temperature will be increased by getting heat from hot solid structures. Then, the air will be expanded following the ideal gas law and will push the remaining helium coolant up out of the core. Figure 2-25 plots the axial profiles of air mole fractions at the center of the core. The x-axis represents the vertical position and the y-axis represents the air mole fractions. This figure clearly shows that the air level becomes higher as the core temperature increases. However, the expansion effect diminishes as the temperature increases because the specific volume is inversely proportional to the core temperature by the ideal gas law. So, at high temperature (higher than 1300K), the expansion effect caused by temperature is very slight.

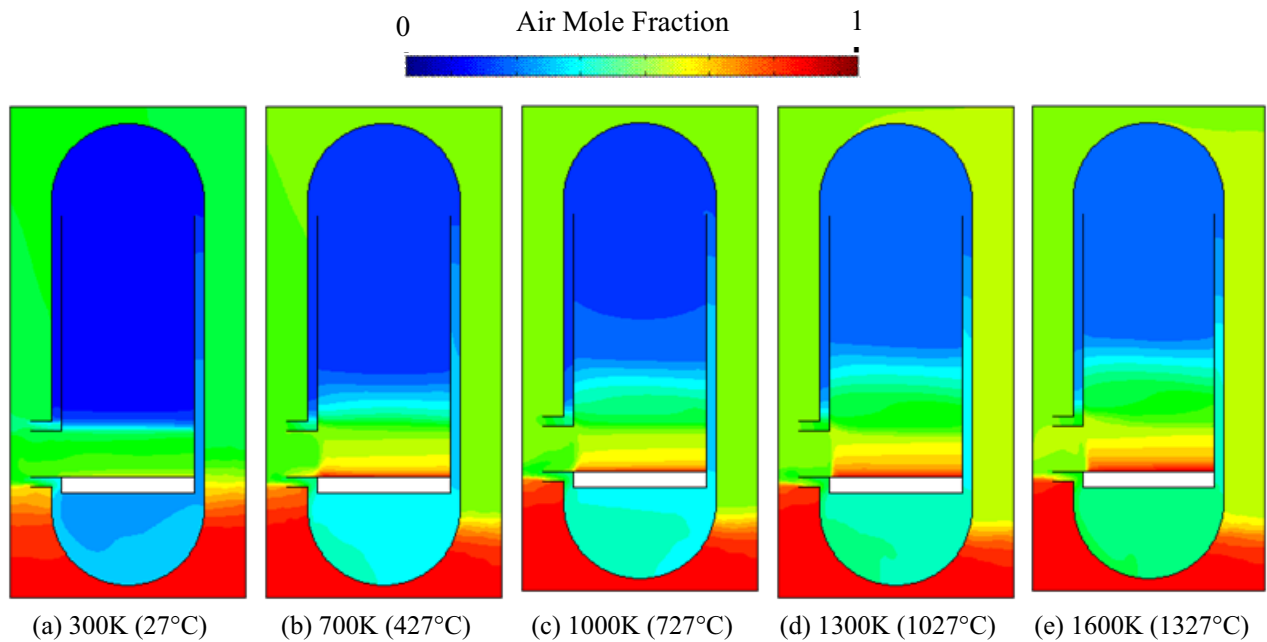


Figure 2-24. Effect of core temperature on the air distribution in the reactor (after 90 sec).

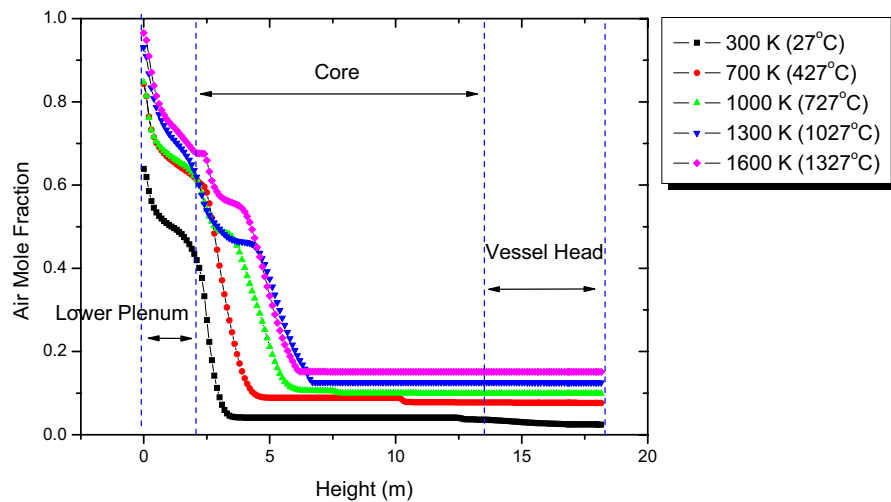


Figure 2-25. Air profile at the center of the reactor core after stratified flow process (k-ε realizable model).

Turbulence Effect

As mentioned, the flow regimes are not clear in the first stage of the air-ingress accident, and therefore the effects of turbulence models were estimated in this section. Four different models (laminar, k- ϵ , k- w , and RSM) were taken into consideration with two different core temperatures. One is isothermal (core temperature = 300K (27°C)) and the other is nonisothermal (core temperature = 1300K (1027°C)). Figures 2-26 through 2-28 show the results of isothermal case, and Figures 2-29 through 2-32 show the results of nonisothermal case. In all cases, the flows started to stabilize within 60 seconds as seen in Figures 2-26, 2-27, 2-29 and 2-30).

In the isothermal condition shown in Figure 2-28, the air distribution in the equilibrium appears sensitive to the turbulence models. As shown, the laminar model predicts that the largest amount of air is ingressed into the reactor core. The main reason is that the laminar model has no additional mixing terms, which are considered in all the other viscous models. The mixing terms in the turbulence models diminish the density gradient leading to the decrease of the driving force. In this work, the practical 2-equation turbulence models were compared to the RSM, which theoretically can provide the most realistic results for highly nonisotropic and complicated turbulent flow as in this case. Among the turbulence models, the k- ϵ realizable model shows the most similar results to the RSM. The k- w model significantly over-predicts the mixing effects.

The turbulence models could not be compared to the RSM for the nonisothermal because of the convergence problem of the RSM. Figure 2-31 shows the air-distributions in the equilibrium condition for three other models: laminar, k- ϵ realizable, and k- w standard. As shown, the distributions of air are quite affected by the turbulence model at the high core temperature. Figure 2-32 shows the air profiles predicted in the vertical direction at the center of the reactor core.

Isothermal (Core Temperature = 300K (27°C))

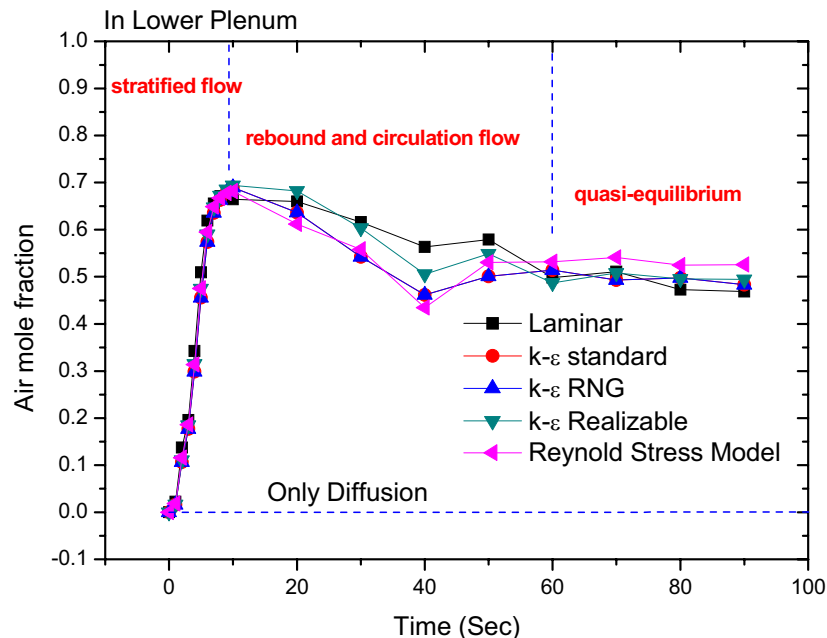


Figure 2-26. Average air mole fractions in the lower plenum for different turbulence models.

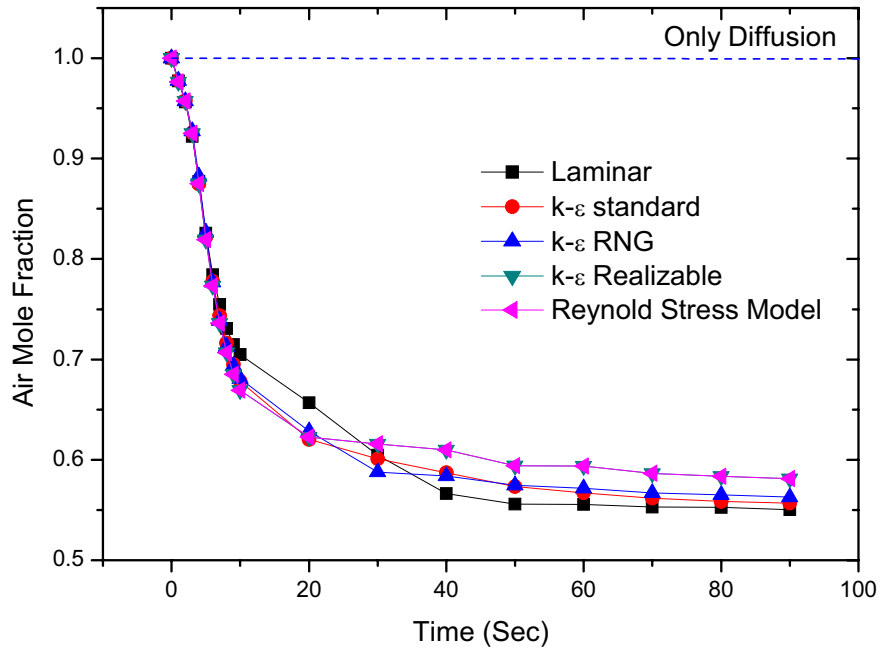


Figure 2-27. Average air mole fractions in the reactor cavity for different turbulence models.

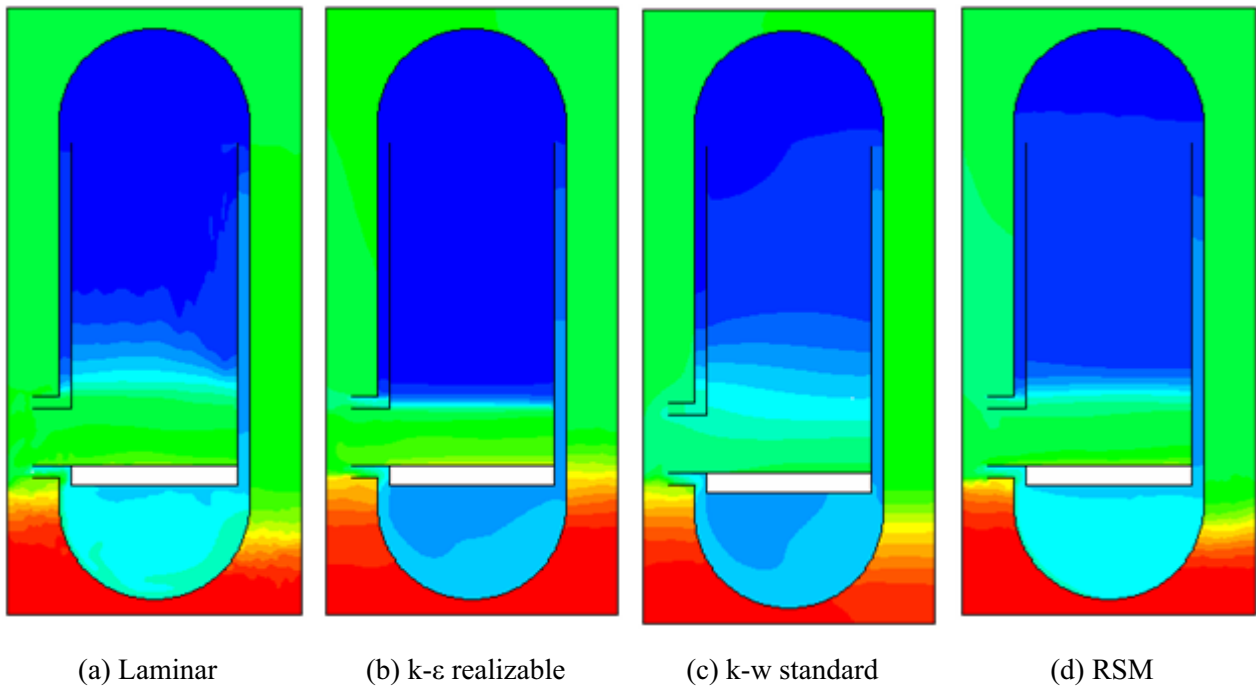


Figure 2-28. Quasi-equilibrium states for different turbulent models. Nonisothermal (core temperature = 300K (27°C)).

Nonisothermal (Core Temperature = 1300K (1027°C))

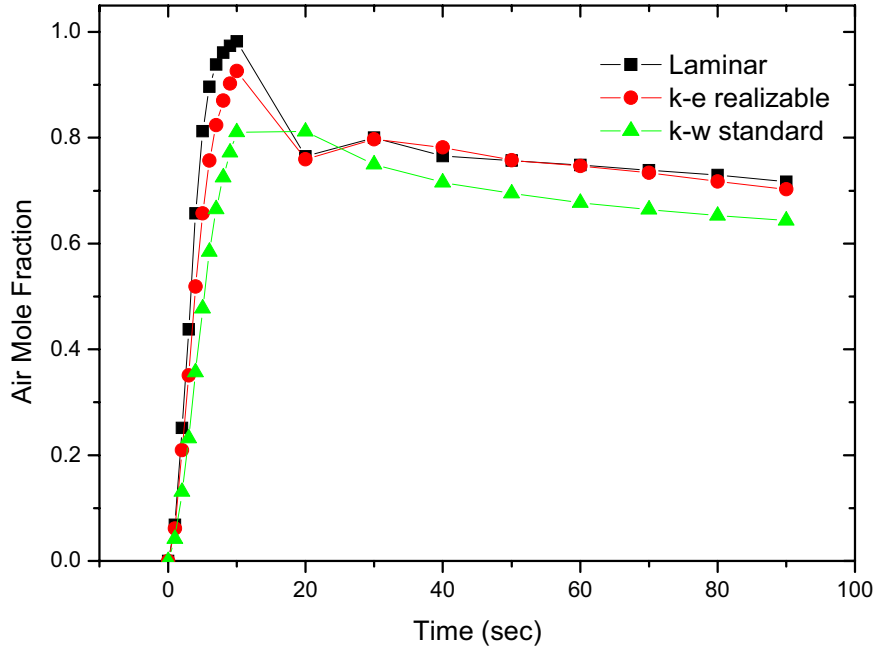


Figure 2-29. Average air mole fractions in the lower plenum for different turbulence model ($T_{\text{core}}=1300\text{K}$ (1027°C)).

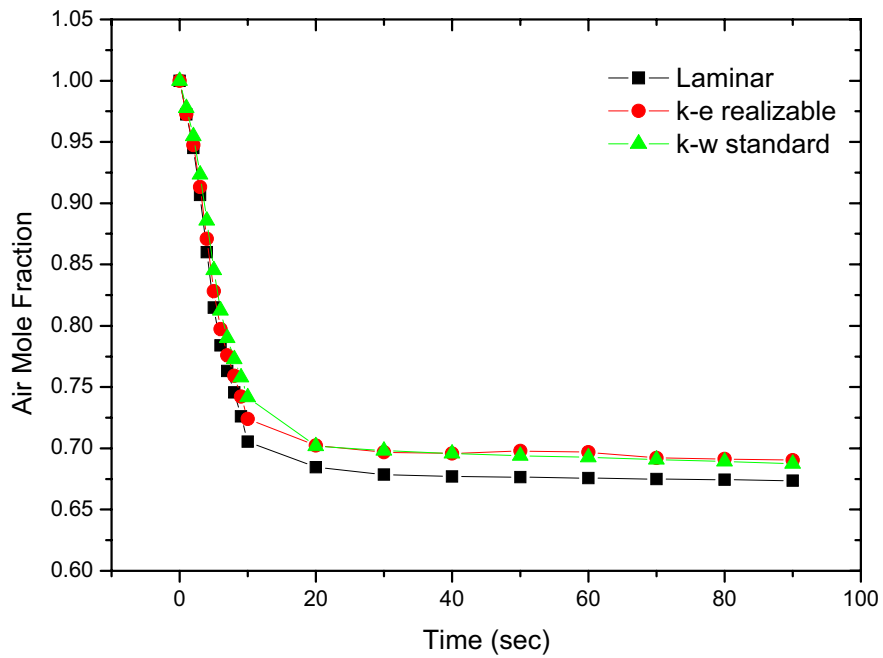


Figure 2-30. Average air mole fractions in the reactor cavity for different turbulence model ($T_{\text{core}}=1300\text{K}$ (1027°C)).

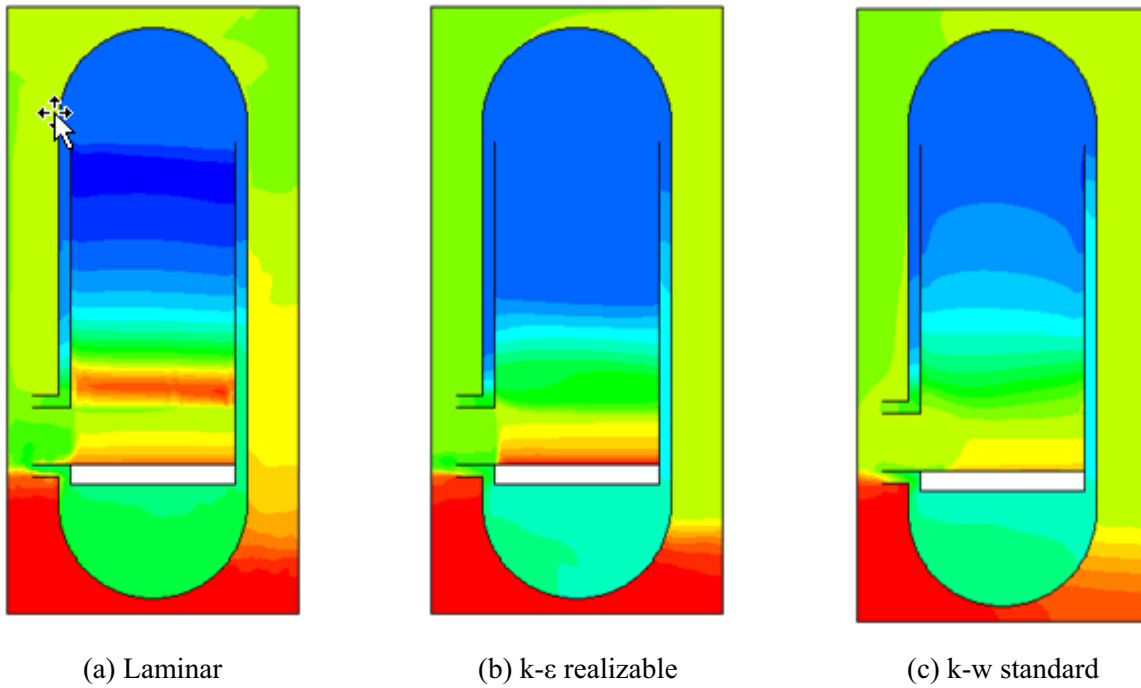


Figure 2-31. Quasi-equilibrium states for different turbulent models ($T_{\text{core}}=1300\text{K}$ (1027°C)).

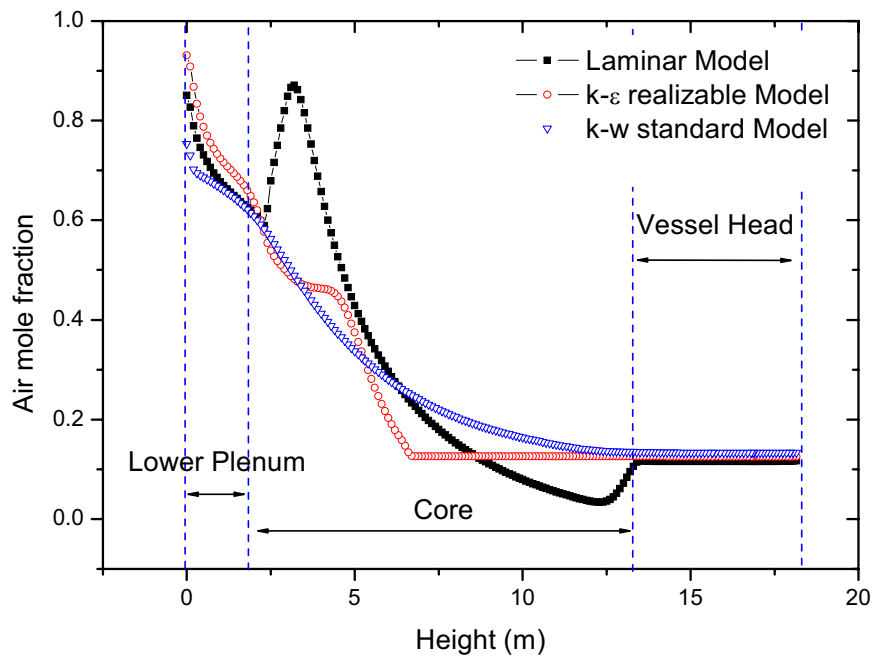


Figure 2-32. Comparisons of air mole fractions at the center of the reactor core between laminar model and k-ε realizable turbulence model ($T_{\text{core}}=1300\text{K}$ (1027°C)).

Effect of Initial Air Mole Fraction in the Reactor Cavity

Initial air mole fraction in the cavity is an important factor in the stratified flow analysis because it determines the main driving force (density gradient) of the air inflow. Both isothermal and nonisothermal conditions were considered in this study. It is generally expected that less initial air mole fractions lead to slower flow transient. As shown in Figure 2-33 (isothermal) and 2-34 (nonisothermal), the change of average air mole fraction in the reactor cavity becomes slower at the lower initial air mole fraction. For example, the actual equilibrium time was delayed up to 90 sec in the case of MF = 0.2 (mf = 0.033) while the equilibrium was achieved within 60 sec in the case of MF = 1.0 (mf = 1.0). Figure 2-35 shows the semi-onset time for equilibrium for different initial cavity air mole fractions. Defining the onset time of the natural convection is highly subjective depending on the observer's decision, and the criteria for the onset time were therefore defined for comparisons as the point that the air mole fraction between Zone 2 (lower plenum) and Zone 5 (reactor cavity) first approach approximately 10%. This definition provides rather faster onset time than the actual onset time for equilibrium, but it could provide the consistent and objective results for analyses and comparisons. For this reason, the onset time in Figure 2-35 was named as semi-onset time for equilibrium. In Figure 2-35, the x-axis represents the initial air mole fraction in the cavity and the y-axis, the semi-onset time for equilibrium. As shown, the onset time exponentially decreases with the air mole fraction. It also shows that if the air mole fraction is reduced lower than 0.4%, the onset time is delayed effectively by twice. Even in this delayed stratified flow transient, the time frame of the stratified flow is still negligibly small compared to the whole accident time frame (usually several days). However, the reduced air mole fraction will highly mitigate the consequences of air ingress accident by retarding the onset of natural convection (ONC) and reducing the graphite oxidation rate.

Figures 2-36 and 2-37 show the air distributions in the reactors in the equilibrium state for isothermal and nonisothermal conditions, respectively. Figure 2-38 shows the comparisons of air profiles at the center of the reactor core for the nonisothermal condition. As shown, the initial air mole fraction in the cavity is not highly sensitive to the level of ingressed air in the core. Figure 2-39 shows that the transition points of air and helium in the core are almost the same, even in the large differences of initial air mole fractions by a factor of 30.

Isothermal (Core Temperature = 300K (27°C))

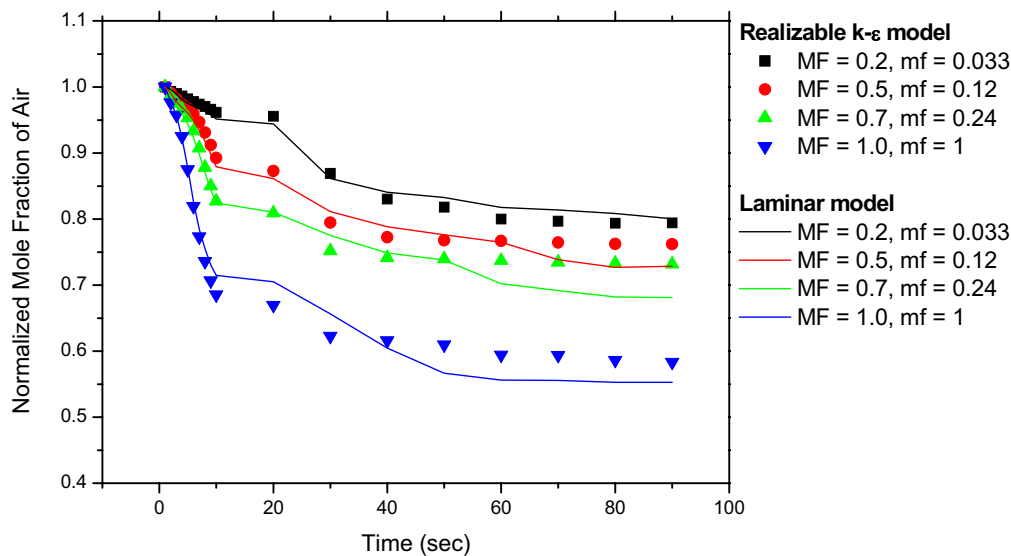


Figure 2-33. Normalized air mole fractions in Zone 5. (MF: initial mass fraction, mf: initial mole fraction)

Nonisothermal (Core Temperature = 1300K (1027°C))

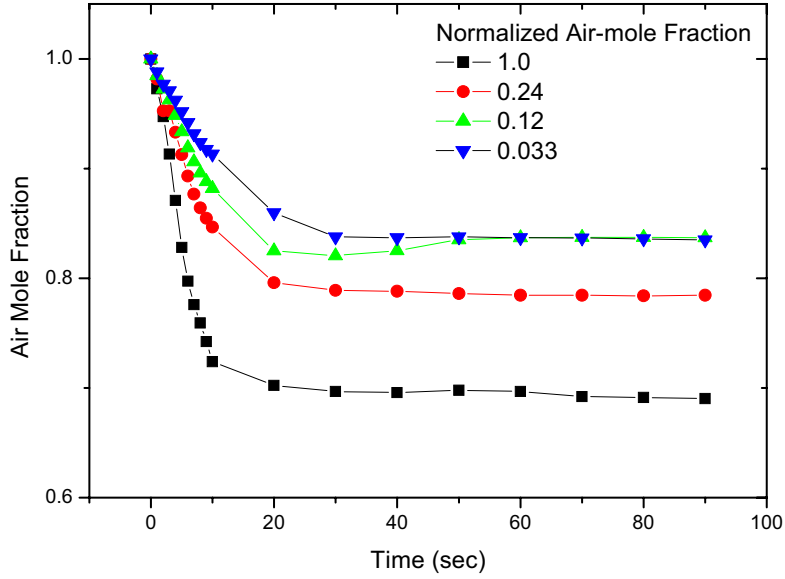


Figure 2-34. Normalized air mole fractions in Zone 5. (MF: initial mass fraction, mf: initial mole fraction)

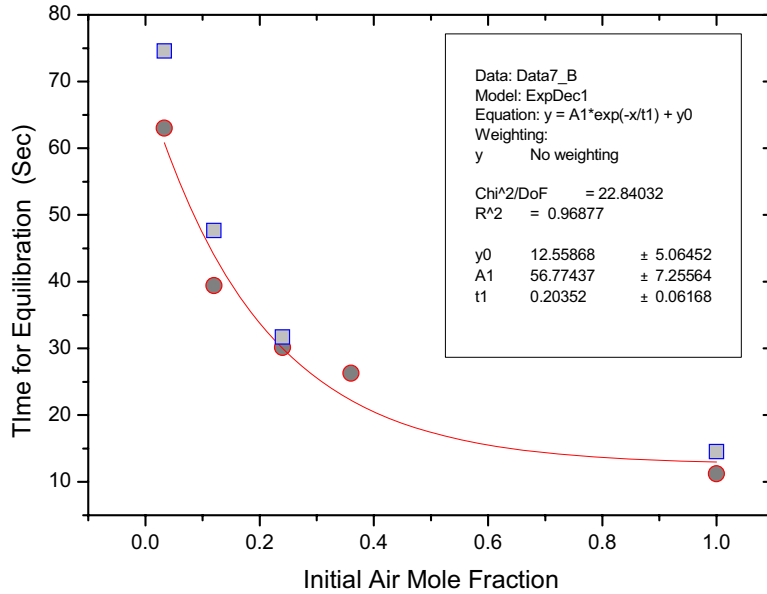


Figure 2-35. Air mole fractions vs. semi-onset time for equilibration.

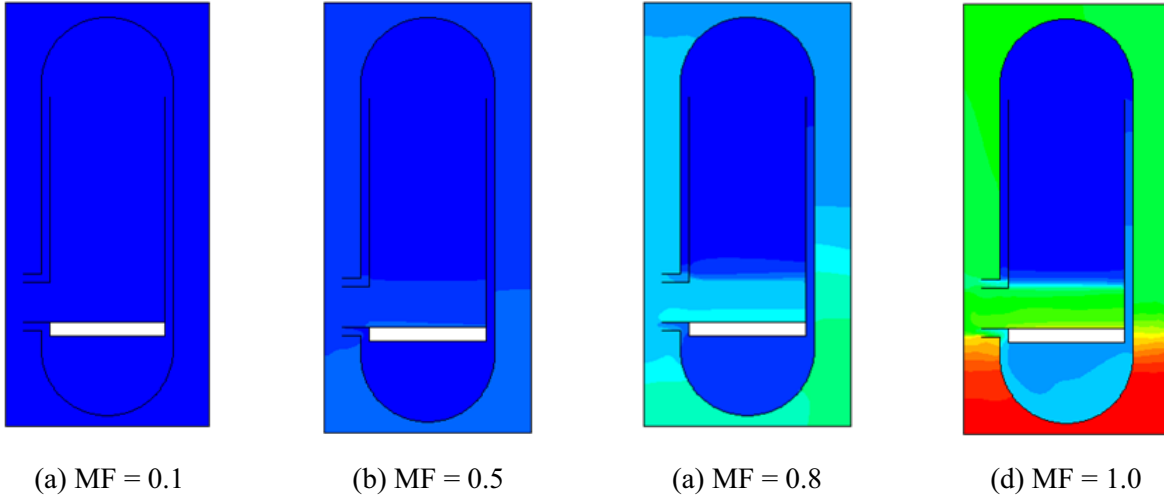


Figure 2-36. Distribution of air-mole fractions for different initial air concentration in the reactor cavity (MF: initial mass fraction)—isothermal.

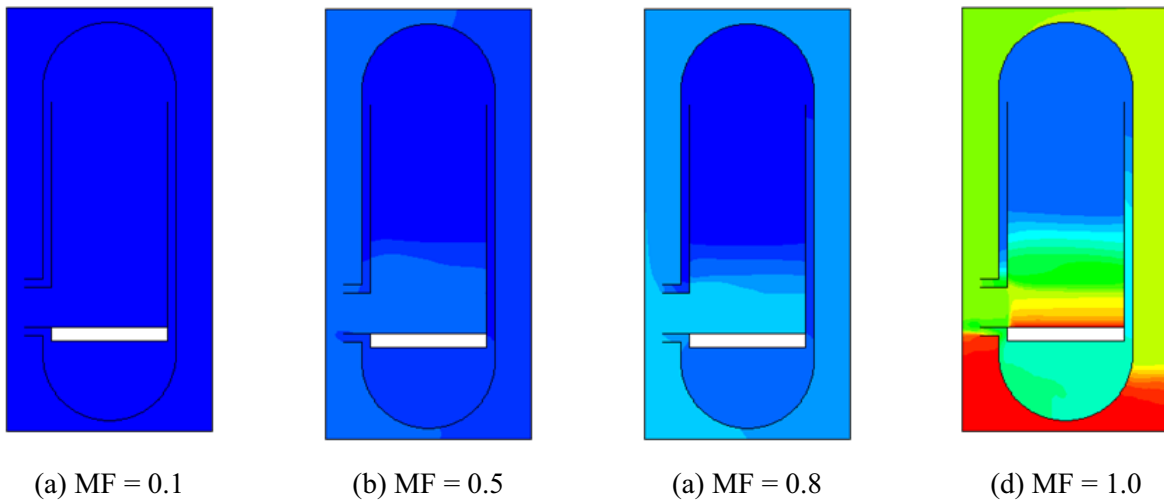


Figure 2-37. Distribution of air-mole fractions for different initial air concentration in the reactor cavity (MF: initial mass fraction)—nonisothermal.

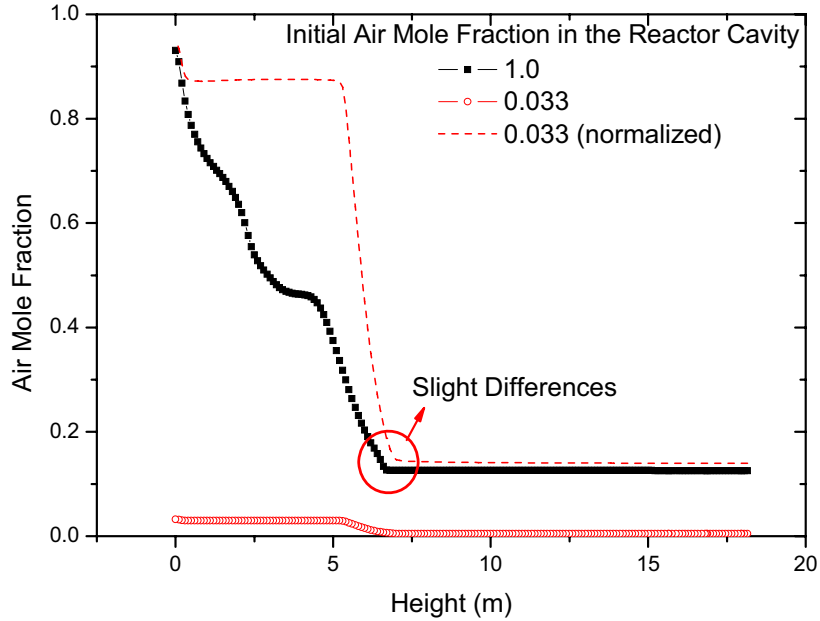


Figure 2-38. Effects of initial cavity concentration in the heated condition. (k- ϵ realizable model, 1300 K (1027°C))

Effect of Flow Resistance in Porous Media

As described in the Section 2.2, the porous media assumption has been used for simplicity in modeling the lower plenum and core. In this assumption, the flow resistance is the main control parameter of the calculations. Circular core channel geometry was used to estimate flow resistance in the core. However, flow resistance in the lower plenum, especially in the x-direction, seems to have rather high uncertainties as shown in Table 2-3 (pages 2-17 and 2-18), which shows a large variety of friction loss correlations, depending on the flow conditions and dimensions. For this reason, a parametric study of flow resistance has been carried out. The flow resistances by factor 0.1 and 10 were considered for estimation.

Figures 2-39 and 2-40 show that the internal resistance in the isothermal condition is not sensitive to the analysis results (for both transient patterns (Figure 2-39) and air distributions (Figure 2-40)). However, for the nonisothermal case shown in Figure 2-41, the internal resistance shows slight effects on the air distributions in the equilibrium state. For example, larger flow internal resistance ($\times 10$) reduces penetration of air into the reactor core and ingress air level by only 10–15%. However, the decrease of internal resistance did not affect air distribution. According to Figure 2-15, which shows that the flow resistance correlation has only 20–30% of the maximum deviations with the data, the effects of flow resistance are expected to be negligible.

Isothermal (Core Temperature = 300K (27°C))

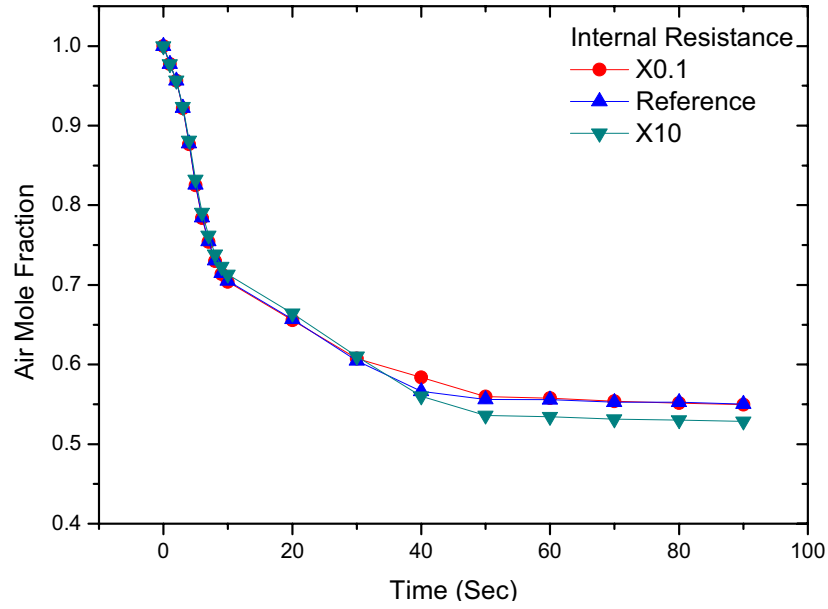


Figure 2-39. Air mole fractions in the reactor cavity.

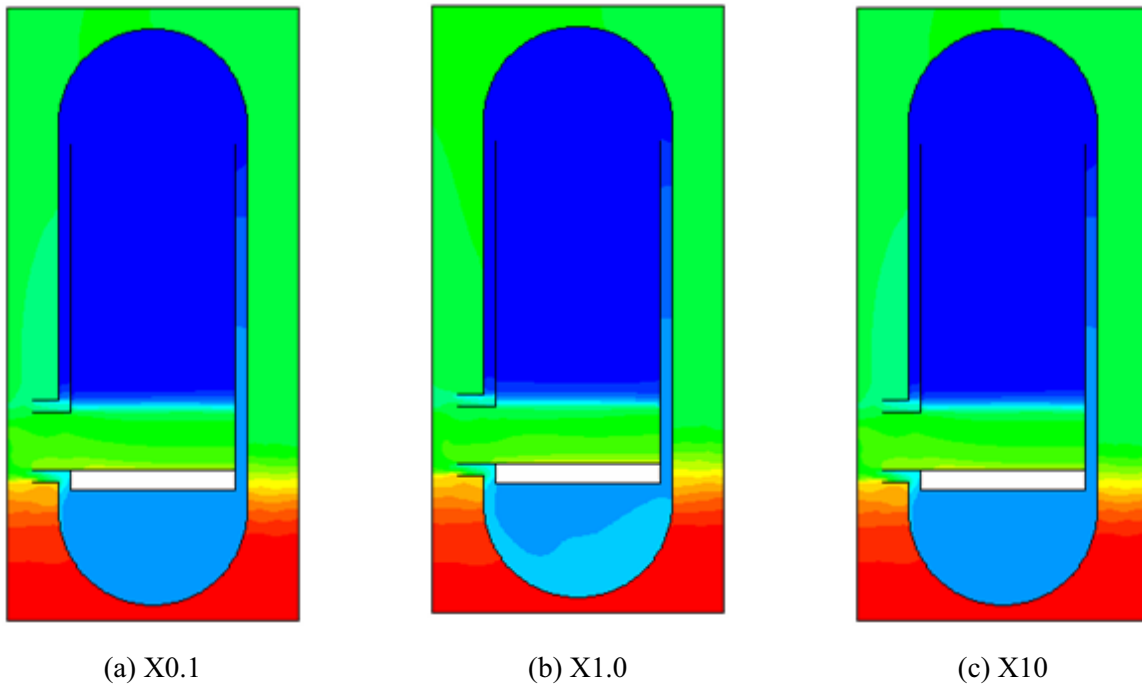


Figure 2-40. Air mole fraction distributions for internal resistance (90 seconds).

Nonisothermal (Core Temperature = 1300K (1027°C))

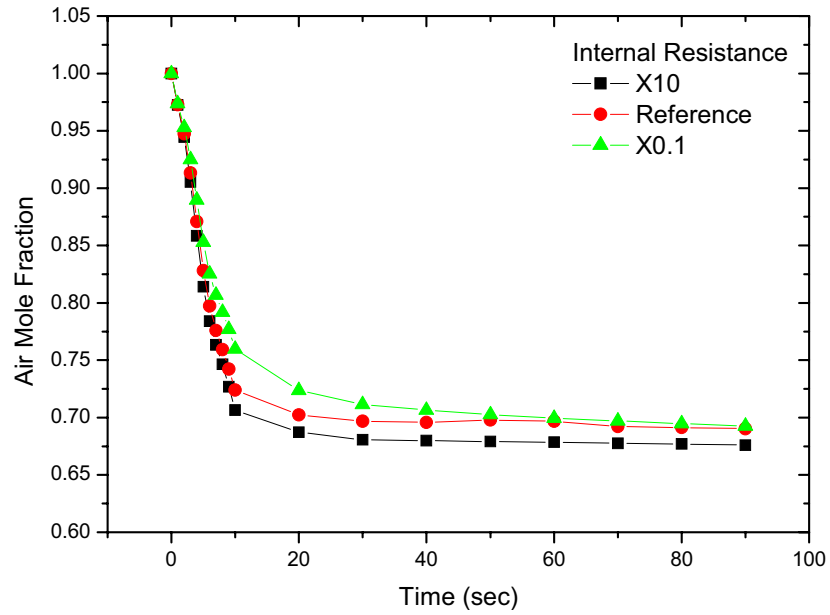


Figure 2-41. Air mole fractions in the reactor cavity.

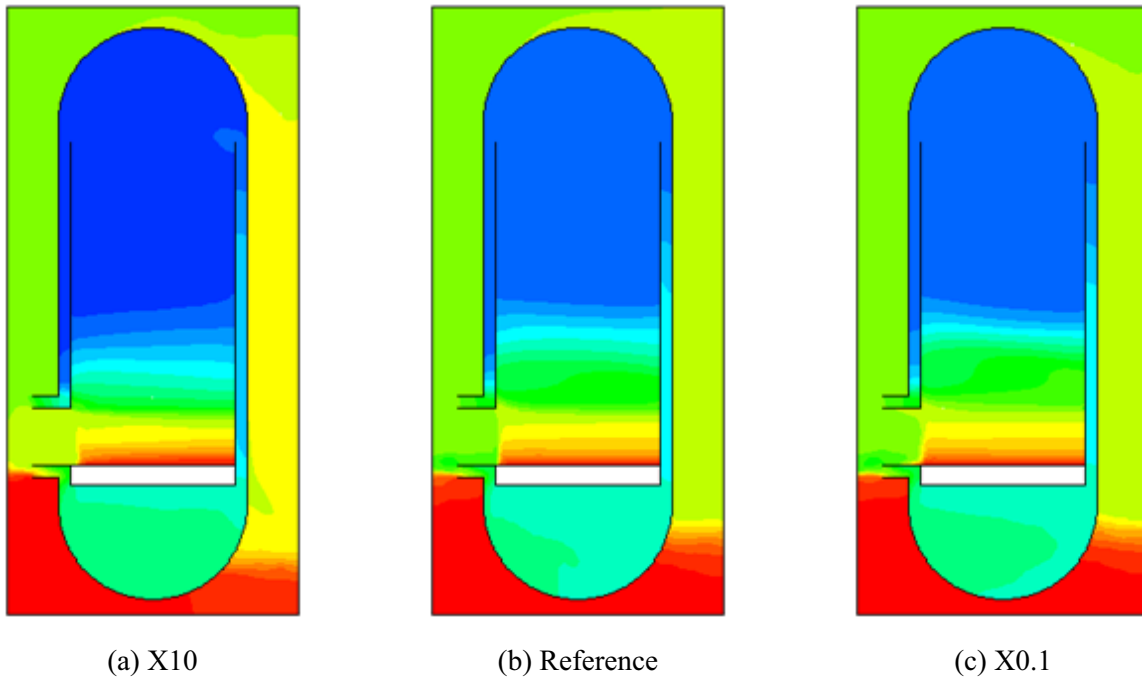


Figure 2-42. Air mole fraction distributions for different permeability (90 sec) ($T_{\text{core}}=1300\text{K}$ (1027°C)).

Summary of Preliminary Analyses

The stratified flow phenomena in the VHTR air-ingress accident was investigated using a commercial CFD software, FLUENT 6.3. Many parameters were extensively estimated including turbulence model, initial air mole fraction in the cavity, permeability in the lower plenum, and core heating effects. The GT-MHR 600 MWt reactor was selected as the reference reactor and modeled in 2-D. The core and the lower plenum were simplified by porous media assumption. The noniterative time advancement method was adapted to increase the calculation speed.

Two parameters were mainly focused on in this study: the time scale of the stratified flow and the air distribution in the equilibrium state. According to this study, the time scale of the stratified flow (~60 sec) was negligibly small compared to that of the diffusion process (~150 hours). It could therefore be assumed that this phenomenon is an instantaneous process in the whole air ingress time-frame. Figures 2-43 and 2-44 show the original and new scenarios of the VHTR air ingress accident, respectively. This study recommends that the original molecular diffusion based air-ingress assumption be replaced with the new assumption considering stratified flow. In the original assumption, the accident scenario is divided into three stages: depressurization, diffusion, and natural convection (see Figure 2-43). However, preliminary calculations showed that the stratified flow effect is very significant in the air-ingress, and even in the low air mole fractions. The newly proposed air-ingress scenario is shown in Figure 2-44. According to preliminary calculations, the stratified flow process was completed and the flow was stabilized within 60–90 seconds for any cases.

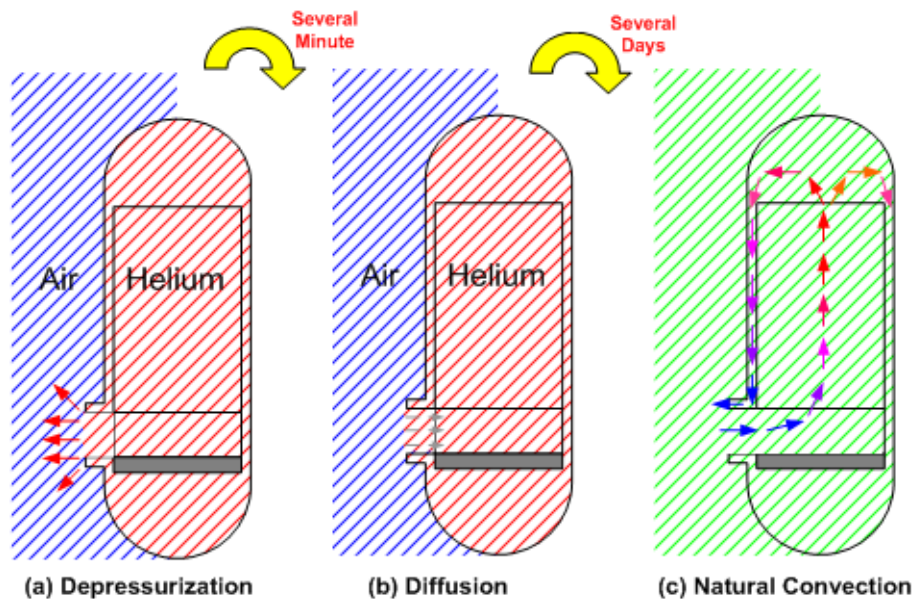


Figure 2-43. Original air-ingress accident scenarios with diffusion assumption.

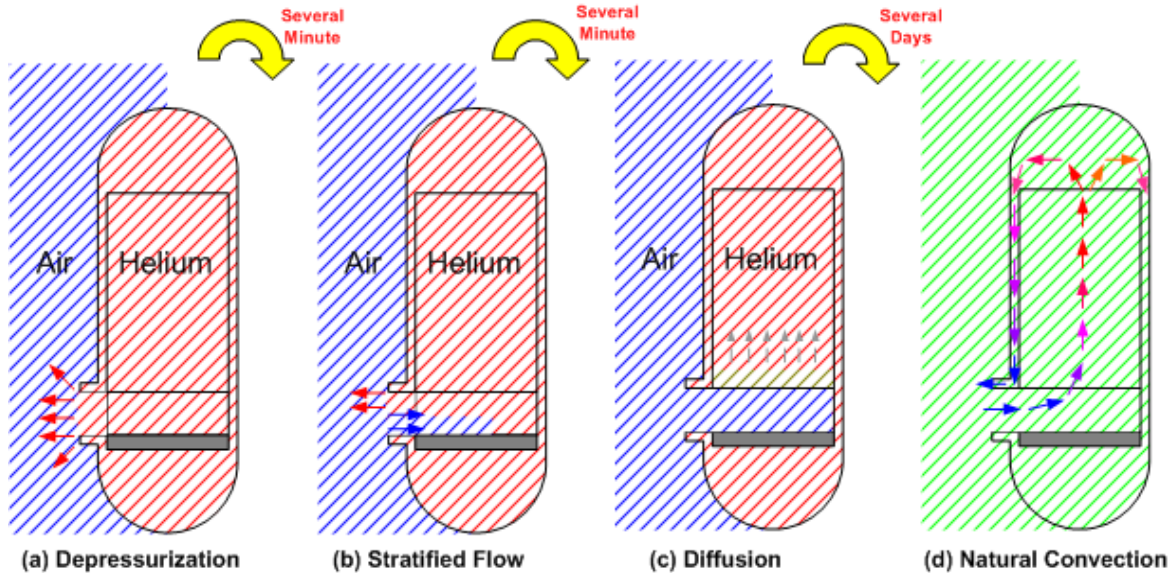


Figure 2-44. Air-ingress accident scenarios, including stratified flow phenomenon.

The air distribution in the reactor core after the stratified flow process is very important because it will highly affect following diffusion process and the final onset natural convection time. Two important parameters affect the air distribution in the final equilibrium state: a viscous model and core temperature distributions. Analyses predicted that more air is penetrated into the reactor core when the flow regime is assumed to be laminar because of less mixing effect in the laminar model than in the turbulence models. The turbulence models with additional mixing terms rapidly mix the air and helium flows and it diminishes the density gradient, which is a main driving force of the stratified flow. Four different turbulence models ($k-\epsilon$ standard, $k-\epsilon$ realizable, $k-w$ standard and Reynolds Stress Model) were considered in the preliminary analyses. In the isothermal calculation, most of the ingressed air was pooled in the bottom of the lower plenum. However, core heating effects (nonisothermal condition) showed very different air distributions in the core, depending on the viscous models. Particularly, the laminar viscous model predicted quite different air profiles in the reactor core with double peak points. Generally, the laminar model seems to provide more conservative results than the other turbulence models because of the lack of mixing effect, which diminish the density gradient, the main driving force of the stratified flow.

The core temperature is another important parameter that affects air distributions. As the temperature increases, more air is ingressed into the reactor core because the heated gas expands. Once the cold air is ingressed into the reactor, it is heated by high temperature structures, causing air temperature rise. It highly expands the air specific volume, finally pushing the air into the core. However, the sensitivity of the core temperature effect significantly decreased with the temperature because the air specific volume is inversely proportional to the temperature.

Our conclusions and recommendations are therefore as follows:

- The original diffusion assumption in the air ingress analysis is incorrect.
- A new stratified flow assumption should be considered in the air-ingress analysis.
- The stratified flow phenomena can be assumed to be an instantaneous process in the whole air ingress scenario, making the final air distributions much more important than the detail transitions of the phenomenon.

- The flow regime (laminar or turbulence) and the core temperature are essential parameters that affect air distributions.
- The laminar model provides more conservative air distributions than the turbulence model because of the lack of mixing terms.
- The determination of the flow regime in the stratified flow process is recommended to be investigated and validated by experimental or numerical methods.

2.3 Air-ingress Analysis Including Stratified Flow in the VHTR

This section discusses the investigation of an air-ingress accident under the new scenario, including density driven stratified flow. Two different codes were used in analyzing the whole air-ingress scenario, with the GAMMA-FLUENT-GAMMA sequence. It also discusses estimates of onset natural convection time, core hot-spot temperature, and graphite structure corrosion.

The main purpose of this investigation was to understand the stratified flow effect in the progression of the air-ingress analysis. To achieve this goal, the analysis was divided into three parts: depressurization, stratified flow, and diffusion and natural convection. Two computer codes were sequentially used for this analysis: The GAMMA code (Oh et al. 2006) and the FLUENT code (FLUENT, 2007). The FLUENT code was used to calculate stratified flow because the GAMMA code does not have turbulence models to calculate the complicated fluid field required for stratified flow. Depressurization and diffusion/natural convection steps were solved by the GAMMA code because it takes much less CPU time compared with that of the CFD code. The results of each step have been used as initial and boundary conditions for the next step. The GT-MHR 600 MWt (GA 1996) was used as the reference reactor by adapting a direct cycle and a prismatic core. Table 2-4 summarizes the assumed sizes of the reference GT-MHR system components. The calculation results in Section 2.3.1 are based on the geometry and initial conditions summarized in this table. In this section, the volume of both cavity and containment were all considered in the total vault volume, while only reactor cavity volume was considered in the Section 2.2. Besides the vault size listed in Table 2-4, infinite vault size was also taken into consideration for conservative analyses. The details are described in the section 2.3.2.

Table 2-4. Assumed size of the GT-MHR 600 MWt system components.

	Confinement	Reactor	PCU	IHX	Vault
Diameter (m)	29	7.6	7.8	3.8	—
Height (m)	43	24	30	14	—
Volume (m ³)	28,388	1,088	1,433	159	25,708
Initial air mole fraction	1	0	0	0	—
Initial pressure	0.1 MPa	7 MPa	7 MPa	7 MPa	—

2.3.1 Simulation of Stratified Flow by CFD

This section summarizes the reference calculations of air-ingress and stratified flow based on Table 2-4. Based on the initial conditions transferred by the GAMMA code depressurization calculation, the stratified flow in the VHTR has been calculated by CFD analysis. The CFD options were:

- Solver
 - 2-D (hexagonal mesh)
 - Segregated Solver
 - 1st order Implicit

- Unsteady
- Noniterative time advancement
- Superficial velocity in porous formulation
- Energy Equation Solve
- Viscous Model
 - Realizable k-e Model
- Species Model
 - Species transport equation
 - Two gas species: Air/Helium (Diffusion coefficients were calculated by kinetic theory)
- Cavity Size was determined by relative volume of vault-to-reactor (22 times larger than the reactor)
- Two different initial air-mole fractions in the cavity were considered: conservative and nonconservative
 - Conservative: The cavity air mole fraction was assumed to be 1.00
 - Nonconservative: Initial air mole fraction in the cavity was assumed to be 0.122 by simple analytic calculation of total air and helium inventories (Table 2-4).

Figure 2-45 shows the reference reactor and the mesh for the FLUENT simulation. The total number of mesh is 51,566. Figure 2-45 was zoomed up only around the core part of the meshes. In the real calculations, a much larger cavity and the real confinement size of the GT-MHR were used using the preconceptual design of GT-MHR.

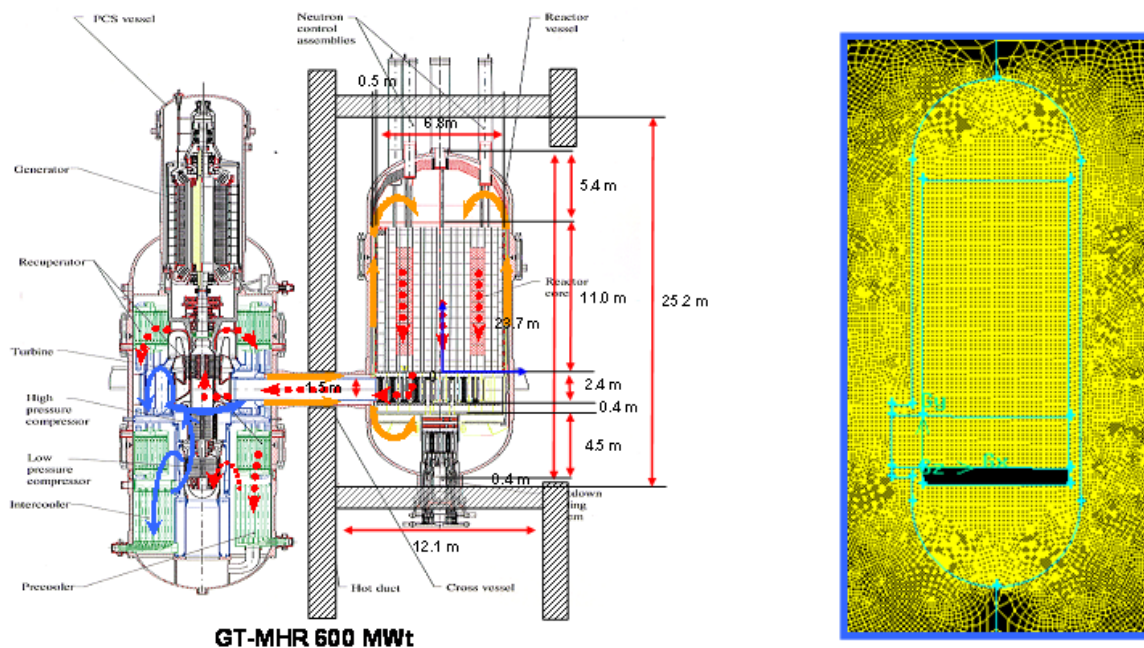


Figure 2-45. Reference reactor (GT-MHR 600 MWt) and Mesh of FLUENT 6.3.

Figure 2-46 shows the initial conditions for the stratified flow calculation for a nonconservative case. The GAMMA code was used to estimate the temperature profile in the reactor core by analyzing depressurization after pipe rupture. Initially, the reactor vessel was filled with helium.

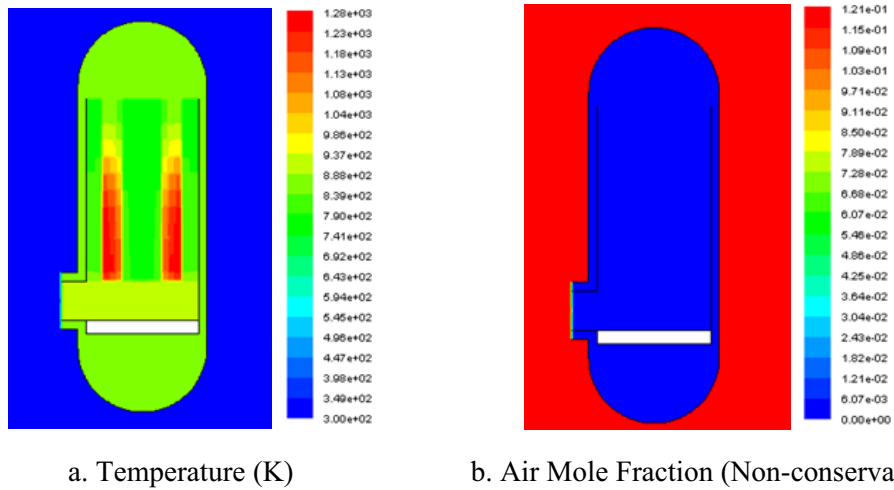


Figure 2-46. Initial condition of temperature and air mole fraction for CFD analysis (nonconservative).

Figure 2-47 is a snapshot of the FLUENT simulation in which the natural convection was initiated about 2–3 minutes after the stratified flow started. And, after 4 minutes, the whole reactor core and vessel was filled with air. It is much quicker than the previous predictions (~150 hrs) using the diffusion driven flow assumption (Takeda [1997], Kadak [2005], Oh et al. [2006]).

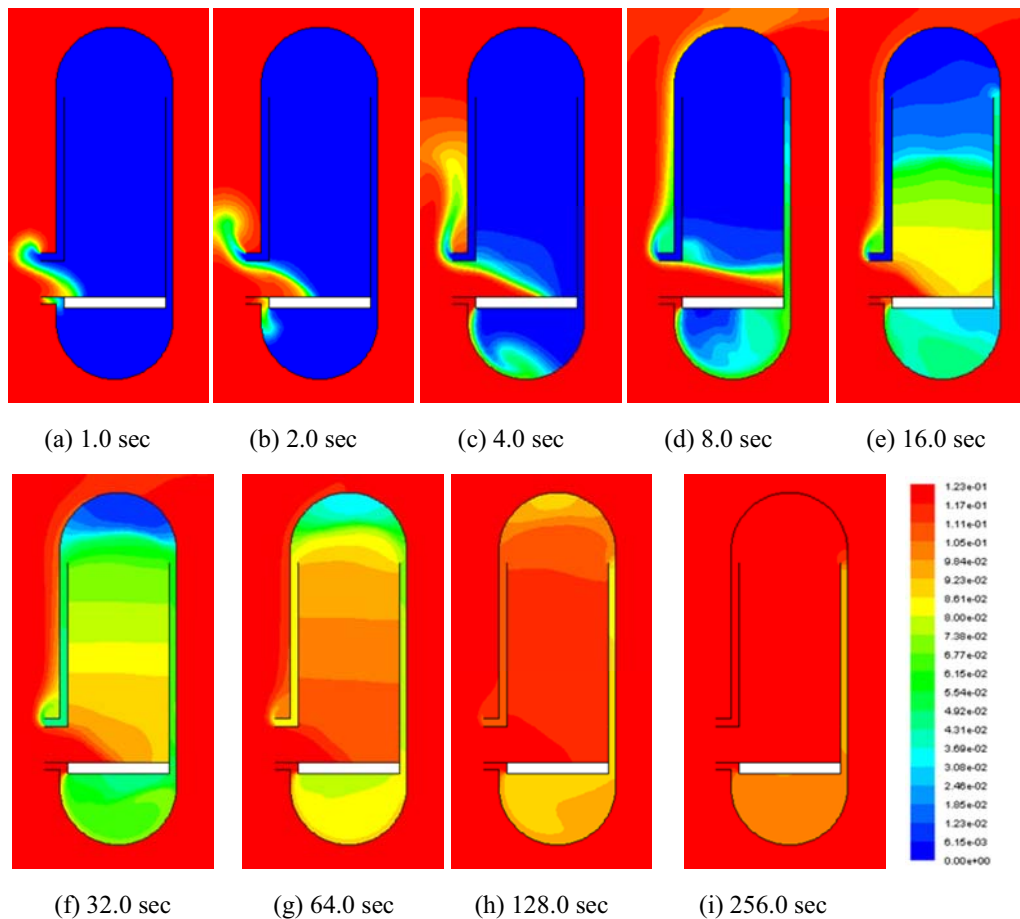


Figure 2-47. CFD analysis results (air mole fraction) of stratified flow in VHTR (nonconservative).

- Natural convection in the cavity.

In the detailed graphite oxidation model, air-ingress analysis was carried out for the following scenarios:

- Diffusion dominated air-ingress in the infinite vault (DDA-1)
- Diffusion dominated air-ingress in the finite vault (DDA-2)
- Stratified flow dominated air-ingress in the infinite vault (SFDA-1)
- Stratified flow dominated air-ingress in the finite vault (SFDA-2).

The diffusion dominated air-ingress scenarios (DDA-1 and DDA-2) are based on the original diffusion assumption so they do not consider the stratified flow effect. These analyses were performed by a single step approach using the GAMMA code for the whole air-ingress process from depressurization to natural convection. The scenario was divided into two cases: in the infinite vault (DDA-1) and in the finite vault (DDA-2). The infinite vault assumes that the air inventory in the reactor cavity and containment is almost infinitely large. The finite vault assumes the size of air inventory ($=25,708 \text{ m}^3$) based on the Table 2-4 (above).

The stratified flow dominated air-ingress scenario (SFDA-1 and SFDA-2) considers the stratified flow effect on the air-ingress analysis. A multistep approach using the GAMMA and FLUENT codes sequentially was applied in considering this as described in the previous sections. The depressurization was first calculated by the GAMMA code and then the calculated air distribution and temperature field have been implemented into the FLUENT initial parameters for stratified flow analysis. The initial air mole fractions in the containment were estimated by the GAMMA code to be 1.0 in the infinite vault case (SFDA-1) and 0.121 in the finite vault case (SFDA-2). It only took 140–160 sec for the onset natural circulation to occur for both SFDA-1 and SFDA-2 cases. Graphite oxidation was not considered in the FLUENT calculations. After calculating stratified flow and onset natural convection by the FLUENT code, the air-distribution, velocity and temperature were reimplemented into the GAMMA code input data. The diffusion and natural convection phase was then calculated by the GAMMA code in the long term.

2.3.2.1 Onset of Natural Convection

The first result summarized is the onset of natural convection. Generally, in the air-ingress analysis, the onset of natural convection is very important because significant chemical reactions will follow this with massive air ingress. Table 2-5 summarizes the results, which show large differences between the two air-ingress scenarios: diffusion dominated air-ingress (DDA-1 and DDA-2) and stratified flow dominated air-ingress (SFDA-1 and 2). The natural convection for DDA-1 was initiated 150 hrs after pipe break, but was not predicted for DDA-2, even within a calculation period of 420 hrs. However, in the case of SFDA-1 and SFDA-2, the natural convections were initiated within several minutes, which might cause much more serious consequences than previously expected because much more air may be ingressed into the reactor core within much less time. This means that the previous analyses by diffusion assumptions do not well represent the real physics with large discrepancies.

Table 2-5. Predicted onset of natural convection time.

Scenario or Assumption	On-Set of Natural Convection
DDA-1	150 hrs
DDA-2	> 420 hrs
SFDA-1	~140 sec
SFDA-2	~160 sec

2.3.2.2 Core Temperature

The core temperature in the VHTR should not be higher than 1600°C (1873K) because of fuel particle failure. Figures 2-49 through 2-52 show the predicted temperature in the reactor core (hot spot), bottom reflector, lower plenum, and top plenum, respectively. The locations of the plotted temperature are marked as blue circles in the small reactor picture in each graph. In the calculation, the maximum temperature at the hot spot in the reactor core was predicted to be around 1500°C (1723K). Note that the core hot spot temperature is not affected by the different scenarios, even after air-ingress by natural convection and also the maximum temperature occurred at approximately 70 hours after the natural convection. The time delay was believed because of the high specific heat of the core graphite that holds and increases the core temperature very slowly. The lack of graphite oxidation in the reactor core hot spot and decay heat removal also contribute to the slow temperature response. According to the analysis data, most of the ingressed air is consumed at the bottom part of the reactor core (bottom reflector and lower plenum) as shown in Figure 2-53. The flow gas mixture in the reactor center and upper core part does not contain any oxygen molecules to be used for oxidation. The core graphite channel diameter is around 2.0 cm and the height of the core hot spot is located around 6–7 m from the bottom of the graphite blocks. Therefore, even air-ingress by natural convection cannot deliver oxygen molecules into this position.

Figure 2-50 shows the temperature variations at the bottom reflector where temperature increases by exothermic graphite oxidation were observed. In the DDA-1 case, the temperature increase was predicted after natural convection because of the exothermic chemical reaction, while it was several minutes later for SFDA-1 and SFDA-2. The SFDA-1 case showed a much larger temperature increase than that of SFDA-2 because of the assumption of infinite air inventory.

Figure 2-51 shows the temperature variations at the lower plenum. In the SFDA-1 case, the temperature drop was very slight because of the oxidation reaction. In the DDA-1 case, sudden temperature increase was predicted after natural convection for the same reason.

Figure 2-52 shows the temperature variations at the top reflector. Even though there is no oxidation reaction at this part, some increase of temperature was observed, potentially because of the heat transfer between heated gas flow and graphite structure at the top reflector.

Figure 2-53 shows the oxygen profile in the reactor core channels during natural convection process in air-ingress for the scenario, SFDA-2. As shown, most of the oxygen is consumed by fast oxidation process before entering the reactor core. The position of the localized hot spot is much higher than this.

As shown in Figures 2-50 through 2-53, the stratified flow effect significantly accelerates the ONC, but the effect on the hot spot temperature was very negligible. It is because most of the reaction is concentrated on the bottom part of the reactor core. This effect increases the temperature at the bottom reflector and lower plenum, but their temperature is still much lower than the maximum temperature criteria, 1600°C.

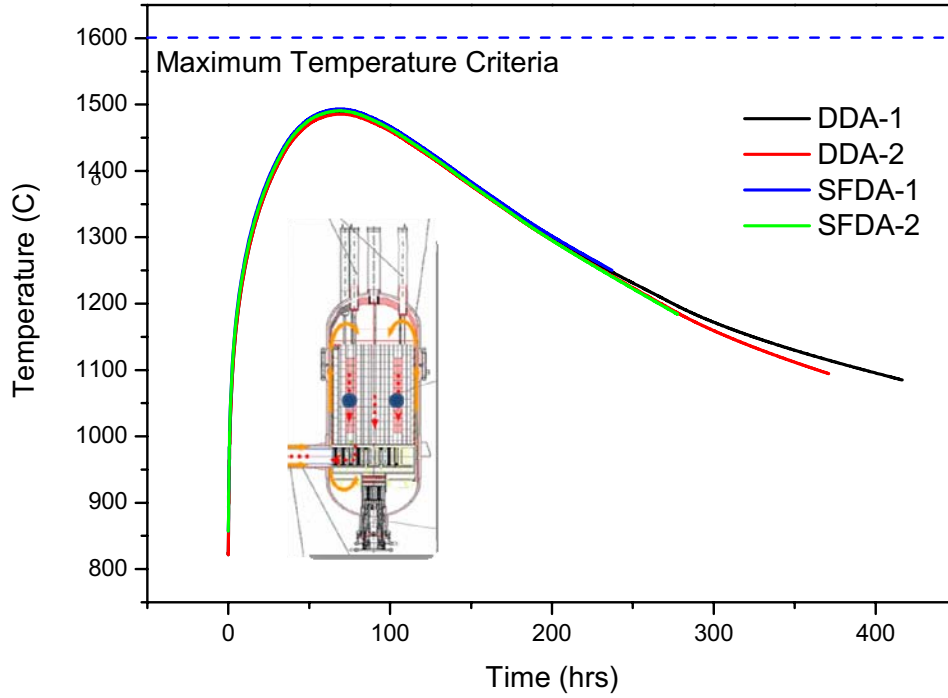


Figure 2-49. Temperature variations at the reactor core (hot spot).

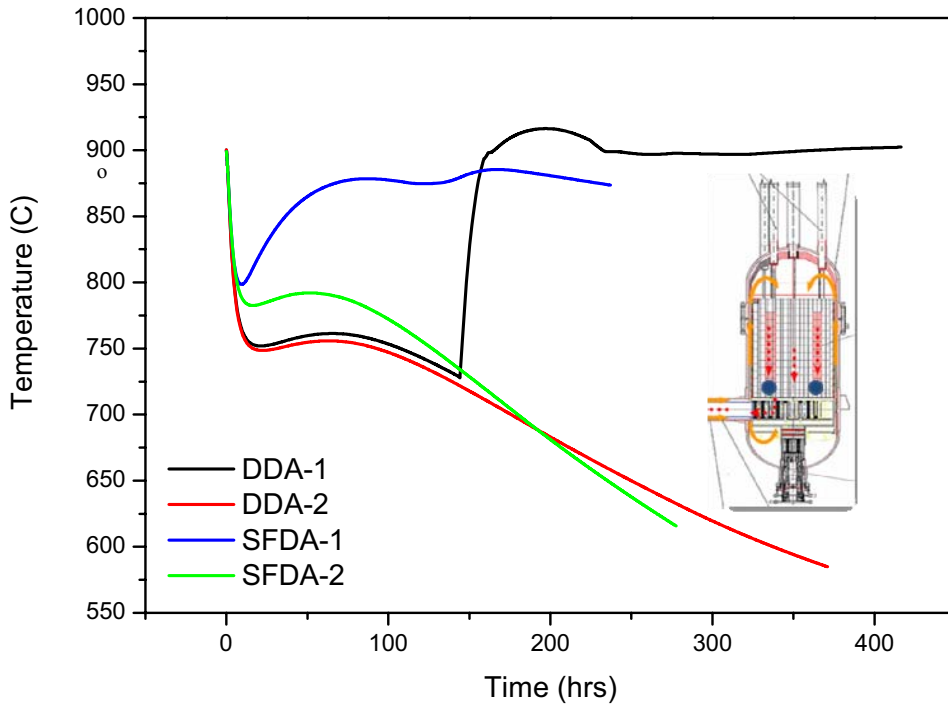


Figure 2-50. Temperature variations at the bottom reflector.

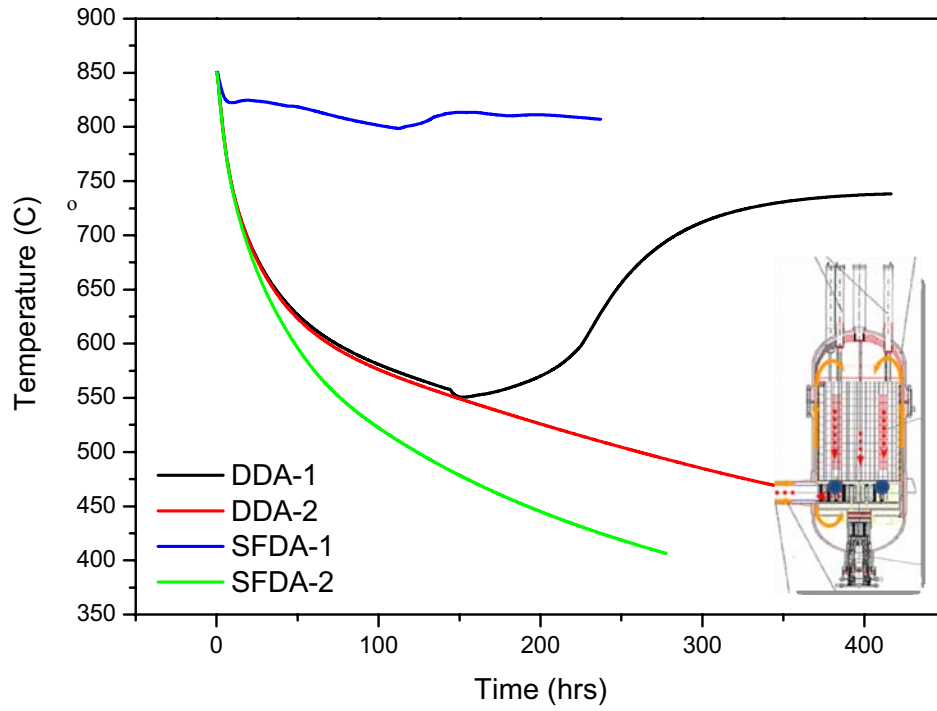


Figure 2-51. Temperature variations at the lower plenum.

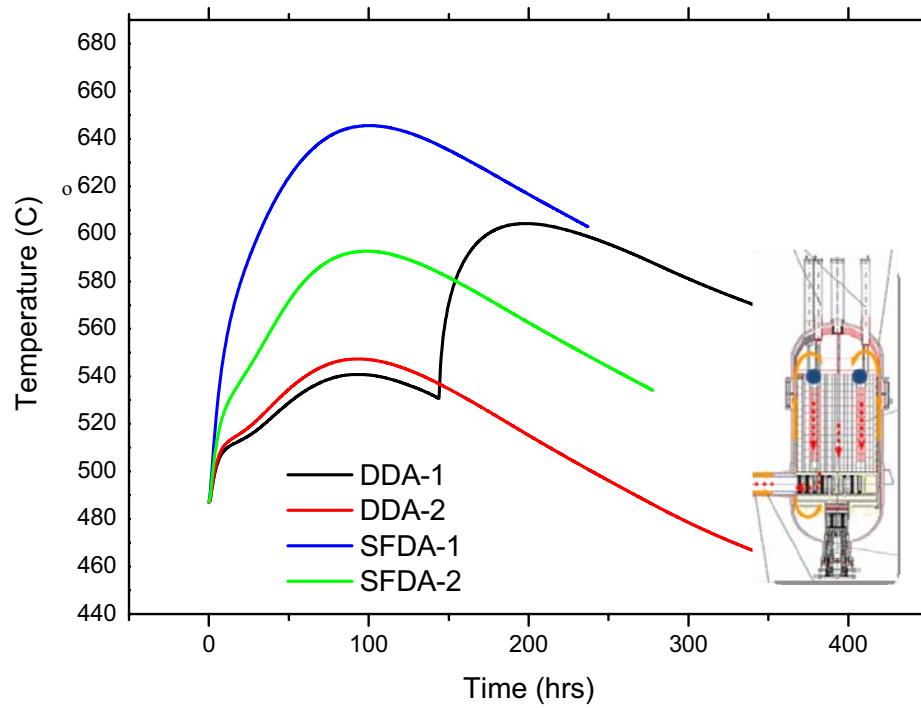


Figure 2-52. Temperature variations at the top reflector.

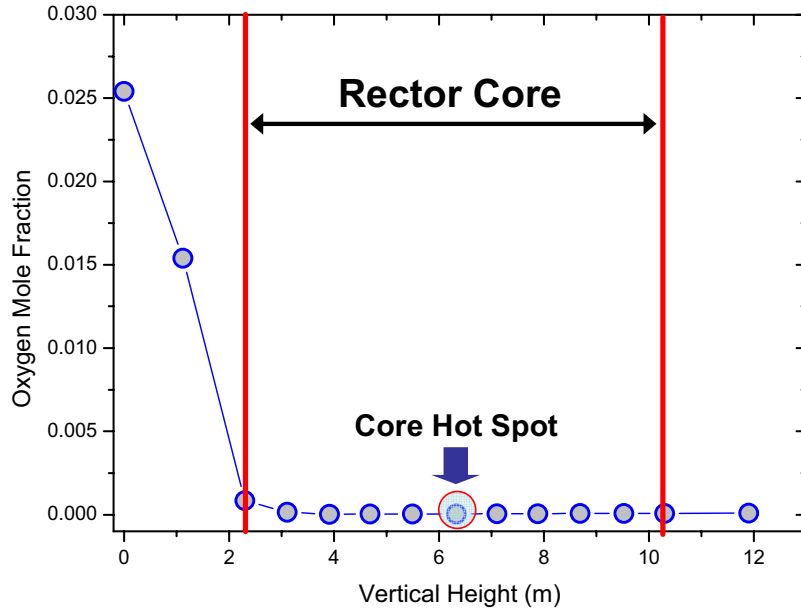


Figure 2-53. Oxygen mole fraction in the reactor core (SFDA-2) during natural convection stage (estimated by the GAMMA code).

2.3.2.3 Graphite Oxidation

The calculated data of the graphite oxidation are summarized here. Estimation of graphite oxidation degree is very important in the VHTR safety because the degraded mechanical strength of the graphite structure would lead to the core structure failure or collapse.

2.3.2.4 Degree of Graphite Oxidation (Graphite Bun-off)

Degree of graphite oxidation can be determined as follows.

$$\Phi = \frac{\rho_0 - \rho(t)}{\rho_0} \quad (2-28)$$

where

Φ = Degree of graphite oxidation

ρ_0 = Density of the original graphite (kg/m^3)

$\rho(t)$ = Density of the oxidized graphite at time, t (kg/m^3).

The physical meaning of Φ is how much graphite density has been decreased by the oxidation. Therefore, $\Phi = 0$ means that no oxidation occurs, and $\Phi = 1$ means that all the graphite is consumed by oxidation. Generally, the mechanical strength of the graphite can be expressed by the degree of oxidation. Figures 2-54, 2-55, and 2-56 show the variation of the degree of oxidation for the lower plenum, bottom reflector, and core, respectively. Each plot shows the largest oxidation degree at the specified structure.

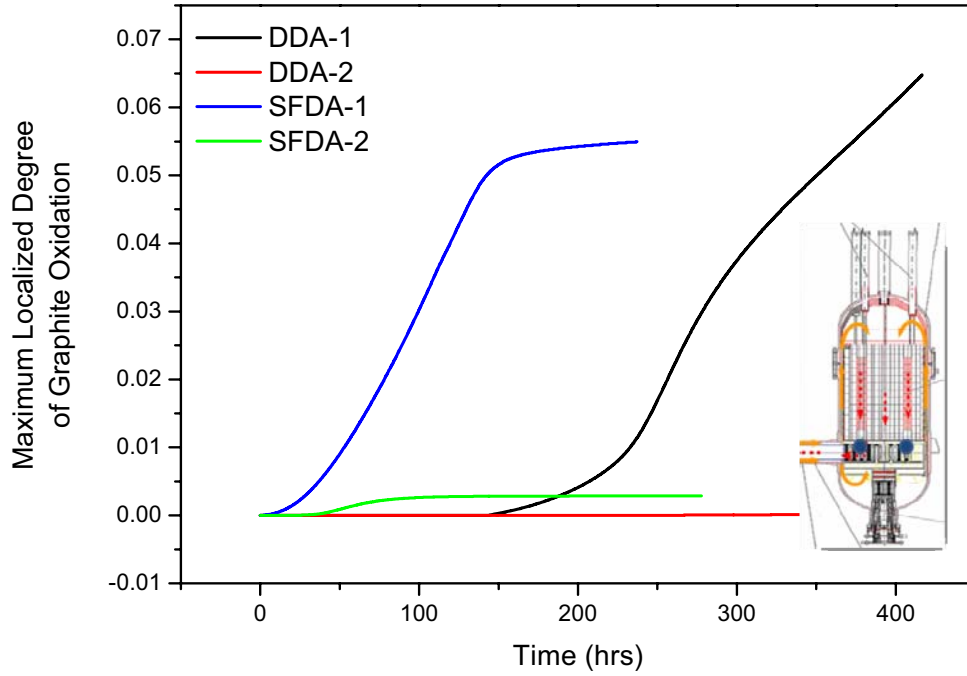


Figure 2-54. Localized degree of graphite oxidation in the lower plenum.

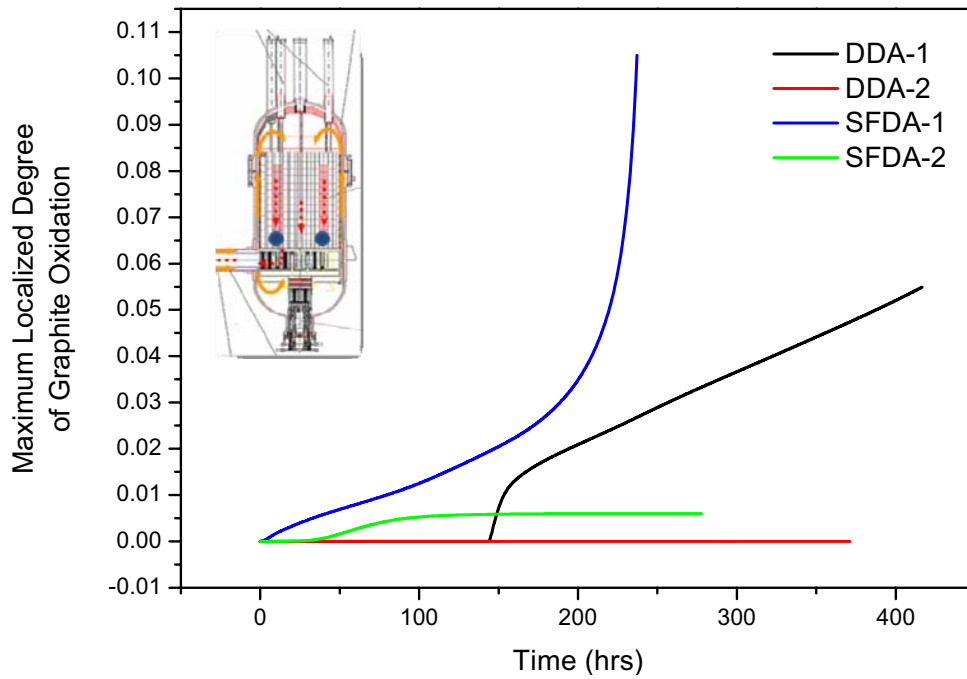


Figure 2-55. Localized degree of graphite oxidation in the bottom reflector.

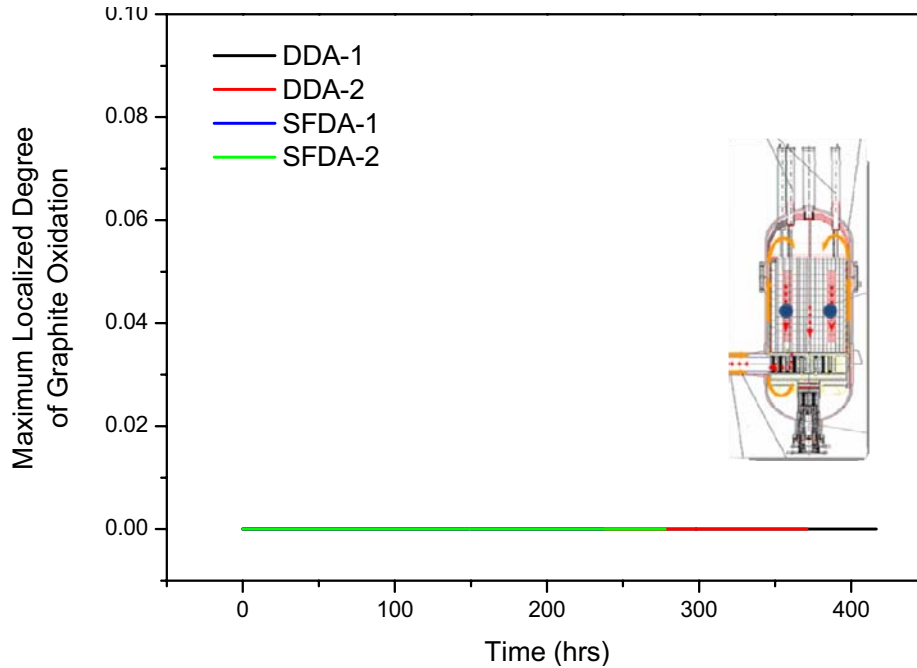


Figure 2-56. Localized degree of graphite oxidation in the reactor core.

As a result, the SFDA-1 case shows the most serious oxidation process. Because DDA-2 and SFDA-2 have small initial air inventories, the change of the oxidation degree is very slight. This means that initial air inventory in the cavity and the confinement is very important for graphite oxidation, and if low oxygen concentration can be maintained in the confinement after depressurization, the oxidation effect can be significantly reduced. In the SFDA-1 case, the massive oxidation initiates about 150 hrs after pipe break, but with natural convection, right after stratified flow, so the problems of the graphite structural integrity seem to be much more serious. In the core, graphite density did not change for any scenario.

2.3.2.5 Void Fraction of the Graphite Structure

There are two different graphite corrosion mechanisms. In the low temperature, since the oxidation is slow, the oxygen can be easily penetrated into the inside pores. It generally changes the graphite density with degradation of mechanical strength. This effect was explained by the degree of graphite oxidation in the previous section. On the other hand, at the high temperature, because the oxidation rate is very fast, the oxidation is highly concentrated on the graphite external surface. In this case, the oxidation does not change the graphite density, but overall size and shape.

This effect can be explained by the void fraction of the graphite structure defined as

$$\Theta = \frac{V_T - V_C}{V_T} \quad (2-29)$$

where

Θ = Void fraction of graphite structure

V_T = Total volume of the graphite structure (m³)

V_C = Volume of the flow channels in the graphite structure (m³).

The graphite structure in the VHTR generally has lots of flow channels. The void fraction of the graphite structures Θ refers to how much of the structures volume is possessed by the channels. If the oxygen corrodes the surface graphite at high temperature, the void fraction will be increased with the size of the channel. It therefore represents how much graphite is oxidized by the external surface reaction.

Figures 2-57, 2-58, and 2-59 show the calculated changes of the void fractions. Significant changes of void fraction were estimated for infinite air inventory cases (DDA-1 and SFDA-1). Especially, SFDA-1 shows very fast increase of void fractions in the bottom reflector, which means that the reaction in the bottom reflector is highly concentrated on the surface because of the relatively high temperature (around 900–1000°C). According to Figure 2-58, most of the graphite structures were corroded by the oxidation process within 250 hrs after the accident.

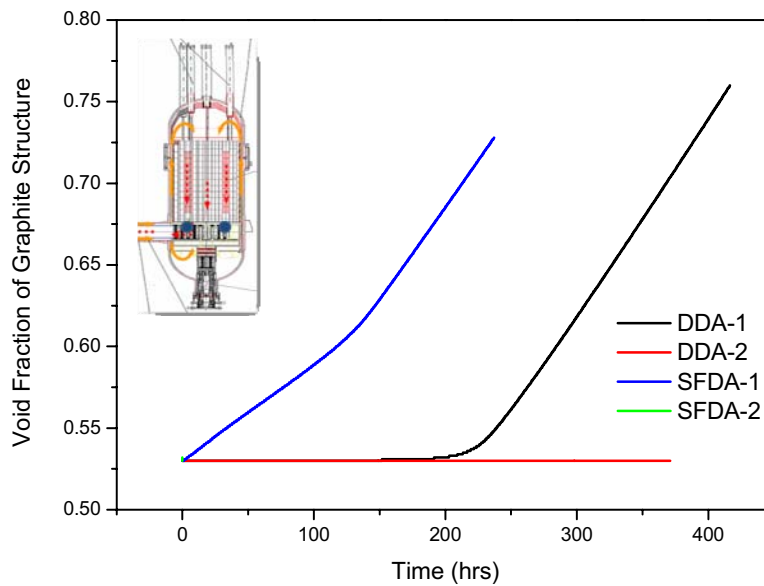


Figure 2-57. Void fraction of graphite structure at the lower plenum.

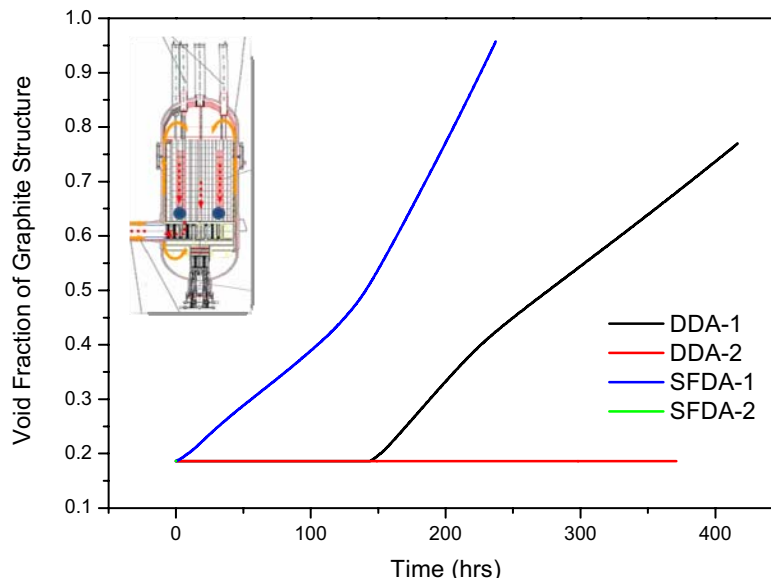


Figure 2-58. Void fraction of graphite structure at the bottom reflector.

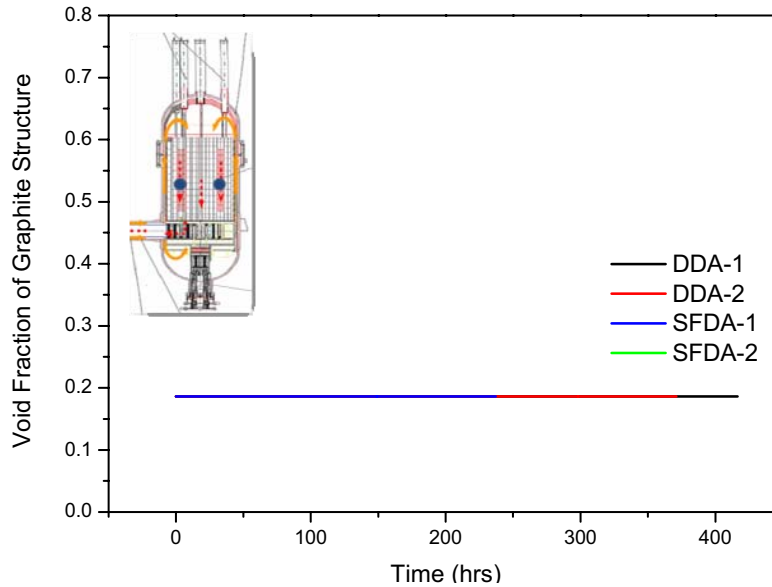


Figure 2-59. Void fraction of graphite structure at the reactor core.

2.3.3 Summary of the Air-ingress Analysis, including Stratified Flow Effect

In the new scenario, the ONC was significantly accelerated by the stratified flow consideration leading to much faster oxidation in the graphite structure. This means that the previous assumptions on the air-ingress accident will lead to the underestimation on their consequences. It is therefore highly recommended that the original air-ingress scenario based on molecular diffusion be replaced with the new assumption considering stratified flow. However, the core hot spot temperature was not changed by the new scenario because of the fast oxygen depletion at the lower plenum passing through the channels. However, the highly concentrated oxidation is predicted, making the potential core collapse problem at the lower plenum much more serious. Thus, further investigation of the core collapse problem is highly recommended.

3. TASK 2: EXPERIMENTAL STUDY ON THE STRATIFIED FLOW (INL)

3.1 Introduction

Air-ingress is potentially the most serious accident in VHTRs. This accident occurs when a pipe breaks inside the reactor, allowing the air surrounding the reactor to be rapidly ingressed into the reactor vessel. This accident scenario will result in serious problems such as chemical reactions between oxygen and the core graphite structures that heat up the reactor core and damage the structural integrity, releasing toxic gases such as CO and CO₂.

This accident scenario can generally be divided into three stages—depressurization, molecular diffusion, and natural convection—which are based on the idea that air-ingress is initially controlled by a molecular diffusion process until the natural convection stage begins. Because molecular diffusion is a very slow process, previous estimations (Takeda 1997, Kadak and Zhai 2005, Oh et al. 2006) show that this scenario has a very slow ONC. The estimated time of ONC after a pipe break was around 150–200 hrs in the previous researches, which says that there is sufficient time to take actions to protect or avoid the problems before the massive air-inflow is triggered. Recently, researchers at the Japan Atomic Energy Agency proposed an air-ingress mitigation method that would use a counter-diffusion process to successfully mitigate or protect the natural convection under the diffusion driven air-ingress situation.

However, some recent studies show that the previous air-ingress scenario may be physically incorrect (Shultz et al. 2006, Liou and Parks 2005, Oh et al. 2008). They point out that air-ingress process is not initially controlled by a molecular diffusion, but by a density-driven stratified flow between helium and air gases. They also believe that it will finally lead to much faster air-ingress into the reactor, which significantly changes the whole accident scenario. A recent CFD analysis by Oh et al. (2008) showed that the natural convection could be started within several hours or minutes after a pipe break, much earlier than the previous predictions of 150–200 hrs. The earlier ONC would lead to much more serious consequences from chemical reactions. It is therefore obvious that an air-ingress accident must be treated more carefully than has been done so far.

One issue regarding stratified flow associated with VHTRs is how to validate the simulation codes for this phenomenon. Previous experiments showed that current multidimensional codes and physical models can predict this phenomenon qualitatively well, but their quantitative results have not yet been validated against reliable experimental data. For instance, an air-ingress accident is complicatedly coupled with molecular diffusion, heat transfer, natural convection and porous media flow, stratified flow, etc., so it is very important to validate the codes at this time.

A couple of sets of experiments were planned to understand stratified flow phenomena and validate the computer codes with physical models. This experimental work covers a separate effort to couple effects related to the stratified flow.

3.2 Required Validation Data for Stratified Flow Driven Air-ingress Analysis

Before the experiments on stratified flow were planned, the experiments and validation process for previous air-ingress analyses were reviewed.

The original diffusion driven air-ingress scenario assumes that the initial air-ingress process is determined by molecular diffusion. Therefore, most of the experiments performed focused on diffusion and its coupling effects. According to the original scenario, the following phenomena were considered important for validation.

- Molecular diffusion
- Natural convection
- Heat transfer
- Radiation
- Chemical reaction
- Porous media.

Table 3-1 summarizes the experimental work and the data sets used for validation of previous air-ingress analyses. Duncan & Toor’s (1962) experiment, Ogawa’s (1993) circular tube test, and SANA-1 after heat test (IAEA 1981) were planned to validate the separate effects on a single phenomenon. All the other experiments also considered some coupling effects between two or three different phenomena. In the previous validation process, codes were validated for the separate phenomena and then, if the code validity and credibility were confirmed for basic phenomena, the coupling effects were validated. For example, molecular diffusion was first validated by the Two Bulb Test. Then, the coupling effect of molecular diffusion and natural convection was validated by the Inverse U-tube experiment. After that, the coupling effect of molecular diffusion, natural convection, and chemical reaction was validated by the Inverse U-tube air-ingress experiment. Similar to this example, stepping from the simplest phenomena to the more complicated ones by sequentially adding more phenomena greatly helps experimenters figure out which part of the code causes problems and which models should be modified when problems occur. In contrast, if the codes are validated directly in a single experiment that contains all of the related affects, it is very difficult to find what is wrong with the code when problems occur.

Table 3-1. Experiments and validation data for the air-ingress analysis.

	Test Facility	D	NC	R	C	P	etc
1	Pipe Network, NWU						○
2	Blowdown, NWU	○					○
3	Buncan & Toor’s Experiment	○					
4	Inverse U-tube single/multiple channel test	○	○				
5	Ogawa’s circular tube test				○		
6	Takahashi’s annular tube test				○		
7	VENTURA pebble bed test				○	○	
8	Inverse U-tube air ingress experiment	○	○		○		
9	HTTR simulated air ingress experiment	○	○		○		○
10	Vertical slot experiment	○	○				
11	NACOK natural convection test		○			○	
12	SANA-1 afterheat removal test					○	
13	HTTR RCCS mockup test		○	○			
14	SNU RCCS test		○	○			

D: Diffusion NC: Natural Convection R: Radiation C: Chemical Reaction
P: Porous Media

Although the stratified flow was not an issue in the previous air-ingress analyses as shown in Table 3-1, the same approach can be used for the new scenario by adding some needed experiments. The separate effects of stratified flow should first be validated by simple experiments. The coupled phenomena can then be validated by more complicated experiments. A design matrix was used to estimate the number of experimental sets required for validation of stratified flow. Design matrices are generally used for understanding a system and its requirements, figuring out if the design of the system is good or not, and how to improve it (Suh 1990). In this study, this method was used to check the requirements and see how many and what kinds of experiments are required for completing the code validations.

To make a design matrix, function requirements (FRs) and design parameters (DPs) should be first determined. In this application, FRs are phenomena and models that should be validated. The FRs required for validation of the original air-ingress analyses are:

- FR1: Validation of the separate effect of diffusion is required
- FR2: Validation of the separate effect of natural convection is required
- FR3: Validation of the separate effect of radiation is required
- FR4: Validation of the separate effect of chemical reaction is required
- FR5: Validation of the separate effect of porous media model is required
- FR6: Validation of the coupling effect of diffusion and natural convection is required
- FR7: Validation of the coupling effect of natural convection and radiation is required
- FR8: Validation of the coupling effect of natural convection and chemical reaction is required
- FR9: Validation of the coupling effect of porous media and natural convection is required.

Other coupling effects such as diffusion/radiation and porous media/radiation were not considered for simplifications because they are considered minor effects. The coupling effects of three different phenomena are also not considered here because three coupling effects can usually be expressed by a combination of two coupling effects, but, this concept should be given additional consideration in the future. Once FRs are determined, DPs that satisfy the FRs should be determined. In this study, the separate experiments can be considered DPs. According to the Axiomatic Design Concept, the number of DPs should be the same as the number of FRs, so nine DPs are required for an ideal design (Suh 1990). Based on the experiments summarized in Table 3-1, the DPs can be arranged as follows.

- DP1: Duncan & Toor's Two Bulbs experiment
- DP2: General natural convection experimental data
- DP3: General radiation heat transfer data
- DP4: Ogawa's circular tube test or other graphite oxidation tests
- DP5: SANA-1 after heat removal test
- DP6: Inverse U-tube single/multiple channel test
- DP7: High Temperature Engineering Test Reactor (HTTR) RCCS mockup test or SNU RCCS test
- DP8: Inverse U-tube air ingress experiment or HTTR mockup experiment
- DP9: NACOK natural convection test.

Table 3-2 shows the design matrix based on the above FRs and DPs. The “X” mark in the table means that the FR and the DP are closely related; the “O” mark means that there is no relationship between them. The Axiomatic Design Concept (Suh 1990) highly recommends that the design matrix be diagonal or tri-diagonal for an ideal design because it will have an independent axiom, which is the most important axiom in this theory. To better understand this theory, refer to some reference books about Axiomatic Design (Suh 1990). Table 3-2 has the tri-diagonal matrix form, indicating that this experimental set provides complete data for code validation, but only if the design conditions cover the VHTR applications and the data obtained is reliable. In the tri-diagonal forms of this type of design matrix, validation should be sequentially performed for FR1–FR9 in order to decouple the related FRs. For example, in Table 3-2, DP8 has two related FRs; FR6 (diffusion/natural convection) and FR8 (natural convection/chemical reaction). In this case, if it is assumed that the prediction by a code does not agree with the experimental data of DP8, it is difficult to determine if FR6 or FR8 is correct. However, if it is assumed that DP6 is already performed and FR6 is validated in advance, then FR8 will be a mismatch problem for data. This process is referred to above as a decoupling process. By this method, the physical phenomena can logically be validated independently.

Table 3-2. Design matrix for diffusion driven air-ingress validation experiments.

	DP1	DP2	DP3	DP4	DP5	DP6	DP7	DP8	DP9
FR1	X	O	O	O	O	O	O	O	O
FR2	O	X	O	O	O	O	O	O	O
FR3	O	O	X	O	O	O	O	O	O
FR4	O	O	O	X	O	O	O	O	O
FR5	O	O	O	O	X	O	O	O	O
FR6	O	O	O	O	O	X	O	X	O
FR7	O	O	O	O	O	O	X	O	O
FR8	O	O	O	O	O	O	O	X	O
FR9	O	O	O	O	O	O	O	O	X

The same process can be also applied to the stratified flow air-ingress situation. In this case, the same FRs from FR1 to FR9 are present, but some additional FRs are needed to consider stratified flow phenomenon. In order to cover the stratified flow in the design matrix, the following four FRs were included:

- FR10: Validation of the separate effect of stratified flow is required
- FR11: Validation of the coupling effect of stratified flow and natural convection is required
- FR12: Validation of the coupling effect of stratified flow and porous media is required
- FR13: Validation of the coupling effect of stratified flow and chemical reaction is required.

To maintain the ideal design of the experimental sets, the following four additional DPs, consisting of the newly designed experiments, were added to match the four FRs:

- DP10: Stratified flow experiment in the horizontal circular pipe
- DP11: Stratified flow and natural convection test
- DP12: Stratified flow and natural convection test with pebbles
- DP13: Stratified flow and natural convection test with graphite pebbles.

The design matrix in Table 3-3 was developed based on the above additional FRs and DPs. This matrix is still a tri-diagonal matrix, but more complicated than Table 3-2 because the molecular diffusion is always coupled with the stratified flow so that all the FRs can be easily decoupled. Details of these experiments are described in the following sections.

Table 3-3. Design matrix for stratified flow driven air-ingress analysis.

	DP1	DP2	DP3	DP4	DP5	DP6	DP7	DP8	DP9	DP10	DP11	DP12	DP13
FR1	X	O	O	O	O	O	O	O	O	O	O	O	O
FR2	O	X	O	O	O	O	O	O	O	O	O	O	O
FR3	O	O	X	O	O	O	O	O	O	O	O	O	O
FR4	O	O	O	X	O	O	O	O	O	O	O	O	O
FR5	O	O	O	O	X	O	O	O	O	O	O	O	O
FR6	O	O	O	O	O	X	O	X	O	O	O	O	O
FR7	O	O	O	O	O	O	X	O	O	O	X	X	X
FR8	O	O	O	O	O	O	O	X	O	O	O	O	O
FR9	O	O	O	O	O	O	O	O	X	O	X	X	X
FR10	O	O	O	O	O	O	O	O	O	X	O	O	X
FR11	O	O	O	O	O	O	O	O	O	O	X	X	X
FR12	O	O	O	O	O	O	O	O	O	O	O	X	X
FR13	O	O	O	O	O	O	O	O	O	O	O	O	X

3.3 Planned Experiment

3.3.1 Isothermal Experiment in the Horizontal Circular Pipe (TEST 1)

The first experiment investigated some separate effects of the stratified flow in a horizontal pipe. It covers DP10 in the Design Matrix of Table 3-3. The main purpose was to provide data for validation of CFD or system analysis codes for application to the VHTR air-ingress analyses.

Figure 3-1 shows a schematic of the experimental facility, which is composed of two tanks and a horizontal pipe. The horizontal pipe is 20 cm diameter and 1.0 m long. The height and diameter of the Tanks are 1–1.5 m and 0–1.0 m, respectively. It operates at ambient temperature and 10.6 atm. A simple scaling method was used to determine the operating pressure. The details are described in the later part of this section. The horizontal tube was made of plexiglass (Acryl) for visualization and the tanks were made of plexiglass or metal. The working fluids are CO₂ and helium. An annular-shaped double-pipe design is proposed to sustain the high pressure (~10.6 atm) with the plexiglass (See Figure 3-1), where the inner tube pressure is 10.6 atm, and the outer tube pressure is 6 atm. The outer tube is filled with nitrogen gas and plays a role as a pressure buffer between the inner tube and environment. The reduced pressure differences will make it possible to use the plexiglass in 10.6 atm.

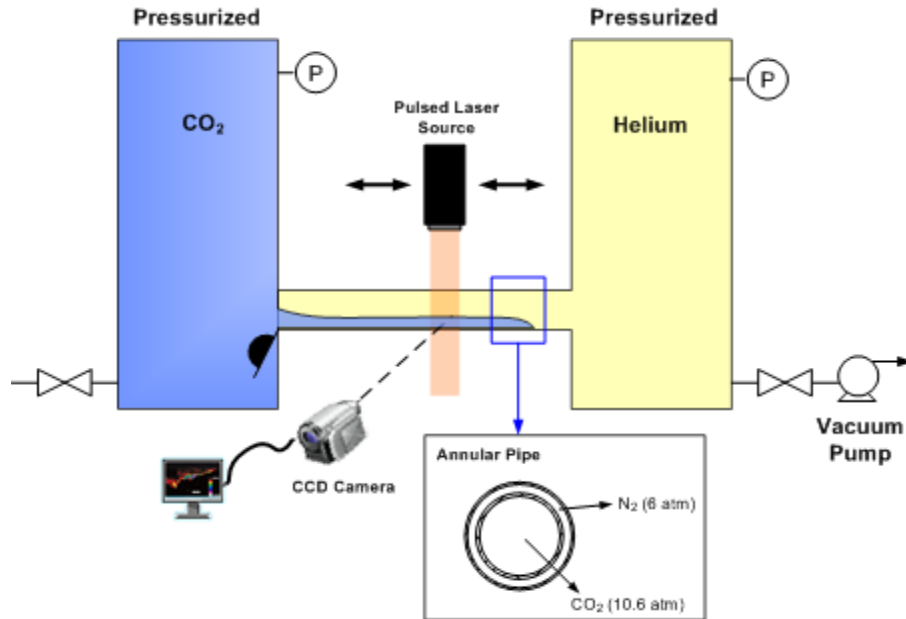


Figure 3-1. Isothermal experiment in the horizontal pipe (schematic).

The experimental procedure is simple: (1) The air is removed from the test section by a vacuum pump. (2) The valve in the horizontal pipe is closed; this valve will be designed to be automatically controlled. (3) If the valve is closed and the two tanks are isolated, helium and CO₂ gases are injected into the tanks, respectively so that one tank is filled with helium and the other one with CO₂. In this case, the pressure in the helium tank will be set to be a little bit higher (about 0.5 atm) than the CO₂ tank. (4) When the gases are stabilized in the tanks, the experiment is started by opening the valve installed in the horizontal pipe. (5) When it starts, since the pressure in the helium side is higher than the CO₂ side, helium flows into the CO₂ tank. (6) After the pressure is balanced at the bottom of the pipe, stratified flow is initiated with heavy CO₂ flowing down and light helium flowing up, forming a counter-current. The planar laser-induced fluorescence (PLIF) method will be used to visualize the flow patterns and the gas concentrations. By using this method, the concentration of some gas species (especially oxygen) and 2-D velocity vectors can be obtained.

The PLIF facility can be prepared by simply modifying a setting in the particle image velocimetry (PIV), currently located at INL. Oxygen gas will be used as a seed material for the PLIF method. As a back-up method for the flow visualization, a smoke generator will be installed on the side of the CO₂ tanks. To keep the smoke particle suspended in the tanks, the smoke particle injector will be located near the pipe entrance. Interactions between smoke particles and the light helium gas should be also considered for selection of the smoke particles. The PLIF method is summarized below. To minimize the reflection effect of the laser on the circular pipe, a rectangular box can be installed at the measurement location.

3.3.1.1 Planar Laser-Induced Fluorescence

Planar laser-induced fluorescence (LIF) is a nonintrusive, in situ, optical diagnostic that can remotely image a selected molecular species in a fluid flow (Kirby 2001). PLIF is a sequence of molecules or atoms being excited to higher electronic energy states via laser absorption followed by spontaneous emission of fluorescence. The spectral absorption regions are discrete, because the energy state of molecules and atoms are quantized. Typically, fluorescence occurs at wavelengths greater than or equal to the laser wavelength. Therefore, LIF offers the possibility to investigate species of interest by selecting the appropriate wavelength (Yokomae 2003).

Figure 3-2 shows the state view of LIF. Because the species under investigation are usually molecules or radicals, not atoms, the electronic levels are divided into sublevels according to the molecular vibration and rotation energy. Electronic, vibration, and rotation energies are quantized (Bombach 2004) because of quantum mechanical effects.

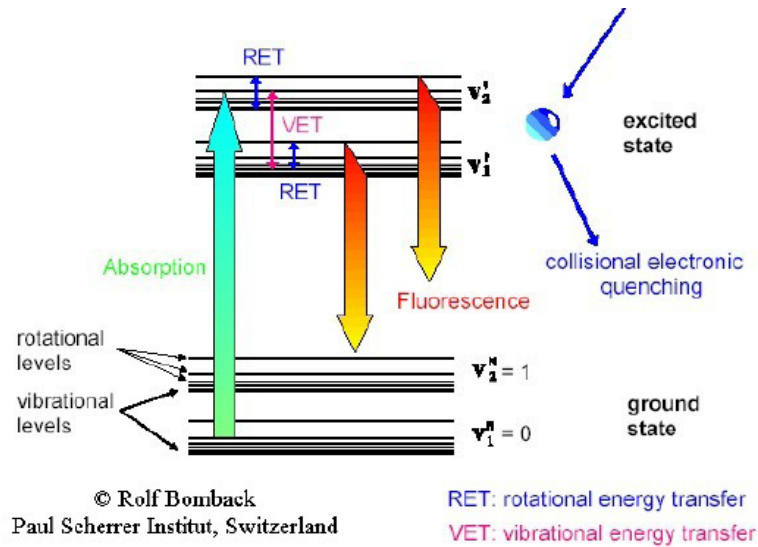


Figure 3-2. State view of laser induced fluorescence.

Figure 3-2 also shows the energy state description of LIF—the molecules or radicals are excited by laser absorption to the metastable state, and then drop down to the stable ground state, emitting fluorescence.

The PLIF is a derivative of the LIF technique, which necessitates the generation of a laser sheet from the probe laser beam in order to facilitate imaging of the fluorescence. PLIF involves illuminating the flow with a thin sheet of laser light tuned to excite electronic transitions in a chemical species in the flow. The fluorescence emitted by laser excitation is focused onto an intensified charge-couple device (ICCD) camera to produce an image of the fluorescence in that region. Besides the species concentration, temperature, pressure, and velocity could be measured with prudent choice of transition and subsequent image processing.

The measured quantity of the fluorescence signal, in photons per pixel, from a single ICCD camera frame can be written as

$$S_{pp} = const \cdot \chi_i \cdot [f_B(T)/T] \quad (3-1)$$

The fluorescence signal is directly proportional to the mole fraction of gas species and a temperature dependent function in brackets. Experimental efficiencies, such as transmission efficiency of the collection lens and filter, the camera's photo-cathode quantum efficiency, and the electronic gain on the camera, are considered constant for a given experimental setup.

The PLIF technique has some disadvantages, the main one being the quenching of fluorescence at higher pressure by numerous collisions of molecules. Such quenching effects can be easily avoided by exciting the molecule to a fast predissociating state from which fluorescence is emitted only during the predissociation lifetime. For sufficiently short predissociation lifetimes, collisions do not occur, which means no quenching within the lifetimes. In some environments where PLIF is unusable, other laser techniques, such as coherent anti-Stokes Raman scattering or Rayleigh scattering are recommended.

3.3.1.2 Scaling Analysis of Stratified Flow in a Simple Channel

Since it was not possible to use a real VHTR pipe size for the bench-top test, a simple scaling method was used to scale-down the facility. The following method is based on the report by Reyes et al. (2006) proposed for design of an air-ingress integral test loop.

Figure 3-3 shows the schematic of countercurrent flow in the hot duct. In this figure, the velocity of the hot helium approaching the cold air plume is u_{LP} , the velocity of the helium flowing countercurrent to the cold air side is u_H , and the hot duct and helium layer thickness are denoted by d and h , respectively.

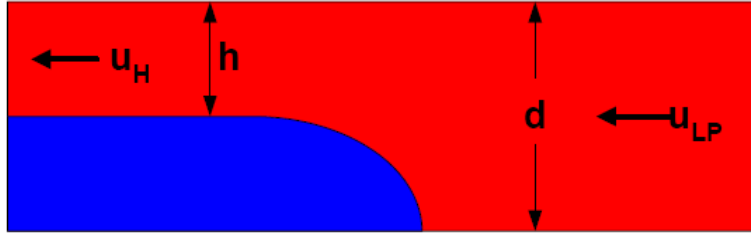


Figure 3-3. Schematics of the countercurrent stratified flow behavior in the VHTR hot duct.

By using Bernoulli's equation, the following theoretical result for the helium velocity approaching the cold side can be obtained (Turner 1973):

$$u_{LP} = 0.5 \sqrt{\frac{g d (\rho_C - \rho_H)}{\rho_C}} \quad (3-2)$$

Experimental measurements indicate that the actual velocities are better predicted by the following expression, which is still quite close to the theoretical value:

$$u_{LP} = 0.44 \sqrt{\frac{g d (\rho_C - \rho_H)}{\rho_C}} \quad (3-3)$$

The helium velocity flowing countercurrent to the cold air side is predicted as

$$u_H = \sqrt{\frac{2g h (\rho_C - \rho_H)}{\rho_C}} \quad (3-4)$$

Equation (3-3) can be rearranged in terms of the modified Froude number to obtain

$$F_H = \frac{u}{\sqrt{g d \Delta\rho / \rho_C}} = 0.44 \quad (3-5)$$

Equation (3-5) can be expressed in terms of a scaling ratio; that is, the ratio of the helium velocity in the model to that of the full scale prototype is related to the hot duct diameter and the density ratio by

$$(u_{LP})_R = \left(\frac{d \Delta\rho}{\rho_C} \right)_R^{1/2} \quad (3-6)$$

For fluid property similitude, Equation (3-6) reduces to the simple expression that the velocity ratio equals the square root of the hot duct diameter ratio as

$$(u_{LP})_R = (d)_R^{1/2} \quad (3-7)$$

$$(Re)_R = (u_{LP} d)_R = (d)_R^{3/2} \quad (3-8)$$

The similitude of Reynolds numbers was used between the prototype and the full scale to maintain the same flow characteristics. Based on the Reynolds number similitude, Equation (3-6) reduces to

$$(d)_R^{3/2} = \frac{(\mu)_R}{(\rho_C \Delta \rho)^{1/2}_R} \quad (3-9)$$

Using the same gas species (Air and Helium), the density ratio has the following relation:

$$(\rho_C)_R = (\Delta \rho_C)_R = (P)_R \quad (3-10)$$

Usually, the effect of pressure on the viscosity is relatively negligible compared to the density. Therefore, Equation (3-10) can be expressed as

$$(d)_R^{3/2} = (P)_R \quad (3-11)$$

Therefore,

$$(P)_R = (d)_R^{-3/2} \quad (3-12)$$

To determine the pressure ratio of the test-section, the diameter of the horizontal pipe was first assumed to be 15 cm, which is 1/10 of full scale. However, the pressure ratio of 31.62 was obtained according to Equation (3-12), which is too high for using plexiglass in the experiment. Even the pipe diameter is increased up to 20 cm, the required pressure in the test section is more than 20 atm. Therefore, using the same gas species (air/helium) in the experiment is not possible. The air was changed to heavier gas to reduce the operating pressure. To determine the types of gas species, the following equation was derived from Equation (3-9):

$$(P)_R = (\mu)_R \cdot (d)_R^{-3/2} \cdot (\rho_C)_{R,std}^{-1/2} \cdot (\Delta \rho)_{R,std}^{-1/2} \quad (3-13)$$

Table 3-4 summarizes the results of these calculations.

Table 3-4. Summary of scaling results (ratio = prototype/full scale).

	Air-Helium		CO2-Helium		Ar Helium	
Diameter ratio (d_R)	0.1	0.133	0.1	0.133	0.1	0.133
Viscosity ratio (μ_R)	1	1	0.833	0.833	1.26	1.26
Density ratio at std (ρ_R)	1	1	1.571	1.571	1.43	1.43
Density different ratio at std ($\Delta \rho_R$)	1	1	1.667	1.667	1.5	1.5
Pressure ratio (P_R)	31.6	20.5	16.2	10.6	26.6	17.2
* std : standard state (1 atm, 15°C)						

CO₂ was selected to be an alternative for air because CO₂ gas has 1.7 times heavier molecular-weight and 0.8 times less viscosity than air, allowing it to significantly reduce the prototype scale. Based on Equation (3-12), the obtained pressure ratio is 10.6 when used with CO₂ instead of air. A pressure range of 10.6 atm is considered possible for Acryl with adequate thickness. Argon gas also has quite large density differences, but its viscosity ratio is larger than 1.0, resulting in a higher pressure (=17.2) ratio than CO₂.

3.3.2 Stratified Flow and Natural Convection Test (TEST 2) under Nonisothermal Conditions

This experiment, which covers DP11 in the Design Matrix of Table 3-3, validated computer codes for the stratified-flow-related effects coupled with natural convection. The experimental facility is composed of a rectangular chamber, an inverse U-tube, heaters, and a water tank (See Figure 3-4). The chamber is made of glass and contains heaters. It has two straight pipes connected on the side and bottom, respectively. The horizontal pipe is designed for stratified flow driven air-ingress phenomena and the vertical pipe for diffusion driven air-ingress. The pipe lengths are short to avoid the misleading phenomena caused by the molecular diffusion in the unheated pipe. On the top of this chamber is a large U-tube connected at one side as shown in Figure 3-4. A water tank is installed around the other side of the U-tube. Water flows in from the bottom of the tank and out the top so the gas is heated up in the chamber and cooled down in the U-tubes. This facility has three valves: one in the horizontal pipe, one in the vertical pipe, and one in the U-tube. The pipes are about 5 cm in diameter. The chamber is 80–100 cm high by 40 cm wide and 40 cm long. The heaters are installed on only two sides so the other sides are available for such optical devices as PIV and PLIF. The maximum planned temperature on the heater wall is 600–800°C, and it will be maintained constant during the test by a PID controller. The large temperature differences of helium in the piping can cause thermo acoustic oscillations that can act as energy transport mechanisms, increasing heat transfer. To eliminate this effect, a temperature buffer layer was placed at the cooling side to relieve the sharp temperature gradient at the interface between the hot side and cold side. The temperature of the buffer layer was monitored during the experiment.

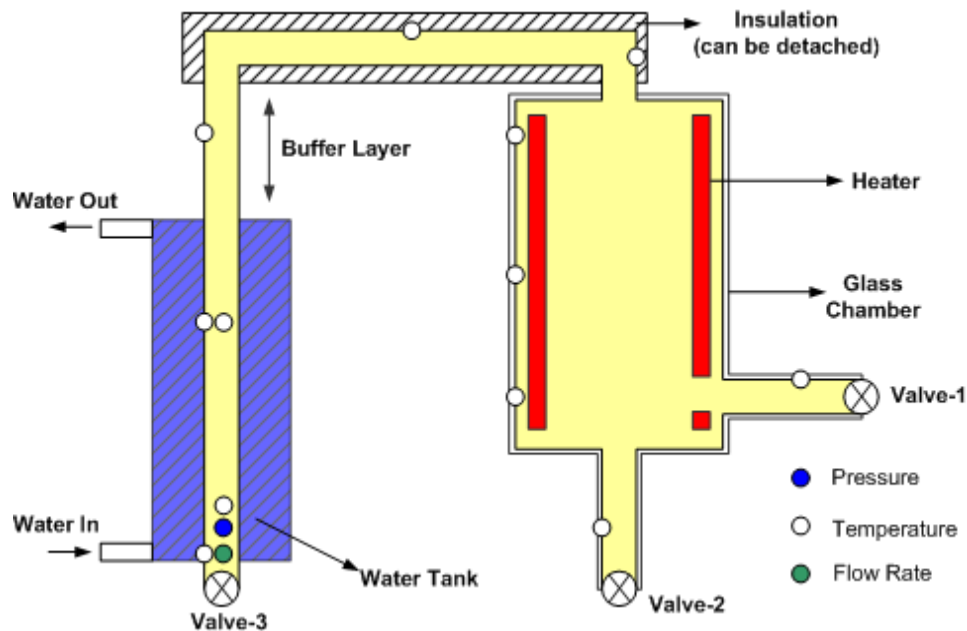


Figure 3-4. Stratified flow and natural convection test (schematics).

Temperatures, pressures and flow rates or velocity were measured at various locations as shown in Figure 3-4, specified by white, blue, and green circles. A K-type thermocouple was used to measure temperature and a pitot tube or hot wire was used to measure flow rate or velocity. PLIF and PIV methods were used to visualize flow behaviors in the chamber. This allowed air concentrations and velocity fields to be measured in the inside of the chamber in 2-D or 3-D. The most important data obtained from this experiment was the time of the ONC, because the main problems in the reactor core are caused by the natural convection flow. The flow sensors caught the time of onset natural convection by detecting a sudden change of flow rates at the U-tube outlet, close to Valve-3. In addition, the temperature sensor was also used as a good back-up indicator for onset natural convection. The pressure in the outside of the test-section was monitored during the test.

The experiment was divided into two tests: (1) stratified flow driven air-ingress test and (2) diffusion driven air-ingress test. The test procedures are as follows.

3.3.2.1 Stratified Flow Driven Air-ingress Test

1. Close all the valves (Valve-1, Valve-2 and Valve-3).
2. Remove all the air by a vacuum pump.
3. Flow water into the water tank in the cold side of the inverse U-tube.
4. Turn on the heater.
5. If the temperature reaches a set point, helium gas is injected into the test section from a gas cylinder.
6. Set the pressure and wait until the test section reaches the steady state.
7. If the test is ready, simultaneously open Valve-1 and Valve-3.
8. Measure temperatures, pressures, and flow rates during the test.
9. If ONC is detected, the test is complete.

3.3.2.2 Diffusion Driven Air-ingress Test

1. Close all the valves (Valve-1, Valve-2 and Valve-3)
2. Remove all the air by a vacuum pump.
3. Flow water into the water tank in the cold side of the inverse U-tube.
4. Turn on the heater.
5. If the temperature reaches a set point, helium gas is injected into the test section from a gas cylinder.
6. Set the pressure and wait until the test section is stabilized to be steady state.
7. If the test is ready, simultaneously open Valve-2 and Valve-3.
8. Measure temperatures, pressures, and flow rates during the test.
9. If ONC is detected, the test is complete.

To make sure the test would be carried out as intended, some simple CFD analyses were performed by the FLUENT code. This is the summary of the FLUENT options used.

- Unsteady
- 2-D segregated solver
- Laminar viscous model

- Air/helium gas species transport equations
- Kinetic theory for gas properties
- Boundary Conditions:
 - Constant wall temperature at the chamber wall of 900K
 - Constant wall temperature at the cooling wall of 330K
 - Insulation for other walls.

Figure 3-5 shows the calculated transient air distributions (from 0 seconds to onset-natural-convection) in the test section. In this calculation, air is initially flowed into the horizontal pipe by a stratified flow and rapidly fills out the bottom part of the chamber. Then, the air slowly diffuses into the upper part of the test section. After 400 seconds, the global natural convection is initiated by heat. Then, the whole test-section is filled with air because of the flow from the horizontal pipe on the right out to the vertical outlet on the left. The FLUENT calculation confirmed that the planned experiment will successfully show similar phenomena to the real scenario expected in the VHTR air-ingress. This FLUENT modeling and calculation were just performed to obtain some preliminary data for facility design confirmation. Once the FLUENT model is validated using a simplified geometry, much more detailed modeling can be performed using the replica of the NGNP core geometry.

Figures 3-6 and 3-7 show the time transient mass flow rate and temperature at the cold side outlet near Valve-3, respectively. According to Figure 3-6, a sudden mass flow increase was estimated at the time of 410-seconds, meaning that ONC is started at this point. Prior to the ONC, air was flowed in the cold pipe showing negative flow and was oscillated until it reached the ONC at 430 seconds.

Figure 3-7 show temperature variations plotted for different times. As shown, a sudden temperature increase was also predicted at the same time as the mass flow, which can be another evidence for the ONC. This result shows that both flow rates and temperatures can be used as a good signal for the ONC.

Figure 3-8 shows the comparisons between the stratified, flow-driven, air-ingress test (left) and the diffusion driven air-ingress test (left). Diffused-driven air is slowly ingressed into the chamber because only diffusion dominates the air-ingress rate. However, stratified air flows rapidly into the chamber within several seconds. These two tests will therefore provide very different results as shown in the comparison.

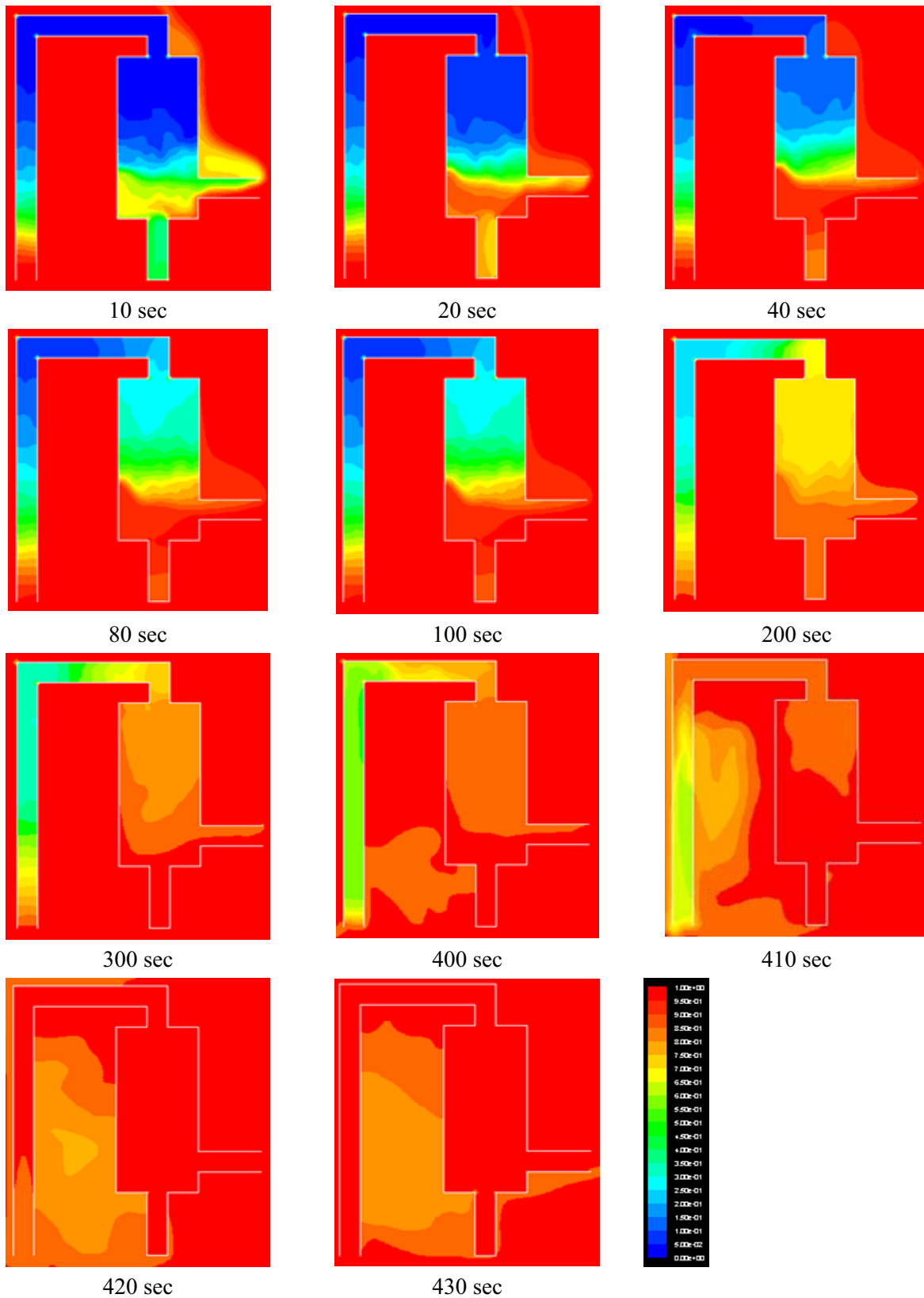


Figure 3-5. FLUENT simulation for flow driven air-ingress experiment (air mole fraction).

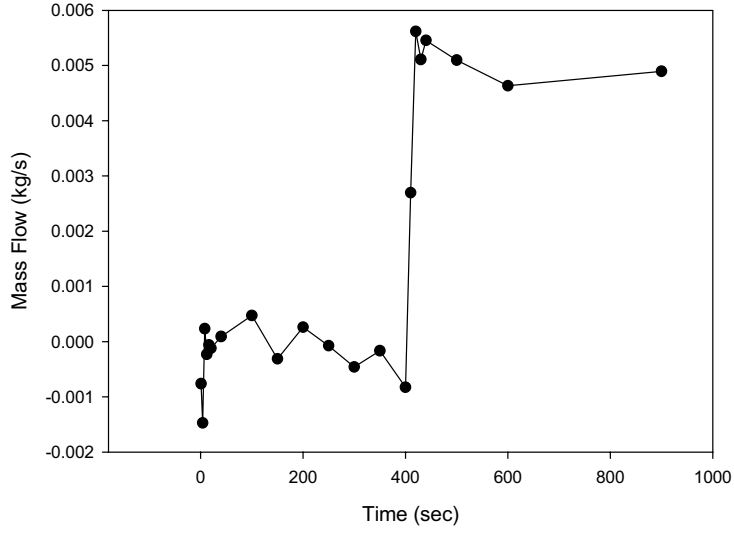


Figure 3-6. Time vs. mass flow at the cold side outlet.

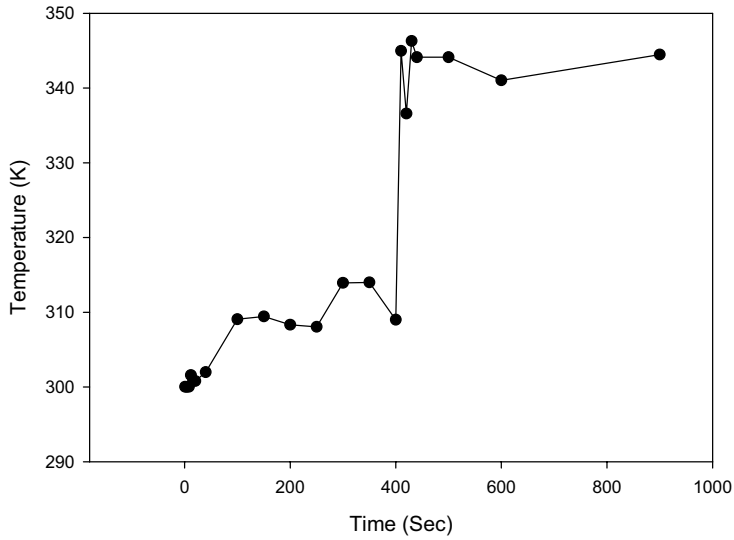
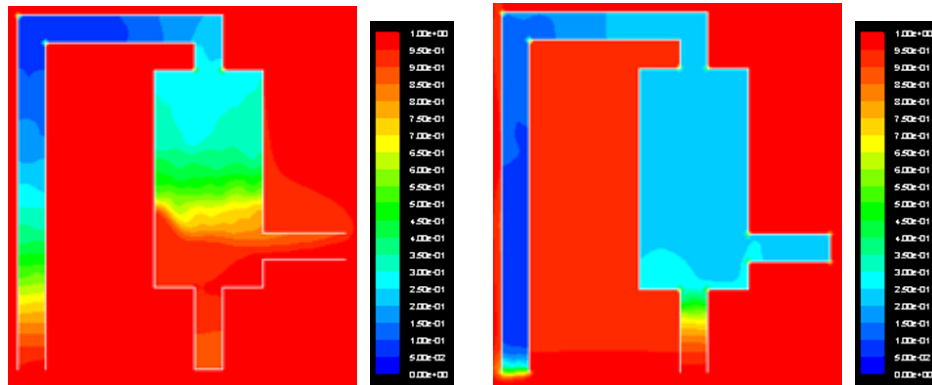


Figure 3-7. Time vs. temperature at the cold side outlet.



(a) Stratified flow driven air-ingress.

(b) Diffusion driven air-ingress.

Figure 3-8. Comparisons of different experimental cases.

3.3.3 Stratified Flow and Natural Convection Tests with Pebbles (or Structure) (TEST 3) Under Nonisothermal conditions

This experiment is basically the same as the previous one, except the chamber is packed with some metallic/ceramic pebbles or structures. The purpose of this experiment is to validate the codes for the stratified flow in porous media. This experiment covers DP12 of Table 3-3.

When air-ingress into a VHTR is analyzed, the reactor core is usually assumed to be a porous media for simplifying the complex core geometries. The porous media assumption is generally accepted to be a good approach. However, one problem might be in the porous media heat transfer model that assumes thermal equilibrium between solid structure and gas flow in the reactor core. This thermal equilibrium model is obvious in porous media having very small pores and high flow resistance. But, it is not clear if this assumption is still valid for a VHTR core having much larger pore size and less flow resistance. This equilibrium model assumes that there is infinitely fast heat transfer between the solid and gas phase. A concern is that it might lead to the over-prediction of gas expansion or natural convection during the accident analysis resulting in much earlier predictions on the ONC. The validation of porous media model coupled with stratified flow and natural convection is therefore a very important issue. Figures 3-9 and 3-10 show the schematics of the experimental facility. The setting and the test procedures are exactly the same as the experiment in the previous section planned for DP11.

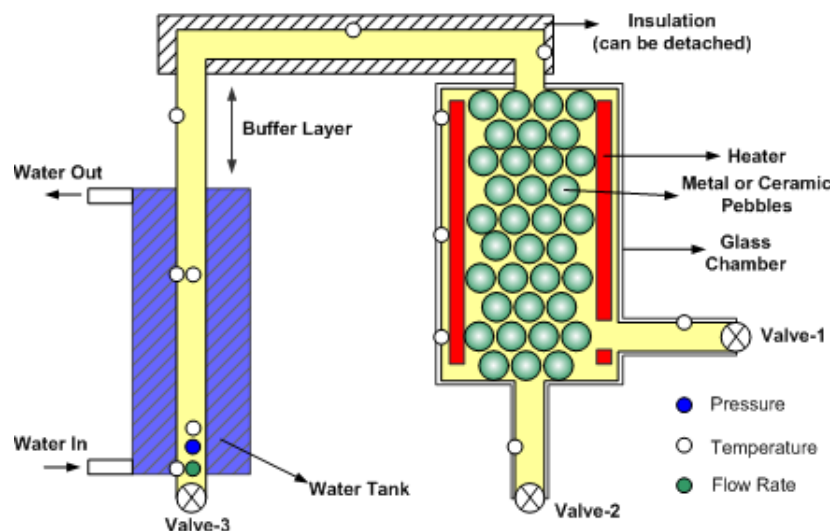


Figure 3-9. Stratified flow and natural convection test with pebbles (schematics).

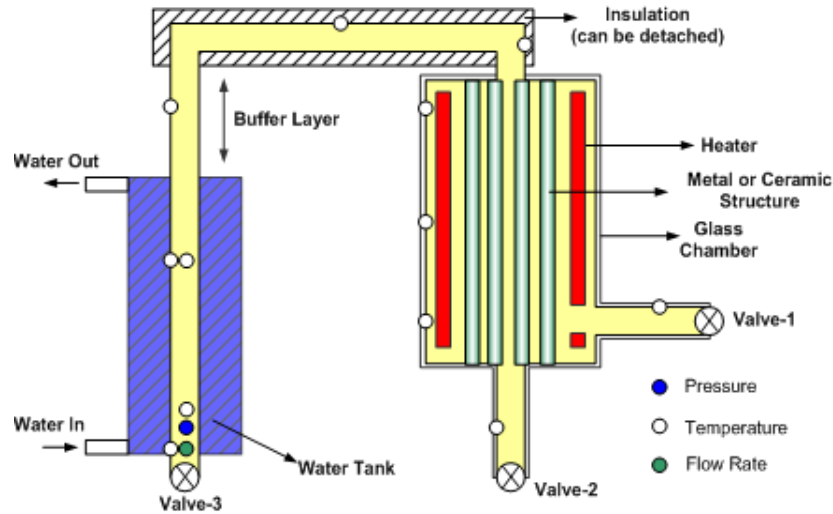


Figure 3-10. Stratified flow and natural convection test with structures (schematics).

3.3.4 Stratified Flow and Natural Convection Test with Graphite Pebbles (or Structure) (TEST 4) Under Nonisothermal Conditions

This experiment was basically the same as those for TEST 2 and TEST 3, but graphite pebbles or structures were used instead of metallic or ceramic ones. Graphite materials chemically reacted with oxygen during the test, a situation very similar to the real air-ingress accident. If the reaction occurs, it produces some gas species like CO and CO₂ that mix with the other gases (helium and nitrogen) already present in the reactor. These mixtures were then diffused into other parts of the test section, changing gas density distributions in the reactor and affecting overall flow behavior. The heat generated also affected the natural convection phenomena. The oxygen concentrations and flow field can be visualized in the chamber via PLIF and PIV methods. The experimental procedures and methods are exactly the same as TEST 2 and TEST 3. This experiment covered DP13 of Table 3-3. Figures 3-11 and 3-12 show the schematics of the experimental facility for graphite pebbles.

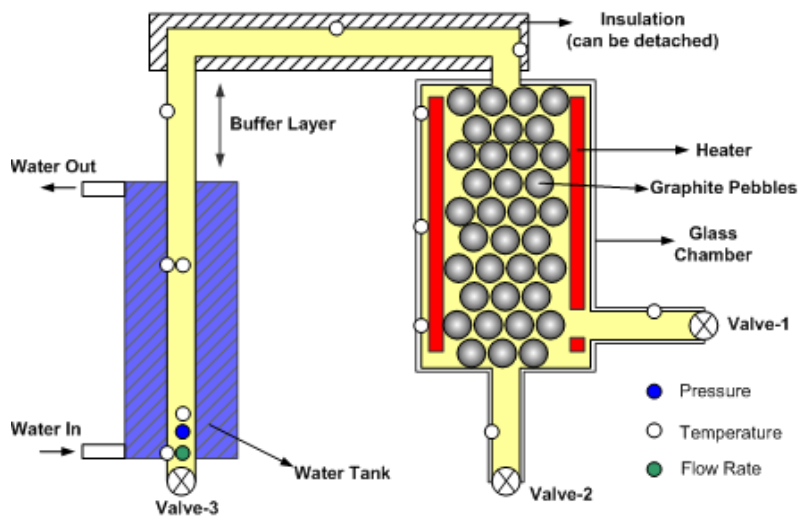


Figure 3-11. Stratified flow and natural convection test with graphite pebbles (schematic).

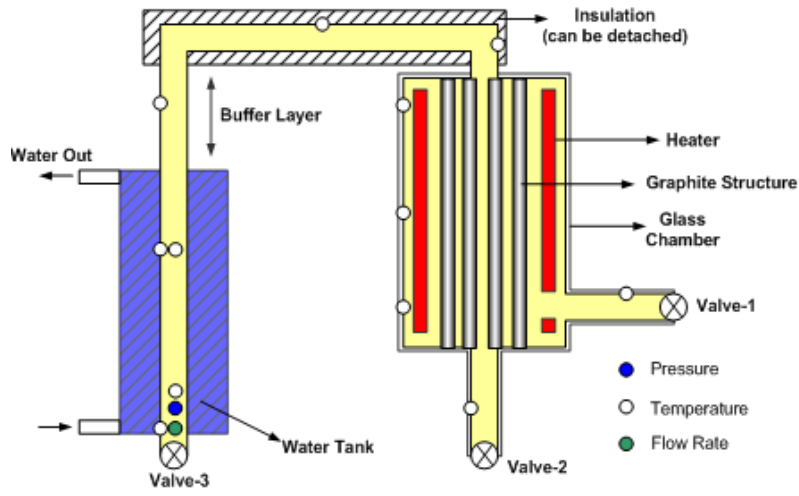


Figure 3-12. Stratified flow and natural convection test with graphite structure (schematic).

3.3.5 Isothermal Stratified Flow Test (TEST 5)

This experiment was planned to validate the separate effects of the air-ingress in the same geometries as TESTs 2, 3, and 4. This test was performed to validate the codes for stratified flow and determine some suitable options before beginning the complicated tests (TESTs 2, 3, and 4) described above. This experiment uses the same test facility as TESTs 2, 3 and 4, but, for visualization, the test section was made of Acryl. Figure 3-13 shows the schematic of the experiment, which follows almost the same test procedure as TEST 2, except the test-section is not heated. Similar to TEST 1, a PLIF method was used for visualization of the oxygen concentration or velocity vectors. Since the purpose of this experiment is only focused on the stratified flow phenomena, the test concerning diffusion driven air-ingress was not performed. This experiment covered D10 in the Design Matrix of Table 3-3.

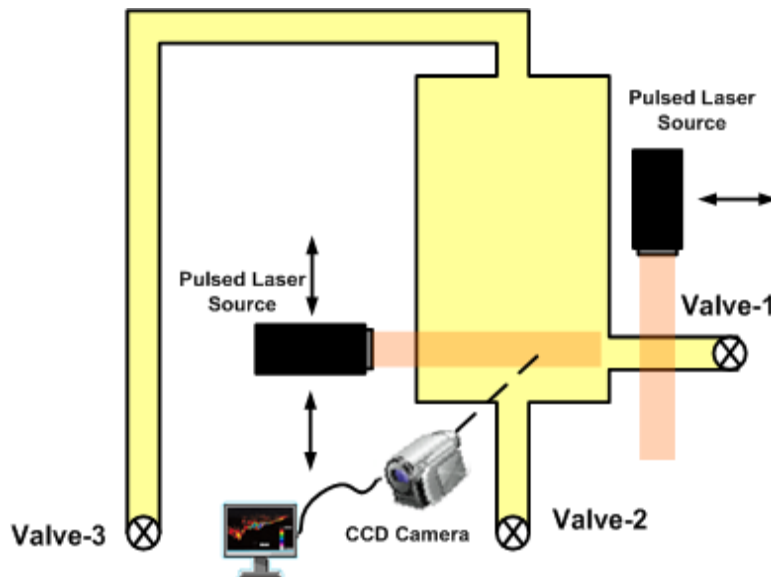


Figure 3-13. Isothermal Stratified Flow Test (Schematic)

4. TASK 3: ADVANCED GRAPHITE OXIDATION STUDY (INL)

4.1 Introduction

Graphite oxidation in an air-ingress accident is presently a very important issue for VHTR safety because of its potential problems such as core heat-up, core collapse, and release of some toxic gases such as CO and CO₂. The oxidation process of graphite is affected by various factors, including temperature, pressure, oxygen concentration, types of graphite, graphite shape and size, flow distribution, etc. The effects of these factors have been documented by a number of previous investigations (Kim et al. 2006, Fuller et al. 1997, Moorman 1984, Ogawa 1993, Contescu et al. 2008, etc.), and good models have been developed for estimating the graphite oxidation process in an air-ingress accident.

One of the main issues regarding graphite oxidation is the potential core collapse problem that may occur following the degradation of graphite mechanical strength. In analyzing this phenomenon, it is very important to understand the relationship between the degree of oxidization and strength degradation. In addition, the change of oxidation rate by graphite oxidation degree (burn-off: ratio of the oxidized graphite density to the original density) should be quantified because graphite strength degradation is followed by graphite density decrease, which highly affects oxidation rates and patterns. Because the density change is proportional to the internal pore surface area, they should be quantified in advance. In order to understand the above issues, the following tasks were performed.

1. Experiment on the fracture of the oxidized graphite and validate the previous correlations.
2. Experiment on the change of oxidation rate using graphite density and data collection.
3. Measure the BET surface area of the graphite.

Among the above tasks, the data for (3) have been measured and provided by Contescu (2008) in Oak Ridge National Laboratory (ORNL), and therefore the data reported in this report are not based on the INL experiment. On the other hand, the experiment (1) and (2) have been performed in INL for H451 (Great Lakes Carbon Corporation) and IG-110 (Toyo Tanso Co., Ltd) graphite. The reason for the use of those graphite materials is because their chemical and mechanical characteristics are well identified by the previous investigations, and therefore it was convenient for us to access the published data, and to apply and validate new methodologies.

4.2 Experiment on Validation for the Fracture of Oxidized Graphite

4.2.1 Introduction

As mentioned, the effect of oxidation on the strength of graphite is an important issue for safety analysis of the air-ingress accident in VHTRs because strength degradation by oxidation leads to potential core collapse problems. Although the relationship between strength and oxidation has been studied by a number of various investigators (Eto and Growcock 1981, Wichner 1976, Engle 1977, etc.), in most cases, the majority of the data has been obtained only under 10% graphite burn-off. This means that the correlations are only valid within very limited burn-off ranges and the use of those correlations for the higher burn-off may not be valid yet. Actually, the potential graphite structure collapse will occur at high burn-off range (higher than 50%). It is therefore very important to confirm the validity of the previous correlations for use at the wider ranges. This experiment attempted to obtain the graphite strength data at high burn-off ranges. To achieve this goal, an experimental method and procedure were newly developed. The degree of burn-off in which the graphite loses its mechanical strength has been measured and was finally used to validate and improve the previous correlations.

4.2.2 Main Idea

From the literature survey, it was technically very difficult to apply the standard methods of the mechanical strength measurement to the highly oxidized graphite. Consequently, most of the data were obtained under 10% burn-off in the pervious investigations (Eto and Growcock 1981, Wichner 1976, Engle 1977 and etc.). Figure 4-1 shows some experimental data for IG-11 graphite measured by Eto and Growcock (1983). As shown in this figure, all the data ranges within 7% burn-off. Eto and Growcock (1983) measured the strength of the three types of oxidized graphite (IG-11, PGX and H451), and recommended the following equation form.

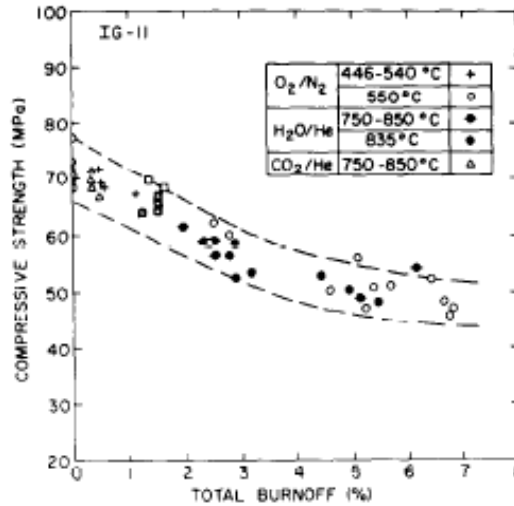


Figure 4-1. Experimental data of compressive strength with burn-off (Eto and Growcock 1983).

$$S / S_0 = \alpha \cdot \rho'^{\beta} + (1 - \alpha) \cdot \rho'^{\delta} \quad (4-1)$$

where

S = Compressive Strength (Pa)

S_0 = Initial compressive strength (Pa)

ρ' = Ratio of the density between oxidized graphite and the original

In their research, the graphite was oxidized up to a certain level of burn-off and then the sample was tested by a standard method and testing machine. Table 4-1 summarizes the parameters in Equation (4-1) for graphite PGX, H451, and IG-11.

Table 4-1. Parameters in Equation (4-1) for various graphite materials (Eto and Growcock 1983).

Graphite	Mode	α	β	γ
PGX	Compression	0.94	9.4	194
PGX	Tension	0.86	10	100
H451	Compression	0.79	3.5	71.5
H451	Tension	0.62	3.5	30
IG-11	Compression	0.83	4.0	40

Equation (4-1) assumes that the graphite's strength will approach zero as the density decreases and finally become zero at 100% burn-off. This assumption is conceptually reasonable, but some experimental observations show that the graphite loses its mechanical strength at a certain burn-off level lower than 100% because the corrosion breaks all the connections between inside pore structures in very high burn-off.

Because of the technical difficulties associated with the direct measurement of highly oxidized graphite strength, a new method is proposed. Figure 4-2 shows the basic idea of this method, which measures the degree of burn-off at which the graphite is collapsed by a very small load. The load is very small compared to the original material strength so that the stress can be assumed to be almost zero. Figure 4-2 depicts this data point as a red circle.

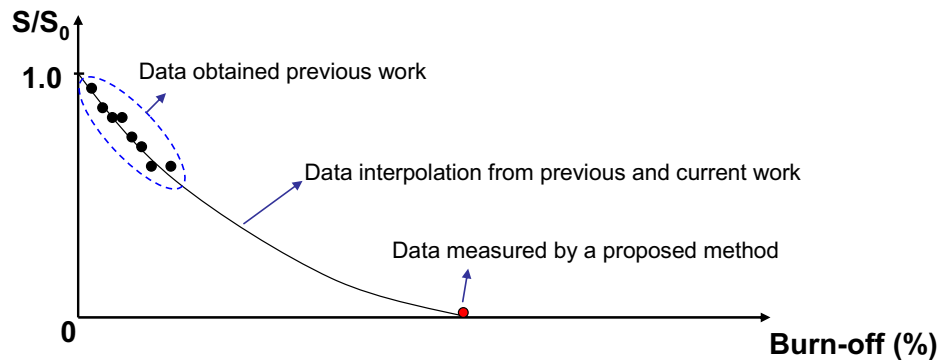


Figure 4-2. Basic idea on the prediction of graphite compressive strength.

The method of measuring this data is simple as described in detail in the next section. Simply putting the graphite with a small load on its top is oxidized at constant temperature and flow rate conditions. If it is collapsed down by the load, the collapsed burn-off will be detected through a sudden drop in the graphite mass signal. Once the data is obtained, the strength can be interpolated between the previous and the new data points. The smooth change of the graphite mechanical strength was assumed in the interpolated region.

4.2.3 Experimental Facility and Setup

The experiments have been carried out on the graphite oxidation test station at INL, which is built for evaluation of the American Society for Testing and Materials (ASTM) standard test method (Contescu et al. 2008) for graphite. The ASTM test standard was developed for determining and rating the oxidation resistance of nuclear grade graphite. A protocol containing instructions for setting up a test station was developed by ORNL and distributed to several laboratories for independent evaluation of the protocol's robustness in terms of repeatability. In this work, basically the same experimental setup as ASTM protocol has been maintained, but it was slightly adjusted for this purpose.

The schematic of the oxidation test station (see Figure 4-3) shows the graphite sample suspended below a balance inside the Inconel tube, which is surrounded by the furnace. The Inconel tube is connected to nitrogen and air supplied from the bottom and desiccated to eliminate oxidation from moisture. The nitrogen is used during this process to avoid oxidation when the furnace is heating up. When the gas temperature is stabilized at target value, it is switched to air to start oxidation. The test can take from a couple of hours to few days, so the data is gathered automatically using LabVIEW (National Instruments) until the desired burn-off is achieved.

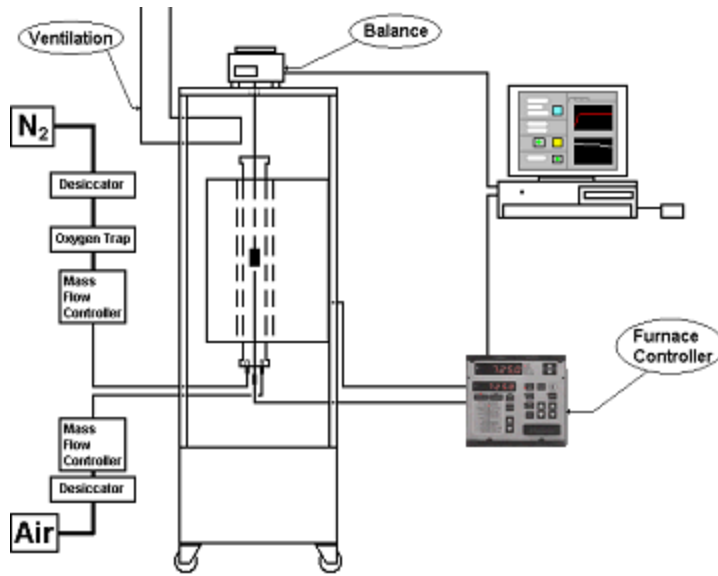


Figure 4-3. Schematic of the graphite oxidation test station setup.

The program has a user interface (see Figure 4-4) that allows the operator to input basic information such as name of sample, sampling rate, target temperature, and sample dimensions and displays the temperature and mass history graphs so the experiment can be monitored. It also gives an indication when the sample temperature is stabilized, and when the sample mass is decreased by 15% or more.

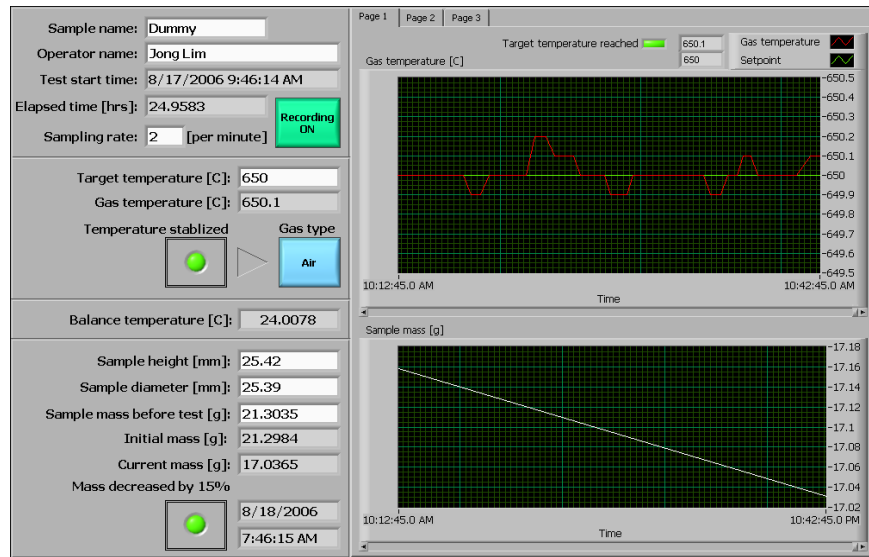


Figure 4-4. LabVIEW program user interface.

The LabVIEW program retrieves the sample mass and temperature at a constant sampling rate and records it in a data file (see Figure 4-5) with useful introductory information. File names are automatically generated to include the sample name, target temperature, test start date, and time.

Microsoft Excel - 8/23/2006 9:58:09 AM Dummy2 650.000000 .xls

File Edit View Insert Format Tools Data Window Help

Arial 10 B I U

	A	B	C	D	E	F
1	Sample name:	Dummy2				
2	Test start date and time:	8/23/2006 9:58:09 AM				
3	Target temperature:	650.000000				
4	Sampling rate:	2				
5	Sample diameter [mm]:	25				
6	Sample height [mm]:	25				
7	Nitrogen flow rate [L/min]:	10				
8	Air flow rate [L/min]:	10				
9	Sample mass before test:	20.7884				
10	initial mass before oxidation:	20.784600				
11						
12	Operator:	Jong Lim				
13	Header:	This is just an arbitrary example.				
14						
15	Date	Time	Elapsed time [hours]	Sample mass [g]	Gas temperature [C]	Gas type
16						
17	8/23/2006	9:58:12 AM	0	20.7874	25.5	nitrogen
18	8/23/2006	9:58:40 AM	0.008333	20.7871	0	nitrogen
19	8/23/2006	9:59:10 AM	0.016667	20.7871	0	nitrogen
20	8/23/2006	9:59:40 AM	0.025	20.7871	33.9	nitrogen
21	8/23/2006	10:00:10 AM	0.033333	20.7871	33.9	nitrogen
22	8/23/2006	10:00:40 AM	0.041667	20.7871	33.4	nitrogen
23	8/23/2006	10:01:10 AM	0.05	20.7871	33.4	nitrogen
24	8/23/2006	10:01:40 AM	0.058333	20.7871	33.2	nitrogen
25	8/23/2006	10:02:10 AM	0.066667	20.7872	33.2	nitrogen
26	8/23/2006	10:02:40 AM	0.075	20.7878	33.3	nitrogen
27	8/23/2006	10:03:10 AM	0.083333	20.7881	33.3	nitrogen
28	8/23/2006	10:03:40 AM	0.091667	20.7883	33.8	nitrogen
29	8/23/2006	10:04:10 AM	0.1	20.7885	33.8	nitrogen
30	8/23/2006	10:04:40 AM	0.108333	20.7887	34.7	nitrogen

Ready NUM

Figure 4-5. Data file example.

Figure 4-6 shows the schematic of the sample holder that was set up for the experiment. It was installed at the center of the electrical furnace. The sample holder is made of Titanium and has a rectangular cage shape with a loading material and graphite sample inside. The loading material is made of titanium and initially placed on the top of the graphite sample.

The graphite sample is a cylinder with a hole at the center. Its dimensions are 1.0 inch outer diameter, 1.0 inch height, and 0.5 inch in inner-hole diameter. The loading material has the cylindrical shape with a small tip at the bottom center to fit the loader to the sample. The size of the tip is made to be a little bit smaller than the hole to avoid thermal expansion problems. The experiment is performed at the low temperature (650°C) during which the reaction kinetics dominate the graphite corrosion process. In this regime, the graphite corrosion mainly decreases the graphite density with degradation of mechanical strength, maintaining its original shape and size. If the graphite is fully corroded, the sample will be collapsed by the loading materials. The broken ashes will then fall down through the metal mesh at the bottom of the cage, sending a sudden decrease signal of graphite mass as detected by the balance connected to the cage and the sample.

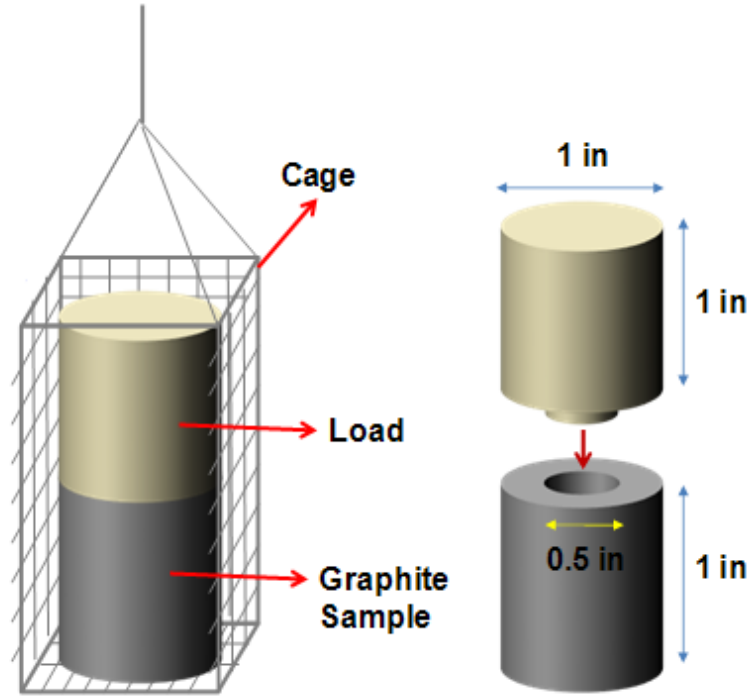
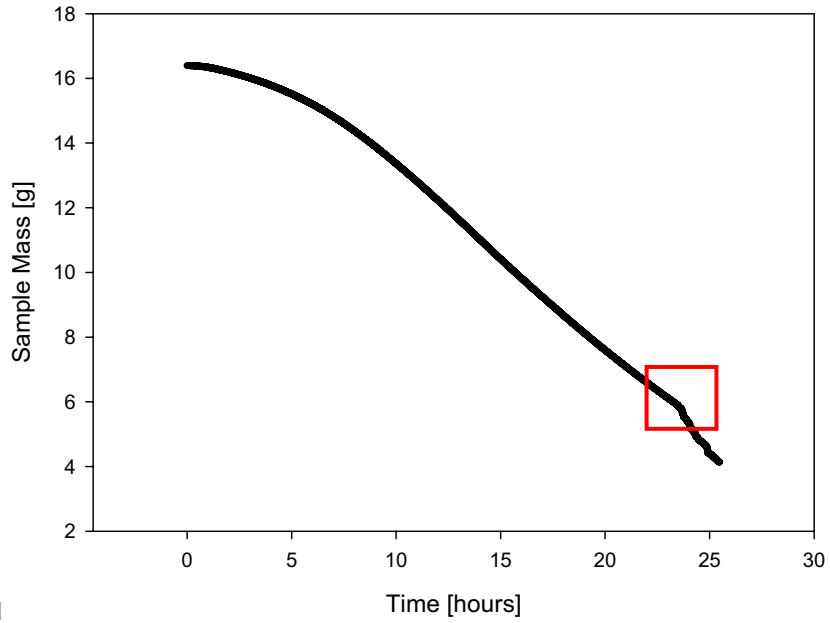


Figure 4-6. Schematic of the sample holder and loader setup.

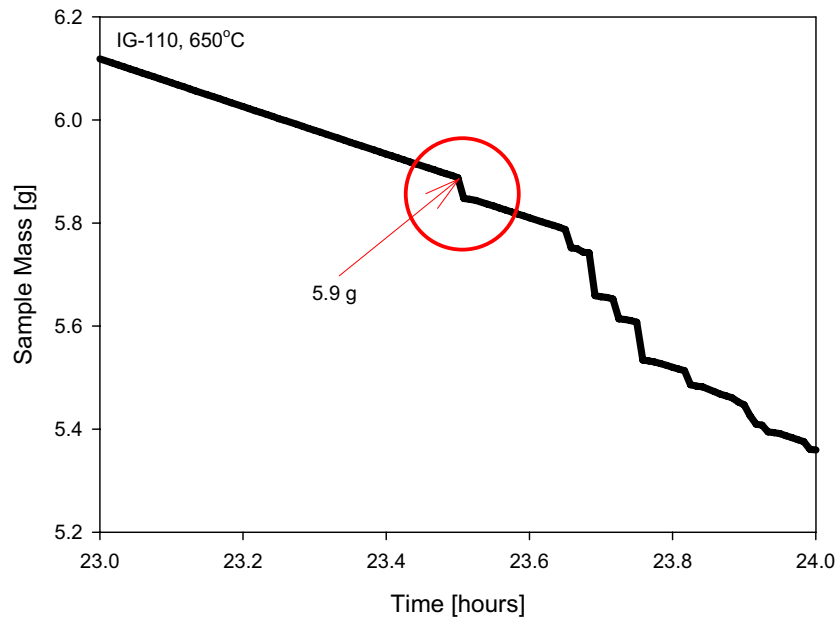
4.2.4 Results and Discussions

Three samples were tested. Figures 4-7, 4-8, and 4-9 show the sample mass change with time measured for IG-110 graphite. The graph in these figures show (a) the overall trend of the sample mass changes for the whole test time and (b) the sudden mass changes in detail at the sample fractured time. These figures show at this experiment provides very good repeatability. The sudden mass drops were observed at almost the same time, regardless of the different samples. The average burn-off for the fracture in IG-110 is 64.7%.

Figures 4-10, 4-11, and 4-12 show the same type of graphs for H451 graphite. According to these graphs, the averaged burn-off for the fracture of H451 graphite is 82.0%. The experimental data are summarized in Table 4-2, which shows that the H451 graphite is stronger than the IG-110 graphite in the oxidized conditions. Samples after the fracture were observed to check the shape and the status, which found that the sample became powder-like and no longer had structure. It was therefore assumed that the strength of this point is zero. The H451 graphite with 65% of burn-off (lower than the fracture point) was also observed, which found that it maintained its shape perfectly at this point.

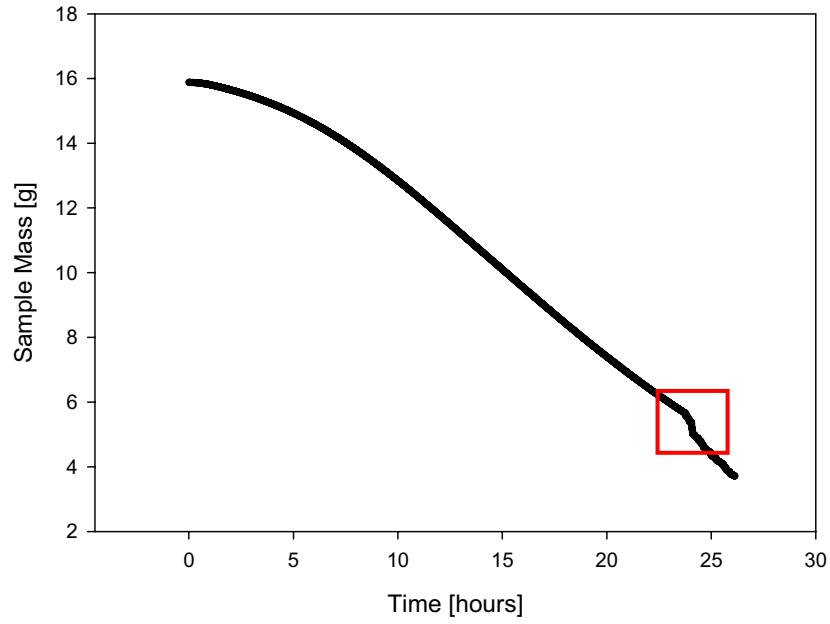


(a) Overall trend of the sample mass change.

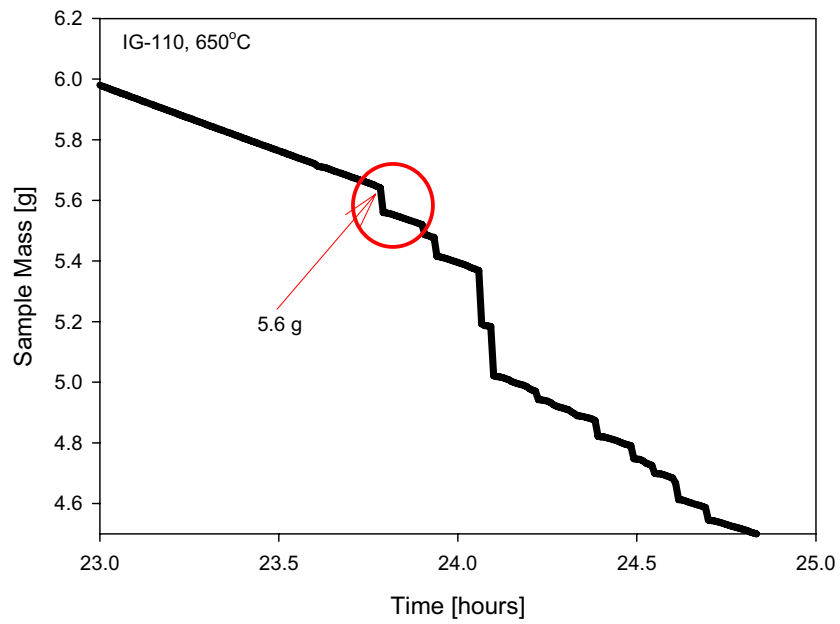


(b) Sudden drop of mass at the broken point.

Figure 4-7. Variations of sample mass with time (IG-110 Case 1, 650°C).

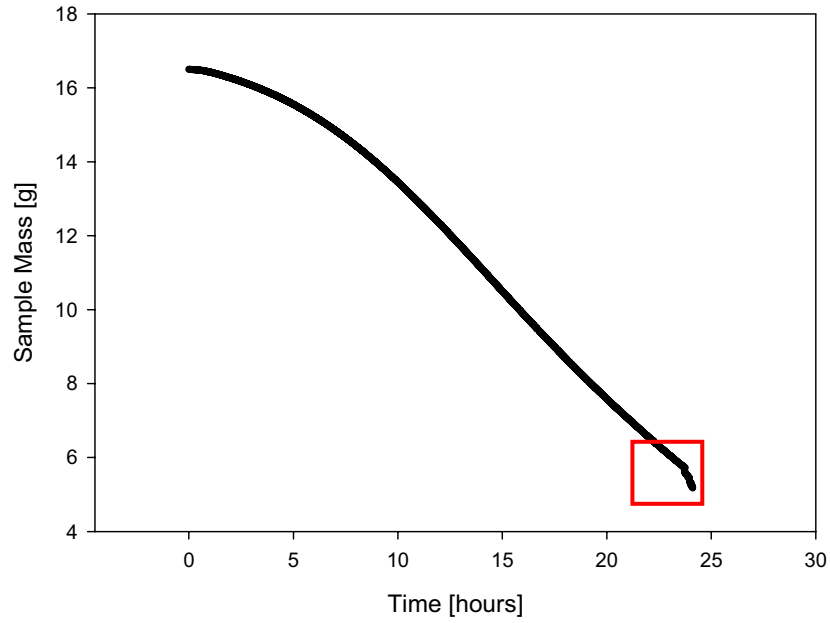


(a) Overall trend of the sample mass change.

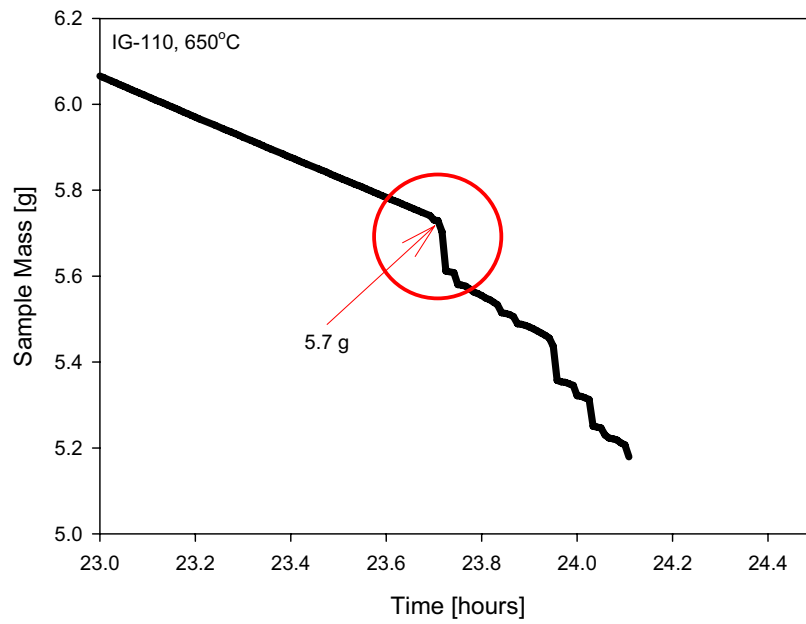


(b) Sudden drop of mass at the broken point.

Figure 4-8. Variations of sample mass with time (IG-110 Case 2, 650°C).

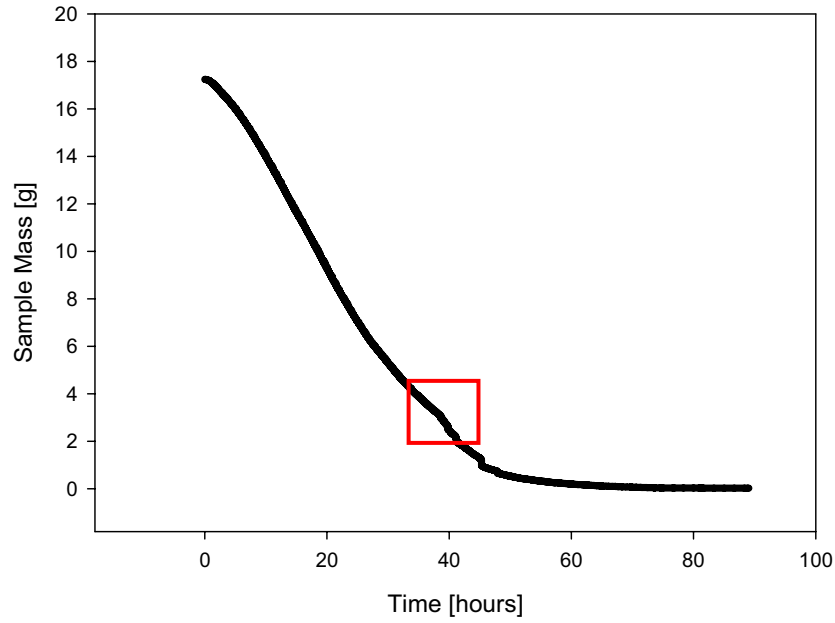


(a) Overall trend of the sample mass change.

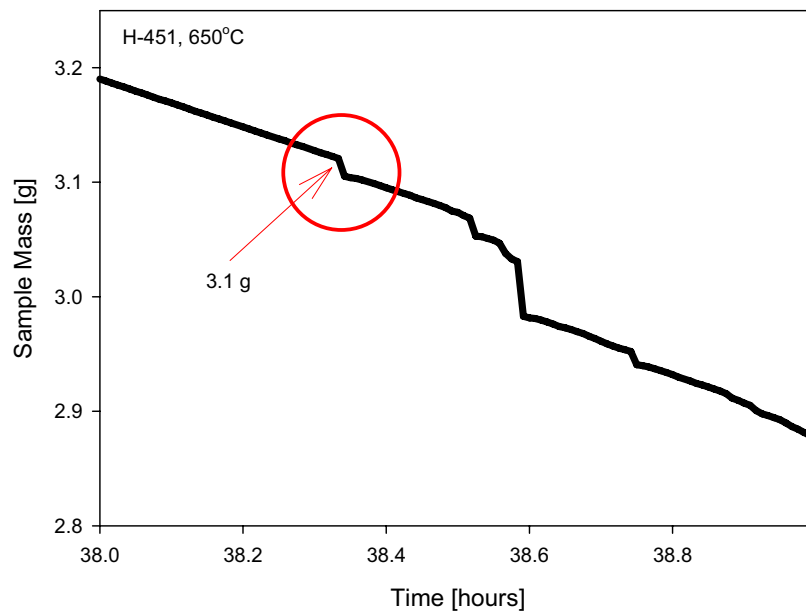


(b) Sudden drop of mass at the broken point.

Figure 4-9. Variations of sample mass with time (IG-110 Case 3, 650°C).

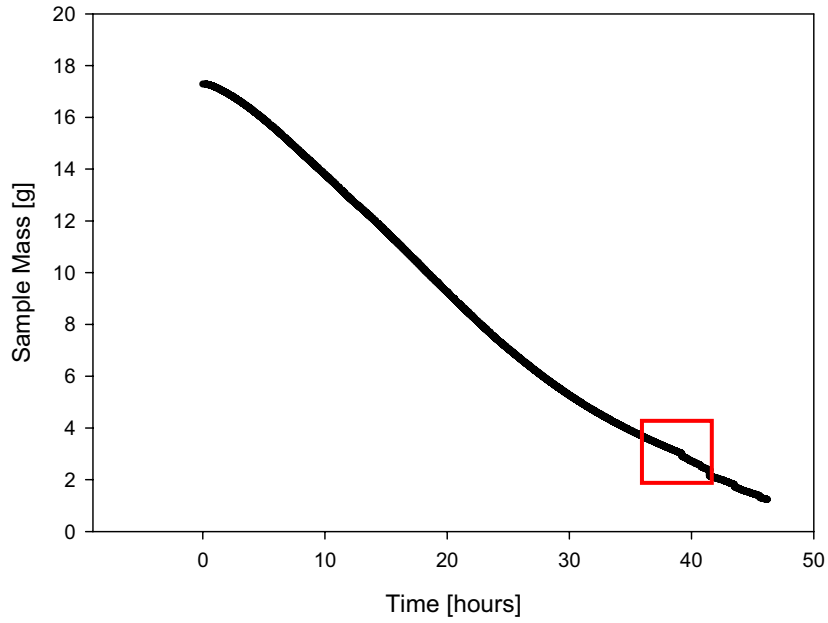


(a) Overall trend of the sample mass change.

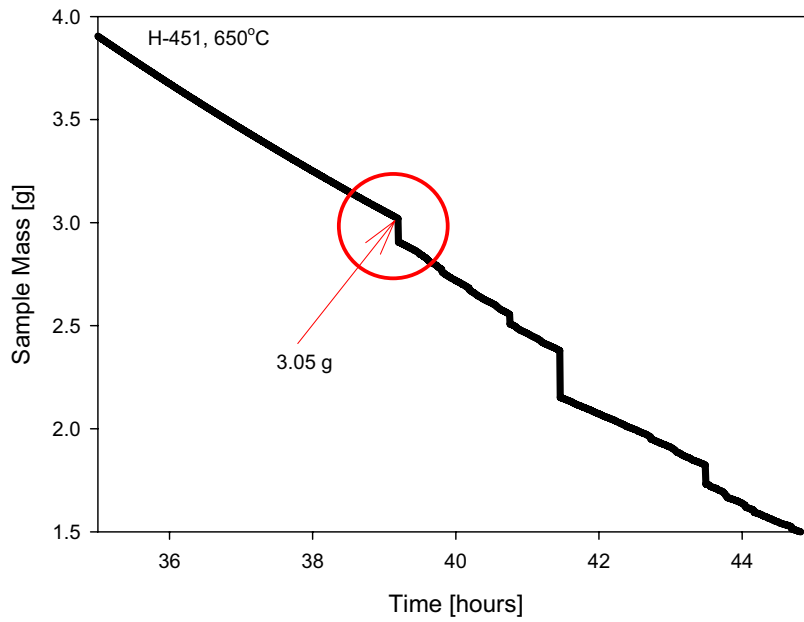


(b) Sudden drop of mass at the broken point.

Figure 4-10. Variations of sample mass with time (H451 Case 1, 650°C).

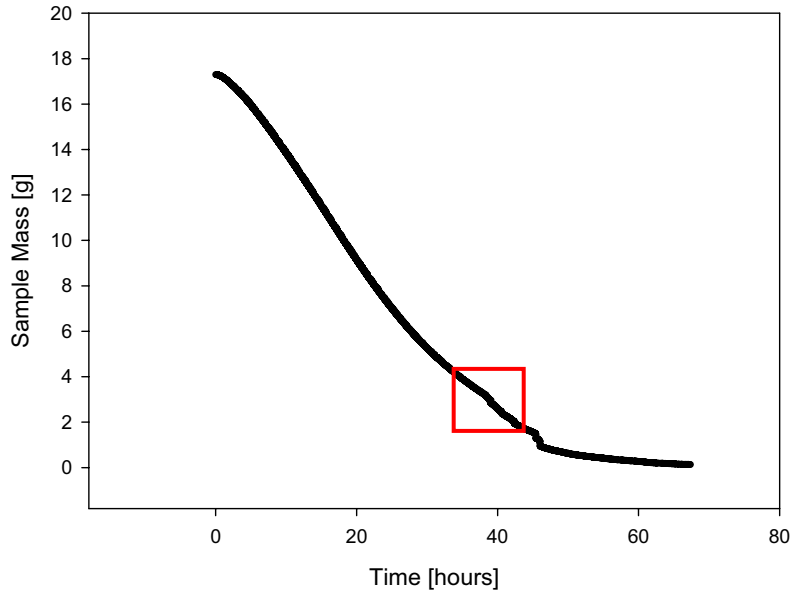


(a) Overall trend of the sample mass change.

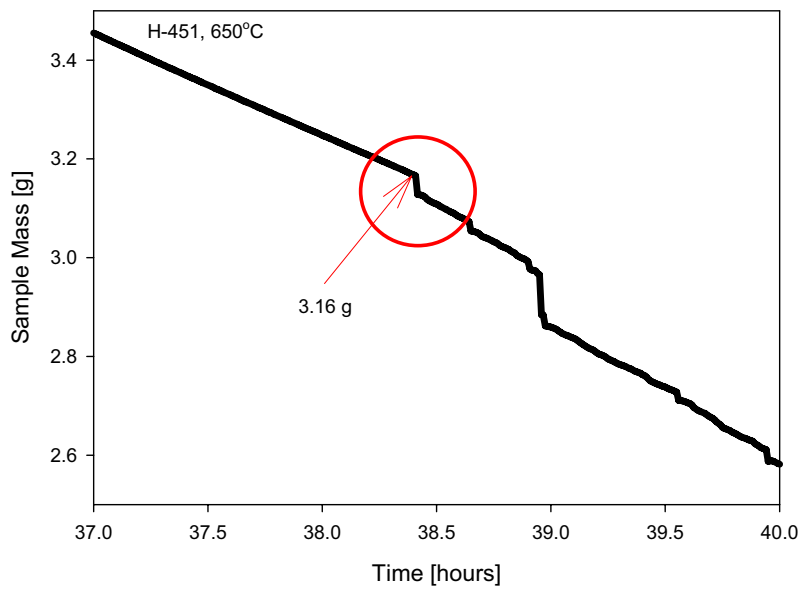


(b) Sudden drop of mass at the broken point.

Figure 4-11. Variations of sample mass with time (H451 Case 2, 650°C).



(a) Overall trend of the sample mass change.



(b) Sudden drop of mass at the broken point.

Figure 4-12. Variations of sample mass with time (H451 Case 3, 650°C).

Table 4-2. Summary of the experimental data.

IG-110			H-451		
Initial Mass [g]	Fractured Mass [g]	Fractured Burn-off [g]	Initial Mass [g]	Fractured Mass [g]	Fractured Burn-off [g]
16.40	5.9	64.02	17.24	3.1	82.01
15.88	5.6	64.74	17.29	3.05	82.36
16.50	5.7	65.45	17.3	3.16	81.73

Figure 4-13 depicts the plot of normal compressive strength vs. burn-off for IG-110 graphite. The graph includes the data from Ishihara et al. (2004) and this work. Two correlations are plotted in the figure: Eto and Growcock's correlation (1983) for IG-11 graphite (See Table 4-1) and the correlation fitted by all the data including this work. Eto and Growcock's correlation shows quite good agreement with the experimental data for the whole ranges, but a small over-prediction of the strength at high burn-off. According to the Eto and Growcock's equation, the strength of the graphite at the 65% burn-off is predicted to be 870,000 Pa, while the stress load at the bottom part of the VHTR graphite structure is 100,000 Pa. The equation will thus estimate that the graphite structure is still secure for fracture, although in the real situation, the support graphite is collapsed at this point. The Eto and Growcock's equation predicts that the fracture point of the graphite support structure will be 79.6% burn-off, which is 14.6% larger than the point at which the IG-110 graphite loses its mechanical strength. In the new conservative fitting, the following correlation shows very good agreement with the whole experimental data, and is recommended for the final IG-110 graphite.

$$S/S_0 = (\rho/\rho_0)^{6.5} \tag{4-2}$$

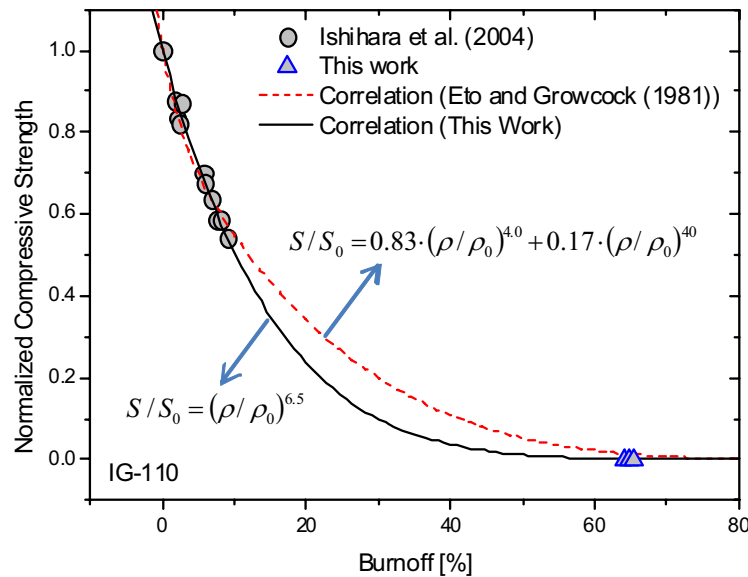


Figure 4-13. Normal compressive strength vs. burnoff (IG-110).

Figure 4-14 presents experimental data about the relationship between normal compressive strength and burn-off for H451 graphite. It also plots two correlations: one is developed by Eto and Growcock (1983), and the other is developed here by fitting all of the data, including this work. Accordingly, both correlations show very good agreement with the experimental data for the whole range. In particular, Eto and Growcock's correlation shows very good agreement at the low burn-off region, while the following correlation provides more conservative predictions:

$$S/S_0 = (\rho/\rho_0)^{6.25} \tag{4-3}$$

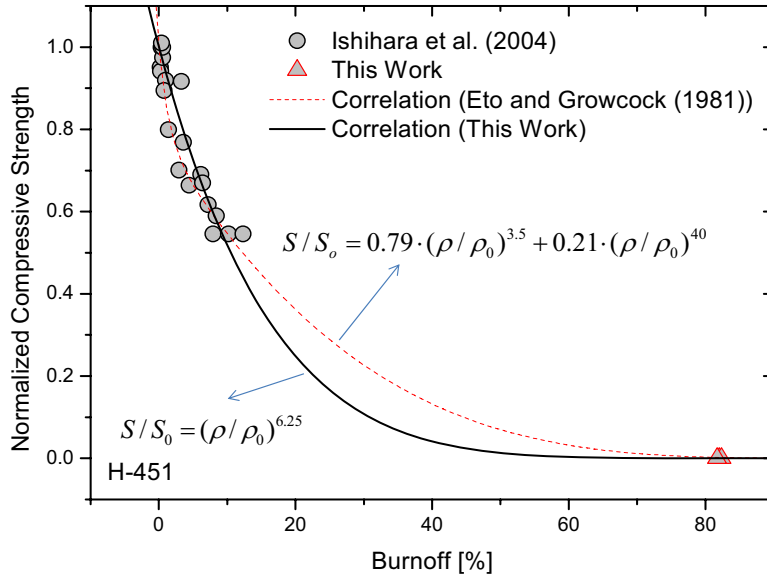


Figure 4-14. Normal compressive strength vs. burnoff (H451).

4.3 Graphite Surface Area Density

Graphite has lots of inside pores. The surface area of those pores is very important for predicting oxidation. This section evaluates the surface area densities for various types of graphite based on the BET specific surface area data provided by Contescu (2008) at ORNL and other literature.

The BET method is used to measure specific surface area based on the BET theory, which is well known for the physical adsorption of gas molecules on a solid surface. This method is based on the following assumptions; (1) homogeneous surface equals energy surface, (2) only the uppermost molecules of a multilayered adsorbate are in dynamic equilibrium with the vapor, (3) the heat of adsorption of the second and higher layers equal the heat of condensation, (4) a molecule covered by another molecule cannot evaporate, (5) at saturation, the number of layers becomes infinite, and (6) there is no lateral interaction between adsorbed molecules. As an adsorption gas, nitrogen at low temperature (77K), krypton at low temperature, water vapor, hydrocarbons of various types, and inert gases are generally used. For more information about this method refer to Bruauer et al. (1938) and Fagerlund (1973).

Figure 4-15 shows the plot of the BET surface area for various graphite materials (NBG18, NBG10, and PCEA) measured by Contescu (2008). Table 4-3 summarizes the collected data for the surface area density for graphite materials.

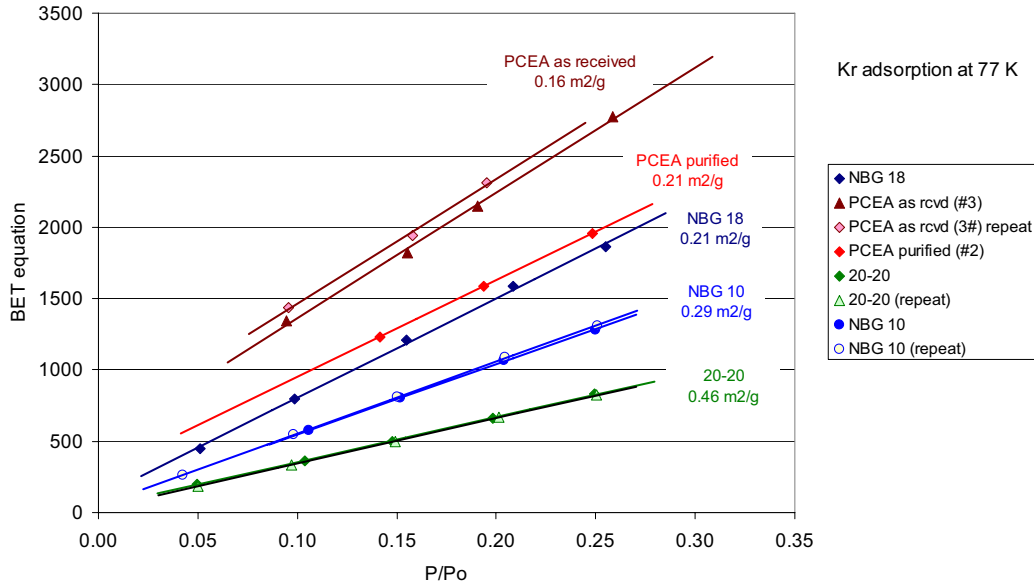


Figure 4-15. Measurement of BET surface area by Contescu (2008).

Table 4-3. Summary of surface area density for graphite.

	Density [g/m ³]	Specific Surface Area [m ² /g]	Surface Area Density [m ² /m ³]
NBG-18 (Contescu 2008)	1790	0.21	375.9
NGB-10 (Contescu 2008)	1790	0.29	519.1
PCEA (Contescu 2008)	1790	0.21	375.9
20-20 (Contescu 2008)	1790	0.46	823.4
IG-11 (Eto and Growcock 1981)	1750	2.8	4900
IG-110 (Nakano et al. 1997)	1780	0.5	890
H451 (Pawelko et al. 2001)	1760	0.75	1320
PGX (Eto and Growcock 1981)	1730	0.7	1211

4.4 Effect of Graphite Burn-off on the Oxidation Rate

The effect of burn-off is very important for predicting the oxidation rate of graphite because the reaction rate is highly dependent on the degree of burn-off. Usually, the reaction rate increases with the increasing burn-off in the beginning (Velasquez et al., 1978). This is because of the increase of the reaction surface as the pores grow larger and the closed porosity opens. Then, the reaction rate decreases at high burn-off because the pores join together, thus decreasing the reaction surface area. The effect of burn-off is usually considered by an empirical factor, F_b , as

$$r_g = k_0 \exp\left(-\frac{E_A}{R \cdot T}\right) \cdot P_{O_2}^n \cdot F_b \quad (4-4)$$

where

$$r_g = \text{reaction rate}$$

k_0 = pre-exponential factor

E_A = activation energy

R = gas constant

T = temperature

$P_{O_2}^n$ = oxygen partial pressure

n = order of reaction

F_b = empirical factor.

The physical meaning of F_b is the ratio of reacting surface area of oxidized graphite to that of original graphite. Therefore, F_b equals to 1.0 for the original graphite and 0.0 for the completely burned graphite. The F_b has the following equation form:

$$F_b = A_{oxidized} / A_{original} \quad (4-5)$$

where

$A_{oxidized}$ = reacting surface area for the oxidized graphite

$A_{original}$ = reacting surface area for the original (unoxidized) graphite (burn-off = 0%).

As described above, the reacting surface area initially increases with the reaction because of the increased pore size. However, as the reaction proceeds, the reacting surface area decreases again because of the collapses of the enlarged pores. Therefore, the F_b value starts at 1.0, and then initially increases with oxidation. After a certain level of burn-off, it starts to decrease again and finally drops to 0.0 at 100% burn-off.

In this report, the F_b factor has been experimentally obtained as a function of burn-off for various forms of graphite: IG-110, H451, NBG-10, NBG-18, and V483T. The F_b factors of IG-110 and H451 were measured by the experimental setup used in Section 4.2, and for NBG-10, NBG-18, and V483T, the data published in Fuller and Okoh (1997), Moorman et al. (1999), and Hinssen et al. (2008) have been used.

Figures 4-16 through 4-20 show the plots of F_b versus burn-off. Figure 4-16 (a) shows the results for IG-110 graphite. This graph includes three datasets: Fuller and Okoh (1997), Kim et al. (2006), and (3) the experimental results obtained in this work. According to the figure, the data from Kim et al. (2006) and this work show very good agreement, but the data from Fuller and Okoh (1997) shows some discrepancies from other data. The reason is not yet identified. In Kim et al.(2006) and the current experiments, the maximum oxidation rate occurs at about 35% burn-off, at which time the oxidation rate is about 6.4 times that of the initial oxidation rate. Figure 4-16 (b) shows the data for H451 graphite. In this material, the maximum oxidation rate occurred between 30–50% burn-off, and it is about 3.5 times larger than the initial rate.

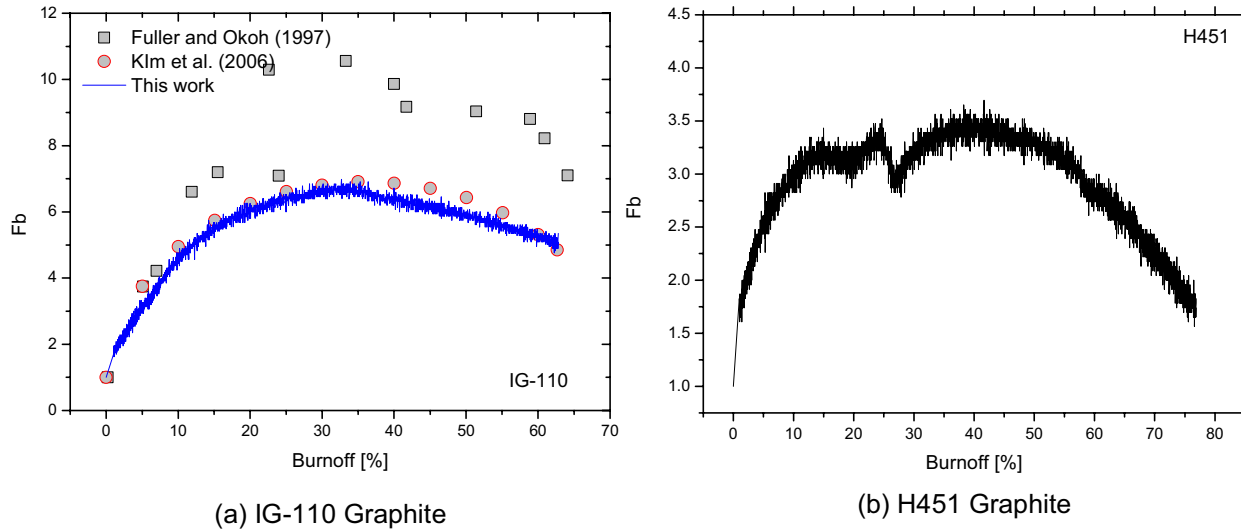


Figure 4-16. Burn-off vs. F_b (IG-110 and H451).

Figure 4-17 plots the surface area densities and the reaction rates for IG-110 and H451 graphite as a function of burn-off. The surface area densities of Figure 4-17(a) were obtained by multiplying the initial surface area density of the graphite in Table 4.3 of Section 4.3 by the F_b value (See Equation 4-5). The reaction rates in the Figure 4-17(b) are the experimental data. Generally, the reaction rates are proportional to the reacting surface area. Therefore, the initial oxidation rate is smaller in IG-110 graphite ($890 \text{ m}^2/\text{m}^3$) than that in H451 graphite ($1,320 \text{ m}^2/\text{m}^3$). However, as the oxidation progresses, the surface area density of IG-110 increases more rapidly than that of H451. And finally, the oxidation rate of IG-110 becomes larger than that of H451 for more than 10% burn-off. It means that only comparisons based on the surface area densities or reaction rates of the original graphite can lead to the misunderstanding on the graphite oxidation characteristics. For example, comparisons show that H451 graphite has better oxidation resistance than IG-110 in the long process, which is more important in the air-ingress accident. Therefore, the comparisons on the other graphite based on this method are highly recommended, and more tests will be carried out in FY-09 and FY-10. It is strongly suggested that this new method be used to select the nuclear graphite for the NGNP.

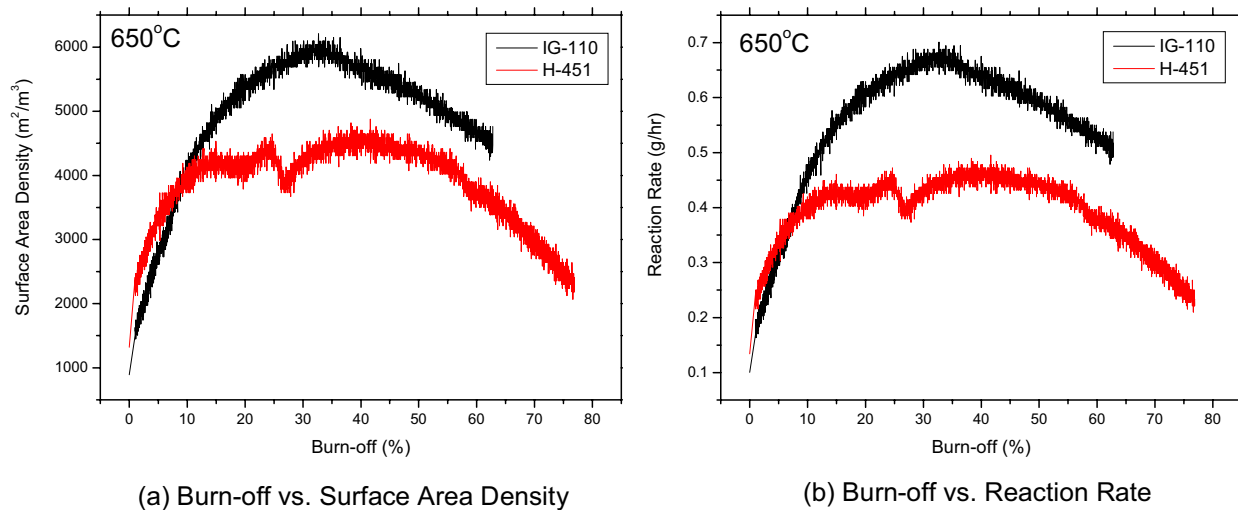


Figure 4-17. Comparisons of surface area density and oxidation rate between IG-110 and H451.

Figures 4-18 and 4-19 show the data for NBG-10 and NBG-18 manufactured by SGL group, respectively. These data are based on the experimental data reported by Hinssen et al. (2008). According to these figures, the maximum oxidation rate occurred at 30% for both graphite types. Figure 4-20 shows the data for V483T, which is based on the data reported by Moorman et al. (1999). All of these graphs and data can be used for predicting the graphite oxidation rate at the specific burn-off in the air-ingress analysis of the VHTRs.

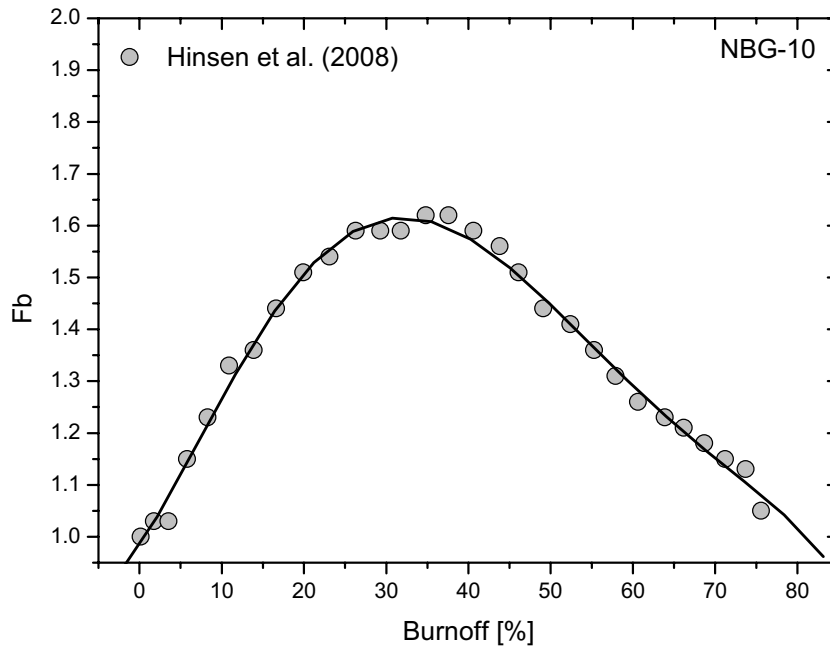


Figure 4-18. Burn-off vs. F_b (NBG-10).

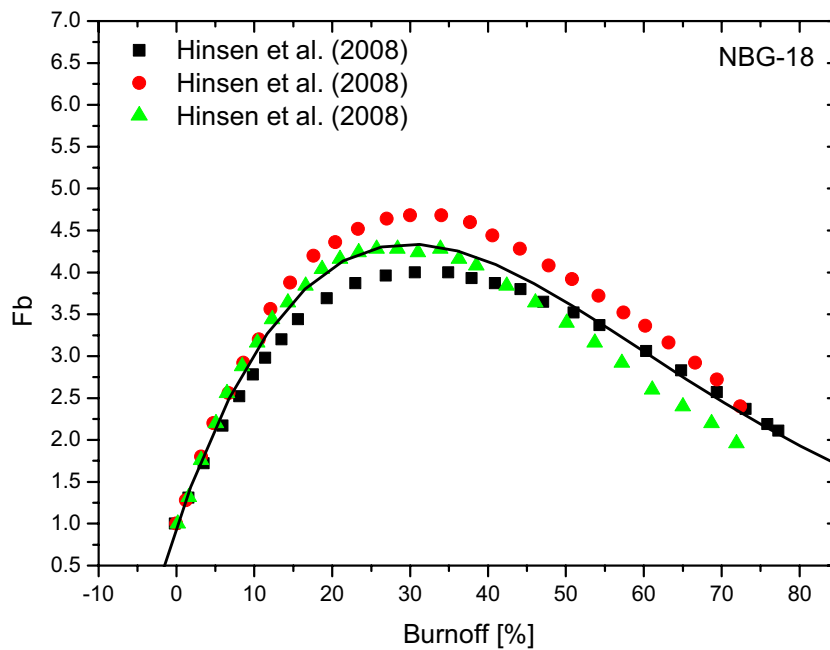


Figure 4-19. Burn-off vs. F_b (NBG-18).

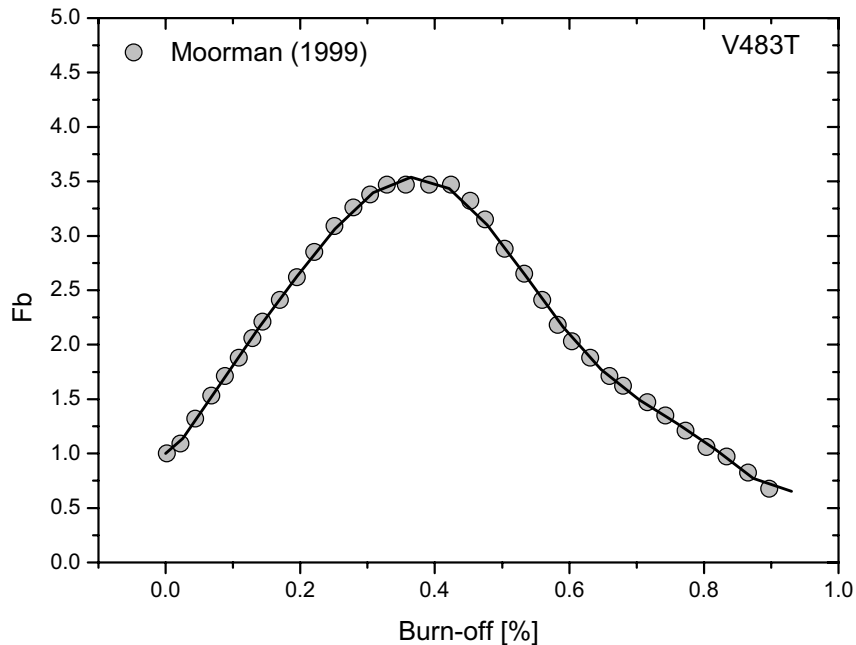


Figure 4-20. Burn-off vs. F_b (V484T).

4.5 Modeling of Graphite Oxidation and Fracture in Air-ingress

The VHTR is the favored concept among designs proposed for the NGNP because of its inherent safety against LOCA and efficient hydrogen production capability. However, the inherent safety feature of the VHTR graphite core design could be compromised if the core support structures collapse and damage the fuel blocks, potentially leading to release of fission products. Such a failure could eventually occur from an air-ingress accident, where the graphite support structures are gradually damaged over time because of oxidation, altering their shapes and mechanical properties. In order to determine the time scale of the graphite support structure failure, computational stress analysis using ABAQUS (Ver. 6.75) was performed for altered shapes and mechanical properties based on the temperature, corrosion depth, and burn-off predicted by the GAMMA—a multidimensional gas multicomponent mixture analysis code developed in the ROK/US I-NERI project (Oh et al. 2006). The air-ingress analysis for this work was based on the assumption that the molecular diffusion dominates the initial air-ingress process, and therefore, the effect of stratification was not considered here. The stress analyses on the oxidized core bottom structures considering stratified flow in the air-ingress accident scenario will be carried out in FY-09 and FY-10.

4.5.1 Stress Analysis Strategy

As shown in Figure 4-21, the core is made of several layers of graphite blocks. So to finish the computational analysis in a reasonable amount of time, instead of modeling the entire core, only one vertical column of the support block and plenum directly below the fuel blocks, the parts subjected to most stress and oxidation damage, were analyzed (indicated by green arrows in Figure 4-21).

As shown in Figure 4-22(b), each block is usually surrounded by six adjacent blocks. However, the presence of adjacent blocks was ignored because there is approximately 2 mm clearance between the block surfaces (GA 1997). Because of the gap vertical columns of the blocks are not exerting force on each other and were therefore assumed to be independent of each other.

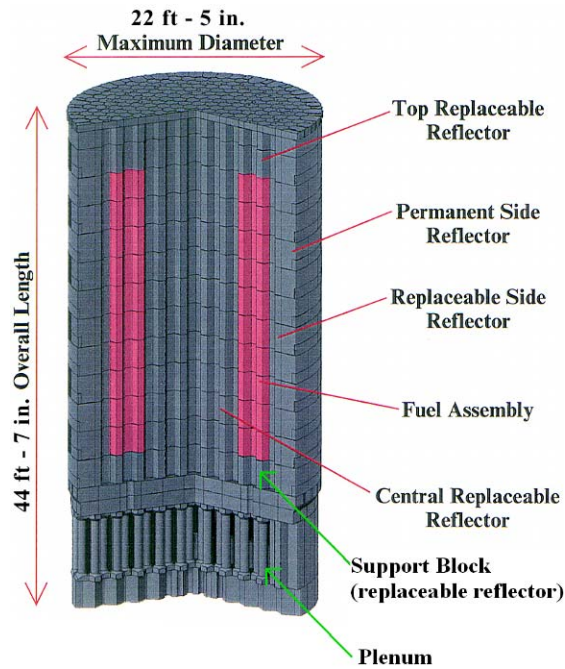


Figure 4-21. GT-MHR core side view(Shenoy 2007).

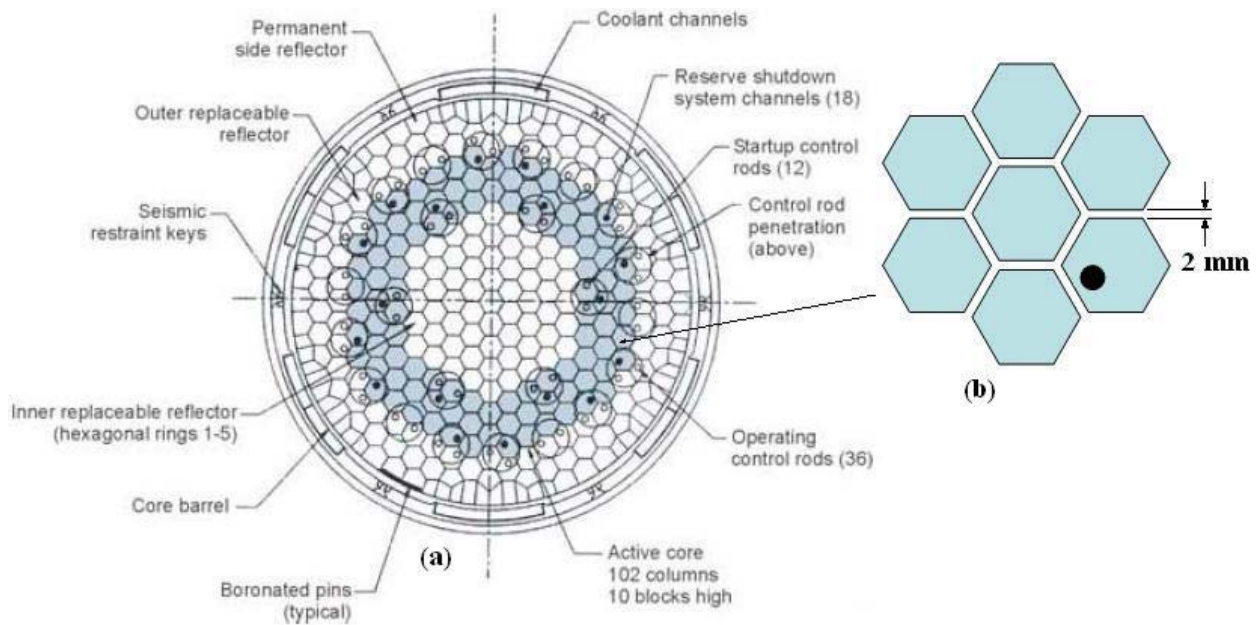


Figure 4-22. Top cutaway view of the core (Cocheme 2004).

Figure 4-23 shows the whole and cut views of the analyzed support block and plenum. Oxidation damages the graphite structure by two different means: burn-off and corrosion. Burn-off refers to the oxidation of the graphite's internal body, causing reduction of density which leads to a reduction of stiffness (young's modulus) and mechanical strength. Corrosion refers to oxidation taking place on the outer surfaces of the structure exposed to airflow. The corrosion decreases the cross-sectional area

available to support the weight. As corrosion continues, the cross-sectional area continues to decrease until the stress concentration exceeds the mechanical strength of the graphite, leading to fracture failure of the structure. Burn-off occurs in the chemical kinetics controls where the temperature is below 650°C. Corrosion takes place at the higher temperature of approximately 900°C where the graphite surface temperature is so high that the oxygen cannot penetrate the pore, which is called the diffusion control regime. In the burn-off process, the shape of the graphite remains in the structure's integrity only, resulting in the reduced density, while the graphite surface is reduced in the corrosion process.

The GAMMA result indicated that corrosion and burn-off are the greatest at the bottom of the plenum head (orange colored part in Figure 4-23), which decreases exponentially toward the top. Corrosion on the support block is expected to be negligible until most of the plenum head is gone, so it was anticipated that structural failure would occur on the plenum head first.

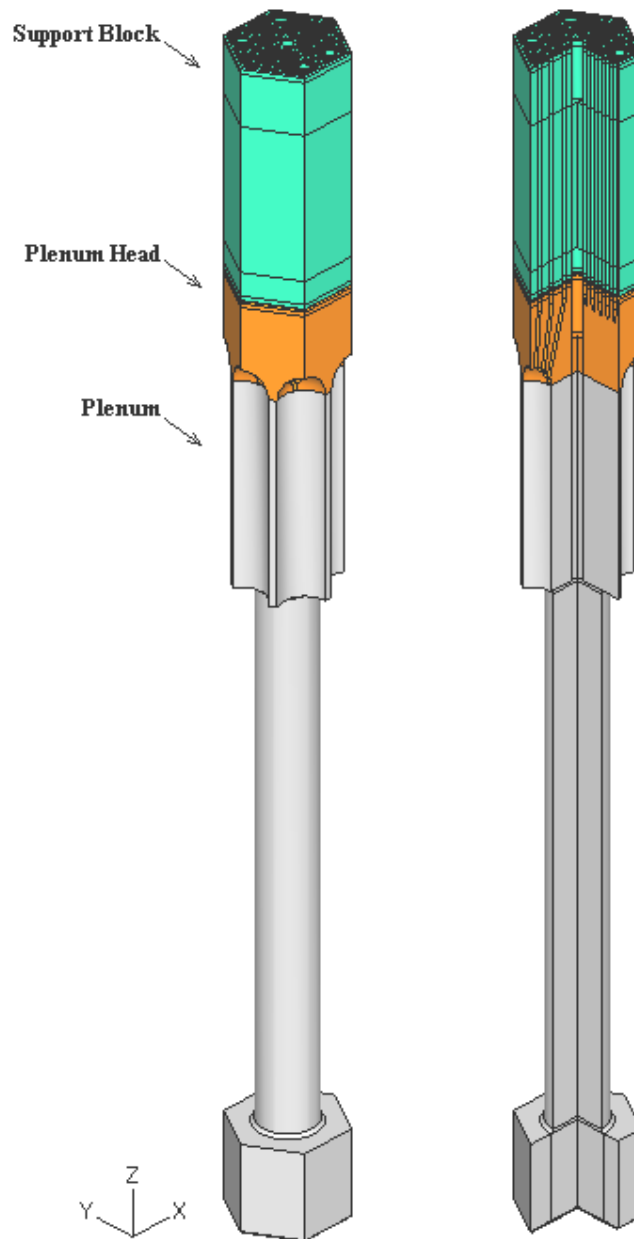


Figure 4-23. ABAQUS generated whole and cut view of the support block and plenum.

4.5.2 Structural Dimensions

4.5.2.1 Support Block Dimensions

The support block is modeled using the dimensions of General Atomics GT-MHR fuel block design, shown in the Figure 4-24. The support block is almost identical to the fuel block except the support block does not have fuel or lumped burnable poison (LBP) holes. Parts without exact dimensions given were approximated from the appearance of the drawing, indicated with an asterisk.

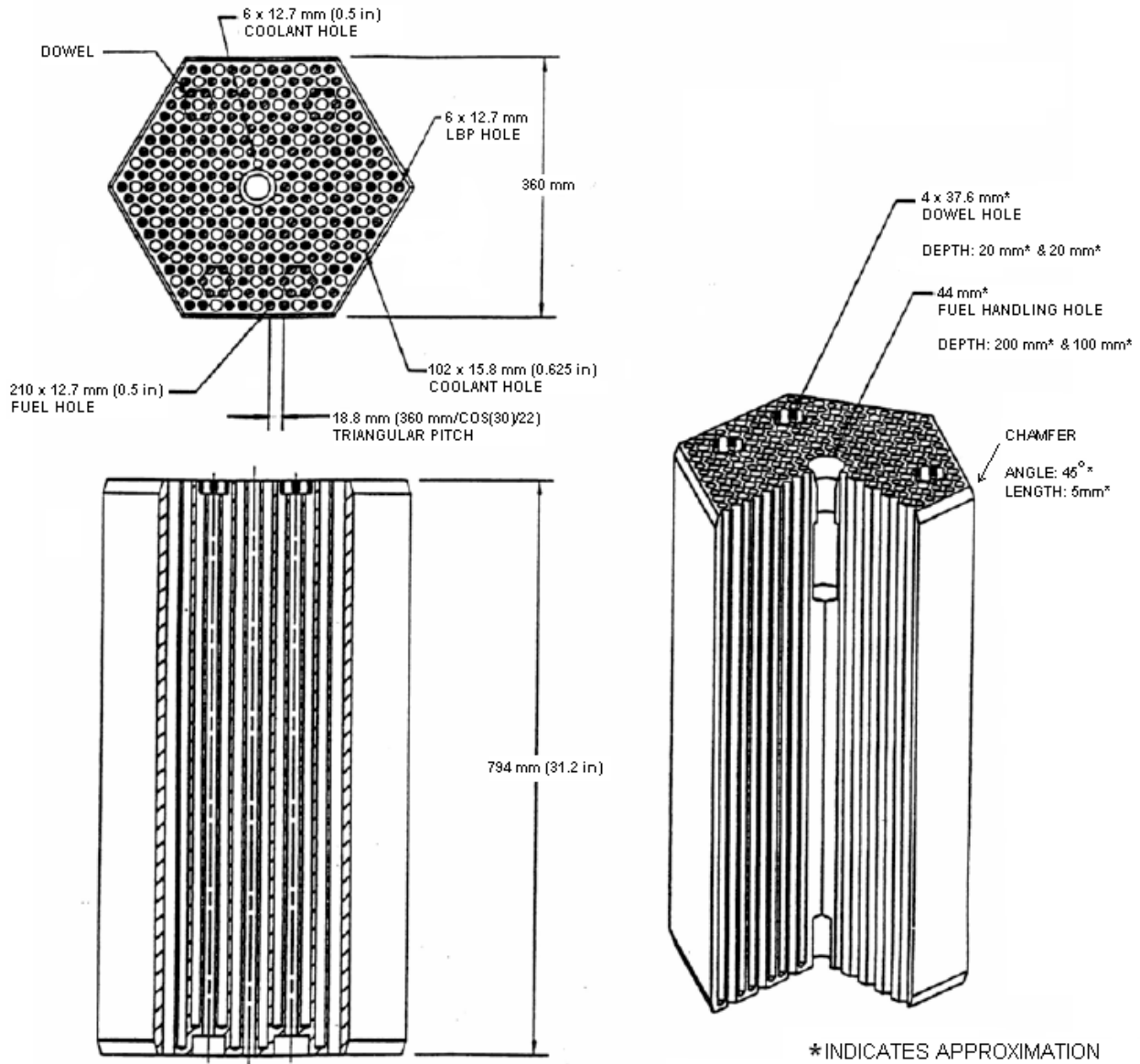


Figure 4-24. The dimensions of a General Atomics GT-MHR fuel block. (GA 1997, Cocheme 2004, GA 2003).

4.5.2.1 Plenum Dimensions

The dimensions used for modeling the plenum, shown in the Figure 4-25(a), are based on the order of magnitude estimates for geometric ratios suitable for normal operation of a 600 MWth GT-MHR (McCreery 2004). The information on how the coolant channels converge into the jet hole was not available; therefore they were personally designed using rotational symmetry such that an equal number of channels converge into each jet hole as shown in the Figure 4-25(b).

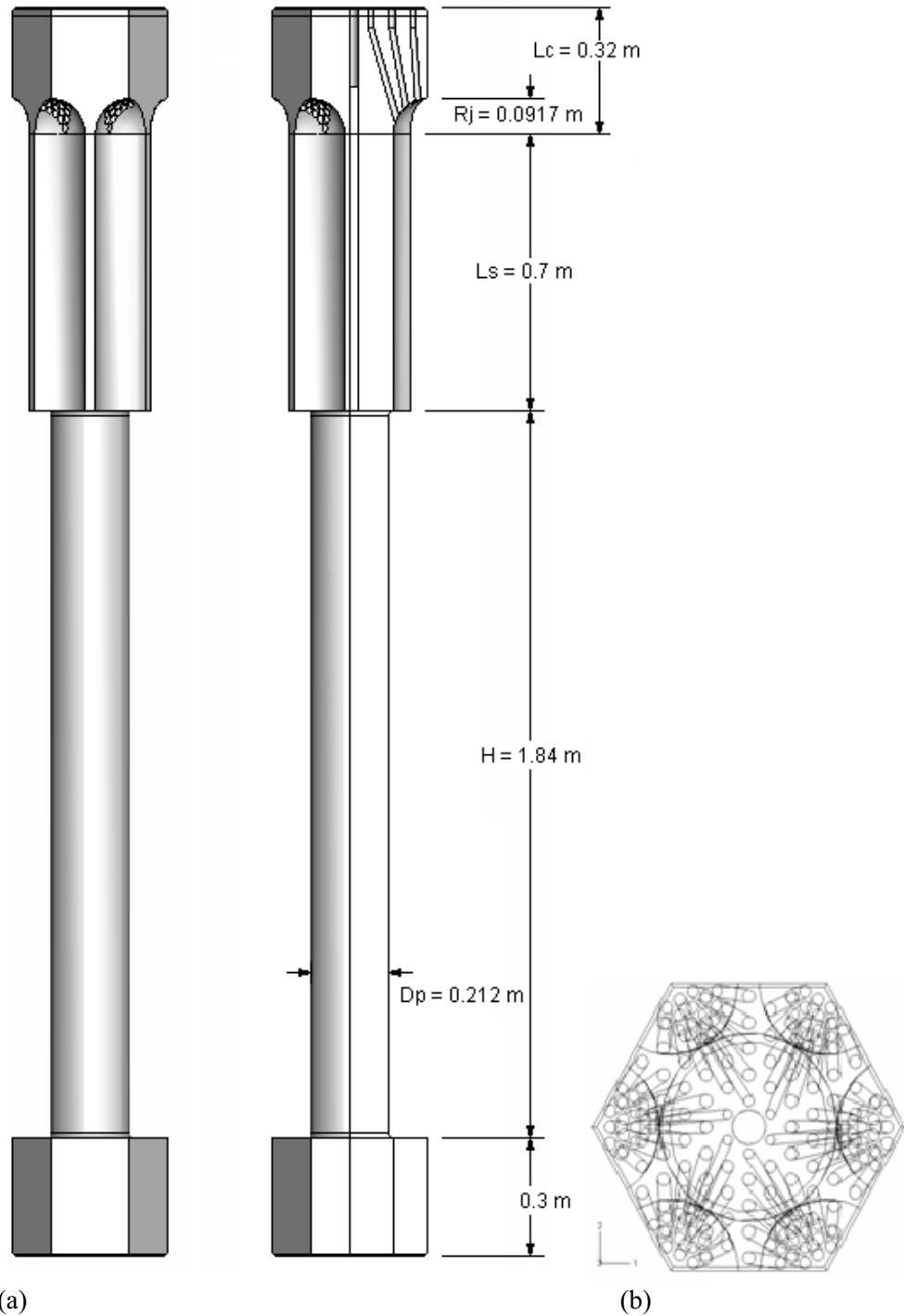


Figure 4-25. Plenum: (a) side views (with dimensions) and (b) wireframe top view.

4.5.3 Change of Temperature, Burn-off and Corrosion Thickness

The graphs in Figures 4-26, 4-27, and 4-28 show the corrosion depth, temperature, and burn-off as a function of time for sections of the support block and plenum. As shown in Figure 4-27 and 4-28, the temperature and burn-off start to rise at about 5.5 days after the LOCA, the time when the natural convection starts. The heat from exothermic oxidation reaction causes the temperature to rise, which also increases the oxidation rate.

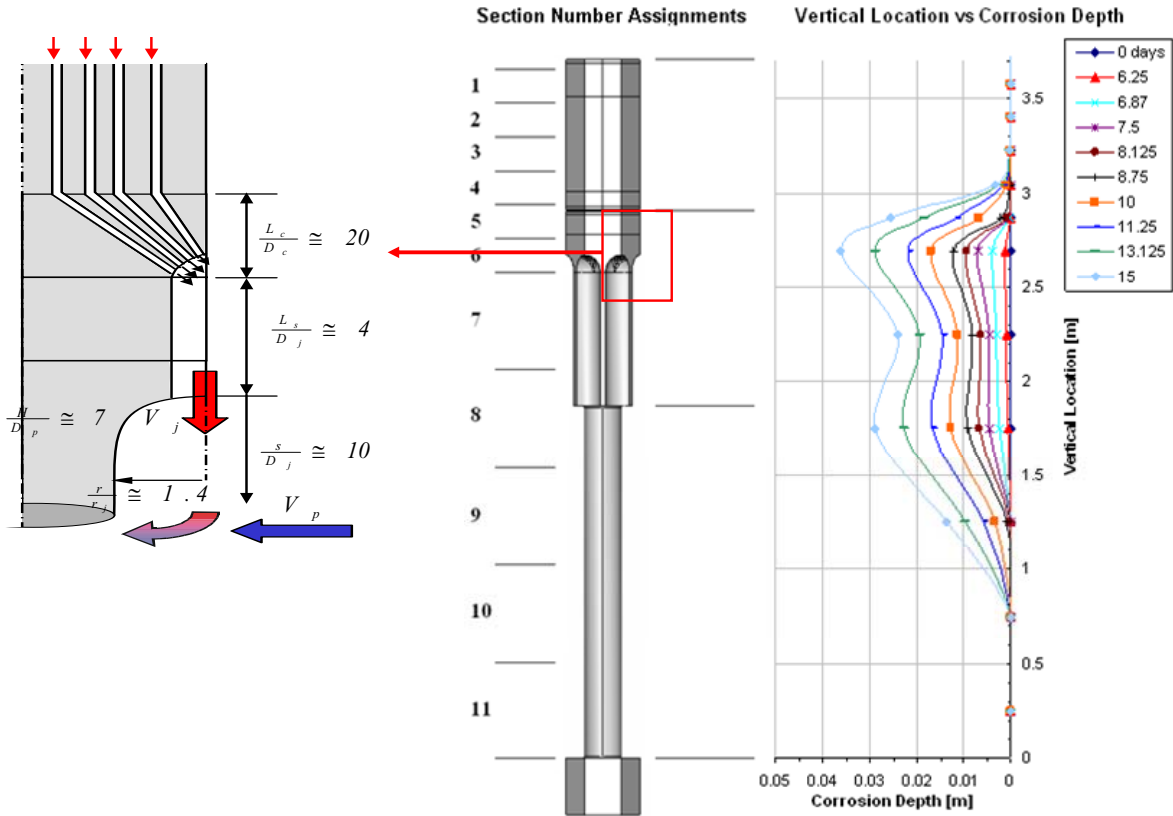


Figure 4-26. Corrosion depths and section assignments.

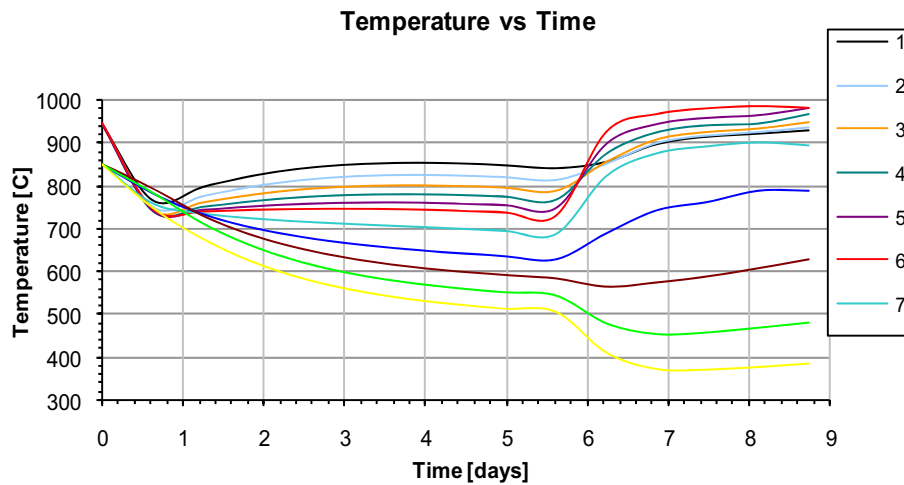


Figure 4-27. GAMMA results of temperature over time.

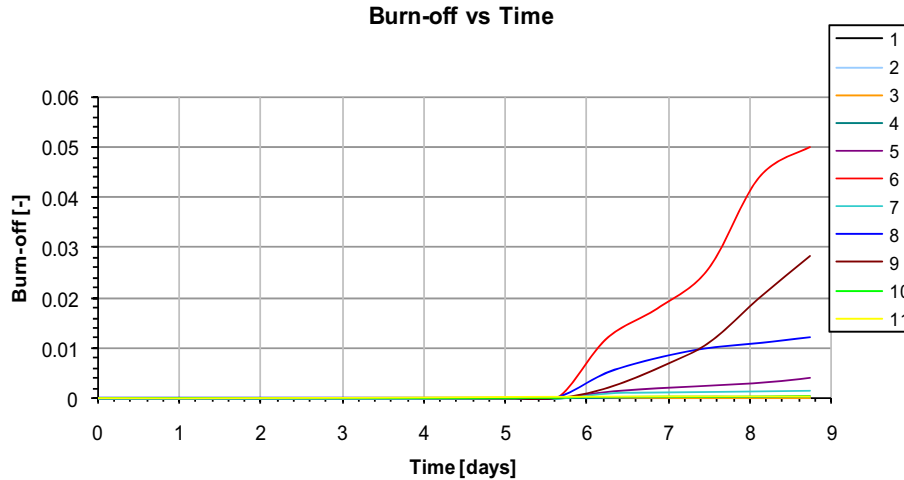


Figure 4-28. GAMMA results of burn-off over time.

4.5.4 Material Database

Mechanical properties are important to the accuracy of the analysis, therefore a detailed material database was built to address the effects of temperature, burn-off, and irradiation.

4.5.4.1 Properties in Standard Conditions

The GT-MHR’s core was assumed to be made of IG-110, a high-strength, fine-grained graphite with isotropic mechanical properties (Ishihara et al. 2004). Thermo-mechanical properties of the IG-110 in normal state are shown in Table 4-4. Because the ultimate strengths exhibit statistical variations, the minimum compressive and tensile strengths were determined from statistical treatment of the strength data such that it can be said with 95% confidence that 99% of the graphite samples survive beyond the specified values (Ishihara et al. 2004).

Table 4-4. Basic thermo-mechanical properties of IG-110 at standard conditions. (Ishihara et al. 2004, Burchell 1991).

Density ⁱⁱ	1,780 kg/m ³
Mean Young’s Modulus ⁱⁱ	7.9 GPa
Poisson Ratio ⁱ	0.14
Mean Compressive Strength ⁱⁱ	76.8 MPa
Minimum Compressive Strength ⁱⁱ	61.3 MPa
Mean Tensile Strength ⁱⁱ	25.3 MPa
Minimum Tensile Strength ⁱⁱ	19.4 MPa
Mean Thermal Expansion Coefficient (293–673°C) ⁱⁱ	4.06x10 ⁻⁶ K ⁻¹
Thermal Conductivity (600°C) ⁱⁱ	80 W/m-K

4.5.4.2 Tensile and Compressive Strength vs. Burn-off

The experimental data for the change of tensile and compressive strength because of burn-off are shown in Figures 4-29(a) and 4-29(b). The relationship between the strengths and the burn-off is exponential. Also, the S/S₀ ratios for both tensile and compressive strengths show a virtually identical trend to that of function of burn-off.

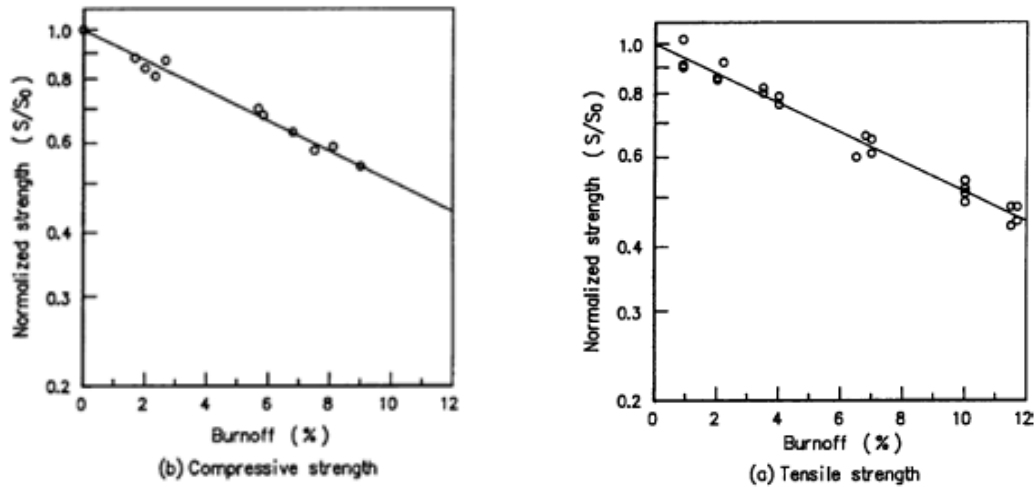


Figure 4-29. (a) Tensile strength as function of the burn-off; (b) compressive strength as function of the burn-off (Ishihara et al. 2004).

4.5.4.3 Tensile and Compressive Strength vs. Temperature

As shown in the Figure 4-30, the young's modulus ratio appears to show square root relationship with the tensile strength. Considering that S/S₀ ratios for tensile and compressive strength behave almost exactly the same as function of burn-off, their behaviors with respect to the temperature change might be very similar with each other. Therefore, the S/S₀ ratio for compressive strength was assumed to behave the same as the S/S₀ ratio for the tensile strength as a function of temperature.

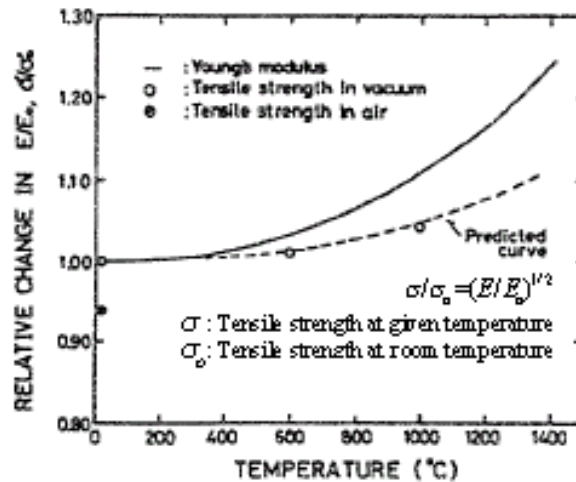


Figure 4-30. Tensile strength as function of temperature (Eto et al. 1986).

4.5.4.4 Young's Modulus vs. Temperature and Burn-off

The experimental data and correlations for the change of Young's modulus because of temperature and burn-off are shown in the Figure 4-31.

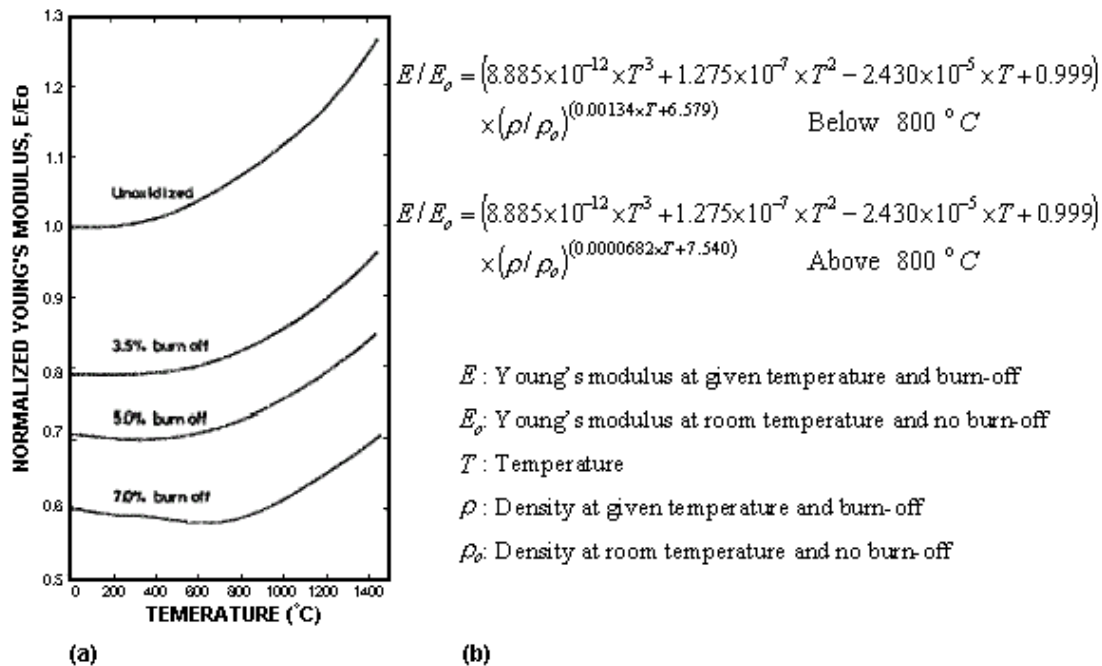


Figure 4-31. (a) The change in Young's modulus because of oxidation as a function of temperature (best fit of experiment data); (b) the correlations for Young's modulus as a function of temperature and burn off (Eto et al. 1986).

4.5.4.5 Young's Modulus and Mechanical Strengths vs. Irradiation

A change of mechanical properties from irradiation is expected to be negligible because of low neutron dose experienced by the support block and plenum. Ishiyama et al. performed mechanical tests on IG-110 samples that were irradiated up to neutron fluence of 3.8×10^{22} n/cm² (neutron energy >0.05 MeV) at a temperature of 600°C, which resulted in neutron dose of ~25 dpa (Burchell et al. 1996). Figures 4-32(a) and 4-32(b) show the change of young's modulus and mechanical strength as a function of dpa.

As a reference example, the central replaceable reflectors (indicated in Figure 4-22) experience the neutron fluence of 6.7×10^{20} n/cm² per year ($E > 0.1$ MeV) with a neutron dose of 0.56 dpa per year (Bratton et al. 2005). On the other hand, the support block and plenum experience neutron fluences of 9.1×10^{15} n/cm² per year [$E > 0.1$ MeV] and 3.7×10^{17} n/cm² per year, respectively, with negligible neutron dose in dpa for both sections (Bratton et al. 2005). Using the central reflector case as the reference and taking the neutron fluence ratio, the neutron dose received by support block and plenum are 7.606×10^{-6} and 3.1×10^{-4} dpa per year, respectively. Considering the projected plant design life is 60 years (Bratton et al. 2005), the total neutron dose received by the support block and the plenum is 4.56×10^{-4} and 1.85×10^{-2} dpa, respectively. As is apparent on Figures 4-32(a) and 4-32(b), mechanical property changes because of irradiation at these dpa are probably negligible, therefore the effect of irradiation was ignored for the stress analysis.

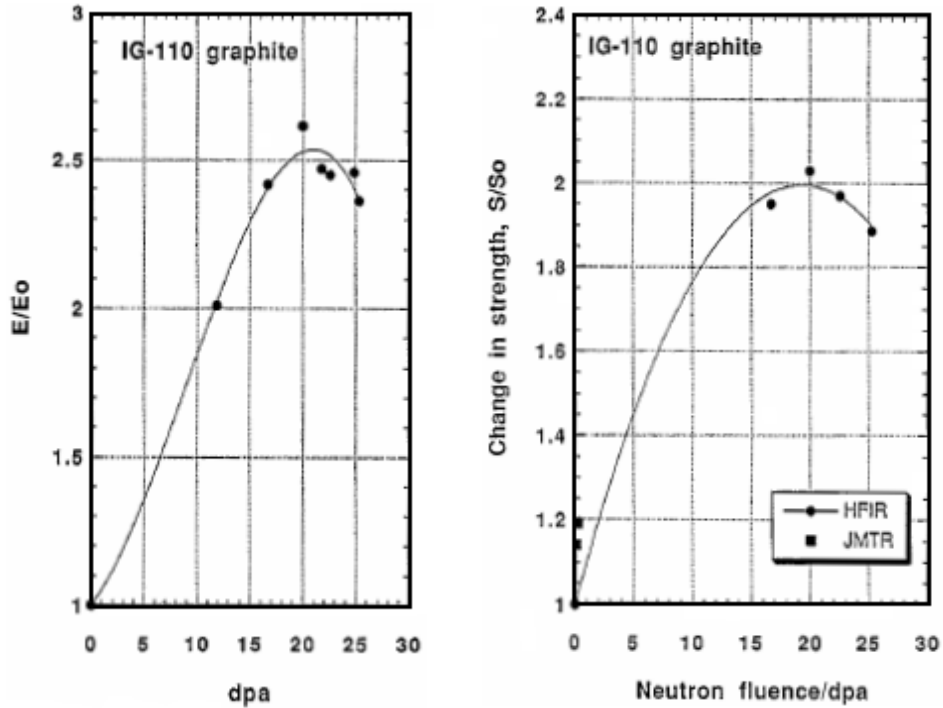


Figure 4-32. Young's modulus (a) and mechanical strength (b) as function of dpa caused by irradiation (Burchell et al. 1996).

Normal operation temperatures for support block and plenum is about 1000°C, and 1000–1200°C, respectively (Bratton et al. 2005). Because they experience irradiation at temperatures higher than the irradiation temperature in Ishiyama et al.'s experiment, the Young's modulus and strength might behave a little differently than the data shown in Figure 4-32. However, considering mechanical properties tend to recover back toward the original values at higher temperature because of annealing effect (Burchell et al. 1996), it is most likely that the effect of irradiation on Young's modulus and strength is less at the higher irradiation temperatures the support block and plenum normally operate at.

4.5.5 Treatment of Material Properties during Analysis

The IG-110 is treated as an ideal brittle material that exhibits elastic behavior with a constant Young's modulus and does not undergo any plastic deformation before reaching the strength limit. This approximation is applicable to IG-110 because IG-110 is a brittle ceramic material that undergoes negligible plastic deformation before failure. As a relative example, Figure 4-33(a) shows the compressive stress-strain curve of UNS31803 steel, a ductile metal. As a ductile metal, its stress-strain curve is characterized by its ability to undergo plastic deformation up to a large strain value. It initially shows elastic behavior, but after the about 700 MPa, it starts to plastically deform until it eventually fails at the strain of 0.35. Figure 4-33(b) shows the stress-strain curve for IG-110. Please note the scale of the strain, which is 10 times smaller than that in Figure 4-33(a). Unlike the steel, IG-110, being a brittle ceramic material, is not able to handle much strain before failure and shows almost no plastic deformation. The IG-110 stress-strain curve plotted on Figure 4-33(a) appears as almost a straight line.

During the analysis, the Young's modulus and density were estimated for the respective temperature and burn-off of the time point and section number shown in the Figures 4-27, 4-28, and 4-26, respectively, where the effect of irradiation was ignored since it is probably negligible.

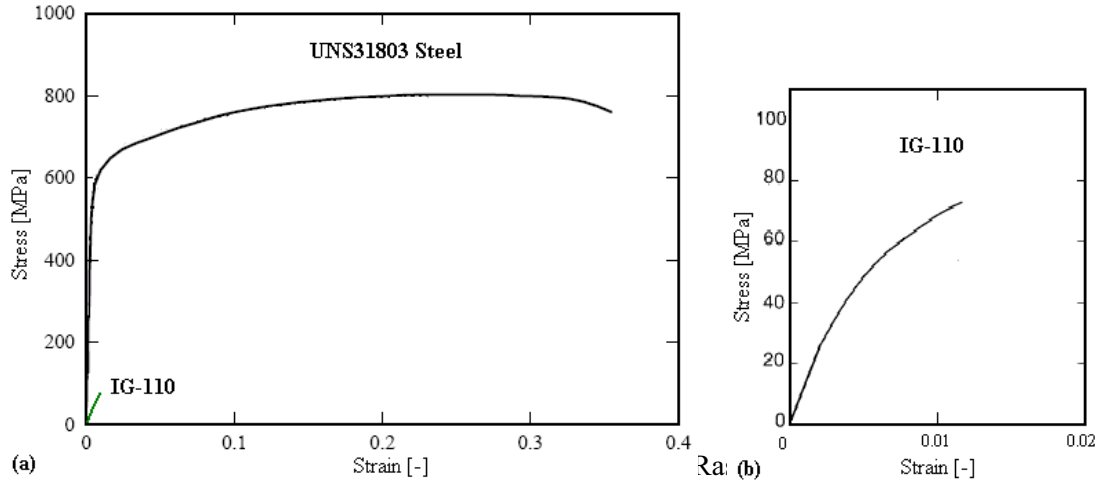


Figure 4-33 (a) stress-strain curve for IG-110 (Fujii et al. 1997).

For this report, the principal stress failure criterion is used as failure criteria. The failure is assumed to occur if the minimum principal stress (maximum compressive stress) exceeds the ultimate compressive strength, or if the maximum principal stress (maximum tensile stress) exceeds the ultimate tensile strength.

4.5.6 Initial Unoxidized State Results

4.5.6.1 Load Stress

As the first step, the support block and plenum in unoxidized condition was analyzed to understand general stress distribution. Figure 4-34 shows the maximum compressive stress distribution on the support block and plenum in unoxidized condition, analyzed using 1/6 cyclic symmetry. As shown in the Figure 4-34, the maximum stress is concentrated on the root of the plenum, indicated in red color, which corresponds to 1 MPa, far below the mechanical strength limit of undamaged IG-110. Although not shown on the figure, the maximum tensile stress is 0.1 MPa, again far below the tensile strength limit. Because the corrosion and burn-off on lower part of the plenum and upper part of the support block are negligible, stress distribution on these parts would be about the same on other time points, and it is unnecessary to include them in analysis, therefore only the part within point L1 to L2, indicated in the Figure 4-34, was analyzed to reduce the size of the model and computation time.

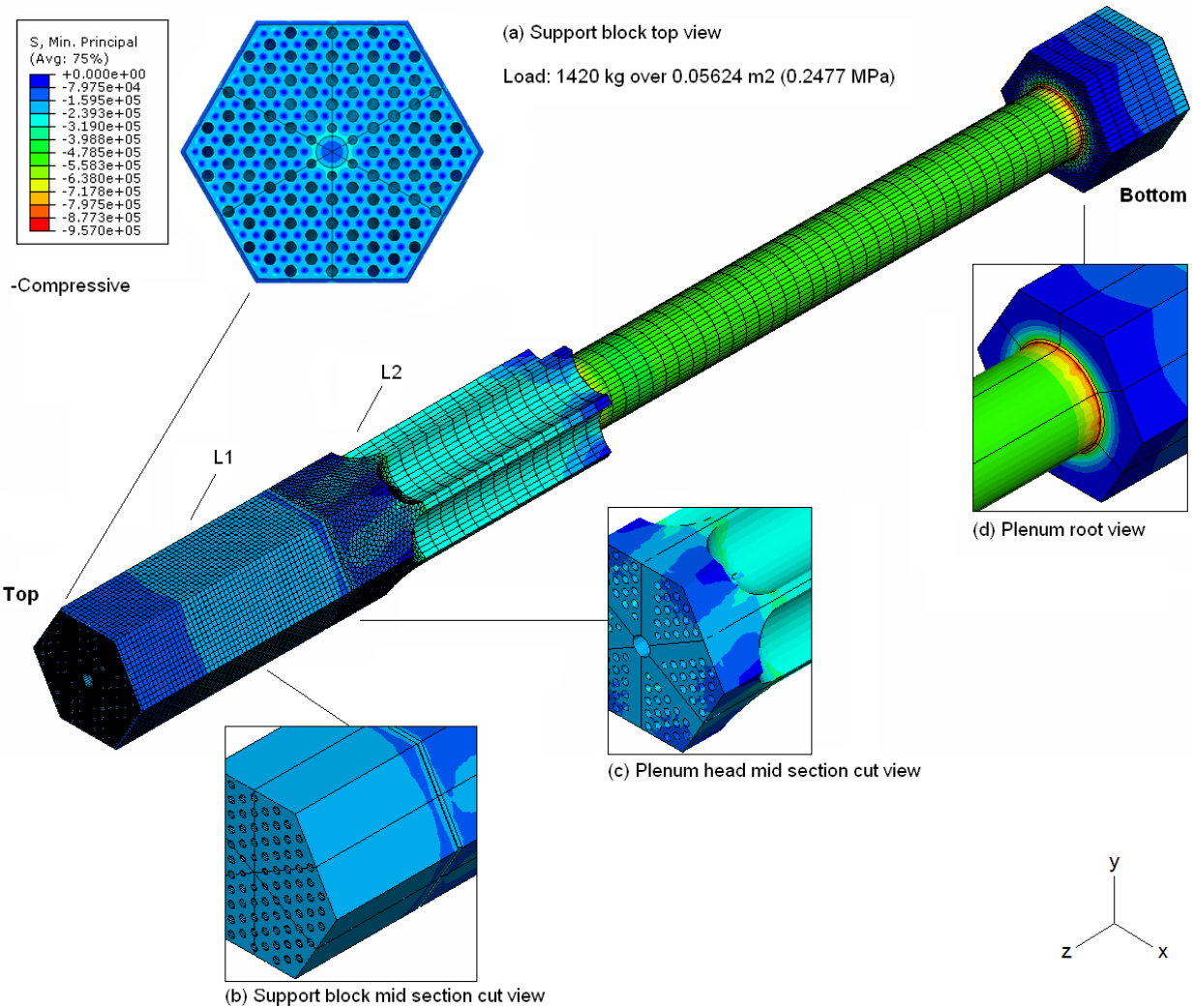


Figure 4-34. Compressive stress distribution on unoxidized support block and plenum.

4.5.6.2 Analytical Validation

For the middle of the support block and the middle of the plenum, analytical solutions to compressive stresses in z-axis direction (top to bottom) can be calculated by the simple stress relationship

$$\sigma = \frac{mg}{A} \quad (4-6)$$

where

m = Total mass of objects being supported by the area [kg]

g = The gravitational constant, 9.81 [m/s²]

A = The cross sectional area perpendicular to the loading [m²]

The two locations were chosen because, at these points, the stress distribution on the cross sectional areas are redistributed to be very uniform, and the loading scheme is almost uniaxial in z-axis direction such that analytical solution using the above equation should yield the same result as Figure 4-35. As shown, there are nine different stress components in 3-D principal stress that are accounted for to determine the maximum tensile and compressive stresses at a given point. However, when the loading scheme is simple such that all stress components except one normal stress component are negligible, the analytical solution using Equation (4-6) is approximately equal to the principal stress. At the middle of the support block and the middle of the plenum, all of stress components except the normal stress in z-axis are negligible.

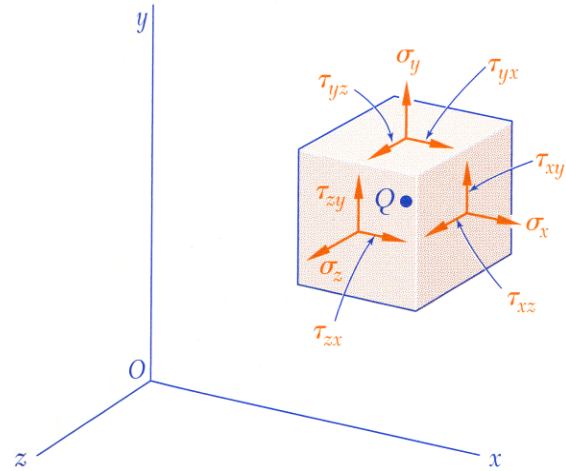


Figure 4-35. The principal stress components (Beer et al. 2006).

As shown in the Table 4-5, analytical calculation agrees with the ABAQUS result, which suggests the finite element analysis was done correctly.

Table 4-5. Comparison of the analytical solution to the ABAQUS result.

Location	Supported Mass (kg)	Cross Sectional Area (m ²)	Compressive Stress (Pa)	ABAQUS Result (Pa)
Middle of the support block	1,500	0.09148	1.636e5	1.625e5
Middle of the plenum	1,800	0.0353	5.002e5	4.915e5

4.5.6.3 Thermal Stress

Thermal stress analysis was done for a small representative part of the support, including the three coolant channels indicated in the Figure 4-36(a). When the outer surface of the coolant channel experiences exothermic surface oxidation reaction, this is the most likely location for the thermal stress fracture. The temperature difference between the outer surface and the inner body is expected to be on the order of tens of degrees, therefore the coolant channel surface temperature of 1300°C and internal body temperature of 1250°C were assumed.

As apparent in the Figure 4-36(c) and 4-36(d), both the compressive and tensile stresses are below strength limits. Considering that the actual temperature difference between the coolant channel surface and the internal body is most likely much smaller than 50°C, the thermal stresses are likely smaller and thus negligible. Combined loading and thermal stress analysis was done for the nonuniform oxidation case for which the effect of thermal stress was again negligible.

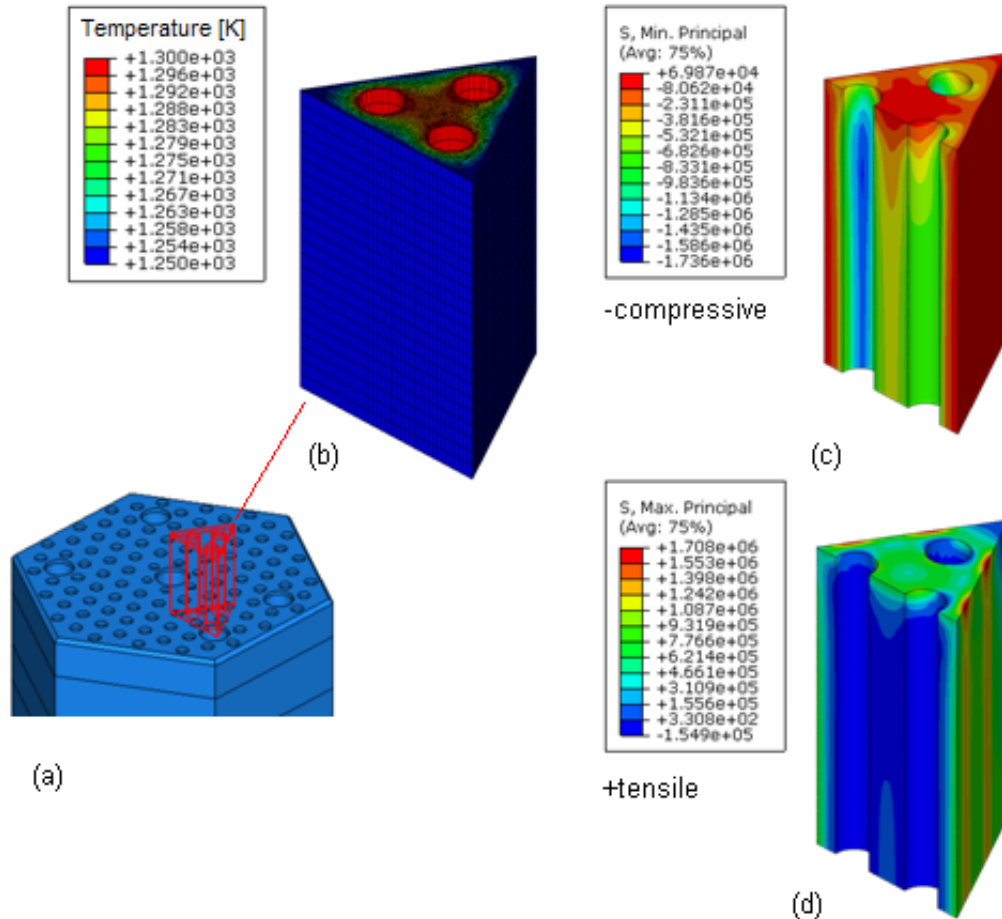


Figure 4-36. (a) Upper part of support block with triangular prism; (b) mesh and temperature distribution; (c) compressive stress; (d) tensile stress.

4.5.7 Oxidized State Results

4.5.7.1 Modification

Before proceeding with nonuniform analysis, simple modifications were made to the height of the plenum head and support block to make them more structurally sound in oxidized condition. Stress concentration would occur at the contact surface between the support block and plenum head, indicated as “critical location” in Figure 4-37. This is primarily because of the chamfer feature, which significantly reduces the size of cross sectional area available to support the load in heavily corroded state. The structure could last longer if the interacting surface is relocated to some other place where oxidation damage is negligible. This is accomplished by adjusting the height of the plenum head and the support block.

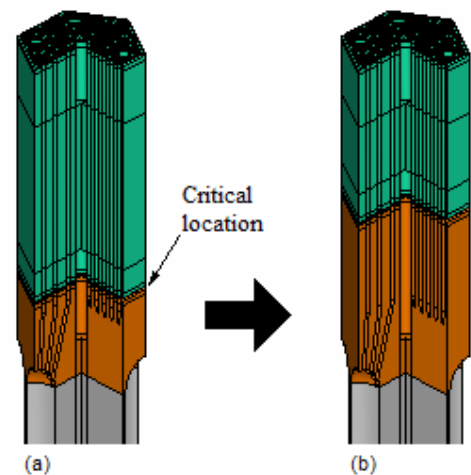


Figure 4-37. Modification of plenum head's height.

Some of the dimensions used for the plenum, such as the height of the plenum head and support block, are open to modification. The plenum head's height was increased by 0.24 m and, consequently, the support block's height was decreased by 0.24 m. From manufacturing standpoint there should be no difficulty in making these modifications. Most of the fuel and support blocks have straight channel holes drilled 0.8 m long. With the height modification, instead of drilling a 0.05-m-long hole from the top of plenum head, it is now increased to 0.24 m, which is still much shorter than 0.8 m. With the height of the plenum increased by 0.24 m, the chamfer and interacting surface are relocated to a place where corrosion and burn-off are almost negligible.

With the interacting surface and chamfer relocated, the cross-sectional area at the critical location is increased, which relieves the stress concentration. And, because critical location is now placed in middle of a continuous body, it is more structurally sound.

4.5.7.2 Corrosion Progression

Figure 4-38 shows the 1/6 cyclic symmetry unit of the modified plenum head for several time points. As corrosion progresses and the coolant holes collapse together, the plenum head eventually develops pillars (remains of the thickest parts of the plenum head), and the stress concentration increases dramatically because of significant reduction in the size of the cross sectional area to support the weight.

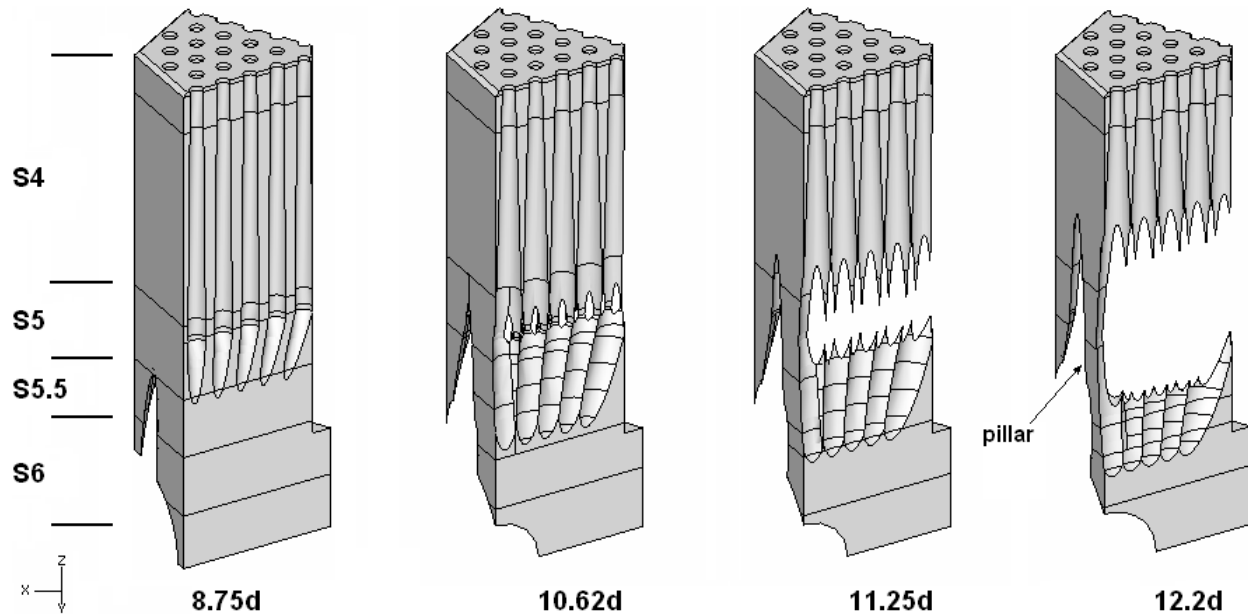


Figure 4-38. 1/6 cyclic symmetry unit of the modified plenum head for each day.

Table 4-6 shows the material properties used for each day. The plenum head was divided into sections to calculate the density—Young's modulus and strengths based on the temperature and burn-off. Although a smooth variation of the properties as a function of height would be more desirable, such is difficult to implement in ABAQUS, so the section method was used.

Table 4-6. Material properties at each day.

Day	Section	T [K]	Burnoff [-]	Density [kg/m ³]	E [GPa]	Compressive Strength [MPa]	Tensile Strength [MPa]
8.75	4	950	0.000	1780	8.6790		
	5	980	0.028	1730	6.9830		
	5.5	980	0.039	1710	6.3831		
	6	980	0.050	1691	5.8287	43.5411	13.7797
10.62	4	950	0.0000	1780	8.6790		
	5	980	0.0070	1768	8.2662		
	5.5	980	0.0434	1703	6.1570		
	6	980	0.0798	1638	4.5339	35.5197	11.2412
11.25	4	950	0.0000	1780	8.6790		
	5	980	0.0100	1762	8.0711		
	5.5	980	0.0498	1691	5.8364		
	6	980	0.0897	1620	4.1622	33.1889	10.5035
12.25	4	950	0.0000	1780	8.6790		
	5	980	0.0148	1754	7.7674		
	5.5	980	0.0602	1673	5.3537		
	6	980	0.1056	1592	3.6227	29.7736	9.4226

4.5.7.3 Load Stress

Figures 4-39(a) and 4-39(b) show maximum compressive and tensile stresses for two different locations (the edge and inside) as indicated in Figures 4-40(b) and 4-40(c). The stress concentrations are increasing almost exponentially over time because they are inversely proportional to the cross sectional area, which is also decreasing over time because of corrosion.

Figure 4-41(a) and 4-41(b) show that the bottom half of the pillar is slanted to the left, which creates counter clockwise bending moment, causing compressive stress toward the left side and tensile stress toward the right side. The top half of the pillar is straight and subjected to compressive stress on the right side and tensile stress on the left side because of the counter clockwise bending moment of the bottom half.

Local maximum near the edge occurs because the bending moment causes the greatest stress on the outer edge, and the stress concentration on the edge gets exacerbated by decreasing cross sectional area toward the edge because of the triangular shape. The stress is relieved toward the inner section where cross sectional area gets relatively larger. Note that the exceeding strength limit on the edge dose not necessarily lead to failure, because after the edge portion crumbles, the stress will get redistributed to inner section, and the cross sectional area of the inner section is most likely wide enough to handle the additional loading without much change in stress concentration. However, exceeding mechanical strength on the inner section is a definite sign of failure, because failure in the inner section results in significant loss of cross sectional area to handle the load.

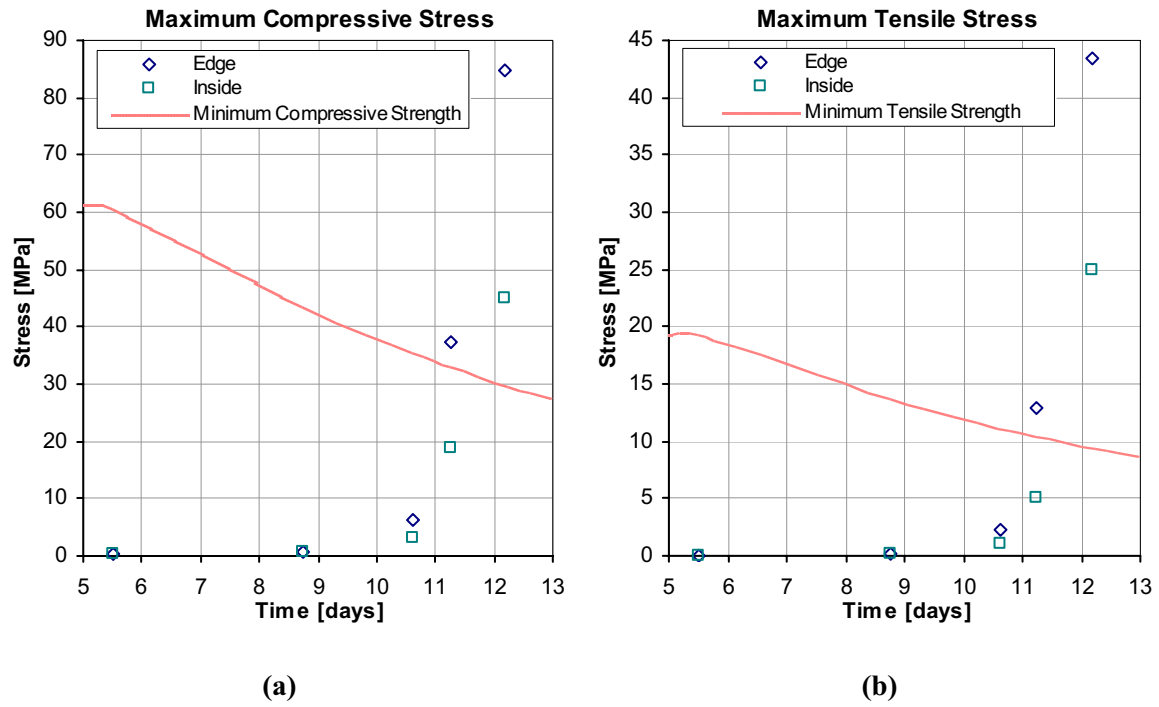


Figure 4-39. Maximum compressive stress (a) and tensile stress (b) over time.

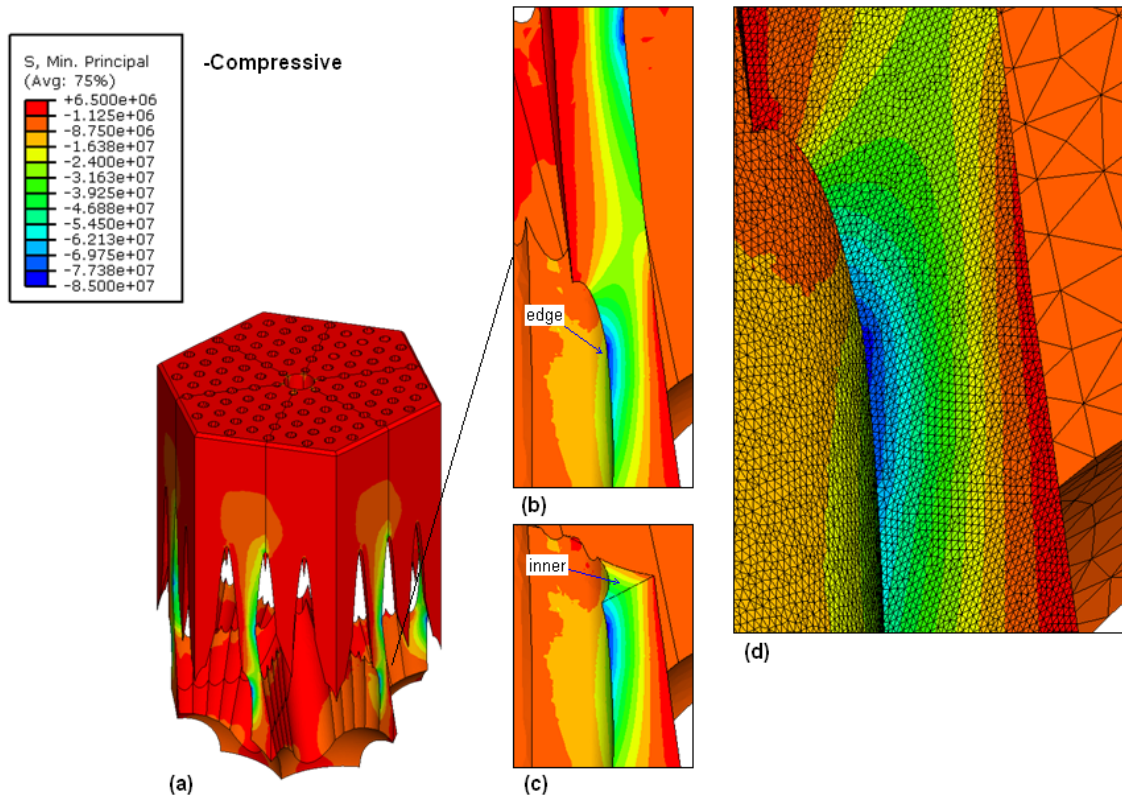


Figure 4-40. Compressive stress distribution on plenum head, 12.25 days after LOCA.

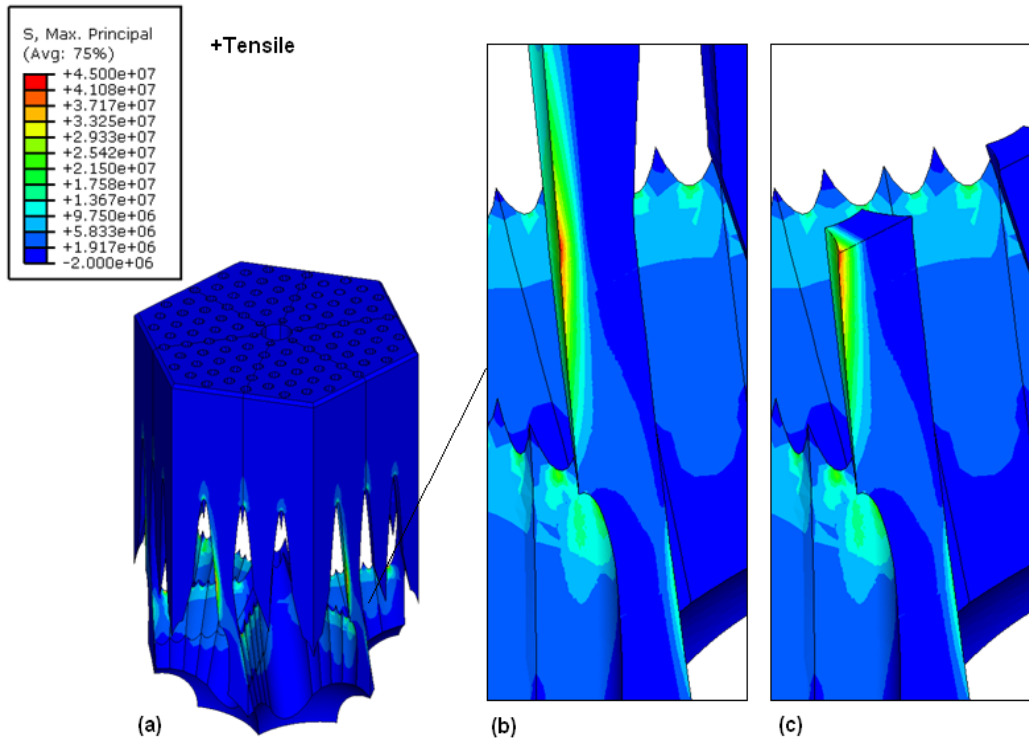


Figure 4-41. Tensile stress distribution on plenum head, 12.25 days after LOCA.

4.5.7.4 Analytical Validation

Because of the pillar’s complex loading scheme, only an order of magnitude estimate for the compressive stress was done. The cross sectional area of the pillar, shown in the Figure 4-40(c), is approximately $8 \times 10^{-5} \text{ m}^2$, and there are six pillars—one per corner. The weight being supported by the pillars are approximately 1,600 kg; thus, the compressive stress should be on the order of $4 \times 10^7 \text{ Pa}$, which compares well with the result shown in Figure 4-40(c), which ranges from 8×10^7 to $1 \times 10^7 \text{ Pa}$. The stress distribution on the cross sectional area is not uniform because of the bending moment, which was ignored for analytical estimation. However, the magnitude of the stress distribution is reasonable compared to the analytical estimation.

4.5.7.5 Thermal Stress

Just like the unoxidized case, the thermal stresses in the oxidized case are negligible. Thermal stress analysis for the nonuniform model was performed for small portion of the 11.25 day model’s surviving pillar, indicated by the red wire-frame in Figure 4-42(a). As shown, the temperature was set to 1350K for the inner surface exposed to air flow, and 1300K for the outer surface not exposed to air flow. Three different schemes were analyzed: thermal stress only (Figures 4-42c and 4-42f), both the thermal and load stresses (Figure 4-42(d) and 4-42(g)), and load stress only (Figure 4-42(e) and 4-42(h)).

Compared to the stress caused by the load alone, thermal stress is an order of magnitude smaller. When both the thermal and load stresses are applied, the result is virtually identical to the case where only the load stress is applied. This indicates that the stresses approximately get super positioned, and net stress is merely the sum of the two.

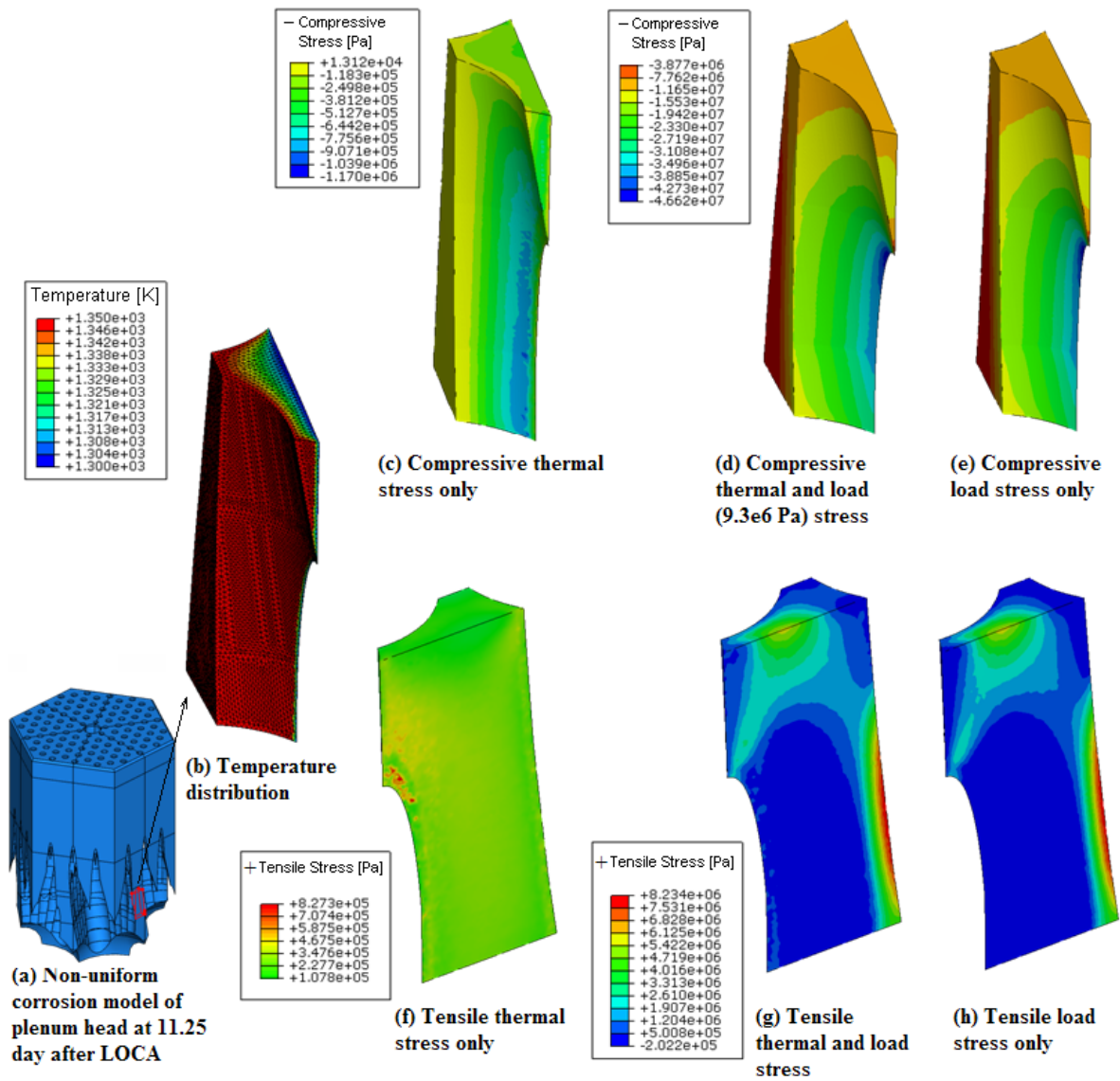


Figure 4-42. Thermal and load stress distributions for bottom half of the pillar, 11.25 days after LOCA.

5. TASK 4: AIR INGRESS MITIGATION STUDY (INL)

******* Air Ingress Mitigation Study is not within the scope of this fiscal year. *******

6. TASK 5: EXPERIMENT OF BURN-OFF IN THE CORE BOTTOM STRUCTURES (KAIST)

The objective of this task is to measure the oxidation rate and density of the nuclear graphite and to develop oxidation models of the core bottom structures that will be directly exposed to the air-ingress event. The main parameters that affect the rate of oxidation and density of the graphite of the core bottom structures are kinetics, mass diffusion, combined effect of kinetics and mass diffusion, moisture, shape and size, and degree of burn-off. Several types of candidate graphite were selected for the experiment.

6.1 Graphite Selection

Candidate graphite materials were proposed in the previous NGNP program (Robert and Timothy 2005); NGNP graphite testing and qualification specimen selection strategy. Some of the candidates were listed in Table 6-1.

Table 6-1. Graphite selection matrix.

Graphite	Vendor	Proposed Use	Remarks
IG-110	Toyo Tanso	Prismatic fuel element, replaceable reflector, and core support pedestals	Historical Reference Currently being used in the HTTR and HTR-10
PCEA	Graftech International	Prismatic fuel and replaceable block Pebble bed reflector and insulation blocks	AREVA wants to construct the entire graphite core out of the same graphite
NBG-17	SGL	Prismatic fuel element and replaceable reflector Pebble bed reflector structure and insulation blocks	AREVA wants to construct the entire graphite core out of the same graphite
IG-430	Toyo tanso	Prismatic fuel element, replaceable reflector, and core support pedestals	Japan Atomic Energy Agency wants to use this graphite in the GTHTTR 300
PGX	Graftech International	Prismatic large permanent reflector	AREVA may use this material; preference is to use PCEA or NBG-17 for permanent reflector HTTR permanent structure
NBG-25	SGL	Core support candidate	Isostatic fine grain
NBG-10	SGL	Prismatic Fuel element and replaceable reflector Pebble bed reflector structure and insulation blocks	pebble bed modular reactor's (PBMR) original choice for replaceable reflector Price/performance will be the basis between NBG-18 and NBG-10

This year, IG-110 and IG-430, which are isotropic and fine-grained graphite produced by Toyo Tanso, were selected for the experiment. The data of IG-110 was obtained from previous (Oh et al. 2006) and current researches. IG-430 data will be obtained in the next fiscal year. Other candidate materials will be selected and tested next year. General properties of IG-110 and IG-430 are presented in Table 6-2.

Table 6-2. Properties of IG-110 and IG-430 manufactured by Toyo Tanso in Japan.

Material	IG-110	IG-430
Vendor	Toyo Tanso	Toyo Tanso
Bulk Density (g/cm ³)	1.77	1.88
Young's Modulus (GPa)	9.8	10.8
Compressive strength (MPa)	78	90
Tensile strength (MPa)	25	37
Hardness (HSD)	51	55
Thermal Conductivity (W/mK)	120	140

6.2 Graphite Oxidation Model

6.2.1 Kinetics Effect

Kinetics tests were performed in Zone I where the kinetics effect controls the rate of reaction. Variables were experimentally investigated. A schematic of the experimental facility is shown in Figure 6-1. He/O₂ mixture gas was injected into the heated test section. Injected mixture gas is controlled by a mass flow controller. A 15 kW induction heater was installed for graphite heating. Gas passing through the test section was cooled and analyzed using a gas analyzer. Figure 6-2 shows the picture of the experimental facility.

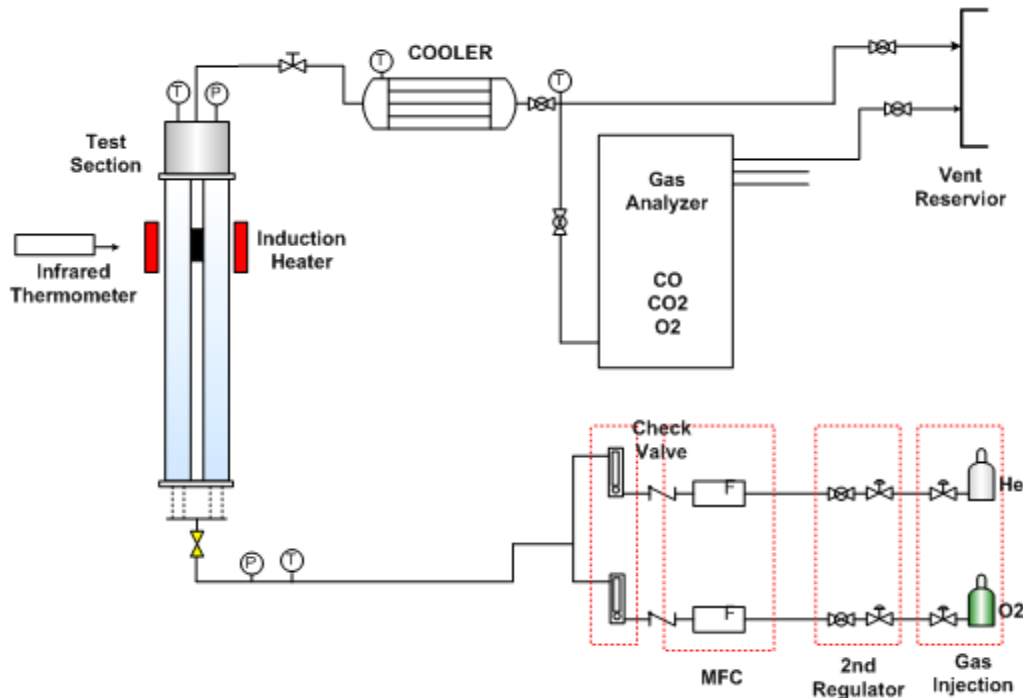


Figure 6-1. Schematic of experimental facility.



Figure 6-2. Experimental facility.

Analysis results are summarized in Table 6-3.

Table 6-3 Activation energy and order of reaction

Material	IG-110
Activation energy (kJ/mol)	218 ± 4
Order of reaction, n	0.75 ± 0.15

6.2.2 Mass Diffusion Effect

Even though the rate of reaction is controlled by chemical parameters at low temperatures, the rate of reaction is limited by a mass diffusion process at high temperatures. The same test loop used in 6.2.1 was also used for heat/mass transfer analogy for predicting the rate of mass diffusion. Five graphite channels with different lengths (3, 5, 7, 9, and 12 cm) were tested. As in the Task 6.2.1, the graphite was heated by the induction heater and controlled by the Infrared (IR) thermometer and controller. Each test was performed at 1070°C, a temperature level high enough to be considered Zone III. The velocity of mixture gas ranges between 0.8 m/seconds and 4.0 m/seconds.

The correlation developed for heat transfer through the laminar boundary layer and averaged through the whole length (Welty et al. 1984) was in good agreement with the experiment data investigated by previous studies. The heat/mass transfer analogy can be applicable for predicting the mass diffusion rate in Zone III.

$$K_m = 0.664 \frac{D_{ij}}{L} \text{Re}_L^{1/2} \text{Sc}^{1/3} \quad (6-1)$$

6.2.3 Combined Effect of Kinetics and Mass Diffusion

The combine effect of kinetics and mass diffusion was investigated using the same test loop. The oxidation rate of IG-11, as shown in Figure 6-3, was saturated at high temperature because mass transfer is a main rate-determining step at high temperature. On the other hand, at low temperature, the trend well follows the general Arrhenius curve.

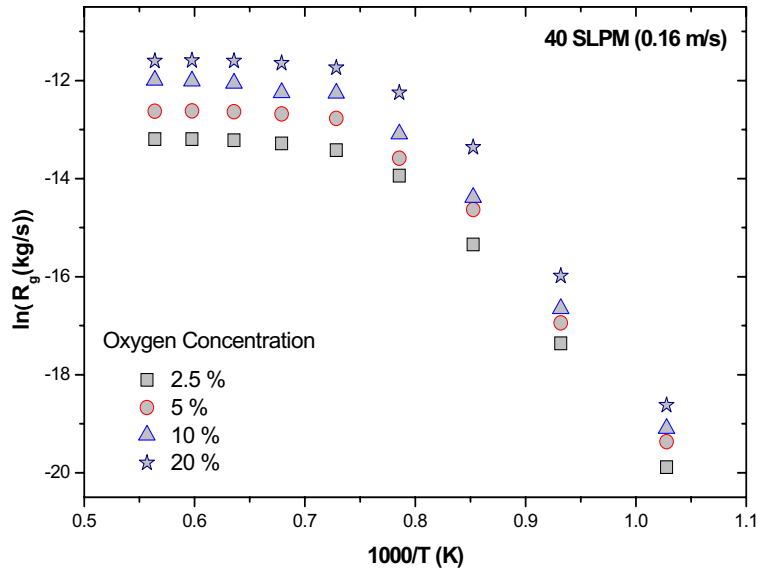


Figure 6-3. Oxidation rate of IG-110 (Oh et al. 2006).

Relative fraction of CO and CO₂ was also obtained. Data of IG-110 are shown in Figure 6-4; an empirical correlation was suggested.

$$f_{CO/CO_2} = 7396 \exp\left(-\frac{69604}{RT}\right) \quad (6-2)$$

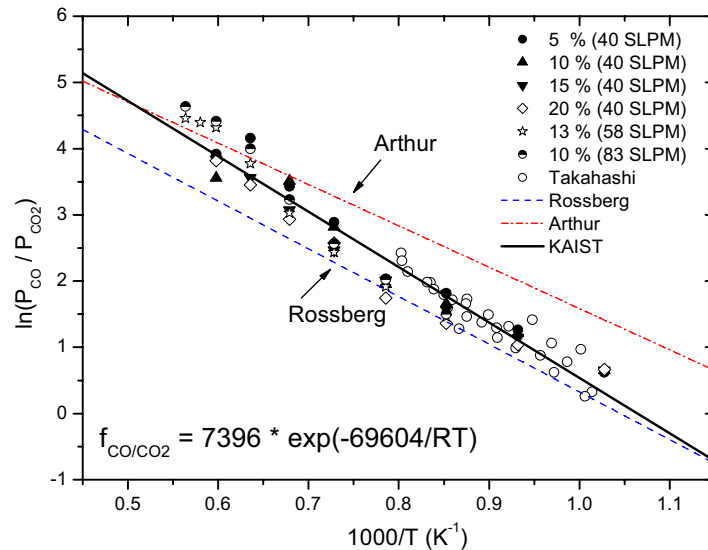


Figure 6-4. CO/CO₂ Ratio for IG-110.

6.2.4 Hybrid Oxidation Model

The following semi-empirical oxidation model was suggested by Oh et al. (2006) in the previous study:

$$\frac{1}{R_g} = \frac{1}{R_{mb}} + \frac{1}{R_{cb}} \quad (6-3)$$

where

$$R_{mb} = K_m \cdot C_{b,O_2} \cdot A \quad (6-4)$$

$$R_{cb} = K_0 \cdot e^{\frac{E_a}{R \cdot T}} \cdot P_{O_2,b}^n \cdot A, \quad n \neq 0 \quad (6-5)$$

Following mass transfer coefficient correlation was used for high reaction condition as

$$k_m^{corrected} = \theta \cdot k_m \quad (6-6)$$

where

$$\theta = \frac{\ln(B_m + 1)}{B_m} \quad (6-7)$$

$$B_m = \frac{X_{O_2,b} - X_{O_2,0}}{X_{O_2,b} - 1} \quad (6-8)$$

To calculate the mass transfer coefficient from Equation (6-5), diffusion coefficient should be decided. The following effective diffusion coefficient, which means an averaged diffusion coefficient for gas mixture, was used:

$$D_{O_2,m} = \frac{(1 - X_1)}{\sum_{i=2}^n (X_i / D_{O_2,i})} \quad (6-9)$$

6.2.5 Burn-off Effect

The rate of reaction between graphite and oxygen is dependent on the degree of burn-off, although it looks constant in a small scale. It is expected that oxidation rate is accelerated by an increase of internal pore size. This burn-off effect is expected to be dominant in Zones I and II. This task will be studied in FY-09.

6.2.6 Effect of Moisture and Boudouard Reaction

Following is the reaction of CO/H₂O/O₂:



When an air-ingress event occurs, moisture can affect graphite oxidation. A water ingress event is also a main consideration in an HTGR design. A schematic of the moisture supply device was shown in Figure 6-5. A task to determine the effect of moisture will be carried out in FY-09.

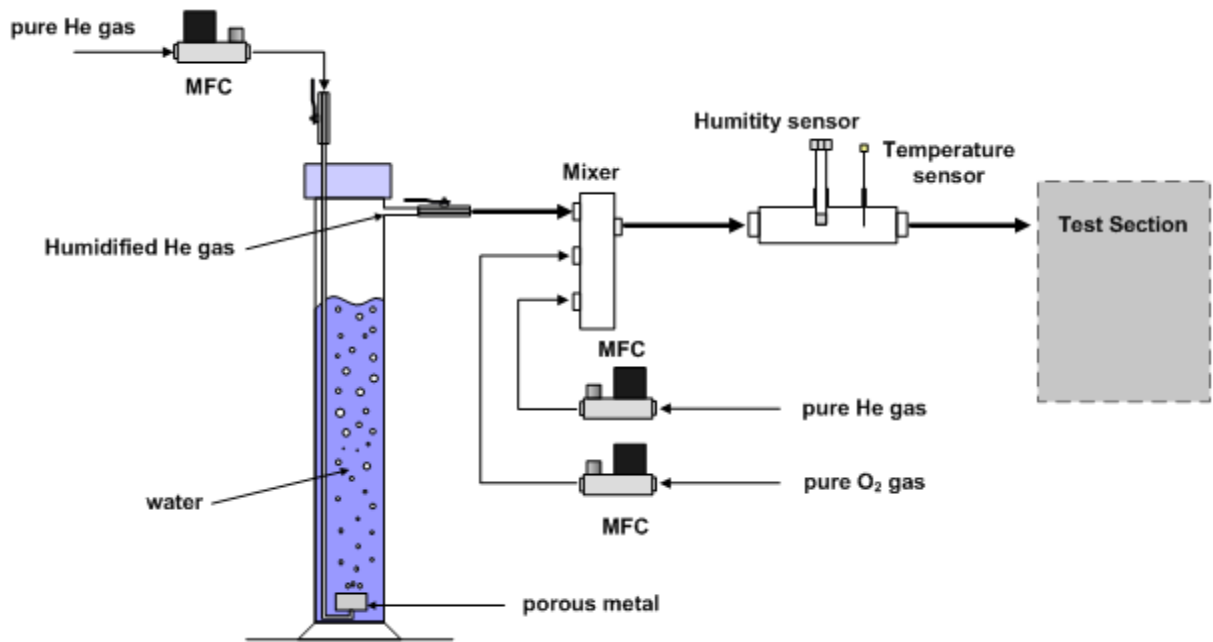


Figure 6-5. Schematic on the moisture supply device (Kim 2005).

The following equation represents the C/CO₂ reaction called the Boudouard reaction:



CO gas, mainly produced, is toxic and explosive. This reaction occurs over 1000°C. The study of this reaction will be carried out in FY-09.

6.3 Nomenclatures for Task 5

K_m	mass transfer coefficient [m/s]
D_{ij}	binary diffusion coefficient of species I and j [m^2/s]
Re	Reynolds number
Sc	Schmidt number
f_{CO/CO_2}	CO/CO ₂ ratio
R	gas constant
T	temperature [K]
R_g	graphite oxidation rate [kg/s]
R_{mb}	asymptotic chemical reaction rate [kg/s]
R_{cb}	asymptotic mass transfer rate [kg/s]
C_{b,O_2}	bulk concentration of oxygen [mol/m ³]
E_a	activation energy [kJ/mol]
θ	internal surface density [m ² /m ³]
$P_{O_2,b}$	pressure of oxygen in bulk flow [Pa]
n	order of reaction
B_m	blowing factor

7. TASK 6: STRUCTURAL TESTS OF OXIDIZED CORE BOTTOM STRUCTURES (KAIST)

The objective of this task is to carry out the structural test of the oxidized graphite in order to develop the fracture model for the oxidized bottom reflector and the lower plenum. The graphite structures of the bottom reflector and lower plenum are oxidized and damaged during an air-ingress event. The reactor core is supported by graphite columns in the bottom reflector and the lower plenum. Schematics of the GT-MHR 600 MWt (GA 2002) and graphite column are shown in Figure 7-1. As shown, the graphite column is relatively long; the slenderness ratio of the cylindrical column part is about 40. The graphite column is encountered first with air when the air ingress event starts. In this case, the failure prediction of oxidized graphite column in the bottom reflector is important for the reactor design and safety analysis of the VHTR because the strength and geometry of the graphite are changed by oxidation.

The oxidation of nuclear graphite is classified into Zone I, Zone II, and Zone III. Zone I is the low temperature range below 600°C, where the nuclear graphite is uniformly oxidized with a bulk density decrease following weight loss. The decrease in bulk density will degrade the strength of the graphite. In Zone III, which generally ranges above 1000°C, the oxidation of the graphite is dominated by mass diffusion limit, and therefore the surface of graphite is mainly corroded resulting in the maximum stress increase of the graphite structure. In Zone II (600 to 1000°C), density decrease and surface corrosion occur at the same time.

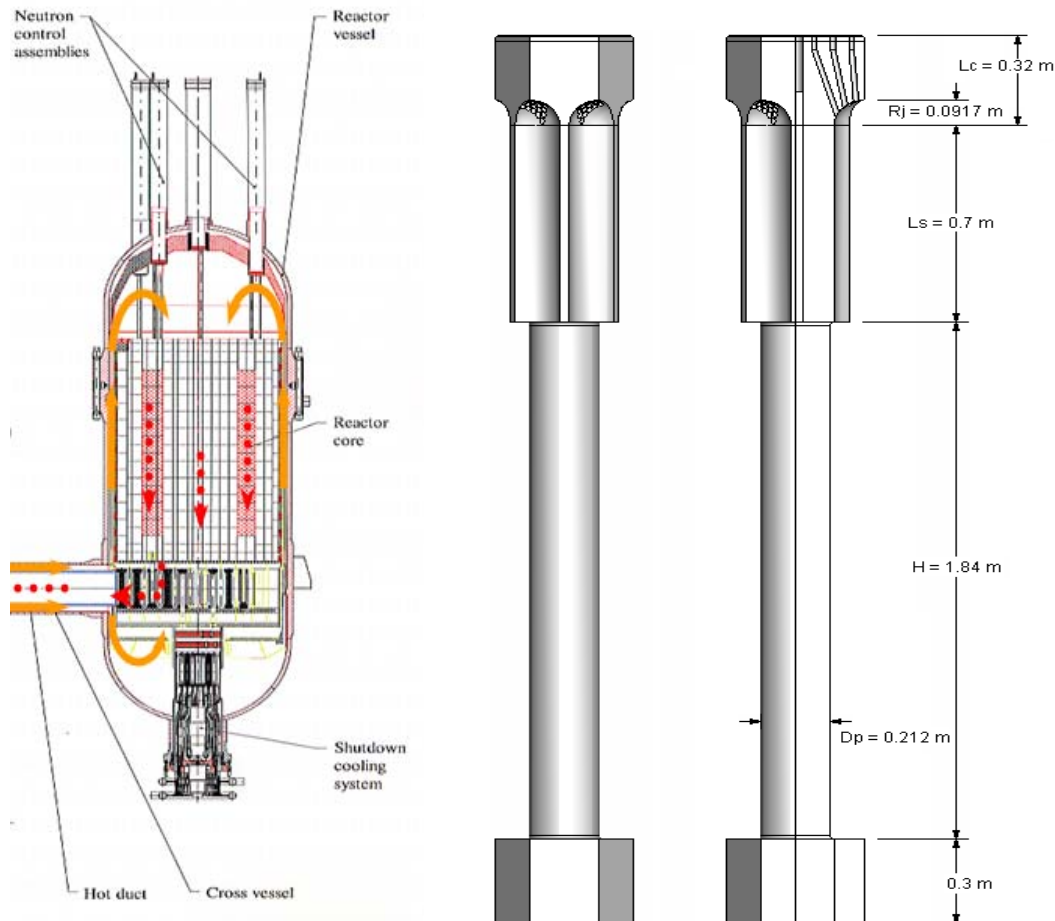


Figure 7-1. Schematics of GT-MHR 600MWt and graphite support column in the lower plenum.

7.1 Failure Mechanism of Graphite Column

Figure 7-2 shows a simplified graphite column and oxidation process where an axial force is loaded on the graphite columns by fuel blocks. A short column under the action of an axial load will fail by direct compression before it buckles, but a long column subjected to high compressive stresses will suddenly fail by buckling before the compression strength is reached. So, a critical load of the short graphite column will be determined by compressive strength and a relatively long critical load will be determined by buckling strength.

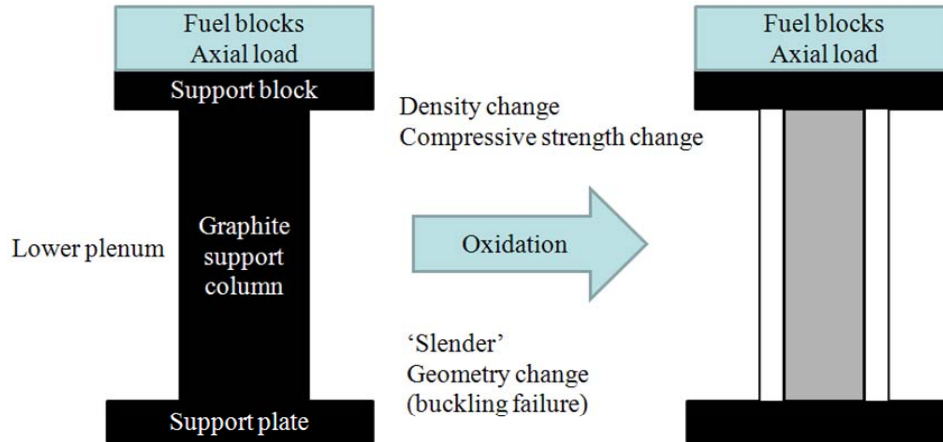


Figure 7-2. Schematics of oxidation in graphite column.

The graphite column becomes slender as oxidation is processed per the following equations.

$$\text{aspect ratio} = \frac{L}{D} \rightarrow \frac{L - 2\delta_L}{D - 2\delta_D} \quad (7-1)$$

Top and bottom surface of graphite column is shielded by support block and support plate. The lateral surface is easy to contact with air.

$$\delta_L \leq \delta_D \quad (7-2)$$

$$L > D \quad (7-3)$$

$$\text{aspect ratio} = \frac{L}{D - 2\delta} \quad (7-4)$$

Therefore, data of compressive strength and the slenderness ratio at which graphite columns fail by buckling are important to predict failure of graphite column.

7.2 Compressive Strength and Buckling without Oxidation

The largest axial force is always loaded on the graphite columns because they are the main component in the core bottom supporter. An INSTRON Model 4204 mechanical testing facility shown in Figure 7-3 was used for this compression test. The maximum loading of this facility was 50 kN. The basic test set-up and procedures were based on ASTM standard C695-91. To perform the test:

1. The specimen was located at the center of the machine between the contact surfaces.
2. An acrylic guard was placed around the specimen.
3. The load was continuously applied to the sample at the constant rate of crosshead movement, and without shock until ultimate failure.
4. Average rupture time is greater than 10 minutes.

Table 7-1 summarizes the test matrix of this experiment. In this study, the test matrix was generated to consider the design variation and maximum burn-off of the graphite support column. Isotropic fine-grained IG-110 was selected as a base material.

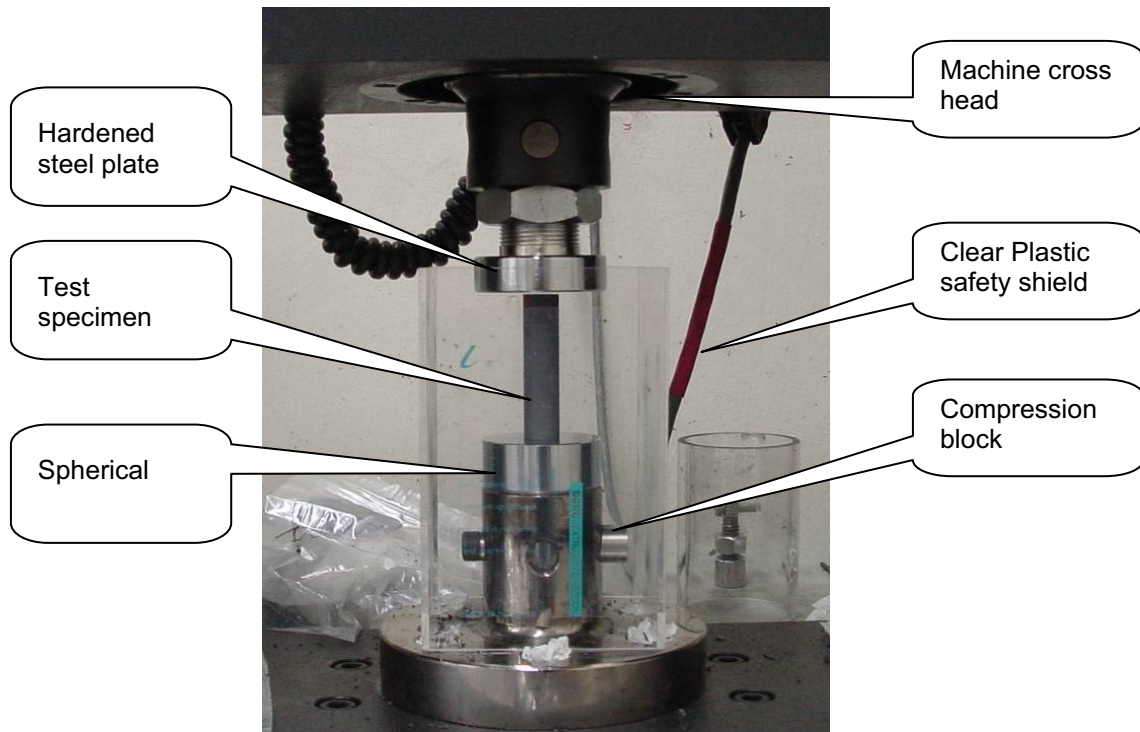


Figure 7-3. Compression test facility, INSTRON Model 4204.

Table 7-1. Test matrix.

Diameter	Length	Slenderness Ratio	Burn-off (%)	Objective	
15	30	8	N/A	To measure compressive strength. ASTM recommend the sample of aspect ratio 1.9–2.1 for compression test.	
25	50	8			
25	50	8		N/A	To estimate a relation between slenderness ratio and strength. Buckling strength data is obtained. It is known that slenderness ratio at which buckling failure started to occur is about 12 at preliminary test.
	75	12			
	80	12.8			
	85	13.6			
	90	14.4			
	95	15.2			
	100	16			
	125	20			
	150	24			
15	200	32		N/A	To confirm applicability of the straight-line formula in different diameter.
	250	40			
	30	8			
15	60	16	0–30%	To measure compressive strength of oxidized graphite.	
15	120	32			
25	50	8			
25	100	16			
25	200	32			
25	50	8			0–30%
15	60	16			
15	120	32			
25	50	8			
25	100	16			
Sample 1	N/A	N/A	N/A	Graphite samples of complicated-shapes closer to the real situation were tested to find the effect of discontinuity in geometry.	
Sample 2					
Sample 3					
Sample 1	N/A	N/A	0–30%	Oxidized graphite samples of complicated-shapes were tested to find the applicable range of Knudsen relation.	
Sample 2					
Sample 3					
15	30	30	1–30%	Wet sample were tested for validation of the bulk density measurement method.	

Samples were machined to have cylindrical shapes with $\Phi 15 \times 30$ mm and $\Phi 25 \times 50$ mm, which are expected to be failed by compressive strength. Five specimens were tested for each sample.

Table 7-2. Compressive strength of IG-110.

	IG-110
$\Phi 15$ mm \times 30 mm	80.16 ± 1.97 MPa
$\Phi 25$ mm \times 50 mm	78.75 ± 2.48 MPa
Average	79.46 MPa

The average compressive strength of IG-110 was measured to be 79.46 MPa. A short column under the action of an axial load will fail by direct compression before it buckles, but a long column subjected to high compressive stresses will suddenly fail by buckling.

The analysis of the critical load for long columns was previously developed by Leonhard Euler (Ferdinand, 1980). The Euler formula for the fixed-fixed column is simply expressed by

$$P_{cr} = \frac{4\pi^2 EI}{L^2} \quad (7-1)$$

The ratio L/r is called the slenderness ratio of the column. A column can be classified as long and short column with the slenderness ratio.

However, there are limitations of Euler's formula, because this formula is not valid for a small slenderness ratio. For a small slenderness, the following empirical formula was proposed by T. H. Johnson (Ferdinand, 1980).

$$\sigma_{cr, buckling} = \sigma_{straight-line} - C \frac{L}{r} \quad (7-2)$$

In this study, the buckling experiment was performed to find the slenderness ratio at which the buckling failure occurs. Finally, this experiment was planned to obtain the graphite column strength as a function of slenderness ratio. Specimens for the test were machined to cylindrical shapes; the detailed specifications are listed in Table 7-3.

Table 7-3. Specimens for the buckling test.

Diameter (mm)	Length (mm)	Slenderness Ratio
25	50	8
25	75	12
25	80	12.8
25	85	13.6
25	90	14.4
25	95	15.2
25	100	16
25	125	20
25	150	24
25	200	28
25	250	32

Figure 7-4 shows the measured bucking strength versus slenderness ratio. It also shows that the critical strength of the graphite columns is reduced with an increase of the slenderness ratio. Based on the data in Figure 7-4, the constant parameters in Equation (7-2) were estimated. The calculated constants of Equation (7-2) for IG-110 graphite are as follows:

$$\sigma_{straight-line} = 91.31 \text{ MPa} \quad (7-3)$$

$$C = 1.01 \quad (7-4)$$

Compressive strength of IG-110 was 79.46 MPa. It was assumed that the intersection of the straight line and compressive strength was the slenderness ratio at which buckling failure started to occur. This is shown as

$$\sigma = 79.46 = 91.34 - 1.01 \frac{L}{r} \tag{7-5}$$

$$\frac{L}{r} = 11.76$$

The range of slenderness ratio in the experiment was 8 to 40. Therefore, the applicable slenderness ratio range of the empirical formula is 11.76–40 for a cylindrical graphite column.

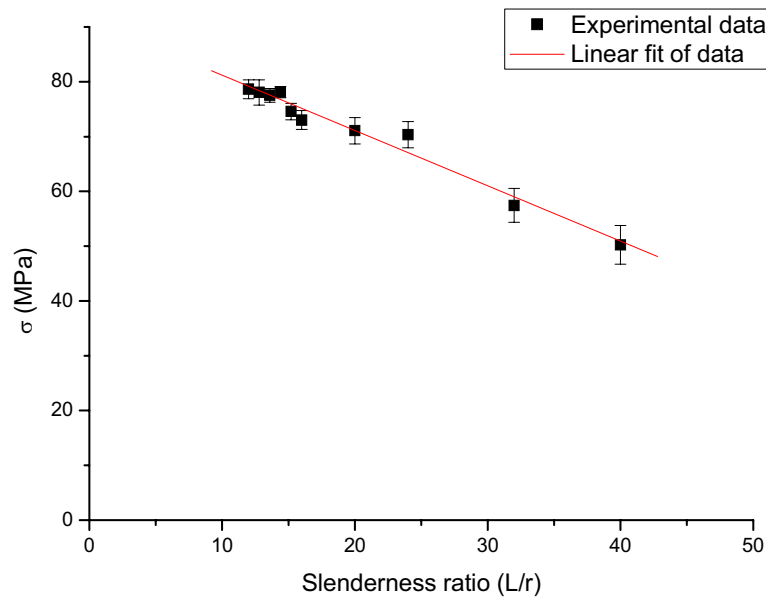


Figure 7-4. Buckling strength.

An additional experiment was performed to confirm the proposed applicable range of the slenderness ratio described above. The specimens used in the additional tests are listed in Table 7-4.

Table 7-4. Specimens for additional buckling test.

Diameter (mm)	Length (mm)	Slenderness Ratio
15	60	16
15	120	32

Figure 7-5 shows the measured buckling strength vs. slenderness ratio for the additional tests. This figure shows good agreement between the experimental data and the line obtained from previous buckling tests (Figure 7-4). From this result, the strength of a graphite column can be determined by the slenderness ratio. Graphite columns having the same slenderness ratio have the same strength but different diameters. The slenderness ratio can therefore be a scaling parameter for a cylindrical graphite column in strength.

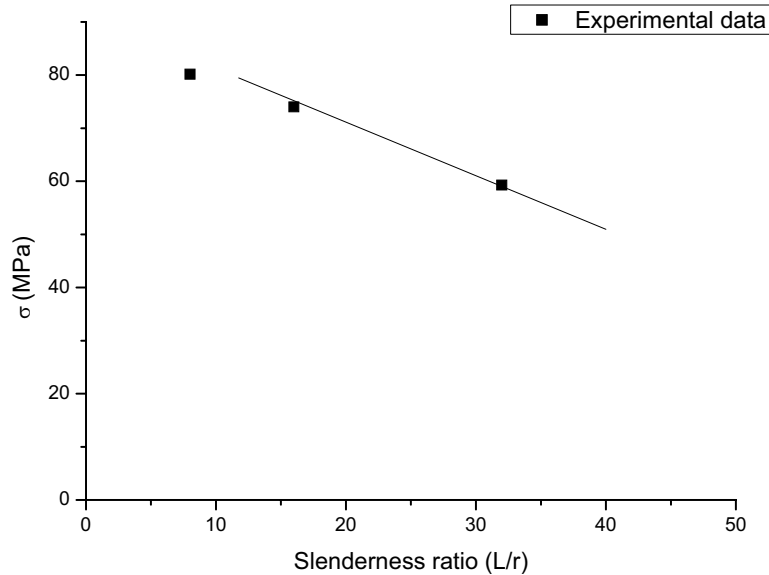


Figure 7-5. Buckling strength of $\Phi 15$ mm columns.

7.3 Estimation of Burn-off of Graphite Support Columns by GAMMA

When an air-ingress accident in gas-cooled reactors was considered, it was common to postulate the pipe to be the 1-D component. According to INL's density-difference induced stratified flow analysis in the hot leg, it is hard to say that the 1-D is a proper approach for the air-ingress situation. Therefore, this calculation uses the GAMMA code to compare results with and without density-difference induced stratified flow. A 1-D hot leg inlet pipe was first assumed as usual, then another case having a 2-D (5×5) hot leg inlet pipe with 2-D reactor cavity connection was set. The GAMMA code calculation was performed to estimate the extent of oxidation of the graphite support column in the lower plenum during the air-ingress accident following the guillotine breaks of the hot and cold pipes.

7.3.1 GAMMA Air Ingress 1-D and 2-D Pipe Comparison

The results with and without density-difference induced stratified flow were used for the comparison using the GAMMA code nodalization as shown in Figure 7-6. Input data were based on GT-MHR 600 MWt. Originally, the bottom reflector was expressed in 9×3 of 2-D wall blocks submerged into 1-D fluid block. 1-D hot leg inlet FB165 was assigned.

For the 2-D calculation, hot leg inlet 1-D fluid block FB165 was replaced with 2-D fluid block 5×5 . To simulate the gravitational effect on 2-D inlet, the 2-D pipe was directly connected to the 2-D cavity at the same elevation as shown by the red lines in Figure 7-7.

The operating temperature of the reactor was 900°C . In early time, the pebble temperature is decreased and the 2-D case temperature is lower than the 1-D case because much more cold air flows into the reactor by density-difference induced stratified flow. But after a couple of 10-second intervals of graphite oxidation in the reactor, the 2-D case temperature catches up to the 1-D core temperatures.

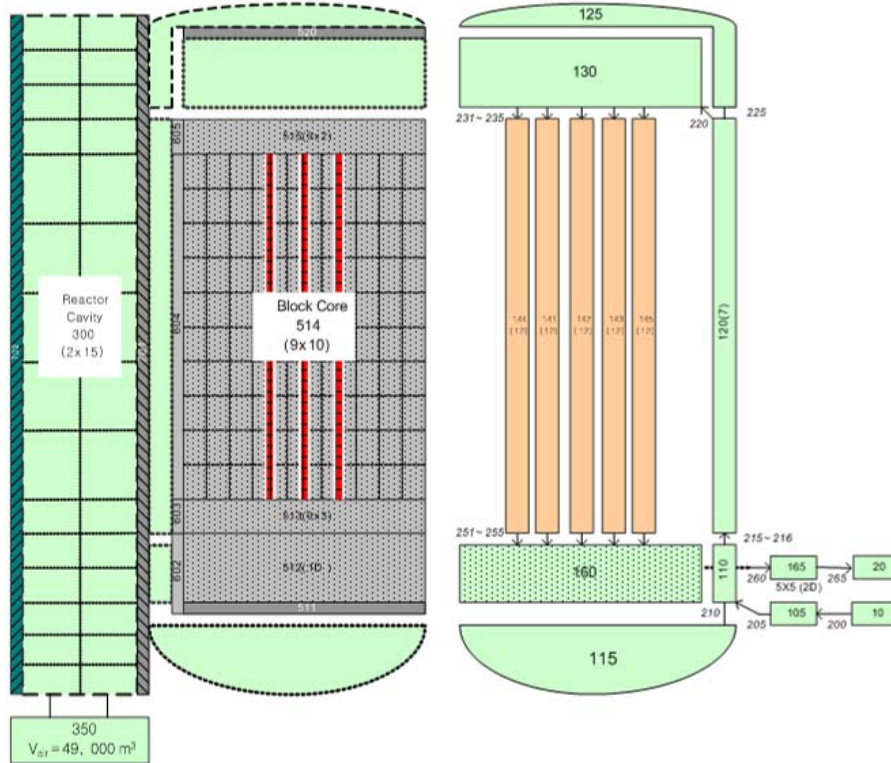


Figure 7-6. GT-MHR 600MWt 1-D pipe nodalization.

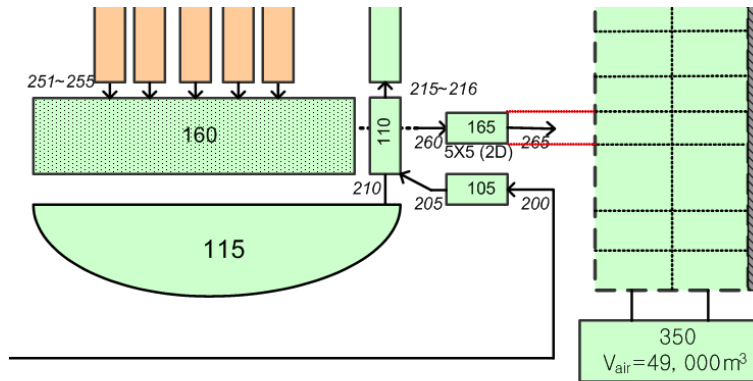


Figure 7-7. GT-MHR 600MWt 2-D pipe nodalization.

The temperature range was placed in Zones II and III. Both geometry and bulk density of oxidized graphite is degraded in Zone II. Corroded graphite volume by graphite oxidation is shown in Figure 7-8. In the 2-D calculation, the graphite corrosion starts right after the pipe break accident because of density driven stratified flow while in 1-D case, the reaction has not yet occurred. It physically shows a very similar accident process to that predicted by the multistep approach described in the Section 2.3. However, a 2-D calculation was performed for a 2.5 hr simulation time, and therefore, for quantitative comparisons with the multistep approach, more calculation results are needed for much longer simulation time. The detail 2-D calculations for the air-ingress accident will be performed in FY-09 and FY-10.

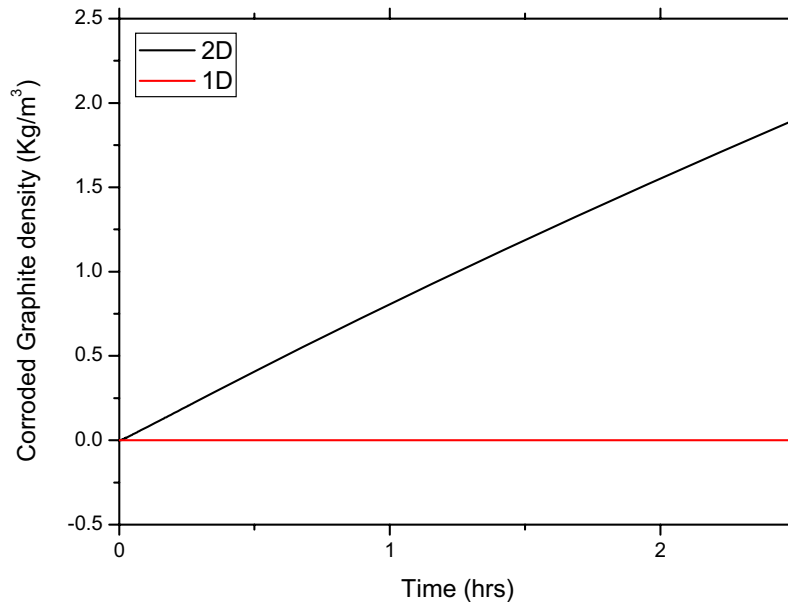


Figure 7-8. Corroded graphite density of bottom reflector after air-ingress occurred.

Both strength of graphite material and geometry of graphite structure are degraded in Zone II. A structural test should be performed in both the uniform and nonuniform oxidation conditions.

7.3.2 GAMMA Air ingress 1-D Pipe with Pulse Signal

Even though the 2-D approach is physically right, its exceedingly long computation time is a big concern. For example, Intel® Core™ 2 Duo CPU E8400 @ 3.00 GHz with 2GB RAM can march only 0.3 simulation hours per day, while 1-D can move forward at least 200 simulation hours. In the diffusion process, inflow of cavity air is weak until pressure balance is broken. Because of lean air mass fraction in the reactor, graphite oxidation is limited. Therefore, the air ingress phenomenon will occur after the long-term diffusion process.

Pressure balance is a critical condition of the diffusion process. By applying additional small pressure pulses to normal pressure at the hot leg entrance, the pressure balance is periodically disturbed, creating a much increased mass flow rate as the 2-D pipe case and rapid natural circulation phase.

At junction 265 in Figure 7-9, the additional pulse signal (0.004 bar) was applied every second during the first 4–1,000 seconds. By this small disturbance on that junction, the mass flow rate of the 1-D pipe is increased up to that of the 2-D case (see Figure 7-9 red line).

The negative mass flow rate in Figure 7-10 means that air flows into reactor from the cavity. Comparing the mass flow rate from the 1-D static analysis, in which diffusion process is dominant during the initial several days, the green line obtained by the 1-D pulse analysis shows that it is definitely in a natural circulation phase.

Based on these results, time can be saved in evaluating accelerated graphite oxidation, which is induced by stratified flow, by applying proper pulse signals to a simple 1-D fluid block, instead of the time consuming 2-D fluid block.

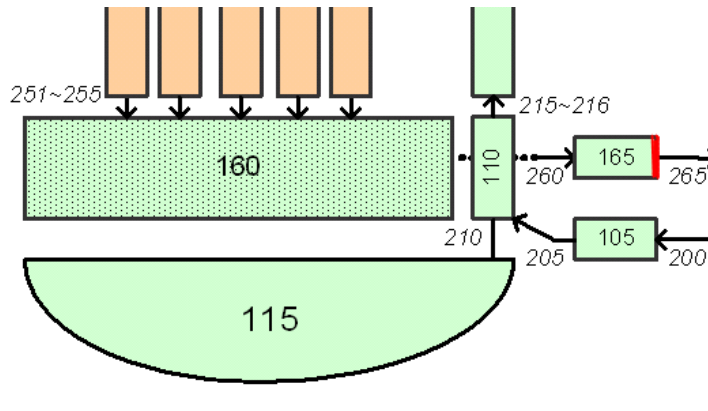


Figure 7-9. Pulse signal applied junction (JB265).

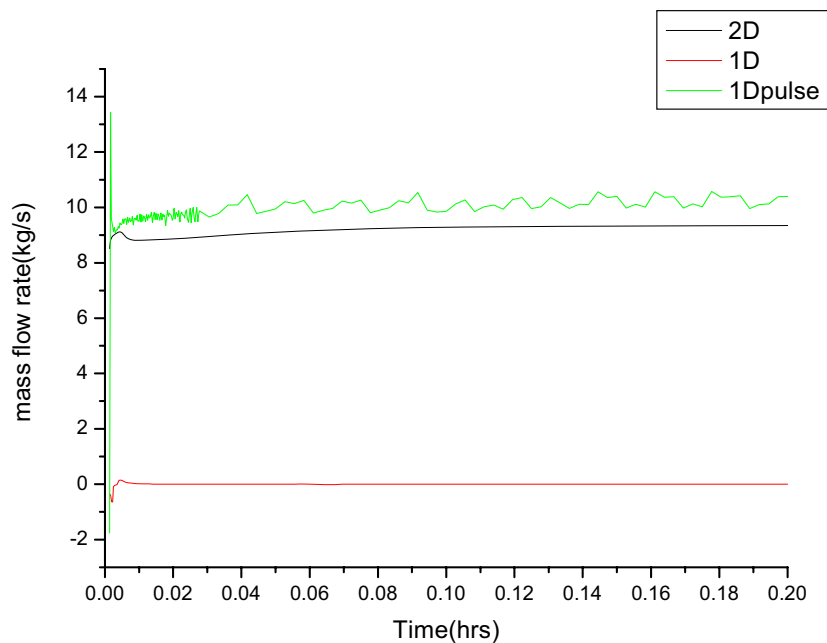


Figure 7-10. Pulse induced mass flow rate at hot leg inlet (JB265).

7.4 Compressive Strength and Bucking Strength with Graphite Oxidation

Oxygen diffused into the graphite internal pores reacts with internal graphite in Zone I. The internal pore size of the graphite then increases as a result of uniform oxidation. The geometrical change of the graphite is expected to be very small in Zone I. It was assumed that mechanical properties of graphite were degraded by oxidation. Samples consisted of cylindrical specimens of $\Phi 25 \times 50$ mm. Oxidation was carried out with the facility with an electrical furnace as shown in Figures 7-11 and 7-12. Filtered air was uniformly supplied into bottom of the furnace and gas was naturally vented out through the top of the furnace. Internal temperature of the furnace was maintained as 600°C.



Figure 7-11. Test facility with an electrical furnace.

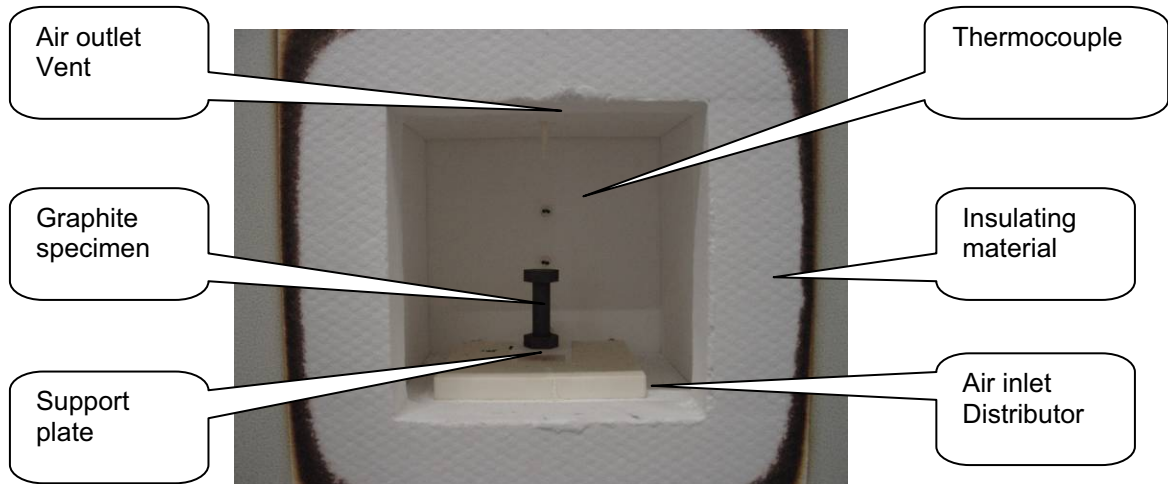


Figure 7-12. Inside of the electrical furnace.

The changes in compressive strength as a function of bulk density are shown in Figure 7-13. The geometry of the oxidized sample did not change. The decreased percent in bulk density is the same decreased percent in weight loss. The relation between the compressive strength and bulk density can be estimated by the Knudsen relation (Neighbour, 2001) as

$$\frac{\sigma}{\sigma_0} = \exp(-kd)$$

$$k = 0.11481$$
(7-6)

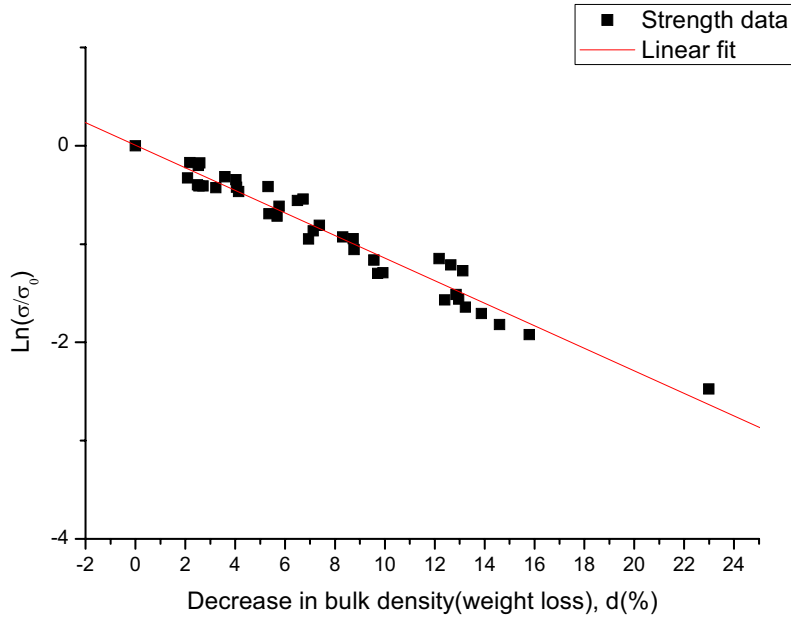


Figure 7-13. Changes in compressive strength as a function of bulk density.

Several shapes of oxidized graphite column samples were tested to find the effect of oxidation on buckling strength. Their geometry and the number of specimens are listed in Table 7-5.

Table 7-5. Geometry and number of graphite columns.

Diameter	Length	Slenderness Ratio	Number of Specimens
15	60	16	18
15	120	32	15
25	50	8	20
25	100	16	10
25	200	32	2

A remarkable trend was not shown in Figure 7-14. The buckling strength of the oxidized graphite column was decreased as the compressive strength was decreased. The relation between buckling strength and the bulk density is shown in Figure 7-15. The nondimensional strength of the oxidized graphite column under axial load was described using the following Knudsen relation (Neighbour, 2001):

$$\frac{\sigma}{\sigma_0} = \exp(-kd) \tag{7-7}$$

$$k = 0.111$$

Exponents of Equation (7-6) and (7-7) were almost the same; buckling strength degradation of oxidized graphite column is independent of the slenderness ratio.

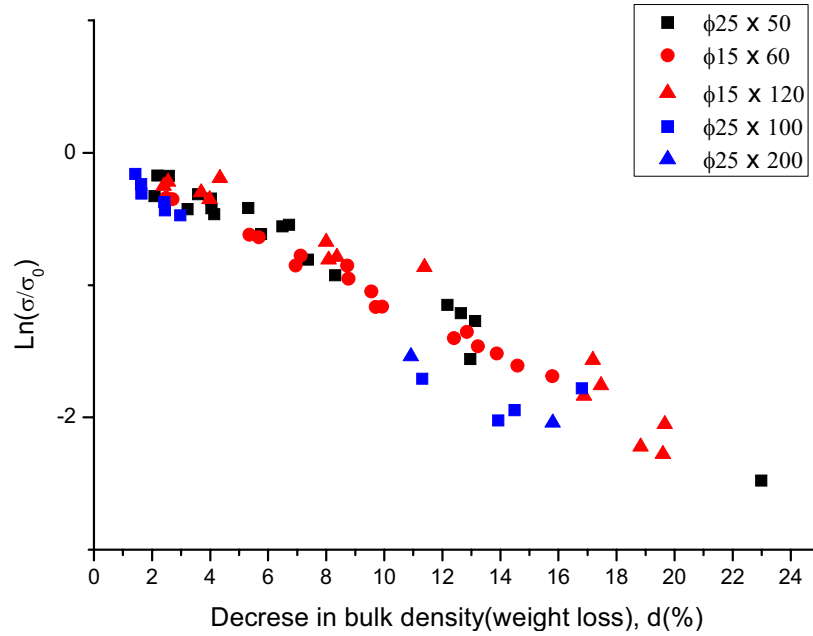


Figure 7-14. Normalized buckling strength of oxidized graphite columns.

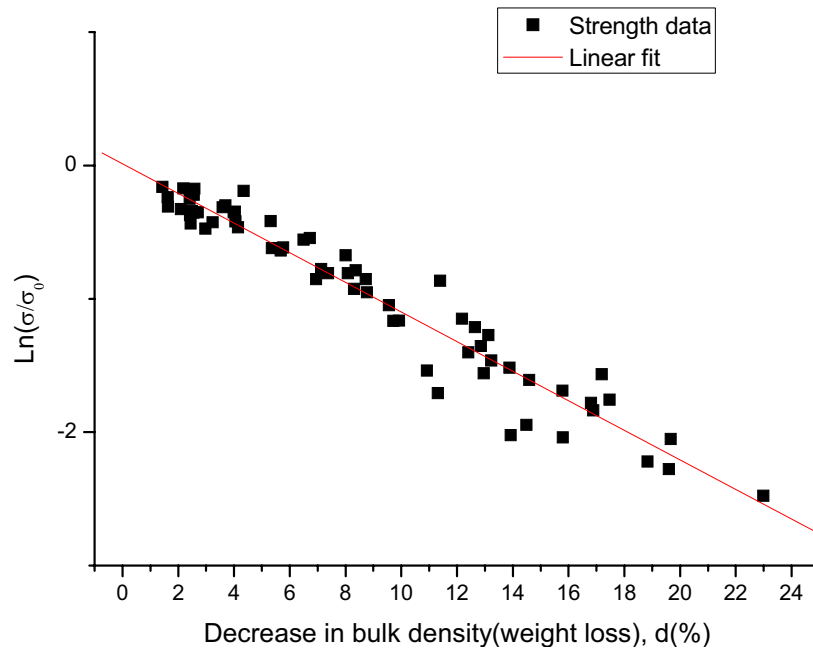





Figure 7-15. Normalized strength of oxidized graphite column.

Graphite samples of complicated-shapes closer to the real situation were tested to find the applicable range of Equation (7-7). Shape, geometry, and fracture load were listed in Table 7-6. As a result, the maximum load degradation of oxidized graphite structure and the strength degradation of oxidized graphite had the same relation. The line shown in Figure 7-16 came from Equation (7-7). It turns out that the strength degradation trend of an oxidized graphite structure is independent of geometry while the strength degradation of a uniformly oxidized graphite structure is dependent on the initial strength of structure and the bulk density change.

Table 7-6. Graphite samples of complicated-shapes.

Sample 1	Sample 2	Sample 3
		
Geometry (Unit: mm)		
Top: $\Phi 10 \times 10$ Bottom: $\Phi 20 \times 10$	Top: $\Phi 10 \times 20$ Bottom: $\Phi 20 \times 20$	Cylindrical column: $\Phi 15 \times 60$ Cap: 15.1×10 (7 in depth)
Average fracture load (Unit: Kgf)		
590.1	531.3	1297.3

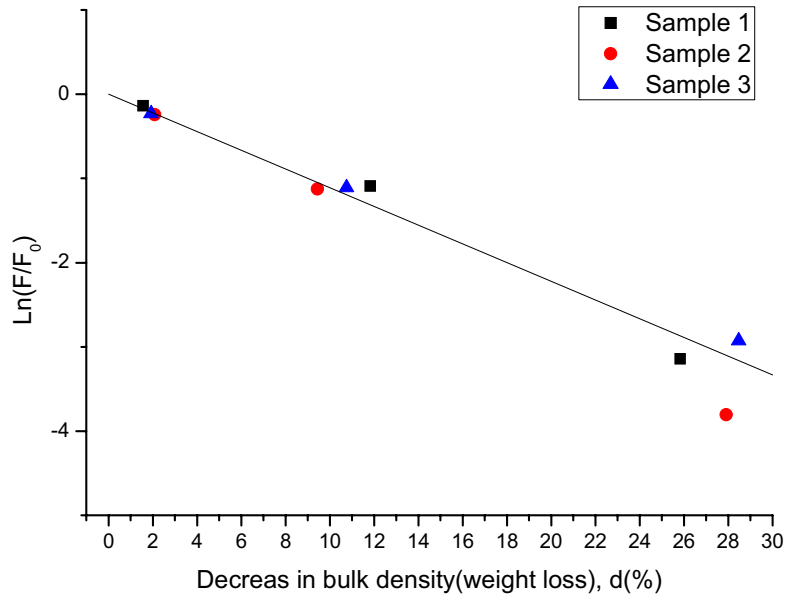


Figure 7-16. Fracture load changes of oxidized samples.

7.5 Measurement Technique

Both geometry and bulk density of oxidized graphite is degraded in Zone II. The geometry and density measurement is important to predict the strength of the graphite structure. True density of graphite is not changed by the oxidation reaction, but bulk density is changed by increasing internal pore size. The strength of oxidized graphite is determined by bulk density. Bulk density of uniformly oxidized graphite is easily obtained by weight loss, but the bulk density of graphite that is oxidized at Zones II and III is hard to measure. Still, there is another method for measuring the bulk density of oxidized graphite; bulk density of fresh graphite is easily measured with the gravimeter. Water is absorbed into oxidized graphite when the density is measured with the gravimeter. Thus, the bulk density of an oxidized graphite sample can be obtained using the equations

$$W_g = \rho_{water} g (V_g - V_{pore}) + W_{g,sink} \quad (7-8)$$

$$V_g - V_{pore} = \frac{W_g - W_{g,sink}}{\rho_{water} g} \quad (7-9)$$

$$V_{pore} = \frac{W_{g,wet} - W_g}{\rho_{water} g} \quad (7-10)$$

$$V_g = \frac{W_{g,wet} - W_{g,sink}}{\rho_{water} g} \quad (7-11)$$

$$\rho_{g,bulk} = \rho_{water} \frac{W_g}{W_{g,wet} - W_{g,sink}} \quad (7-12)$$

If the gravimeter shows the buoyancy force, then the equations can be changed to

$$\rho_{g,bulk} = \rho_{water} \frac{W_g}{W_{g,wet} - W_g + W_{buoyancy}} \quad (7-13)$$

Experimental tests were carried out to know the effect of water absorption in oxidized graphite using the experimental facility as shown in the above equations. If the wetted sample has a strength change, this measurement method cannot be used. Graphite specimens of $\Phi 15 \times 30$ were oxidized in the electric furnace. Oxidized graphite samples were fully wetted in a water beaker and then dried at room temperature for 24 hrs. The strength of the samples is shown in Figure 7-18. The line shown in Figure 7-17 came from Equation (7-7). The degradation of a wet sample was not found.

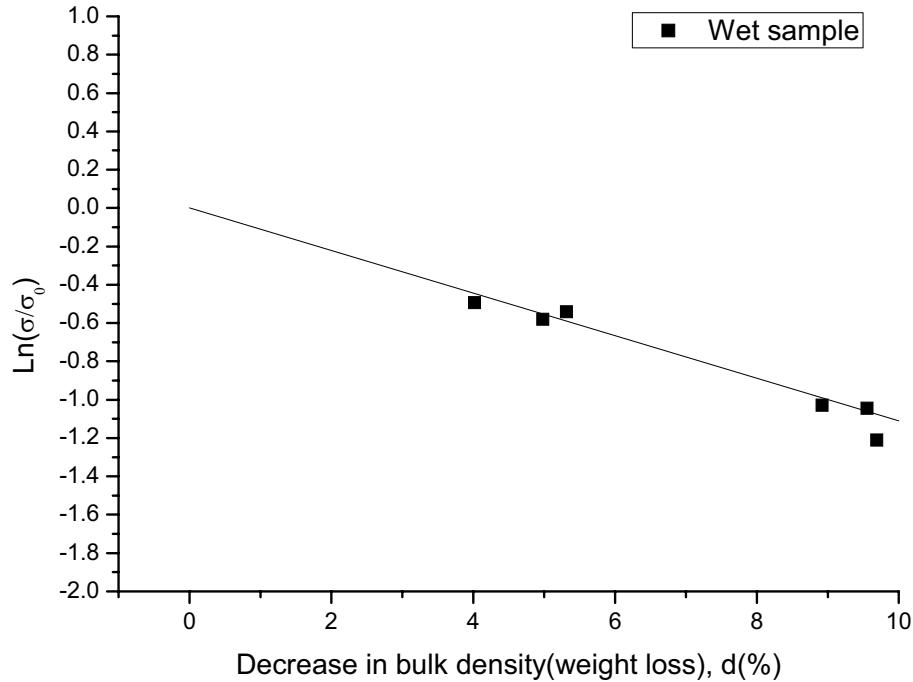


Figure 7-17. Strength changes of wet samples.

An experiment was performed to confirm validity of this method. The results of the experiment are shown in Table 7-7.

Table 7-7. Comparison of bulk density.

#	M0 (g)	M (g)	Weight loss (%)	ρ_{water} (g/cm ³)	ρ_{mass} (g/cm ³)	Error (%)
1	9.51	8.43	11.36	1.61	1.58	1.78
2	9.53	8.53	10.49	1.62	1.60	1.41
3	9.49	9.12	3.89	1.72	1.72	0.03
4	9.46	9.04	4.44	1.70	1.71	0.47
5	9.46	9.04	4.44	1.15	1.71	0.28
6	9.41	9.24	1.81	1.75	1.76	0.62
7	9.47	9.29	1.90	1.77	1.76	0.77
8	9.43	9.25	1.90	1.68	1.76	4.04
9	9.51	9.19	3.36	1.74	1.73	1.00
10	9.53	9.32	2.20	1.77	1.75	1.21

ρ_{water} is obtained by this method and ρ_{mass} is obtained with weight loss by assuming that the geometry of oxidized graphite was not changed. From this result, the difference between ρ_{water} and ρ_{mass} is small. Therefore, this measurement technique is available for measuring bulk density and will be used in analyzing nonuniform oxidation.

7.6 Summary

The failure prediction of the oxidized graphite column in the core bottom structures is an important consideration in the VHTR design. The simplified graphite column has two main failure mechanisms: the short graphite column critical load will be determined by compressive strength while the relatively long critical load will be determined by buckling strength. The critical strength of the graphite columns was reduced with an increase in the slenderness ratio. The slenderness ratio at which buckling started to occur was about 11.76. The strength of a graphite column is determined by the slenderness ratio. A graphite column with the same slenderness ratio has the same strength, even though it may have a different diameter. The slenderness ratio can therefore be used as a scaling parameter for a simple cylindrical graphite column in strength.

The GAMMA code calculation was performed to know the trend and condition of oxidation in the bottom reflector. The critical strength of graphite that is uniformly oxidized can be expressed by the Knudsen relation. It turns out that the strength degradation trend of oxidized graphite structure is independent of geometry, while the strength degradation of a uniformly oxidized graphite structure is dependent on the initial strength of the structure and the bulk density change.

The bulk density measurement method using the gravimeter is available for oxidized graphite. This method will be used to analyze graphite that is not uniformly oxidized at Zones II and III.

7.7 Nomenclature for Task 6

L	length [m]
D	diameter [m]
δ	oxidized length [m]
S	surface [m ²]
P	load [kg m/sec ²]
EI	constant flexural rigidity
$\sigma_{cr, buckling}$	buckling strength [MPa]
$\sigma_{straight-line}$	a constant for straight line formula [MPa]
r	radius of gyration
C	a constant for straight line formula
σ	strength of oxidized graphite Structure [MPa]
σ_0	compressive strength of fresh graphite
k	constant for Knudsen relation
W	weight [Kgf]
W _g	weight of fresh graphite
W _{g,sink}	weight of oxidized graphite in water
W _{g,wet}	weight of wet oxidized graphite
V	volume [m ³]
V _g	volume of fresh graphite

V_{pore}	volume of internal pore
g	gravitational constant [m^2/s]
ρ	density [g/cm^3]
$\rho_{\text{g,bulk}}$	bulk density of oxidized graphite

8. TASK 7: COUPLING NEUTRONIC-THERMAL HYDRAULIC TOOLS (KAIST)

8.1 Coupling Procedure

***** This Task is not within the scope of this fiscal year. *****

When a neutronics code is used to analyze a reactor core, it is necessary to reflect thermal effect for accurate calculation. For this coupling calculation, it is proposed to couple the GAMMA and COREDAX codes into the GAMMA/COREDAX code. In the coupled system, even though a neutronics code has its own thermal calculation module, it is advisable that a thermal hydraulic system code take all thermal-hydraulic calculations and a neutronics code charge only for neutronics calculations. Both GAMMA and COREDAX codes are programmed in C language. Plans are to make the COREDAX code a power distribution calculation engine in the GAMMA/COREDAX system code. In this task, several coupling variables are defined: map calculation nodes between the GAMMA and COREDAX codes and calculated procedures in the coupling system.

8.1.1 Coupling Variables

The thermal variables that determine thermal feedback effect are fuel temperature, coolant temperature, and coolant density. These variables should be provided by a T/H code to the neutronics code. The neutronics code calculates power distribution after reflecting thermal effect and transmits the results to the T/H code.

These coupling variables were developed as a data structure for a node and transmitted to each other. The variables are described in Table 8-1.

Table 8-1. Coupling variables.

Variables	Variables Name	Unit	Code in Charge
Coolant density	dm	g/cc	T/H
Coolant temperature	tm	K	T/H
Fuel temperature	tf	K	T/H
Graphite matrix temperature	tgm	K	T/H
Total power	qtot	W	Neutronics
Relative power density	qrel	-	Neutronics

8.1.2 Calculation Node Mapping Method

Generally, T/H nodes are larger than those of neutronics. These calculation nodes had to be mapped to transmit coupled variables. This mapping system can be done automatically in the code or, to reduce the calculation time, it can be provided by input file. Figure 8-1 shows a case in mapping nodes between T/H and neutronics codes.

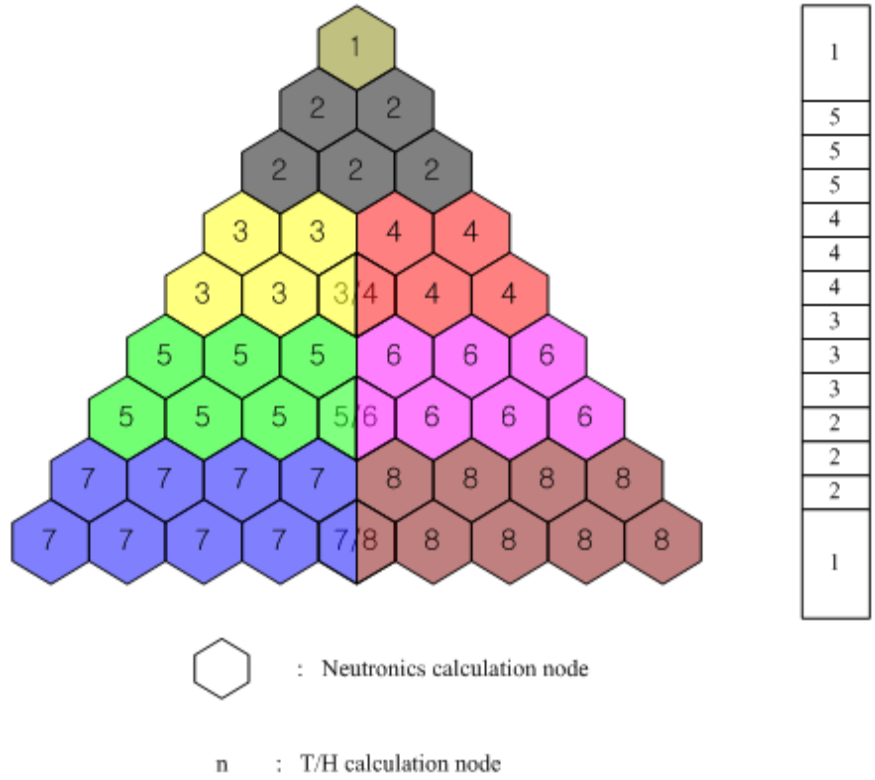


Figure 8-1. Example of calculation node mapping.

8.1.3 Calculation Procedure in a Coupling System

Generally, a steady state calculation is completed before taking a transient calculation. When transmitting coupled variables, a proper calculation state needs to be determined to the neutronics code. The neutronics code has four different calculation modes: initialization mode, steady state mode, transient mode, and output mode. The calculation scheme in Figure 8-2 shows the neutronics part in an envisioned coupled code system.

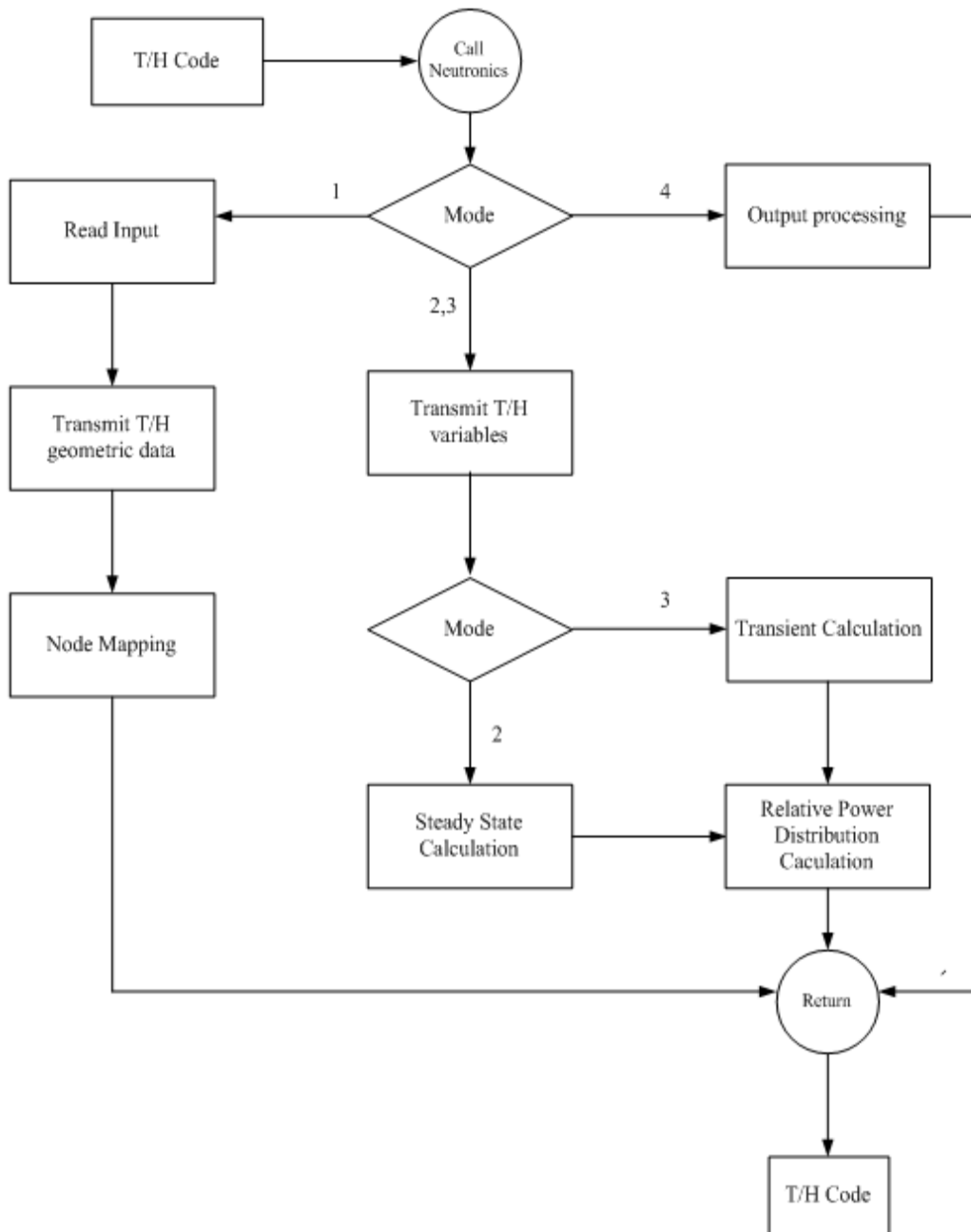


Figure 8-2. Calculation procedure in neutronics code.

9. TASK 8: CORE NEUTRONIC MODEL (KAIST)

There is growing interest in making high fidelity nodal codes available in hexagonal-z geometry for use in VVER, SMART, and VHTR core analysis. The COREDAX code is a hexagonal-z 3-D diffusion nodal code based on the AFEN method. It consists of several unique features: (1) implementation of the AFEN method that employs no transverse integration and that represents the solution in terms of analytic solution bases, (2) inclusion of transverse gradient basis functions, (3) use of interface flux moments, (4) implementation of the coarse group rebalance (CGR) acceleration scheme, and (5) kinetics calculation capability based on the solution decomposition.

This report presents the research of the AFEN method in hexagonal-z geometry, multigroup formulation, and CGR acceleration scheme. The COREDAX code is verified through tests of the VVER-440, a simplified VVER-1000, and the SNR-300 benchmark problems.

9.1 Basic Theory and Method

9.1.1 Nodal Unknowns and Nodal Equations

To describe the AFEN method, begin from the following 3-D hexagonal-z geometry multigroup diffusion equation:

$$-[D]\nabla^2\vec{\phi}+[A]\vec{\phi}=\frac{\vec{\chi}}{k_{eff}}\vec{F}^T\vec{\phi} \quad (9-11)$$

where

[D] = diffusion coefficient matrix

[A] = removal and scattering cross section matrix

\vec{F} = fission production cross section vector

$\vec{\chi}$ = fission spectrum vector

k_{eff} = multiplication factor

$\vec{\phi}$ = neutron flux.

Following the AFEN methodology, express the solution of the diffusion equation for nod n in the following form:

$$\vec{\phi}^n(x, y, z) = \vec{\phi}_1^n(x, y, z) + \vec{\phi}_2^n(x, y, z) + \vec{\phi}_3^n(x, y, z) + \vec{\phi}_4^n(x, y, z), \quad (9-2)$$

where

$$\begin{aligned} \vec{\phi}_l^n(x, y, z) = & \sinh(\sqrt{\Lambda^n} x_l) \vec{a}_{1l}^n + \cosh(\sqrt{\Lambda^n} x_l) \vec{a}_{2l}^n \\ & + y_l \sinh(\sqrt{\Lambda^n} x_l) \vec{b}_{1l}^n + y_l \cosh(\sqrt{\Lambda^n} x_l) \vec{b}_{2l}^n \\ & + z \sinh(\sqrt{\Lambda^n} x_l) \vec{c}_{1l}^n + z \cosh(\sqrt{\Lambda^n} x_l) \vec{c}_{2l}^n, \quad l = 1, 2, 3, \end{aligned} \quad (9-2a)$$

$$\vec{\phi}_4^n(x, y, z) = \sinh(\sqrt{\Lambda^n} z) \vec{d}_{10}^n + \cosh(\sqrt{\Lambda^n} z) \vec{d}_{20}^n, \quad (9-2b)$$

and

$$[\Lambda^n] = [D^n]^{-1} \left([A] - \frac{\vec{\chi}}{k_{eff}} \vec{F}^T \right)^n. \quad (9-3)$$

The coordinates x_1 , x_2 , and x_3 are defined in Figure 9-1. Note that each of the 20 terms in Equation (9-2) is an analytic solution of Equation (9-1). In particular, Equation (9-2) includes terms of transverse gradient basis functions. Evaluation of the matrix functions is facilitated by spectral decomposition in functional theory of linear operators.

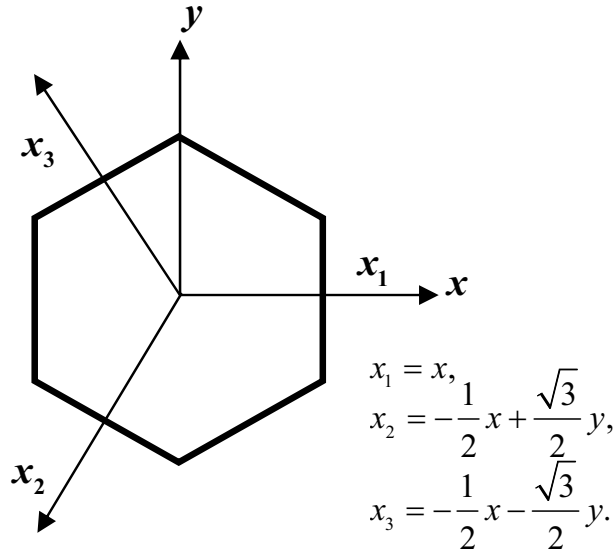


Figure 9-1. Coordinates in a hexagon.

The coefficients in Equation (9-2) flux expansion are expressed in terms of nodal unknowns, such as the node average flux, the node-interface fluxes, and the node-interface flux moments. In particular, 12 node-interface flux moments (y- and z-weighted average fluxes \times 6 radial interfaces) were included as nodal unknowns in this research. The six radial interfaces are shown in Figure 9-2 and all the nodal unknowns are defined as follows:

- one average flux

$$\phi_{g_{avg}} = \frac{2}{3\sqrt{3}h_r^2 h_z} \left(\int_{\frac{h_z}{2}}^{\frac{h_z}{2}} \left(\int_{\frac{\sqrt{3}h_r}{2}}^{\frac{h_r+h_r}{2}} \int_{\frac{h_r-h_r}{2}}^{\frac{h_r+h_r}{2}} \phi_g(x, y, z) dy dx + \int_0^{\frac{\sqrt{3}h_r}{2}} \int_{\frac{h_r-h_r}{2}}^{\frac{h_r+h_r}{2}} \phi_g(x, y, z) dy dx \right) dz, \quad (9-4)$$

- two axial interface fluxes of the form

$$\phi_{g_{z1}} = \frac{2}{3\sqrt{3}h_r^2} \left(\int_{\frac{\sqrt{3}h_r}{2}}^{\frac{h_r+h_r}{2}} \int_{\frac{h_r-h_r}{2}}^{\frac{h_r+h_r}{2}} \phi_g(x, y, \frac{h_z}{2}) dy dx + \int_0^{\frac{\sqrt{3}h_r}{2}} \int_{\frac{h_r-h_r}{2}}^{\frac{h_r+h_r}{2}} \phi_g(x, y, \frac{h_z}{2}) dy dx \right), \quad (9-5)$$

- six radial interface fluxes of the form

$$\phi_{g1} = \frac{1}{h_r h_z} \int_{-\frac{h_r}{2}}^{\frac{h_r}{2}} \int_{-\frac{h_z}{2}}^{\frac{h_z}{2}} \phi_g \left(\frac{\sqrt{3}}{2}, y, z \right) dz dy, \quad (9-6)$$

- six y-momented radial interface fluxes of the form

$$\phi_{g1}^y = \frac{1}{h_r h_z} \int_{-\frac{h_r}{2}}^{\frac{h_r}{2}} \int_{-\frac{h_z}{2}}^{\frac{h_z}{2}} y \phi_g \left(\frac{\sqrt{3}}{2}, y, z \right) dz dy, \quad (9-7)$$

- six z-momented radial interface fluxes of the form

$$\phi_{g1}^z = \frac{1}{h_r h_z} \int_{-\frac{h_r}{2}}^{\frac{h_r}{2}} \int_{-\frac{h_z}{2}}^{\frac{h_z}{2}} z \phi_g \left(\frac{\sqrt{3}}{2}, y, z \right) dz dy. \quad (9-8)$$

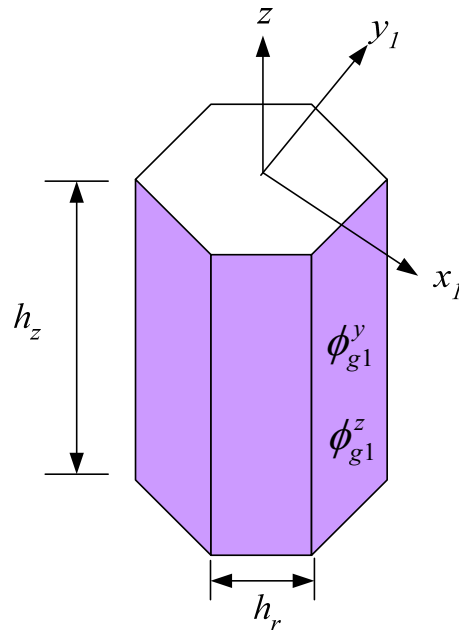


Figure 9-2. Interface flux moments on six radial interfaces.

In determining these nodal unknowns, as many solvable nodal equations were built as the number of these nodal unknowns. The solution procedure of nodal equations is usually a conventional one that involves two levels of iterative schemes: inner iteration and outer iteration.

The nodal equation for each node is composed of a nodal balance equation and associated coupling equations. The coupling equations consist of interface current continuity equations and interface current moment continuity equations. The nodal equations are interface current moment continuity equations. expressed as:

- One node balance equation of the form

$$\frac{1}{V} \int_V \nabla \cdot \vec{J}(r) dV + [A] \vec{\phi}_{avg} = \frac{\vec{\chi}}{k_{eff}} \vec{F}^T \vec{\phi}_{avg}, \quad (9-9)$$

- Eight interface current continuity equations of the form

$$\vec{J}_{(x,y,z)}\left(\frac{\sqrt{3}}{2}h_r\right) = \vec{J}_{(x',y',z')}\left(-\frac{\sqrt{3}}{2}h_r\right), \quad (9-10)$$

- Twelve interface current moment continuity equations of the form

$$\vec{J}_{(x,y,z)}^y\left(\frac{\sqrt{3}}{2}h_r\right) = \vec{J}_{(x',y',z')}^y\left(-\frac{\sqrt{3}}{2}h_r\right). \quad (9-11)$$

9.1.2 Multigroup Extension

The eigenvalues of the matrix in Equation (9-3) are always real in two-group problems. But in multigroup problems, the eigenvalues (and thus eigenvectors) can be complex. The AFEN method was extended to multigroup formulation using a transformation matrix defined by real and imaginary parts of a complex eigenvector. Thus, this transformation method requires the knowledge of the eigenvectors in addition to the eigenvalues. The method for multigroup problems in this research is based on the use of the spectral decomposition property in the matrix function theory. This method only requires the knowledge of the eigenvalues (the eigenvectors are not required), facilitating the computation involved in the nodal equations. The matrix function theory is applied to the matrix functional evaluations of

$$f(A), \quad (9-12)$$

where f is an analytic function and A is a matrix.

The matrix functions arising in the AFEN method for multigroup (G groups) problems belong to the following class of functions (see Eqs. (9-2a) and (9-2b): trigonometric, hyperbolic, or exponential functions of matrices of dimension $G \times G$.

According to the spectral decomposition property of the matrix functional theory,

$$f(A) = \sum_{i=0}^{G-1} b_i A^i, \quad (9-13)$$

where the decomposition coefficients b_i can be obtained from the following polynomial interpolation:

$$p(\lambda_k) = f(\lambda_k), \quad k = 0, 1, \dots, G-1, \quad (9-14)$$

where λ_k 's are the eigenvalues of A (with complex conjugates allowed) and

$$p(\lambda) = \sum_{i=0}^{G-1} b_i \lambda^i. \quad (9-15)$$

Therefore, the matrix functions can be easily evaluated if the eigenvalues of matrix A are known.

9.1.3 Coarse Group Rebalance Acceleration

To apply CGR acceleration, the net current variables in Equations (9-9) to (9-11) above are reformulated in terms of partial currents as

$$\vec{J}_s = \vec{J}_s^{outgoing} - \vec{J}_s^{incoming}, \quad \vec{\phi}_s = 2(\vec{J}_s^{outgoing} + \vec{J}_s^{incoming}), \quad \text{and} \quad (9-16)$$

$$\vec{J}_s^{outgoing} = \frac{\vec{\phi}_s}{4} + \frac{\vec{J}_s}{2}, \quad \vec{J}_s^{incoming} = \frac{\vec{\phi}_s}{4} - \frac{\vec{J}_s}{2}, \quad (9-17)$$

where s is surface index.

Then, Equation (9-9) can be rewritten after group summation (e.g., for the two group case) as

$$\begin{aligned} & \frac{S_{xy}}{V} \sum_{d=1,6} \sum_{g=1,2} J_{0d,g}^{outgoing} + \frac{S_z}{V} \sum_{d=7,8} \sum_{g=1,2} J_{0d,g}^{outgoing} + \sum_{g=1,2} \Sigma_{ag} \phi_{av,0,g} \\ & - \frac{S_{xy}}{V} \sum_{d=1,6} \sum_{g=1,2} J_{0d,g}^{incoming} - \frac{S_z}{V} \sum_{d=7,8} \sum_{g=1,2} J_{0d,g}^{incoming} \\ & = \frac{1}{k_{eff}} \sum_{g=1,2} \nu \Sigma_{fg} \phi_{av,0,g}. \end{aligned} \quad (9-18)$$

Let us define a rebalance factor per node as follows:

$$\phi_{av,d,g}^{new} = f_d \phi_{av,d,g}^{old}, \quad d = 0, g = 1, 2, \quad (9-19a)$$

$$J_{0d,g}^{outgoing,new} = f_d J_{0d,g}^{outgoing,old}, \quad d = 1, 2, \dots, 8, g = 1, 2, \quad (9-19b)$$

$$J_{0d,g}^{incoming,new} = f_d J_{0d,g}^{incoming,old}, \quad d = 1, 2, \dots, 8, g = 1, 2. \quad (9-19c)$$

The rebalance factors are depicted in Figure 9-3.

Substituting Equation (9-19) in Equation (9-18) leads to

$$R_0 f_0 - \frac{S_{xy}}{V} \sum_{d=1,6} \sum_{g=1,2} J_{0d,g}^{incoming} f_d - \frac{S_z}{V} \sum_{d=7,8} \sum_{g=1,2} J_{0d,g}^{incoming} f_d = \frac{P_0}{k_{eff}} f_0, \quad (9-20)$$

where

$$R_0 = \frac{S_{xy}}{V} \sum_{d=1,6} \sum_{g=1,2} J_{0d,g}^{outgoing} + \frac{S_z}{V} \sum_{d=7,8} \sum_{g=1,2} J_{0d,g}^{outgoing} + \sum_{g=1,2} \Sigma_{ag} \phi_{av,0,g}, \quad (9-21)$$

$$P_0 = \sum_{g=1,2} \nu \Sigma_{fg} \phi_{av,0,g}. \quad (9-22)$$

Equation (9-20) is the CGR acceleration equation with eigenvalue k_{eff} and eigenvector \vec{f} composed of rebalance factors as shown in Figure 9-3.

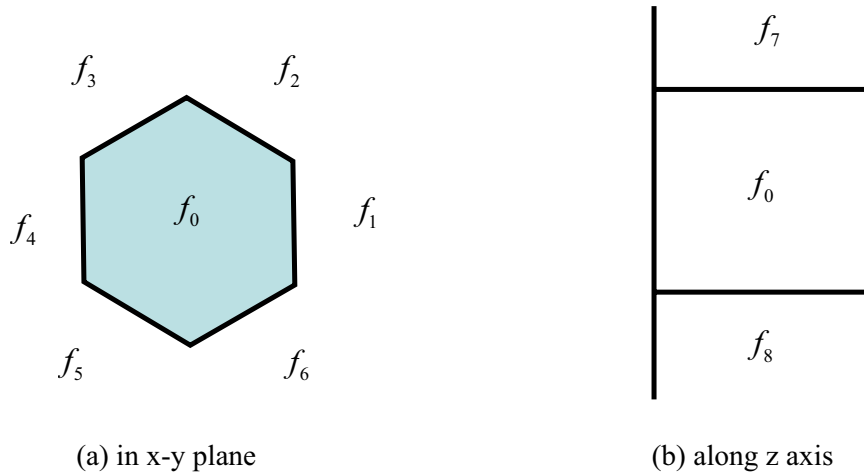


Figure 9-3. Rebalance factors.

9.2 Verification of the COREDAX Code

To verify the improved AFEN method implemented in COREDAX, the 3-D version of the VVER-440 benchmark problem (a simplified VVER-1000 benchmark problem) and the SNR-300 benchmark problem were solved.

9.2.1 VVER-440 Benchmark Problem

The VVER-440 benchmark problem is a hexagonal-z 3-D two-group VVER-400 core. It has 1/12 reflective symmetry geometry and the outer boundary conditions are vacuum. Table 9-1 shows the results compared with those of the PARCS code, the COREDAX code, and the reference solution and Figure 9-4 shows the core configuration. The COREDAX code provides very accurate nodal solutions.

Table 9-1. Results of VVER-440 benchmark problem^a.

# of Planes	PARCS (keff % error)	COREDAX (keff % error)
	(Node power maximum% error)	(Node power maximum% error)
12	1.010297 (-0.101)	1.01126696 (-0.0052)
	(21.71)	(1.28)
24	1.010918 (-0.040)	1.01125753 (-0.0062)
60	1.010866 (-0.045)	1.01125544 (-0.0063)

a. Reference solution $keff = 1.01132$ from DIF3-D-FD runs extrapolation

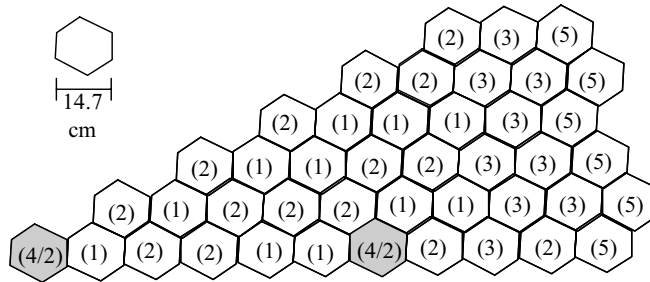
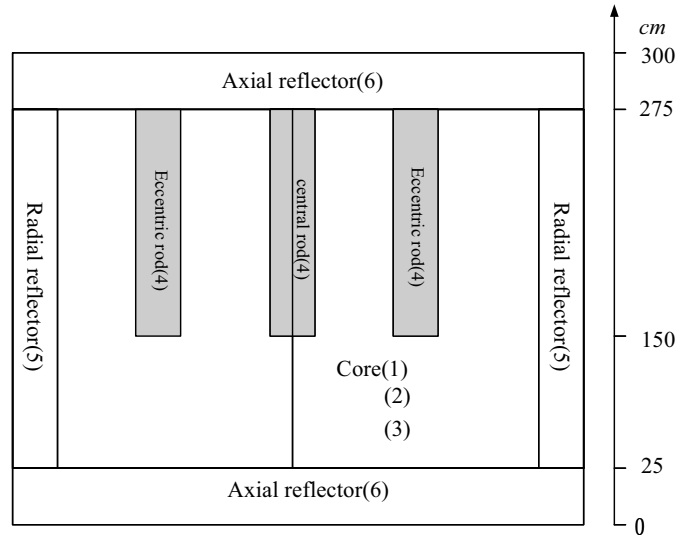


Figure 9-4. Core configuration of 3-D VVER-440.

The VVER-440 benchmark problem was also used to test CGR acceleration by testing for 12 and 60 axial nodes. Table 9-2 shows the results. CGR provides very high, speeded-up, and accurate results.

Table 9-2. Results on CGR acceleration of VVER-440 benchmark problem^a.

Number of Axial Nodes	Number of Iterations	Computing Time ^b (sec)	K _{eff} (% error)
12	3857	144	1.01096708(0.0349)
	58	3	1.01096706 (0.0349)
60	6599	1130	1.01096260(0.0353)
	37	14	1.01096266(0.0353)

a. Reference solution $k_{eff} = 1.01132$ from DIF3-D-FD runs extrapolation
b. Pentium IV 3.0 GHz, 2 G RAM

9.2.2 A Simplified VVER-1000 Benchmark Problem

The data of the original VVER-1000 benchmark problem (every fuel assembly has differing cross sections) is too big to fit in the VENTURE code for the referenced solution. Therefore, a simplified core data structure maintaining the same geometry was constructed. The material data numbers were just changed from 283 to 7, such that the core contains five radially different nodes and 12 axial planes with

two reflectors and 10 fuel planes. There was no change in axial node components. The core has 1/6 reflective symmetry and the outer boundary conditions are zero flux. The side length of each assembly is 13.6 cm. The geometrical configuration of the core is shown in Figures 9-5 and 9-6. The core temperature is 552.15°C and coolant density is 767.1 kg/m³. Table 9-3 shows the results of k_{eff} compared with the VENTURE reference. The reference was obtained by the VENTURE code using 384 triangles \times 20 axial meshes per hexagonal prism node. Two sets of results are compared: one using zero flux boundary condition and the other using incoming zero current boundary condition. Both results show that COREDAX gives very accurate solutions because the axial calculational modeling (via interface flux moments) uses an enlarged set of analytic functions to provide more accurate axial dependence.

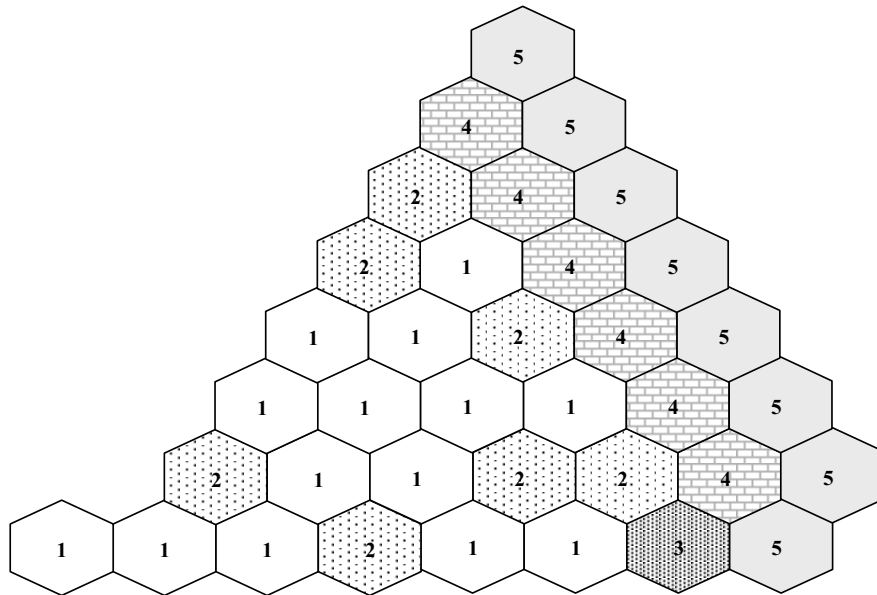


Figure 9-5. Radial core geometry of simplified 3-D VVER-100.

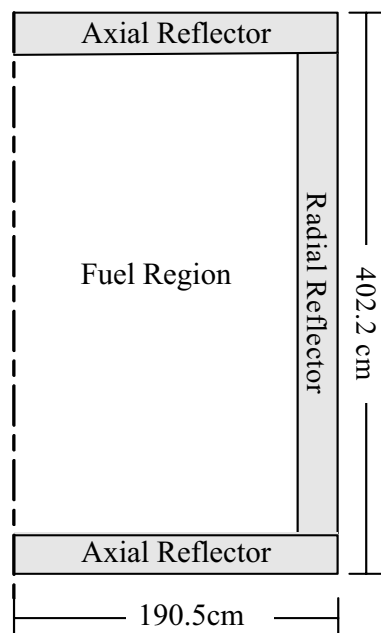


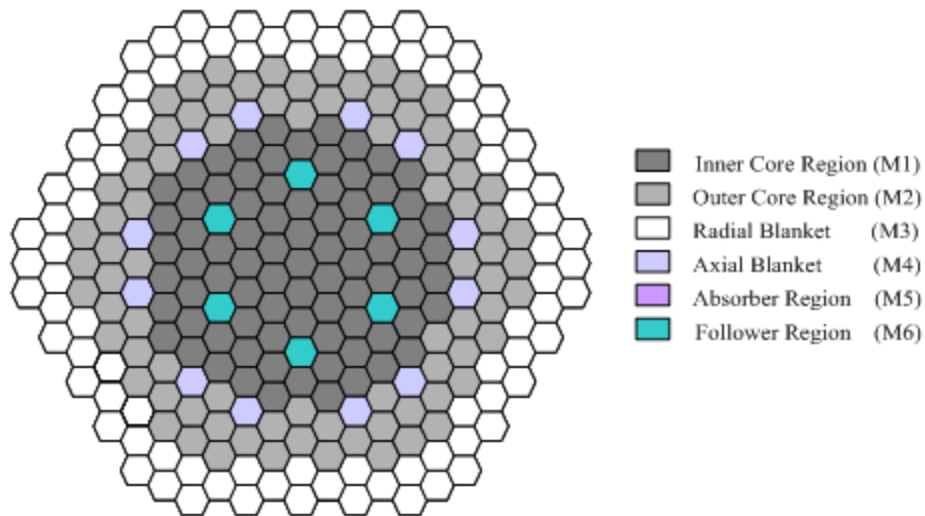
Figure 9-6. Axial core geometry of 3-D VVER-1000.

Table 9-3. Results on k_{eff} of simplified VVER-1000 benchmark problem.

Boundary Conditions	VENTURE (ref.) (384 × 20 per node)	COREDAX (% error)
Flux zero B.C.	1.0000503	1.0000055 (-0.0045)
Incoming current zero B.C.	1.0000534	1.0000476 (-0.0006)

9.2.3 SNR-400 Benchmark Problem

SNR-300 was solved to test the multigroup extension in the COREDAX code. SNR-300 is a four-group problem modeling a small liquid-metal fast breeder reactor core. The geometry of the 3-D core is shown in Figures 9-7 and 9-8. The core has 1/6 reflective symmetry and the outer boundary condition is vacuum. The results are shown in Table 9-4. The reference solution was obtained with DIF-D-FD.



Sidlength of each subassembly
corresponds to 6.4665 cm

Figure 9-7. Radial core geometry of 3-D SNR-300.

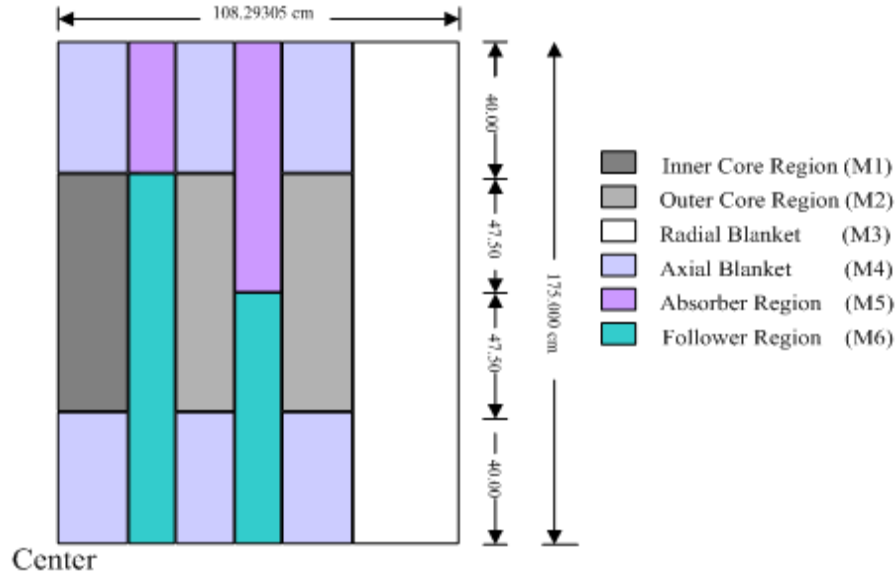


Figure 9-8. Axial core geometry of 3-D SNR-300.

Table 9-4. Results of SNR-300 benchmark problem.

Code	Number of Axial Nodes	Keff (% error)
Reference (DIF3-D-FD)	Richardson extrapolation	1.00989
DIF3-D Nodal	8	1.01151 (0.160)
	18	1.01125 (0.135)
COREDAX (Transformation matrix)	8	1.01376 (0.383)
	16	1.01134 (0.185)
COREDAX (Matrix function theory)	8	1.01006 (0.017)
	16	1.01001(0.012)

9.3 Test on GT-MHR Core Model

9.3.1 Description

A neutronics calculation of a simple GT-MHR core model was performed in preparation to verify and validate the coupled code. The GT-MHR is one of the most significant HTGR gas turbine plant designs currently under investigation in various places and is being developed on an international basis to optimize the HTGR capabilities and resources of many countries.

The GT-MHR reactor core (Figure 9-9) represents an annular stack of hexahedral prismatic fuel assemblies (FAs) 36 cm across flat sizes (Figures 9-10 and 9-11) that form 102 columns 800 cm high consisting of 10 FAs stacked axially in each column. The FA columns are arranged with 0.25 cm gaps to ensure performance of FA reloads during the reactor core life.

The active core is enclosed by graphite reflectors and surrounded by radial reflectors contiguous with internal reflectors as shown in Figure 9-9. The upper and lower axial reflectors are located over and under the core, respectively. The upper axial reflector consists of stacks of columns 130 cm high assembled from hexahedral prismatic graphite blocks located above the core and separated by a gap of 0.25 cm.

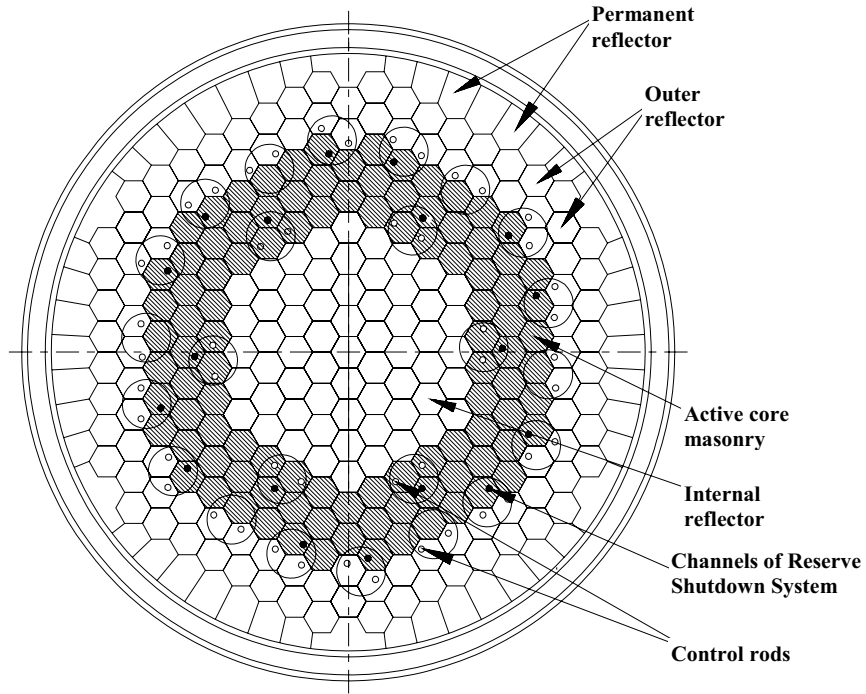


Figure 9-9. Active core and its component arrangement.

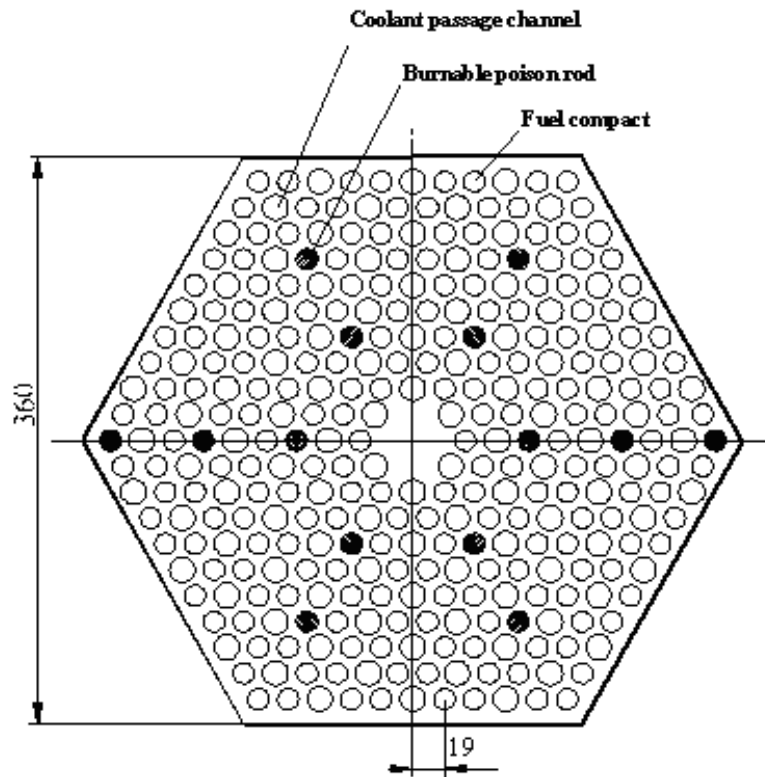


Figure 9-10. Fuel block cell (type 1FA).

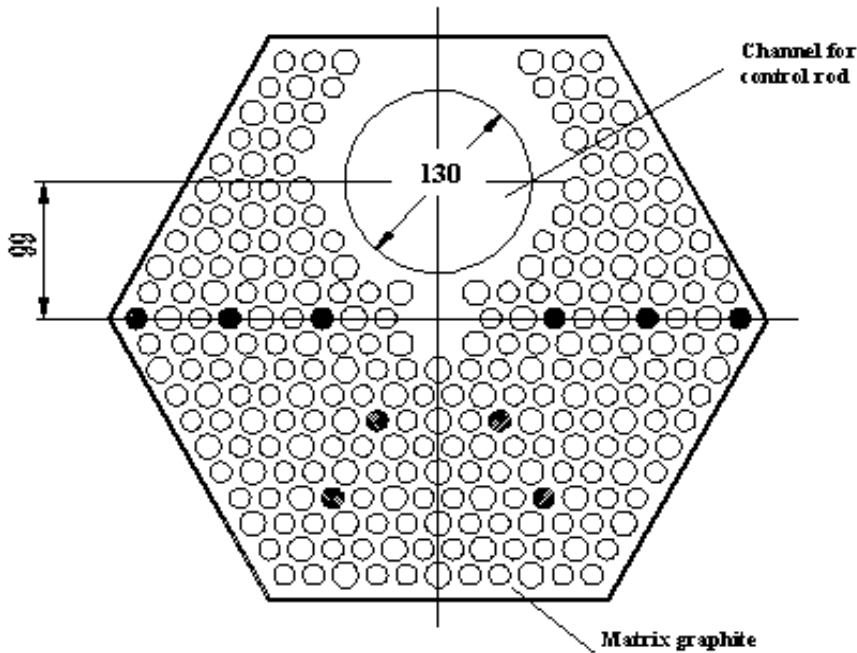


Figure 9-11. Fuel block with cavity for control rod or reserve shutdown system (type 2FA).

9.3.2 Test Results

Because the GT-MHR benchmark problem gives nuclear data as nuclide density, homogenized cross-sections must be generated for nodal calculation. Generating homogenized cross sections is an involved and distinct task outside the scope of this project. In this research, simple 10-group homogenized cross-sections are used for GT-MHR FAs, which are obtained informally from KAERI (and that are incomplete, e.g., cross sections for rodded blocks are not available).

The FA radial configuration is described in Figure 9-12. In the configuration, FA1 to FA3 are fuels blocks and FA4 and FA5 are graphite blocks. Test calculation results by the COREDAX code are shown in Table 9-5.

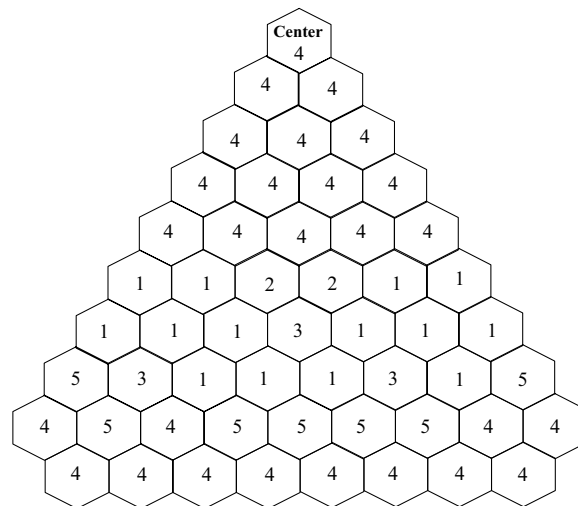


Figure 9-12. Radial core configuration of simplified 3-D GT-MHR.

Table 9-5. Results on k_{eff} of simplified GT-MHR benchmark problem.

Case	VENTURE (ref.)	COREDAX (% error)
All Rods Out	1.52712	1.52503 (0.1365)
All Rods In	0.82419	0.82360 (0.0718)

10. TASK 9: COUPLED CORE MODEL V&V (KAIST)

******* This Task was not within the scope of Fiscal Year 2008. *******

This task involves the verification of the GAMMA code coupled with COREDAX code and validation of the prediction results of thermal power distribution in the hexagonal reactor core. The following activities will be carried out in this task in FY-09:

- Verification of the GAMMA and COREDAX coupling
- Validation of coupled code with reference data.

11. SUMMARY AND CONCLUSIONS

Seven of the nine tasks proposed in the FY-08 scope were carried out as summarized below.

Task 1—Density-driven induced stratified flow analysis using a CFD code

Task 1 consists of a preliminary CFD analysis to understand the density-driven stratified flow in the VHTR air-ingress accident. This task was motivated by the issue that the previous assumption, based on the molecular diffusion, is physically incorrect because of different densities between helium coolant and air. According to the new theory, the density of helium is much lower than that of air, so the air has significant tendency to flow down the helium coolant for stabilization. It eventually forms the counter-current flow, and significantly accelerates the air-ingress process. Various calculation parameters were considered for CFD analyses, including a number of turbulence models, core temperature, initial air mole-fraction, and flow resistance in the core. The GT-MHR 600 MWt was selected as the reference reactor, which was simplified to be 2-D geometry. The core and the lower plenum were assumed to be porous bodies.

The calculation results showed that the air rapidly ingresses into the reactor core with counter-current stratified flow shape. In this calculation, it only took 60 seconds for the air to fill up the whole lower plenum, located at the bottom part of the reactor core, and be stabilized. The final air distribution in the core is highly affected by the core temperature; the higher the temperature, the more the air is ingressed upward into the core because the relatively cold air is stretched in the reactor core by heating, which pushes out the remaining helium coolant; the buoyancy force is also greater than the hydrostatic head. However, the effect of temperature is significantly reduced as the temperature increases because the gas expansion effect is inversely proportional to the temperature.

As a viscous model, a laminar model shows the most conservative results because of the lack of mixing terms. The turbulent mixing term, such as kinetic energy and dissipation, theoretically reduces the density-gradient leading to lower driving force. Among the practical two-equation turbulence models, the k- ϵ realizable model shows the most similar results to the RSM, which is generally known to be the most accurate and precise. Decreasing the initial cavity air-mole fraction greatly delayed the stratified flow process, however its time scale (60–90 seconds) is still instantaneously small compared to the whole air-ingress time frame (~150 hrs).

Following the preliminary CFD results, the air-ingress analysis for the whole scenario was performed using two different codes: The GAMMA system code and the FLUENT code. The analysis procedure is as follows.

1. The depressurization process was calculated by the GAMMA code and the results of temperature and gas concentrations were implemented into the FLUENT code as initial and boundary conditions.
2. The FLUENT code was used for calculating the stratified flow at the initial stage of air-ingress.
3. The calculated FLUENT results of quasi-steady state values of temperature and gas concentrations at the onset natural convection were implemented back into the GAMMA code as initial boundary conditions.
4. The GAMMA code calculated the rest of the air-ingress process, including diffusion and natural convection processes.

Based on these analyses, the onset of natural convection time was predicted to be about 160 seconds, significantly earlier than the previous predictions based on the molecular diffusion mechanism, which leads to the conclusion that the consequences of this accident would be much more serious than previously expected. The temperature effect was not recognized from these calculations for four different

scenarios because (a) the limited oxygen is consumed in the lower plenum and negligible oxidation occurs in the core, (b) the unique high heat capacity of the graphite holds the temperature rise very slowly, and (c) the decay heat removal from the core.

Task 2—Test loop design for experiments of the stratified flow using the FLUENT code as a design-aid numerical tool

Task 2 consists of an experimental plan for the density-driven stratified flow, which was motivated by the need to validate the codes. Some important phenomena to be validated were identified and summarized in the design matrix with the required experiments. The experiments are divided into two parts: nonisothermal and isothermal. The isothermal test focuses on the validation of the codes for the separate effect of the stratified flow phenomenon. The test-section dimensions and sizes were determined by the simple scaling analysis in order to make the flow similar to that of the reference VHTR. The nonisothermal tests were designed to validate various coupling effects with the stratified flow, including heat transfer, porous media, and chemical reactions. The main measurement parameter in the nonisothermal tests is the onset time of the natural convection, which can be detected by flow rate and temperature monitoring. All experiments were designed to be instrumented and detected by optical devices. CFD calculations were performed as part of FY-08 task to make sure to understand the stratified flow phenomena to be visualized in the test loop and to determine the indicator of the onset of the natural convection.

Task 3—Advanced graphite oxidation study for the high burn-off region

Task 3 consists of experimental investigation of graphite oxidation in the air-ingress, especially focusing on the collapse of the graphite structure by corrosion. The following characteristics of graphite were considered to predict this phenomenon: (a) effect of oxidation degree on the graphite strength, (b) effect of oxidized graphite density on the oxidation rate, and (c) surface area density in the graphite internal pores. The previous correlation in the literature between oxidation and graphite strength is well documented, using measurements at burn-off below 10%. The actual collapse of the graphite structure in the accident is expected to occur at burn-off above 50%, so the previous correlations needed to be validated for use in the extrapolated beyond 10% range. To achieve that validation, a new methodology was developed that measured the degree of burn-off at which the graphite loses its mechanical strength at higher burn-off using the sample holder developed in this study (see Figure 4.6). That measurement was performed for nuclear graphite IG-110 and H451. The data obtained was then compared to the previous correlations for validation, and two new correlations containing the data from low burn-off to high burn-off were developed for IG-110 and H451 graphite. These new correlations predict the oxidized graphite strength more conservatively than the previous correlations. The effect of burn-off on the oxidation rate was previously investigated for the same graphite. Using that previously published data, the relationships between burn-off and oxidation rate were obtained for other graphite: NBG-10, NBG-18 and V484T. These relationships can be used in transient analysis of the later air-ingress analysis.

Generally, the reaction rates are proportional to the reacting surface area. The initial oxidation rate is therefore smaller in IG-110 graphite ($890 \text{ m}^2/\text{m}^3$) than in H451 graphite ($1,320 \text{ m}^2/\text{m}^3$). However, as the oxidation progresses, the surface area density of IG-110 increases more rapidly than that of H451 because of the unique characteristic of internal graphite pore structure behaviors. The internal pore surface area increases by oxidation and decreases by joining or collapsing around the expanded pores at the higher burn-off. From the test, the oxidation rate of IG-110 becomes larger than that of H451 as the burn-off progresses (see Figure 4-17). This means that only comparisons based on the initial surface area densities or reaction rates of the original graphite can lead to the misunderstanding of graphite oxidation characteristics. For example, comparisons show that H451 graphite has better oxidation resistance than IG-110 over the long term, which is more important in the air-ingress accident. Therefore, the comparisons of other graphites based on this method are highly recommended, and more tests will be

carried out in FY-09 and FY-10. It is strongly suggested that this new method be used to select the nuclear graphite for the NGNP.

The surface area densities of some nuclear graphite have been calculated about BET surface areas from the published data of previous investigators. In parallel with the experimental works, an analysis has been performed to predict the graphite collapse time in the air-ingress accident. In this analysis, changes of graphite oxidation and corrosion were calculated by the GAMMA code, and the corrosion and oxidation data were implemented to the ABAQUS stress analysis code. As a result, the collapse of the graphite structure has been estimated to occur about 5 days after natural convection starts. The broken part is at the top of the lower plenum. However, the effect of stratified flow has not been considered, so the results are different from those of a real accident. The effect of the stratified flow will be considered in the continued research.

Task 4 will be performed in FY-09 and FY-10.

Task 5—Experiment on burn-off in the core bottom structure in the lower burn-off region

Task 5 consists of experimentally investigating the effects of graphite oxidation on the bottom reflector of a VHTR for the air-ingress accident. The effects of temperature, oxygen concentration, flow rate, graphite shape and size, moisture, and the degree of burn-off in the bottom reflector were considered.

Task 6—Structural tests of oxidized core bottom structures

Task 6 considers the failure prediction of oxidized graphite column in bottom reflector in high temperature gas-cooled reactor design. A simplified graphite column has two main failure mechanisms. The short graphite column critical load is determined by compressive strength and the relatively long critical load is determined by buckling strength. The critical strength of graphite columns was reduced with an increase in the slenderness ratio. The slenderness ratio at which buckling started to occur was about 11.76. The strength of a graphite column is determined by its slenderness ratio. Graphite columns of the same slenderness ratio have the same strength, even though their columns have different diameters. The slenderness ratio can therefore be a strength scaling parameter for a simple cylindrical graphite column. In this task, the GAMMA code calculation was performed to know the trend and condition of oxidation in the bottom reflector. The critical strength of graphite that is uniformly oxidized can be expressed by the Knudsen relation. It turns out that the strength degradation trend of oxidized graphite structure is independent of geometry, while the strength degradation of a uniformly oxidized graphite structure is dependent on the initial strength of the structure and the bulk density change. The bulk density measurement method using the gravimeter is available for oxidized graphite. This method will be used in analyzing graphite that is not uniformly oxidized at Zones II and III.

Task 7—Coupling neutronic-thermal hydraulic tools

Task 7 involves preparatory work consisting of determining coupling factors, mapping nodes between the GAMMA and COREDAX, and organizing calculation logic to couple T/H and neutronics codes into a system code GAMMA/COREDAX.

Task 8—Development of the core neutronic model

Task 8 describes the COREDAX code based on the AFEN method in 3-D hexagonal geometry. The AFEN method includes the use of node-interface flux moments as nodal unknowns. These nodal unknowns increase the accuracy of 3-D calculation results. The multigroup extension, based on matrix function theory and coarse group rebalance acceleration, is described in detail. The COREDAX code implementing the AFEN method was verified by testing the VVER-440 benchmark problem, a simplified

VVER-1000 benchmark problem, and the SNR-300 benchmark problem. A neutronics calculation of a simple GT-MHR core was performed. This core is geometrically based on the GT-MHR benchmark problem, but the cross-sections are informally obtained.

Task 9—Coupled core model V&V (KAIST)

Task 9 involves the verification of the GAMMA code coupled with COREDAX code and the validation of the prediction results of thermal power distribution in the hexagonal reactor core. This task will be performed in FY-09 and FY-10.

12. REFERENCES

Executive Summary and Chapter 1 (Introductions)

Oh, C. H., Davis, C., Siefken, L., Moore, R., NO, H. C., Kim, J. , Park, G. C., Lee, J. C. and Martin, W. R., *Development of Safety Analysis Codes and Experimental Validation for a Very High Temperature Gas-Cooled Reactor, Final Report*, Idaho National Laboratory, INL/EXT-06-01362, March 2006.

Schultz et al., *Next Generation Nuclear Plant Methods Technical Program Plan*, INL/EXT-06-11804, Rev 0.26, September 2006.

Chapter 2 (Task 1)

Bergelin, O. P., Colburn, A. P., and Hull, H. L., "Heat Transfer and Pressure Drop during Viscous Flow across Unbaffled Tube Banks," Engineering Experimental Station, Bulletin No.2, University of Delaware, Newark, DE, 1950.

Chilton, T. H. and Generaux, R. P., "Pressure Drop Across Tube Banks," *Trans. Am. Inst. Chem. Eng.*, Vol 29, pp. 161–173, 1933.

Damerow, W. P., Murtaugh, J. C., and Burgraf, F., "Experimental and Analytical Investigation of the Coolant Flow Characteristics in Cooled Turbine Airfoils," NASA, CR-120883, 1972.

FLUENT Inc., Lebanon, N.H., FLUENT 6.3 User's Guide, 2007.

Gaddis, E. S. and Gnielski, V., "Pressure Drop in Horizontal Cross Flow across Tube Bundles," *Int. Chem. Eng.*, 25s1-D, pp. 1–15, 1985.

General Atomic, Internal Design Review Presentation Material, December 8–12, 1997.

General Atomics Co., *Gas Turbine-Modular Helium Reactor (GT-MHR) Conceptual Design Description*, Report 910720, Revision 1, July, 1996.

Gunter, A. Y. and Shaw, W. A., 1945, "A General Correlation of Friction Factors for Various Types of Surfaces in Cross Flow," *Mech. Eng. Am. Soc. Mech. Eng.*, 67, pp. 643–660, 1945.

Jacob, M., "Discussion-Heat Transfer and Flow Resistance in Cross Flow of Gases Over Tube Banks," *Mech. Eng. Am. Soc. Mech. Eng.*, 60, pp. 381–392, 1938.

Kim, E., NO, H. C., Kim, B., and Oh, C. H., "Estimation of Graphite and Mechanical Strength Variation of VHTR during Air-Ingress Accident," In press to Nuclear Engineering and Design, 2007.

Kosar, A., Mishra, C. and Peles, Y., "Laminar Flow Across a Bank of Low Aspect Ratio Micro Pin Fins," *J. Fluid Engineering*, Vol. 127, pp 419-423, 2005.

Lauder, B. E. and Spalding, D.B., "The numerical computation of turbulence flows," *Cop. Math. App. Mech. Eng.*, Vol. 3, pp. 269-289, 1974.

Lindeburg, M. R., *Mechanical Engineering Reference Manual*, Professional Publications, INL, ISBN 1-888577-13-4, 1997.

Liou, C. P., Parks, D. L., Schultz, R. R., and Williams, B. G., "Stratified Flows in Horizontal Piping of Passive Emergency Core Cooling Systems," *13th International Conference on Nuclear Engineering, ICONE 13-50450, May 16-20, Beijing, China*, 2005.

McEligot, D. M., and McCreery, G. E., *Scaling Studies and Conceptual Experiment Designs for NGNP CFD Assessment*, INEEL/EXT-04-02502, 2004.

- Metzger, D. E., Fan, Z. N., and Shepard, W. B., "Pressure Loss and Heat Transfer Through Multiple Rows of Short Pin Fins," *Journal of Heat Transfer*, Vol. 3, edited by U. Grigull et al., Hemisphere, Washington, pp.137–142, 1982.
- Moores, K. A. and Joshi, Y. K., "Effect of Tip Clearance on the Thermal and Hydrodynamic Performance of a Shrouded Pin Fin Array," *J. Heat Transfer*, 125, pp. 999–1006, 2003.
- NIST Chemistry Webbook, <http://webbook.nist.gov/chemistry/fluid/>
- NO, H. C., Lim, H. S., Kim, J., Oh, C. H., Siefken, L. and Davis, C., "Multi-component diffusion analysis and assessment of GAMMA code and improved RELAP5 code," *Nuclear Engineering and Design*, 237, 2007. pp. 997-1008.
- Oh, C. H., Davis, C., Siefken, L., Moore, R., NO, H. C., Kim, J., Park, G.C., Lee, J.C. and Martin, W. R., *Development of Safety Analysis Codes and Experimental Validation for a Very High Temperature Gas-Cooled Reactor*, Final Report, Idaho National Laboratory, INL/EXT-06-01362, March 2006.
- Schultz, R. R., Krusch, S. E., McCreery, G. E., McIlroy, H., Oh, C. H., Lucas, D. S., Farmer, M. T., Lomperski, S. W., Tzanos, C. P., Pointer, W. D., Wei, T. Y., and Liou, C. P., *Next Generation Nuclear Plant Methods Thermal-Fluids Experiment Plan*, INL/EXT -07-13289, September, 2007.
- Short, Jr., B. E., Price D. C., and Raad P. E., "Design of Cast Pin Fin Cold walls for Air-Cooled Electronic Systems," *J. Electron. Packag.*, 126, pp. 67–73, 2004.
- Sparrow, E. M. and Kang, S. S., "Longitudinally-finned Cross Flow Tube Banks and their Heat Transfer and Pressure Drop Characteristics," *Int. J. Heat Mass Transfer*, 28s 2d, pp. 339–350, 1985.
- Taborek, J., "Shell-and-Tube Heat Exchangers: Single phase Flow," *Handbook of Heat Exchanger Design*, Hemisphere, New York, Chap. 3.3, 1983.
- Takeda T., "Air Ingress Behavior during a Primary-pipe Rupture Accident of HTGR," JAERI-1338, Japan Atomic Energy Research Institute, 1997.
- Takeda T., *Mixing Process of a Binary Gas in a Density Stratified Layer*, JAERI-Research 97-061, Japan Atomic Energy Research Institute, 1997.
- Takeda, T. and M. Hishida, 1996, "Studies on Molecular Diffusion and Natural Convection in a Multicomponent Gas System," *International Journal of Heat and Mass Transfer*, 39, Vol. 3, 1996, pp. 527-536.
- Vassallo, P. and Symolon, P., *Friction Factor Measurements in an Equally Spaced Triangular Tube Array*, LM-07K012, March 19, 2007.
- Yih, C. S., *Stratified Flows*, Academic Press, 1980.

Chapter 3 (Task 2)

- Bombach, R., "Laser Spectroscopy in Combustion Research," Ch. 2, Paul Scherrer Institut, Switzerland, Internet URL: <http://cdg.web.psi.ch/Summerschool/chap2.pdf>, 2004.
- Duncan, J. B. and Toor, H. L., "An experimental study of three component gas diffusion," *A.I.Ch.E. Journal*, 8, 1, 38, 1962.
- Hishida, M and Takeda. T., "Study on air ingress during an early stage of a primary-pipe rupture accident of a high temperature gas-cooled reactor," *Nuclear Engineering & Design*, 126, 175, 1991.
- International Atomic Energy Agency, *Heat Transport and Afterheat Removal for Gas Cooled Reactors under Accident Conditions*, IAEA-TECDOC-1163, 1981.

- Jose N. Reyes, Jr. and John T. Groome, “Developing Core Flow Analysis Methods for the VHTR and GFR Designs,” *Annual Report 2006*, Idaho National Laboratory.
- Kadak A. C., and Zhai T., “Air ingress benchmarking with computational fluid dynamics analysis,” *Nuclear Engineering and Design*, Vol. 236, pp. 587-602, 2005.
- Kirby, B. J., “Infrared Planar Laser-Induced Fluorescence Imaging and Applications to Imaging of Carbon Monoxide and Carbon Dioxide,” Ph D. dissertation, 2001.
- Liou, C. P., Parks, D. L., Schultz, R. R., and Williams, B. G., “Stratified Flows in Horizontal Piping of Passive Emergency Core Cooling Systems,” *13th International Conference on Nuclear Engineering, ICONE 13-50450, May 16-20, Beijing, China, 2005*.
- Ogawa, M., “Mass Transfer with Graphite Oxidation in Gas Mixture Laminar Flow through Circular Tube,” *J. At. Energy Soc. Jpn.*, 35, 3, 245, 1993.
- Oh, C., Kim, E., Schultz, R., Petti, D. and Liou, C., *Implication of Air Ingress Induced by Density-Difference Driven Stratified Flow*, ICAPP'08, Anaheim, USA, June 8–12.
- Oh, C. H., Davis, C., Siefken, L., Moore, R., NO, H. C., Kim, J., Park, G. C., Lee, J. C., and Martin, W. R., *Development of Safety Analysis Codes and Experimental Validation for a Very High Temperature Gas-Cooled Reactor*, Final Report, Idaho National Laboratory, INL/EXT-06-01362, March 2006.
- Schultz, R. et al., *Next Generation Nuclear Plant Methods Technical Program Plan*, INL/EXT-06-11804, Rev 0.26, September 2006.
- Suh, N. P., *The Principles of Design*, Oxford University Press, Inc., ISBN 0-19-504345-6 1990.
- Takeda T., *Air Ingress Behavior during a Primary-pipe Rupture Accident of HTGR*, JAERI-1338, Japan Atomic Energy Research Institute, 1997.
- Turner, J. S., *Buoyancy Effects in Fluids. Cambridge Monographs on Mechanics and Applied Mathematics*, Cambridge University Press, 1973.
- Yokomae, T., “Planar Laser-Induced Fluorescence (PLIF) of H₂-O₂ Combustion,” Master Thesis, University of Texas at Arlington, 2003.

Chapter 4 (Task 3)

- ABAQUS, Inc, 2007, “Getting Started with ABAQUS (ver. 6.75).”
- Beer, F. P., Dewolf, J. T., Johnston, E. R., *Mechanics of Materials*. (4th ed). New York: McGraw-Hill, 2006.
- Bratton, R. L., Burchell, T. D., Corwin, W. R., Hayner, G. O., Katoh, Y., Klett, J. W., *Next Generation Nuclear Plant Materials Research and Development Program Plan*, INL/EXT-05-00758 Rev. 2, September 2005.
- Brauauer, S., Emmett, P. H., Teller, T., “Adsorption of gases in multimolecular layers,” *J. Amer. Chem. Soc.*, 60, 1938, 309–319.
- Burchell, T. D., Eto, M., Ishiyama, S., Strizak, J. P., “The Effect of high Fluence Neutron Irradiation on the Properties of a Fine-Grained Isotropic Nuclear Graphite,” *Journal of Nuclear Materials*, 230, pp. 1–7, 1996.
- Burchell, T. D., Romanoski, G. R., “The Effects of Specimen Geometry and Size on the Fracture Toughness of Nuclear Graphites,” ORNL CONF-9109266-1, January 1991.

- Cocheme, F. G., "Assessment of Passive Decay Heat Removal in the General Atomic Modular Helium Reactor," Unpublished master's thesis, Texas A&M University, Texas, U.S.A., 2004.
- Collins, A. C., Masterson, H. G. and Jennings, P. P., *Journal of Nuclear Materials*, 15, 145, 1965.
- Contescu, C., "Current R&D Activities on Graphite Oxidation at ORNL," personal communication, NGNP R&D Technical Review Meeting, Idaho National Laboratory, May 5–8, 2008.
- Contescu, C. I., Azad, S., Miller, D., Lance, M. J., Baker, F. S., and Burchell, T. D., "Practical aspects for characterizing air oxidation of graphite," *Journal of Nuclear Materials*, in press (available online), 2008.
- Engle, G. B., *General Atomics Co. Report*, GA-A14690, 1977.
- Eto, M. and Growcock, F. B., "Effect of oxidizing environment on the strength of H451, PGX and IG-11 graphites," *Carbon*, Vol. 21, No. 1, pp. 135–147, 1983.
- Eto, M., Konishi, T., Oku, T., "High Temperature Young's Modulus of IG-110 Graphite," *JAERI Conference article from Specialists' meeting on graphite component structural design, JAERI Tokai (Japan)*, September 8-11, 1986, conducted by the International Atomic Energy Agency, Vienna (Austria). "International Working Group on Gas-Cooled Reactors," IWGGCR-11, pp. 133–137, 1986.
- Eung Soo Kim* and Hee Cheon NO, "Experimental study on the oxidation of nuclear graphite and development of an oxidation model," *Journal of Nuclear Materials*, 2006, Vol. 349, pp. 182–194.
- Fagerlund, G., "Determination of specific surface by BET method," *Materiaux et Constructions*, 1973, 6(33), 239–245.
- Fujii, K., Nakano, J., Yamada, R., "Mechanical Properties of Oxidation-Resistant SiC/C Compositionally Graded Graphite Materials," *Journal of the American Ceramic Society*, Vol. 80, No. 11, pp. 2897–2902, 1997.
- Fuller, E. L., Okoh, J. M., "Kinetics and mechanisms of the reaction of air with nuclear grade graphites: IG-110," *J. Nuclear Materials*, 1997, Vol. 240, pp. 241–250.
- General Atomics, "International GT-MHR Project Internal Design Review Presentation Material," 1997.
- General Atomics, *Screening Tests for Selection of VHTR Advanced Fuel*, Contract No. DE-AC03-01SF22343, Revision 0, 2003.
- Hinssen, H. K., Kuhn, K., Moorman, R., Schlogl, B., Fechter, M. and Mitchell, M., "Oxidation experiments and theoretical examinations on graphite materials relevant for the PBMR," *Nuclear Engineering and Design*, in press (accessible on the website), 2008.
- Ishihara, M., Iyoku, T., Oku, T., Shibata, T., Sumita, J., "Principle Design and Data of Graphite Components," *Nuclear Engineering and Design*, Vol. 233, pp. 251–260, 2004.
- McCreery, G. E., McEligot, D. M., *Scaling Studies and Conceptual Experiment Designs for NGNP CFD Assessment*, INEEL/EXT-04-02502, November 2004.
- Moorman, R., Alberici, S., Hinssen, H. K., Krussenberg, A. K., Wu, C. H., "Oxidation behavior of carbon-based materials used for HTGRs and fusion reactors." *Adv. Sci. Technol.*, Vol. 24, 331–339, 1999.
- Ogawa, M., "Mass Transfer with Graphite Oxidation in Gas Mixture Laminar Flow through Circular Tube," *J. At. Energy Soc. Jpn.*, 35, 3, 245, 1993.
- Rasmussen, K., *Full-range Stress-strain Curves for Stainless Steel Alloys*, Published Ph.D research, Report No R811, University of Sydney, Sydney, Australia., 2001.

Shenoy, “Modular Helium Reactor Design, Technology and Applications,”
<http://cer.ucsd.edu/SEMINARS/Shenoy.ppt>, 2007.

Velasquez, C., Hightower, G., and Burnette, R., *The oxidation of H-451 graphite by steam, Part 1: reaction kinetics*, General Atomics Report GA-A14951.

Wichner, R. P., *Oak Ridge National Laboratory Report*, ORNL/TM-5534, 1976.

Chapter 5 (Task 4)

Task 4 is not in the scope of this year.

Chapter 6 (Task 5)

KIM, E. S., *Development of Graphite Oxidation Models for Air-ingress Analysis in HTGR*, pp. 52, KAIST, 2006.

Oh, C.H. et al., *Development of Safety Analysis Codes and Experimental Validation for a Very High Temperature Gas Cooled Reactor*, INL/EXT-06-01362, pp. 112–141, March 2006.

Robert Bratton and Timothy Burchell, *NGNP Graphite Testing and Qualification Specimen Selection Strategy*, INL/EXT-05-00269, pp. 8–14, May 2005

Welty, J. R., Wicks, C. E., Wilson, R. E., *Fundamentals of Momentum, Heat and Mass Transfer*, John Wiley and Sons, pp. 615-618.

Chapter 7 (Task 6)

Singer, F. L., and Pytel, A., *Strength of Material*, pp. 441–453, Harper & Row, New York, 1980.

Neighbour, G. B., Hacker, P. J., “The Variation of Compressive Strength of AGR Moderator Graphite with Increasing Thermal Weight Loss,” *Materials Letters*, Vol. 51, p. 307, 2001.

Eto, M., and Growcock, T., “Effect of Oxidizing Environment on the Strength of H451, PGX and IG-11,” *Carbon*, 21, 2, pp. 135–147, 1983.

KIM, E. S. et al., “Estimation of Graphite Density and Mechanical Strength Variation of VHTR during Air-ingress Accident,” *Nuclear Engineering and Design*, 238, 4, pp. 837–847, 2008.

Chapter 8 ~ 10 (Task 7, 8, 9)

Cho, N. Z. and Noh, J. M., “Analytic Function Expansion Nodal Method for Hexagonal Geometry,” *Nucl. Sci. Eng.*, 121, p. 245, 1995.

Woo, S. W., Cho, N. Z., and Noh, J. M., “The Analytic Function Expansion Nodal Method Refined With Transverse Gradient Basis Functions and Interface Flux Moments,” *Nucl. Sci. Eng.*, 139, p. 156, 2001.

Kim, D. S. and Cho, N. Z., “Kinetics Calculation under Space-Dependent Feedback in Analytic Function Expansion Nodal Method via Solution Decomposition and Galerkin Scheme,” *Nucl. Sci. Eng.*, 140, p. 267, 2002.

Cho, N. Z., and Lee, J., “Analytic Function Expansion Nodal (AFEN) Method in Hexagonal-Z Three-Dimensional Geometry for Neutron Diffusion Calculation,” *Journal of Nuclear Science and Technology*, 43, p. 1320, 2006.